Transport and Superconductivity in Spin-Orbit Coupled Electron Systems

by

Joel Gordon Hutchinson

A thesis submitted in partial fulfillment of the requirements for the degree of

Doctor of Philosophy

Department of Physics

University of Alberta

Abstract

This thesis provides a theoretical discussion of several new phenomena associated with spin-orbit coupling in systems that lack inversion symmetry. Chapter 1 gives an introduction to the context of spin-orbit coupling in condensed matter physics and the role of inversion symmetry breaking. The remainder of the thesis is divided into two parts. Part 1 explores the effects of spin-orbit coupling on low-energy electron-impurity scattering. First, we study the single-particle scattering problem (Chapters 3 and 4) and find a host of unusual properties at ultra-low energies, including a quantized cross section. Chapter 5 extends these results to transport in a many-body system, where the quantized cross section manifests itself as a quantized conductivity. Part 2 explores the effect of spin-orbit coupling on superconductivity within BCS theory. In Chapter 7, we find that the critical temperature can be tuned by this coupling. In Chapter 8 we discuss the symmetry of the superconducting order parameter in the presence of attractive interactions between nearest-neighbour electrons. There we find that the gap function symmetry can change as a function of all the material parameters, including the temperature and spin-orbit coupling.

Preface

Chapters 3, 4, 5, and 7 of this dissertation are an elaboration and summary, with permission, of references [1–5], of which I am the first author. Many results are taken directly from these papers. All figures and tables are my original work. Joseph Maciejko supervised the projects outlined in Part 1. Frank Marsiglio supervised the projects outlined in Part 2. The setup and motivation for Chapter 7 was provided by our collaborator Jorge Hirsch.

"The task is, not so much to see what no one has yet seen; but to think what nobody has yet thought, about that which everybody sees."

Erwin Schrödinger

Acknowledgements

I would like to start by thanking both of my supervisors Joseph Maciejko and Frank Marsiglio. Their support and encouragement over the last four years has been truly invaluable. Their passion for physics is infectious, and their ability to think through difficult research challenges is inspiring. It is a rare privilege to have a mentor that puts their students first, and communicates freely and effectively with them. It is even more rare to have two such mentors. I count myself lucky because of this.

I would also like to thank my committee member Lindsay LeBlanc. Over the course of my PhD she has injected some crucial experimental questions and insights into this otherwise theoretical work.

I wish to thank my collaborator Jorge Hirsch as well. He is a genuine person and a brilliant physicist. His perseverance in following his own ideas has led to some very interesting concepts and paved the way for Chapter 7 of this thesis.

A special thanks goes to my friends and colleagues in the department for their support and discussion, both academic and otherwise. In particular, I would like to acknowledge David Purschke, whose insatiable curiosity, and long discussions with me led to the pump-probe proposal described in Section 5.1.2.

Several funding agencies made this work possible, including the National Science and Engineering Research Council (NSERC) and Alberta Innovates - Technology Futures. Their support allowed me to dedicate my efforts to research without worrying about finances.

I am eternally grateful to my partner Farah Elawar. Her countless hours of support, from helping me prepare talks to editing this thesis, got me through my degree. I have never met such a loving person and I am humbled to be the recipient of her relentless encouragement and support. I only hope I can return the favour when she writes her PhD thesis.

I owe a huge thanks to my entire family. In particular, I would like to thank my parents, not only for their support and compassion throughout this degree, but also for recognizing my dreams early in life and standing behind them. My mother's generosity and work ethic is truly inspirational and has given me the confidence needed to complete this work. My father is proof that curiosity is one of the most important assets for parenting. Little actions, like leaving a popular physics book on the coffee table, or asking me whether light was a particle or a wave when I was too young to understand either, set me on this path. For that reason, I dedicate this dissertation to him.

Table of Contents

List of Tables

List of Figures

Abbreviations

SOC	Spin-orbit coupling
ARPES	Angle-resolved photoemission spectroscopy
Irrep	Irreducible representation
DOS	Density of states
2D	Two-dimensional
3D	Three-dimensional
2DEG	Two-dimensional electron gas
FET	Field-effect transistor
DC	Direct current
AC	Alternating current
SCBA	Self-consistent Born approximation
SCFBA	Self-consistent full Born approximation
BCS	Bardeen-Cooper-Schrieffer

Physical Constants

Speed of light	c	=	$2.99792458 \times 10^{8}\text{m/s}$
Electron mass	m	=	$9.10938356 \times 10^{-31}\text{kg}$
Electron charge (magnitude)	e	=	$1.60217662 \times 10^{-19}\text{C}$
Reduced Planck's constant	$\hbar$	=	$1.05457180 \times 10^{-34}\text{J·s}$
Boltzmann constant	k_B	=	$1.38064852 \times 10^{-23}\text{m}^2\text{kg·s}^{-2}\text{K}^{-1}$

Symbols

$\|\nu\rangle$	Dirac ket for state ν
$\langle\nu\|$	Dirac bra for state ν
$a_\mu^\dagger$, a_μ	bosonic creation and annihilation operators
$c_\mu^\dagger$, c_μ	electron creation and annihilation operators
c_v	specific heat per unit volume at constant volume
$d_{\boldsymbol{k}}$	d-wave basis function
E	scattering energy (part 1)
E_0	energy at the Dirac point (part 1)
E_g	ground state energy (part 2)
$E_{\boldsymbol{k}s}$	quasi-particle dispersion (part 2)
$\boldsymbol{\mathcal{E}}$	electric field vector
f	free energy density (part 2)
$f_{\mu\nu}$	scattering amplitude (part 1)
$f(E)$	Fermi-Dirac distribution function
$\mathcal{F}_s(\boldsymbol{k},\tau)$	anomalous Matsubara Green's function in helicity band s
$g(E)$	single-particle density of states
$G^A_{\alpha\beta}(\boldsymbol{k},E)$	advanced Green's function in helicity basis
$G^R_{\alpha\beta}(\boldsymbol{k},E)$	retarded Green's function in helicity basis
$\mathcal{G}_s(\boldsymbol{k},\tau)$	Matsubara Green's function in helicity band s
H	general Hamiltonian
H_0	unperturbed Hamiltonian
H'	perturbed part of a Hamiltonian
H_{MF}	mean-field Hamiltonian
$H_l^\pm(x)$	Hankel function of order l (part 1)

H_{ij}	Hessian matrix (Appendix H)
I	tunnelling current (Chapter 7)
$\mathbb{I}$	identity matrix
$\boldsymbol{j}$	probability current
$J_l(x)$	Bessel function of order l
$\boldsymbol{J}$	charge current
$\boldsymbol{k}$	general wavevector
$\boldsymbol{k}_0$	ground-state wavevector
$\boldsymbol{k}_F$	Fermi wavevector
l	partial wave number
$\boldsymbol{L}$	angular momentum operator
n	electron density
n_0	electron density at the Dirac point (Chapter 5)
$n_c(t)$	density of conduction electrons (Chapter 5)
n_i	impurity density (Chapter 5)
$n_{i\sigma}$	electron density on site i with spin σ (part 2)
N	number of sites
$N_l(x)$	Neumann function of order l
$N^{\mathrm{SC}}(\omega)$	superconducting density of states
$\boldsymbol{p}$	general momentum vector
$P^{AR}(E)$	advanced-retarded response function
$P^{RR}(E)$	retarded-retarded response function
$\boldsymbol{q}$	general wavevector
$\boldsymbol{r}$	general position vector
R	potential radius (part 1)
s	helicity index
$s_{\boldsymbol{k}}$	extended s-wave basis function
$\boldsymbol{S}$	spin operator
$S_{\mu\nu}$	lower helicity S-matrix
$S^l_{\mu\nu}$	partial wave component of lower helicity S-matrix
t	general time variable (part 1)
t	hopping amplitude (part 2)
T	temperature

T_c	critical temperature
$T^{\boldsymbol{r},\boldsymbol{r}'}_{\sigma\sigma'}$	T-matrix in real space and spin basis
$T^{\boldsymbol{k},\boldsymbol{k}'}_{\sigma\sigma'}$	T-matrix in momentum space and spin basis
$T^{\boldsymbol{k},\boldsymbol{k}'}_{ij}$	T-matrix in momentum space and helicity basis
T^{l}_{--}	partial wave component of the lower helicity T-matrix
$u_{\boldsymbol{k}}$	BCS coherence factor
U	on-site Hubbard interaction (part 2)
$\hat{U}(t,t_0)$	time evolution operator in the interaction picture (part 1)
$\boldsymbol{v}_g$	group velocity
$v_{\boldsymbol{k}}$	BCS coherence factor (part 2)
V	nearest-neighbour interaction (part 2)
$V(\boldsymbol{r})$	potential in real space (part 1)
$V_{ij}(\boldsymbol{k},\boldsymbol{k}')$	potential in momentum space and helicity basis (part 1)
$V^{l}(\boldsymbol{k},\boldsymbol{k}')$	partial wave components of the lower-helicity potential (part 1)
$V_{\alpha\beta\gamma\delta}(\boldsymbol{k},\boldsymbol{k}')$	electron-electron interaction in spin basis (part 2)
$V_{ss'}(\boldsymbol{k},\boldsymbol{k}')$	electron-electron interaction in helicity basis (part 2)
$V^{\mathrm{sing}}(\boldsymbol{k},\boldsymbol{k}')$	parity-even part of the electron-electron interaction (part 2)
$V^{\mathrm{trip}}(\boldsymbol{k},\boldsymbol{k}')$	parity-odd part of the electron-electron interaction (part 2)
V_{SO}	Rashba coupling (lattice)
$W^{\phi_{\boldsymbol{k}}\phi_{\boldsymbol{k}'}}_{\mu\nu}$	lower helicity transition rate
Z	atomic number
$\alpha^{\dagger}_{\mu}$, α_{μ}	Rashba quasiparticle creation and annihilation operators
β	Dresselhaus coupling (Chapter 1)
β	inverse temperature
δ	dimensionless scattering energy parameter (part 1)
δ_{ij}	Kronecker delta
$\delta(\boldsymbol{r})$	Dirac-delta function
Δt	correlated hopping amplitude (part 2)
Δ_i	component of the gap function with respect to the basis function $x^i_{\boldsymbol{k}}$
$\Delta_{\boldsymbol{k}\sigma\sigma'}$	gap function in spin basis
$\Delta_{\boldsymbol{k}s}$	gap function for pairing in helicity band s
$\bar{\Delta}_{\boldsymbol{k}s}$	irreducible part of the gap function for pairing in helicity band s

$\Delta_{\boldsymbol{k}}^{\text{sing}}$	singlet gap function
$\Delta_{\boldsymbol{k}}^{\lambda}$	triplet gap function
ϵ_{ijk}	Levi-Civita symbol
$\epsilon_{\boldsymbol{k}}$	single-particle dispersion
$\epsilon_{\boldsymbol{k}s}$	single-particle dispersion in helicity band s
η^i	eigenspinor for helicity band i
γ	Euler-Mascheroni constant (part 1)
γ_i	critical point index (Appendix H)
$\gamma_\mu^\dagger$, γ_μ	quasiparticle creation and annihilation operators (part 2)
$\Gamma_0(\boldsymbol{p})$	bare vertex part
$\Gamma^{\text{AR}}(\boldsymbol{p}, E)$	advanced-retarded vertex part
$\Gamma^{\text{RR}}(\boldsymbol{p}, E)$	retarded-retarded vertex part
λ	Rashba coupling (continuum)
$\tilde{\lambda}^{\text{AR}}(E)$	advanced-retarded renormalized Rashba coupling
$\tilde{\lambda}^{\text{RR}}(E)$	retarded-retarded renormalized Rashba coupling
Λ	dimensionless momentum cutoff
$\tilde{\Lambda}$	momentum cutoff
μ	chemical potential
ω	angular frequency
$\omega_{\mu\to\nu}$	transition rate
$\Pi_{\text{ret}}(\omega)$	retarded current-current correlator
$\psi(l)$	Digamma function (Chapter 5)
$\psi_\mu(\boldsymbol{r}; E)$	single-particle wavefunction
$\psi_\mu^{\text{in}}(\boldsymbol{r}; E)$	incident wavefunction
$\sigma_x, \sigma_y, \sigma_z$	Pauli matrices
σ	cross section
σ_μ	lower helicity cross section in the μ channel
σ_{DC}	DC conductivity
$\sigma(\omega)$	AC conductivity
$\sigma^{\text{Drude}}(\omega)$	Drude AC conductivity
$\Sigma_{\alpha\beta}(\boldsymbol{k}, E)$	self-energy in the helicity basis
τ	scattering time
τ^{tr}	transport time

τ_n	recombination time
$\theta_{\boldsymbol{k}'-\boldsymbol{k}}$	angle between wavevectors $\boldsymbol{k}$ and $\boldsymbol{k}'$
$\theta(x)$	Heaviside step function
$\xi_{\boldsymbol{k}s}$	single-particle dispersion shifted by the chemical potential

Chapter 1

Introduction

Some of the most poignant insights in physics arise when we are forced to bridge the gap between seemingly disparate realms of description. For example, the macroscopic world that surrounds us is usually well described by classical mechanics and electrodynamics, but as any condensed matter physicist will point out, there are many macroscopic phenomena that require a quantum description to even qualitatively understand, despite the fact that quantum mechanics is a framework built for the atomic world. One prominent bridge between the quantum and macroscopic worlds is the phenomenon of superconductivity, where the Meissner effect and the complete lack of electrical resistance are hallmarks of a macroscopic phase-coherent state. Indeed, quantum physics plays an important role in transport even when the resistance is finite.

Another such bridge was provided in 1928 by Paul Dirac and Ralph Fowler, who connected special relativity and atomic physics to partially explain splittings in the energy level of a Hydrogen atom [6]. The predominant term in the low-velocity limit of Dirac's Hamiltonian is the spin-orbit coupling (SOC). In a sense, this thesis lives between all of these bridges, where relativistic SOC enters in quantum physics and becomes subsequently amplified in a variety of macroscopic phenomena. One might be tempted to neglect such effects in the slow-moving ultra-cold world typical of condensed matter experiments, but our aim is to show how spin-orbit coupling can have unique and drastic consequences both to electron kinematics and interactions within a solid state system.

1.1 Spin-orbit coupling

To begin, let us first understand exactly what is meant by spin-orbit coupling. Dirac's Hamiltonian for an electron in a potential V, expanded to order $(v/c)^4$ (where v is the electron's speed and c is the speed of light) is given by

$$H = \frac{\boldsymbol{p}^2}{2m} + V - \frac{\boldsymbol{p}^4}{8m^3c^2} - \frac{[\boldsymbol{p}, \cdot\, [\boldsymbol{p}, V]]}{8m^2c^2} - \frac{i\boldsymbol{\sigma} \cdot \boldsymbol{p} \times [\boldsymbol{p}, V]}{4m^2c^2}, \tag{1.1}$$

Here $\boldsymbol{\sigma}$ is a vector of Pauli matrices, m is the electron mass, and $\boldsymbol{p}$ is the electron's momentum. The first two terms constitute the non-relativistic Hamiltonian, the third term is a kinetic correction that is negligible for our purposes where the typical kinetic energy is much smaller than the rest mass energy, and the fourth term is the Darwin term[1], which affects only states of zero angular momentum. It is the last term that contains the physics we are interested in. This is the spin-orbit coupling. The name only really makes sense in the context of an atomic potential with atomic number Z, and $V = -Ze^2/r$, where e is the electron charge and r is the distance to the atomic center. In that case, the SOC term becomes

$$H_{\text{SOC}} = -\frac{Z\hbar e^2}{4m^2c^2r^3}\boldsymbol{\sigma} \cdot \boldsymbol{p} \times \boldsymbol{r} = \frac{Ze^2}{2m^2c^2r^3}\boldsymbol{S} \cdot \boldsymbol{L}, \tag{1.2}$$

where $\boldsymbol{S} = (\hbar/2)\boldsymbol{\sigma}$ is the spin (or intrinsic) angular momentum of the electron, while $\boldsymbol{L}$ is its orbital angular momentum and $\hbar$ is the reduced Planck's constant. That this kind of coupling should exist, can be understood in a classical picture. In the electron's rest frame, the orbiting nucleus forms a current with a magnetic field directed perpendicular to the orbital plane in accordance with the right-hand rule. This magnetic field couples to the magnetic moment associated with the electron spin, so that it is energetically favourable for the spin to be anti-aligned with the field, or equivalently in the frame of the nucleus, with the vector $\boldsymbol{L}$.

1.2 Rashba spin-orbit coupling

In this thesis, we are not interested in atomic physics, but rather, solid state systems or analogues where the potential the electron is in is much more complicated than a simple

[1] Named after the physicist Charles Darwin, grandson of the infamous biologist Charles Darwin!

Coulomb potential. Nonetheless, the fifth term in (1.1) exists for any electron in an external potential, and is always referred to as spin-orbit coupling even as it applies to itinerant electrons. The important point to keep in mind is that this a ubiquitous term that couples motional degrees of freedom to spin degrees of freedom. Every electron is sensitive to electric fields in its environment. These are gradients of a potential for which $[\boldsymbol{p}, V] \neq 0$. The simplest such potential is $V = -eEz$, for which the spin-orbit coupling term becomes the so-called continuum Rashba term

$$H_R = \lambda \hat{z} \cdot (\boldsymbol{\sigma} \times \boldsymbol{k}). \tag{1.3}$$

Much of this thesis will be focused on fleshing out the significance of the Rashba term. Here $\boldsymbol{k} = \boldsymbol{p}/\hbar$ is the wavevector and the constant λ is the Rashba coupling, which has dimensions of velocity. In this simple example, it is given by $\lambda = -\hbar^2 eE/(4m^2c^2)$, but in a more realistic model, it will be more complicated. It is clear that strong gradients in the electric potential have significant contributions to SOC, and in a solid material, these will be dominated by ionic potentials. Strong atomic SOC is required for strong Rashba SOC; we should understand this statement to mean that λ is related to the local Coulombic potential and increases with atomic number. For a given material, its value can be assessed theoretically with ab initio methods or experimentally from Angle Resolved Photoemission Spectrosocpy (ARPES) or Shubnikov-de Haas oscillations [7]. As will be seen later, H_R causes states with opposite spin to split in energy; some examples of materials whose spectra exhibit large spin-splitting due to H_R are given in Table 1.1 in terms of the energy scale $E_0 \equiv (1/2)m\lambda^2$ corresponding to the Rashba coupling. For our purposes we will treat λ as a phenomenological parameter. Most results in this thesis are qualitatively independent of its value.

Given the complex spatial dependence of the electric field in a solid material, one might wonder why a term like (1.3), derived from such a simple potential, should exist at all. Yet the fact remains that (1.3) is a real and important term for conduction electrons in many solid state materials. In section 1.3, we will show why this is true on symmetry grounds. The result may be derived using perturbation theory as well, providing a more accurate description of the band structure for specific crystal structures [19]. First, note that unlike the Coulomb potential, the linear potential above breaks inversion symmetry, i.e $H(\boldsymbol{r}) \neq H(-\boldsymbol{r})$. This is an important point. Spin-splitting of the spectrum is fundamentally connected to inversion symmetry breaking in the same way

Material	E_0 (meV)	E_F (meV)	Ref.
Au(111) surface	2.1	400	[8]
InGaAs/InAlAs heterostructure	0.016	$79 - 111*$	[9]
Xe/Au(111) doped surface	7.3	487	[10]
HgTe/HgCdTe heterostructure	$0.3*$	220	[11]
Bi(111) surface	14	65	[12]
Ag thin film on Au(111) surface	< 0.2	> 100	[13]
Bi/Si(111) doped surface	140	1200	[14]
Bi/Ag(111) doped surface	200	-200	[15]
Ir(111) surface	24	-340	[16]
$CH_3NH_3PbBr_3$ surface (valence band)	-160	1000	[17]
BiTeI surface (also contains bulk splitting)	100	300	[18]

TABLE 1.1: A sampling of systems with large spin-splitting E_0. The E_F column refers to the Fermi level measured with respect to the spin-split band minimum (or maximum in the case of a valence band). *These values can change significantly with gate voltage.

that Zeeman splitting is connected to time-reversal symmetry breaking. That such an asymmetry must have an interesting effect on the band structure is easily seen from Kramers degeneracy. Every state in a time-reversal invariant system of electrons (we will exclusively consider systems without an external magnetic field), must be degenerate with its time-reversed partner

$$E(\boldsymbol{k}, \uparrow) = E(-\boldsymbol{k}, \downarrow). \tag{1.4}$$

In a system that lacks inversion symmetry ($\boldsymbol{k} \to -\boldsymbol{k}$), the spin degeneracy $E(\boldsymbol{k}, \uparrow) = E(\boldsymbol{k}, \downarrow)$ is no longer protected and is generally lifted. This can only be accomplished by a Hamiltonian that couples to the spin degrees of freedom, and in the absence of a magnetic field, this coupling must come from the relativistic corrections due to the Dirac equation as discussed above.

1.3 Group theory and chronology of spin-orbit coupling

The field of asymmetry-induced spin-orbit coupling can be quite daunting, so it is worth pausing here to organize its different aspects. A powerful organizing principle in this regard is group theory. Group theory is the natural language within which to consider symmetry-imposed restrictions. Each element of a group corresponds to a particular symmetry transformation, and different objects (scalars, vectors, pseudovectors, etc.) transform according to different representations of each symmetry element [20]. Since

inversion is a symmetry element of point groups, we must consider the structure of different crystallographic point groups, that is, groups of symmetry operations that leave a point fixed and maintain crystallinity. There are 32 such point groups in three dimensions. Of these, 21 are noncentrosymmetric, i.e. they lack a point through which inversion symmetry can be established. Consider one of the simplest (though important) of these groups, C_{2v}. This group consists of a π rotation (say about the $\hat{z}$ axis), and two mirror reflections (in the xz and yz planes). The Hamiltonian must be invariant under all of these operations, but both the spin $\boldsymbol{\sigma}$ and momentum $\boldsymbol{k}$ are not. If there exists a spin-momentum coupling term in the Hamiltonian, then these two quantities must be combined in an invariant way. In this particular example, the transformations of these quantities are simple. Under a π rotation

$$\begin{pmatrix} k_x \\ k_y \\ k_z \end{pmatrix} \to \begin{pmatrix} -k_x \\ -k_y \\ k_z \end{pmatrix}, \quad \begin{pmatrix} \sigma_x \\ \sigma_y \\ \sigma_z \end{pmatrix} \to \begin{pmatrix} -\sigma_x \\ -\sigma_y \\ \sigma_z \end{pmatrix}, \tag{1.5}$$

while under a mirror reflection in xz,

$$\begin{pmatrix} k_x \\ k_y \\ k_z \end{pmatrix} \to \begin{pmatrix} k_x \\ -k_y \\ k_z \end{pmatrix}, \quad \begin{pmatrix} \sigma_x \\ \sigma_y \\ \sigma_z \end{pmatrix} \to \begin{pmatrix} -\sigma_x \\ \sigma_y \\ -\sigma_z \end{pmatrix}, \tag{1.6}$$

and under a mirror reflection in yz,

$$\begin{pmatrix} k_x \\ k_y \\ k_z \end{pmatrix} \to \begin{pmatrix} -k_x \\ k_y \\ k_z \end{pmatrix}, \quad \begin{pmatrix} \sigma_x \\ \sigma_y \\ \sigma_z \end{pmatrix} \to \begin{pmatrix} \sigma_x \\ -\sigma_y \\ -\sigma_z \end{pmatrix} \tag{1.7}$$

(recall that $\boldsymbol{\sigma}$ is an axial or pseudovector). By looking at these transformations, we see that the sign acquired by transforming k_x can always be compensated by the transformation of σ_y and similarly with k_y and σ_x. In other words, symmetry only allows the couplings $k_x\sigma_y$ and $k_y\sigma_x$, and nothing involving the out-of-plane spin.

This was a simple group, but the above reasoning can easily be extended to all the noncentrosymmetric groups as follows. In second quantization, a generic spin-orbit coupling

kinetic term can be written as

$$H = \sum_{\boldsymbol{k}} \sum_{\sigma\sigma'} c^{\dagger}_{\boldsymbol{k}\sigma} H^{\sigma\sigma'}_{\mathrm{SOC}}(\boldsymbol{k}) c_{\boldsymbol{k}\sigma'}, \tag{1.8}$$

where $c^{\dagger}_{\boldsymbol{k}\sigma}$ and $c_{\boldsymbol{k}\sigma}$ are electron creation and annihilation operators respectively, while $H^{\sigma\sigma'}_{\mathrm{SOC}}(\boldsymbol{k})$ comprises all the terms coupling spin and momentum. This term must be linear in the σ_i, owing to the identity

$$\sigma_i \sigma_j = \delta_{ij}\mathbb{I} + i\epsilon_{ijk}\sigma_k, \tag{1.9}$$

where $\mathbb{I}$ is the identity matrix, δ_{ij} is the Kronecker delta, and ϵ_{ijk} is the Levi-Civita symbol. We choose to write it in the following form. First we break up $\boldsymbol{\sigma}$ into a sum of vectors $\boldsymbol{\sigma}^a$ of possibly different sizes n_a that each transform under an irreducible representation (irrep) of the symmetry group. Generically then, this term may be written as a sum of matrix products

$$H_{\mathrm{SOC}}(\boldsymbol{k}) = \sum_a (\boldsymbol{\sigma}^a)^T \alpha^a \boldsymbol{f}^a(\boldsymbol{k}), \tag{1.10}$$

where α^a is an $n_a \times n_a$ matrix and $\boldsymbol{f}^a(\boldsymbol{k})$ is vector of size n_a consisting of polynomials of $\boldsymbol{k}$ whose form is to be determined. Let $\boldsymbol{\sigma}^a$ transform according to the irrep U^a and $\boldsymbol{f}^a$ transform according to V^a. Then for $H_{\mathrm{SOC}}(\boldsymbol{k})$ to be invariant under the group symmetry operations, we must have

$$(\boldsymbol{\sigma}^a)^T (U^a)^T \alpha^a V^a \boldsymbol{f}^a(\boldsymbol{k}) = (\boldsymbol{\sigma}^a)^T \alpha^a \boldsymbol{f}^a(\boldsymbol{k}) \tag{1.11}$$

for each a, or equivalently,

$$(U^a)^T \alpha^a V^a = \alpha^a. \tag{1.12}$$

Since the point groups are subgroups of the orthogonal group $O(n)$, their irreps are orthogonal matrices and we have[2]

$$\alpha^a V^a (\alpha^a)^{-1} = U^a. \tag{1.13}$$

So V^a and U^a are related by a similarity transformation which means they correspond to the same irrep. The upshot of all this is that for any point group, the SOC terms will

[2]Note that here we impose the restriction that the unknown α^a matrix is invertible.

consist of any polynomials $f^a(\boldsymbol{k})$ that transform under the same irrep as some subset $\boldsymbol{\sigma}^a$ of the spin vector. The identification of a basis of such polynomials can be found in any standard character table [21], we provide a selection of these tables in Appendix A.

Let us consider some examples, starting, for historical reasons, with the point group T_d. T_d is the full symmetry group of a tetrahedron without inversion. This makes it a very large group consisting of 24 symmetry operations and therefore provides strict constraints on the allowed terms in the Hamiltonian. Nevertheless, this was the first point group in which spin-orbit coupling was studied. This was done by Gene Dresselhaus in 1955 in the context of the band structure of zinc blende crystals[3] [22]. The character table for T_d (Table A.5) reveals that the full spin pseudovector transforms under the three-dimensional irrep T_1, that is $\boldsymbol{\sigma}^a = \boldsymbol{\sigma}$. Furthermore, the lowest order polynomial that transforms under the same irrep is cubic: $\boldsymbol{f}^a(\boldsymbol{k}) = (k_x(k_z^2 - k_y^2), k_y(k_z^2 - k_x^2), k_z(k_x^2 - k_y^2))$. As it turns out, there is only one coupling constant for the components of $\boldsymbol{\sigma}$ and $\boldsymbol{f}(\boldsymbol{k})$ giving rise to the so-called Dresselhaus term

$$H_{\mathrm{D}} = \beta(\sigma_x k_x(k_y^2 - k_z^2) + \sigma_y k_y(k_z^2 - k_x^2) + \sigma_z k_z(k_x^2 - k_y^2)). \tag{1.14}$$

Such a cubic coupling has a relatively weak effect on the low energy band structure. However, four years later, Emmanuel Rashba derived a different spin-split band structure, this time examining Wurzite crystals (such as ZnO) consisting of two interpenetrating hexagonal lattices [23]. Such crystals are not only non-centrosymmetric, they are also polar, which means there is a well-defined electric field vector within each unit cell. Wurzite belongs to the point group $\mathrm{C_{6v}}$. Looking at the character table for this group (Table A.3), we find that σ_z transforms under the one-dimensional irrep A_2, while (σ_x, σ_y) transforms under the two-dimensional (2D) irrep E_1. To cubic order, there are no polynomials that transform under A_2, but the linear vector (k_x, k_y) transforms under E_1. Thus, this point group admits a linear in-plane spin-momentum coupling term. It should be noted that while the character table can immediately tell us whether an SOC term of any order is allowed, we must look at the precise transformation of the spin and momentum under each symmetry element in order to determine the exact form of the invariant. Fortunately, since in this case we are dealing with two-component (pseudo)vectors, this task is very simple. Spin and momentum transform the same way under rotations and with opposite sign under reflections. The corresponding U^a and V^a

[3] A diamond structure with a two-atom basis.

representations are 2×2 matrices given in Table 1.2 (in the form of Pauli matrices) for a few important symmetry operations.

Symmetry	U^a (acts on (σ_x, σ_y))	V^a (acts on (k_x, k_y))
σ_d (reflection in xy diagonal)	$-\sigma_x$	σ_x
σ_v (reflection in yz diagonal)	$-\sigma_z$	σ_z
C_ϕ (rotation about z by ϕ)	$\mathbb{I}\cos\phi - i\sigma_y \sin\phi$	$\mathbb{I}\cos\phi - i\sigma_y \sin\phi$
C_2' (rotation about x by π)	σ_z	σ_z

TABLE 1.2: Two-dimensional (E) representations of some important symmetry elements of C_{nv}. Note that in the second column the 2×2 representations are acting on the spin vector. e.g. for the first row, $-\sigma_x \begin{pmatrix} \sigma_x \\ \sigma_y \end{pmatrix} = \begin{pmatrix} 0 & -1 \\ -1 & 0 \end{pmatrix} \begin{pmatrix} \sigma_x \\ \sigma_y \end{pmatrix} = \begin{pmatrix} -\sigma_y \\ -\sigma_x \end{pmatrix}$.

Eq. (1.12) then fixes α as follows. For the 2D representations considered here, α can be written generically as

$$\alpha = a\mathbb{I} + b\sigma_x + c\sigma_y + d\sigma_z. \tag{1.15}$$

Invariance under σ_d (which is present in C_{6v} as well as T_d, D_{2d} and C_{4v}) means that

$$-\sigma_x \alpha \sigma_x = \alpha. \tag{1.16}$$

Using, Eq. (1.9), we see that $a = d = 0$, which we would also find by considering the σ_v operation. Likewise, for any discrete rotation about the z axis by ϕ (in C_{6v} this would be $\pi/3$), we have

$$(\mathbb{I}\cos\phi - i\sigma_y \sin\phi)\alpha(\mathbb{I}\cos\phi - i\sigma_y \sin\phi) = \alpha, \tag{1.17}$$

which enforces $c = 0$ for any $\phi \neq 0$. These exhaust all the symmetry constraints of C_{6v} (as well as C_{4v} and C_{8v}), leaving $\alpha \propto \sigma_y$, which gives the Rashba invariant as promised.

$$H_R(\boldsymbol{k}) = \lambda(\sigma_x k_y - \sigma_y k_x). \tag{1.18}$$

The above result lay mostly dormant for many years after Rashba's publication. Part of the reason for this was that the paper was largely inaccessible and not translated to English until very recently [24], but another reason was that the advent of 2D semiconductor quantum wells in the 1970's was needed to catalyze interest in this area [25]. These are heterostructures with electronic bands that are non-dispersive in the direction of a confining potential so that electrons within the well are effectively two-dimensional. In 1984, Rashba pointed out that the bulk Wurtzite spin-splitting he had derived before, would apply to such systems as well, provided the confining potential imposed a polar

asymmetry [26]. From the perspective of point groups, we expect that a 2D electron gas (2DEG) will have in-plane and out-of-plane momentum components that transform under different irreps, and so much of the above reasoning applies. Indeed, most quantum wells in this category are described by the point group C_{4v} which we have seen contains exactly the linear Rashba invariant (1.18).

It should be noted that spin-splitting in 2D quantum wells is not exclusively Rashba-like. Shortly after Rashba's 1984 paper, a study of zinc blende quantum wells with a symmetric confining potential came out [27]. These systems typically have a non-polar point group D_{2d}. While this group also has a σ_d symmetry, it has an important distinction from C_{nv} in that instead of a rotation about z (C_ϕ), D_{2d} contains a two-fold rotation about x (C_2' in Table A.6). Returning to Table 1.2, and repeating the same analysis as before, we find that

$$-\sigma_x \alpha \sigma_x = \alpha, \tag{1.19}$$

$$\sigma_z \alpha \sigma_z = \alpha, \tag{1.20}$$

so that $a = b = d = 0$ and $\alpha \propto \sigma_z$, which gives the invariant

$$H_D(\boldsymbol{k}) = \beta(\sigma_x k_x - \sigma_y k_y). \tag{1.21}$$

This term is also named Dresselhaus SOC because it can be considered as a projection of the zincblende bulk splitting (1.14). In the symmetric 2D quantum well, we have $\langle k_z \rangle = 0$, while $\langle k_z^2 \rangle = \text{constant} \equiv \beta$. Projecting (1.14) onto this subspace and retaining only the linear terms in $\boldsymbol{k}$ gives the Hamiltonian (1.21). Often, Dresselhaus SOC is referred to as bulk inversion asymmetry, while Rashba SOC is referred to as structural inversion asymmetry. This terminology is a bit misleading since, as we have seen, Rashba SOC can occur in bulk systems and Dresselhaus SOC can occur in heterostructures. Furthermore, there are many systems that mix the two. Returning to our first point group example C_{2v}, the character table (Table A.1) shows that k_x and σ_y transform under one irrep while k_y and σ_x transform under another. Such materials would contain a linear combination of Rashba and Dresselhaus SOC. These combinations are interesting in their own right, particularly for $\alpha = \beta$ where there is a persistent spin helix [28]. However, such combinations ruin many of the interesting features of the band structure that we will discuss below. Indeed, one of the major difficulties in simulating these

SOC Hamiltonians in ultracold atoms is that the often used Raman scheme inherently produces a mixture of Rashba and Dresselhaus couplings [29].

To summarize, the distinction between different types and orders of SOC can appear confusing, particularly with the proliferating terminology. In the end though, the dispersion and spin texture are fixed by the symmetry of the system. For a given system, one only needs to look up the corresponding point group and write down the invariant combinations of spin and momentum. Lastly, we should mention that the jurisdiction of SOC expands well beyond the examples discussed here. For one, many of the examples listed in Table 1.1 are surfaces. Just like the asymmetric quantum wells, surfaces are polar, and so all surface states have some amount of Rashba SOC. Furthermore, it has recently been pointed out that Rashba and Dresselhaus SOC even play a role in some centrosymmetric materials [30]. If the unit cell is large enough, then local inversion asymmetry within the unit cell can cause detectable spin-splitting.

1.4 Basic properties of the continuum Rashba model

Regardless of its origin, let us consider the band structure implications of the Rashba model, first in the continuum, then on a lattice. The 2D continuum Rashba Hamiltonian in momentum-space is

$$H(\boldsymbol{k}) = \frac{\boldsymbol{k}^2}{2m} + \lambda \hat{z} \cdot (\boldsymbol{\sigma} \times \boldsymbol{k}), \tag{1.22}$$

where $\boldsymbol{k} = (k_x, k_y)$, $\boldsymbol{\sigma} = (\sigma_x, \sigma_y)$. From here on, we will work in natural units unless otherwise indicated. This hamiltonian is readily diagonalized to produce the spectrum

$$E_{\pm}(k) = \frac{k^2}{2m} \pm \lambda k, \tag{1.23}$$

where $k = |\boldsymbol{k}|$. The corresponding eigenspinors are

$$\eta^{\pm}(\theta_{\boldsymbol{k}}) = \frac{1}{\sqrt{2}} \begin{pmatrix} 1 \\ \mp i e^{i\theta_{\boldsymbol{k}}} \end{pmatrix}, \tag{1.24}$$

where $\theta_{\boldsymbol{k}}$ is the in-plane angle of $\boldsymbol{k}$ with respect to the x-axis. The spectrum consists of two helicity bands that meet at a Dirac point as shown in Fig. 1.1a). The spin $\langle \boldsymbol{\sigma} \rangle$

rotates in the plane, in opposite directions for the different helicities. We should note that the Dresselhaus dispersion is identical but with a different spin texture.

Spin is no longer a good quantum number, but the $\mathbb{Z}_2$ helicity index $s \equiv \text{sign}(\hat{z} \cdot (\boldsymbol{k} \times \boldsymbol{\sigma}))$ is. Here $s = 1$ for the upper (orange) helicity band and $s = -1$ for the lower (blue) helicity band. For a given energy E, the wavenumber corresponding to each helicity band is

$$k_{\pm} = \mp k_0 + \sqrt{k_0^2 + 2mE}, \tag{1.25}$$

where

$$k_0 \equiv m\lambda \tag{1.26}$$

is the wavenumber corresponding to the ground state.

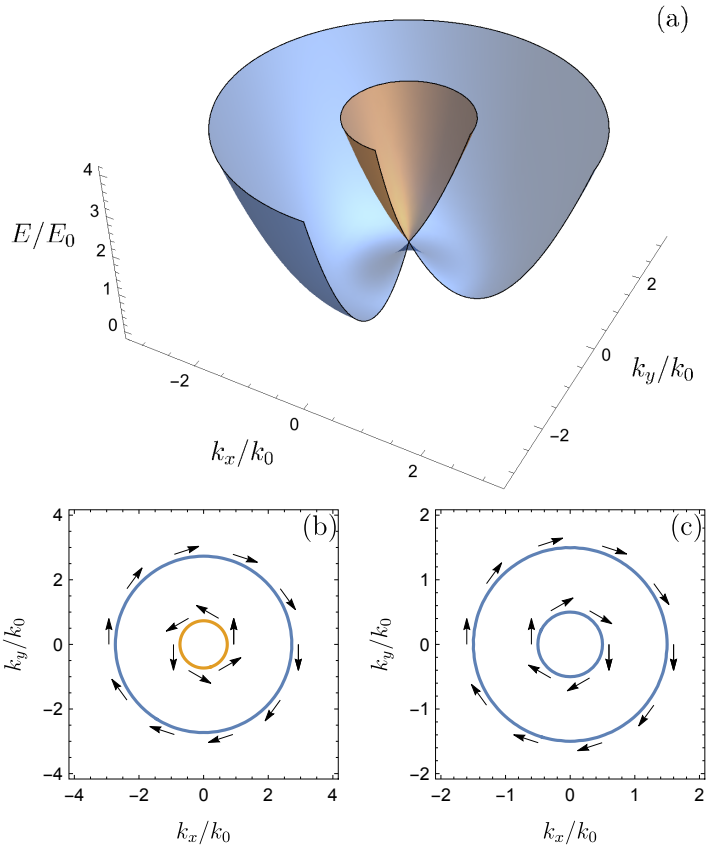

FIGURE 1.1: a) Rashba dispersion showing helicity bands in blue and orange. b) Constant energy contour and spin texture above the Dirac point. c) Constant energy contour and spin texture below the Dirac point.

Above the Dirac point, where both bands are present, the density of states (DOS) is given by

$$g(E>0)=\int\frac{d^2\boldsymbol{k}}{(2\pi)^2}\delta\left(E-E(\boldsymbol{k})\right)=\frac{m}{2\pi}\left(\frac{k_-}{|k_--k_0|}+\frac{k_+}{|k_++k_0|}\right)=\frac{m}{\pi}. \tag{1.27}$$

As expected for a 2D system, the DOS is constant. However, below the Dirac point the situation is different. There are still two wavenumbers that intersect with any given energy E, but their helicity index is the same. They are given by

$$k_{\gtrless}=k_0\pm\sqrt{k_0^2+2mE}, \tag{1.28}$$

where $k_>$ corresponds to the outer ring in Fig. 1.1c) and $k_<$ corresponds to the inner ring. The density of states in this regime is

$$g(E<0)=\frac{m}{2\pi}\left(\frac{k_<}{|k_<-k_0|}+\frac{k_>}{|k_>-k_0|}\right)=\frac{mk_0}{\pi\sqrt{k_0^2+2mE}}. \tag{1.29}$$

The striking inverse square root dependence on the energy is characteristic of a one-dimensional system. This apparent dimensional reduction will be a common theme in the first part of this thesis. We see that the DOS exhibits a singularity at the ground state energy $E=E_0$ as shown in Fig. 1.2. Singularities in the density of states are referred to as van Hove singularities [31]. This singularity is responsible for many unusual features in the scattering properties and interactions of Rashba electrons.

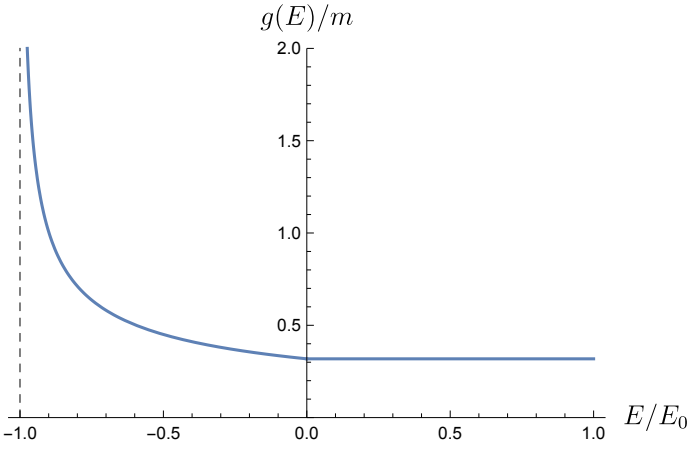

FIGURE 1.2: Density of states for the continuum Rashba model. The dashed line indicates the singularity at the band bottom.

1.5 Basic properties of the Rashba model on a square lattice

The discussion so far has exclusively dealt with continuum models. In the second part of this thesis we switch to models on a square lattice. The symmetry arguments used to derive the Rashba model apply in this case as well, but must be translated into the tight-binding language (discussed in detail in Chapter 6). Since SOC modifies the kinetic energy, it will appear as a hopping term. Restricting to nearest neighbour hops, the most generic coupling to spin will appear as

$$H_{SO} = \sum_{i\alpha\beta} \left(c^\dagger_{i\alpha} \boldsymbol{a} \cdot \boldsymbol{\sigma}^{\alpha\beta} c_{i+\hat{x},\beta} + c^\dagger_{i\alpha} \boldsymbol{b} \cdot \boldsymbol{\sigma}^{\alpha\beta} c_{i+\hat{y},\beta} + H.c. \right), \tag{1.30}$$

where i is the site index (we work in units where the lattice parameter is unity), α, β are the spin indices and *h.c.* stands for hermitian conjugate. The square lattice has a rotational symmetry of $\pi/2$ about the $\hat{z}$ axis through each site. Applying such a rotation to this term using $R_{\pi/2} c_{j\alpha} R^{-1}_{\pi/2} = e^{-i\alpha\pi/4} c_{R^{-1}_{\pi/2} j,\alpha}$ (note this rotation is generated by the *total* angular momentum J_z, hence the spin-dependent phase) gives

$$H_{SO} = \sum_{i\alpha\beta} e^{i(\alpha-\beta)\pi/4} \left(c^\dagger_{i+\hat{y},\alpha} \vec{a} \cdot \vec{\sigma}^{\alpha\beta} c_{i,\beta} + c^\dagger_{i\alpha} \vec{b} \cdot \vec{\sigma}^{\alpha\beta} c_{i+\hat{x},\beta} \right) + h.c. \tag{1.31}$$

Matching this to (1.30) restricts the values of $\boldsymbol{a}$ and $\boldsymbol{b}$ to be

$$a_x = b_y = 0 \tag{1.32}$$

$$-a_y = b_x \equiv -iV_{SO}. \tag{1.33}$$

We have introduced a new Rashba coupling V_{SO} to distinguish it from the continuum model, but we will see that one can identify $|V_{SO}| = \lambda/(2a)$ in the long-wavelength limit (where a is the lattice constant). Thus the Rashba hopping term on the lattice is

$$H_{\mathrm{SO}} = -V_{\mathrm{SO}} \sum_{i\alpha\beta} \left(i c^\dagger_{i\alpha} \sigma_x^{\alpha\beta} c_{i+\hat{y},\beta} - i c^\dagger_{i\alpha} \sigma_y^{\alpha\beta} c_{i+\hat{x},\beta} \right) + \mathrm{h.c.}. \tag{1.34}$$

Combining this with the usual nearest-neighbour hopping term

$$H_t = -t \sum_{\substack{\langle i,j \rangle \\ \sigma}} \left(c^\dagger_{i\sigma} c_{j\sigma} + c^\dagger_{j\sigma} c_{i\sigma} \right), \tag{1.35}$$

and Fourier transforming gives,

$$H = \sum_{\boldsymbol{k},\sigma} \left(\epsilon_{\boldsymbol{k}} - \mu \right) c^\dagger_{\boldsymbol{k}\sigma} c_{\boldsymbol{k}\sigma} + 2V_{\mathrm{SO}} \sum_{\boldsymbol{k}} \left[\sin k_y \left(c^\dagger_{\boldsymbol{k}\uparrow} c_{\boldsymbol{k}\downarrow} + c^\dagger_{\boldsymbol{k}\downarrow} c_{\boldsymbol{k}\uparrow} \right) + i \sin k_x \left(c^\dagger_{\boldsymbol{k}\uparrow} c_{\boldsymbol{k}\downarrow} - c^\dagger_{\boldsymbol{k}\downarrow} c_{\boldsymbol{k}\uparrow} \right) \right], \tag{1.36}$$

where $\epsilon_{\mathbf{k}} \equiv -2t \left(\cos k_x + \cos k_y \right)$. Once again we can diagonalize this in the Rashba basis to produce the spectrum

$$\epsilon_{\boldsymbol{k}s} = \epsilon_{\boldsymbol{k}} + 2sV_{\mathrm{SO}} \sqrt{\sin^2 k_x + \sin^2 k_y}, \tag{1.37}$$

which reduces to the dispersion of the continuum model in the small k limit. The full spectrum is shown in Fig. 1.3 along with a cut through the Brillouin zone. The DOS may be determined by numerically integrating

$$\begin{aligned} g(E) &= 4 \sum_s \int_0^\pi \frac{dk_x}{2\pi} \int_0^\pi \frac{dk_y}{2\pi} \delta \left(E - \epsilon_{\boldsymbol{k}s} \right) & (1.38) \\ &= \lim_{\tau \to 0} \frac{1}{\pi^{5/2} \tau t} \sum_s \int_0^\pi dk_x \int_0^\pi dk_y e^{-\left(E/t - \epsilon_{\boldsymbol{k}s}/t \right)^2 / \tau^2}, & (1.39) \end{aligned}$$

using the Gaussian limit formula for the Dirac delta function $\delta(x) = \lim_{\tau \to 0} \frac{1}{\tau\sqrt{\pi}} e^{-(x/\tau)^2}$.

The resulting density of states for each helicity band is shown in Fig. 1.4 as well as the combined DOS. There are now four singularities: two are split apart near $E = 0$ (these merge together for $V_{SO} = 0$) and two are near the top and bottom of the band. Unlike the continuum model, the singularity does not occur precisely at the ground state energy, but is instead shifted upwards slightly. The ground state consists of four degenerate minima with energy $E_g = -4t\sqrt{1 + V_{SO}^2/(2t^2)}$, and the singularity occurs at the saddle point energy just above this $E_{\mathrm{sad}} = -2t \left[1 + \sqrt{1 + \left(V_{\mathrm{SO}}/t \right)^2} \right]$ [32, 33]. This value is extremely close to the ground state energy, so that the difference is imperceptible in Figs. 1.3 and 1.4, but in Fig. 1.5, we zoom in on the band bottom for large values of the spin-orbit coupling. For reference, one of the largest spin-splittings in Table 1.1, BiTeI, has $V_{SO}/t \approx 0.8$ [34], for which the singularity is shifted from the band bottom by about 0.4% of the bandwidth.

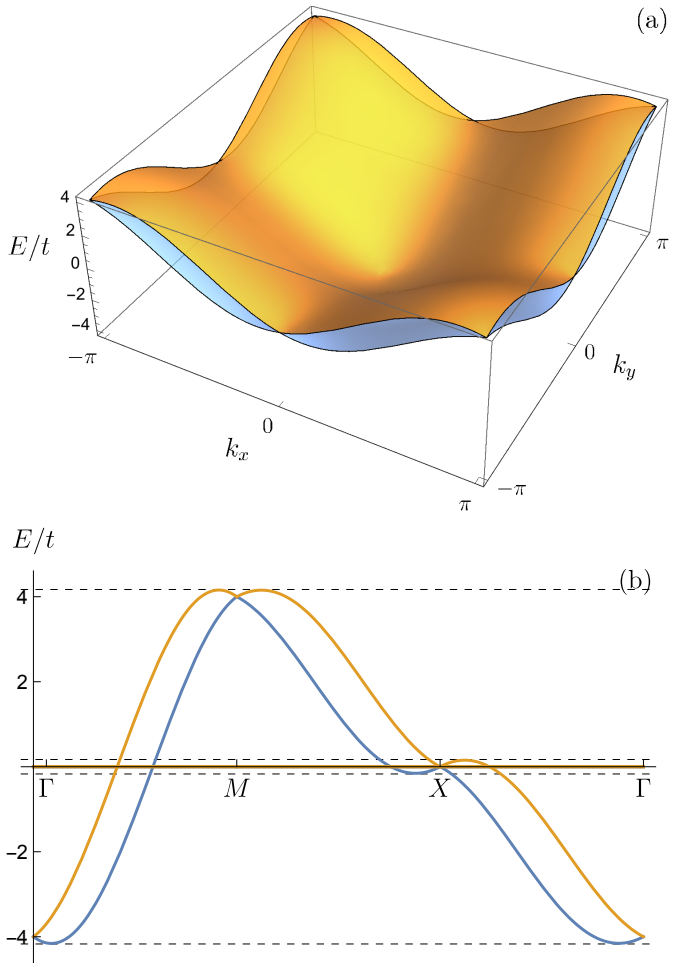

FIGURE 1.3: a) Rashba dispersion on a square lattice. b) Cut through the high symmetry points of the first Brillouin zone. Dashed lines indicate the location of Van Hove singularities. For both plots $V_{SO} = 0.4t$.

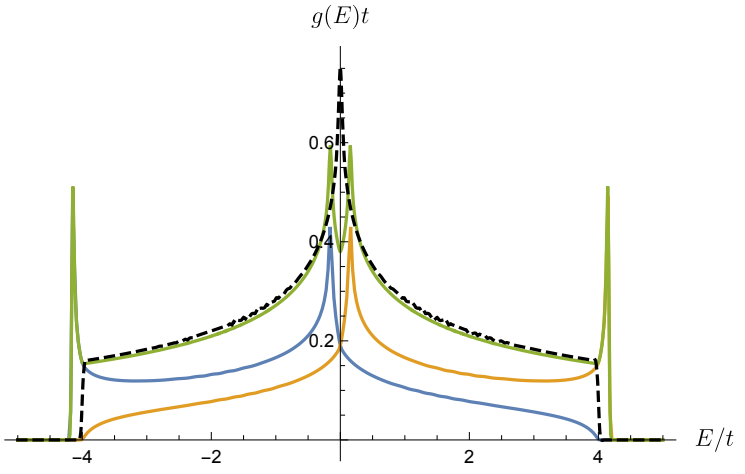

FIGURE 1.4: Density of states for the lower (blue) helicity band, upper (orange) helicity band and the combined DOS (green) for $V_{SO} = 0.4t$. For comparison, we include the density of states for $V_{SO} = 0$ (dashed black).

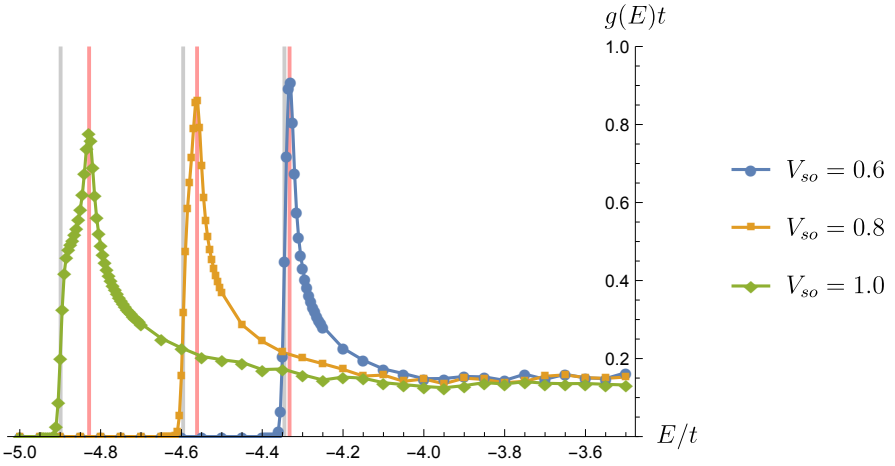

FIGURE 1.5: Low energy density of states for the Rashba model on a square lattice for different values of the Rashba coupling. The grey and red lines are guides for the eye indicating the band edges and singularities respectively for each value of V_{SO}.

1.6 How to read this thesis

This thesis reports research advances on various aspects of Rashba SOC physics. The first study is about how the unusual low energy Rashba spectrum and DOS affect scattering and transport. It occupies the entirety of Part 1, but is divided into three chapters following three papers [1, 3, 5] that progress from a simple single-particle scattering model (Chapter 3), to universal scattering properties (Chapter 4), to a realistic picture of transport in an SOC material (Chapter 5). Chapter 2 provides an introduction to the subject. Part 2 is largely independent of Part 1 and addresses different aspects of Bardeen-Cooper-Schrieffer (BCS) superconductivity. It includes a study about how SOC can enhance the critical temperature (Chapter 7) [4], as well as an exploration of the symmetry of the superconducting order parameter in the case of the extended Hubbard model with and without SOC (Chapter 8). Chapter 6 provides some background and motivation for both of these studies. In principle, the two parts could be read in any order. Conclusions are provided in Chapter 9.

Part I

Rashba scattering and transport

Chapter 2

Introduction

2.1 Motivation: spintronics

In the previous chapter we mentioned that the ability to reliably create 2D heterostructures was a catalyst for interest in Rashba SOC. The main reason for this is the impact that Rashba physics had on spintronics. Spintronics is an extension of ordinary electronics in which circuit elements, often involving 2D heterostructures, are constructed in such a way that information is encoded or transferred using the spins of electrons. This area originated from the ability to both transfer and block electrons at the interface between ferromagnets and normal metals via spin injection and giant magnetoresistance [35–37]. In a ferromagnet, the band structure is Zeeman split so that the majority of spins are anti-aligned to the magnetic field. The band corresponding to the minority spins (typically a hybridized *spd* band) has a much higher density of states, and correspondingly a higher scattering rate which is observed as giant magnetoresistance [38]. The impact of the density of states on scattering rate will be a recurring theme in this thesis and will be addressed in detail in Chapter 5. The inverse of this effect is spin-transfer torque. By forcing a large current of polarized spins through a junction, with polarization direction misaligned with the ferromagnet's magnetization, a spin accumulation layer develops which can build up enough of a magnetic moment to flip a magnetic domain. Such phenomena play a promising role in the development of magnetic memories [39].

Where does Rashba SOC enter all this? About a year after the discovery of giant magnetoresistance, Supriyo Datta and Biswajit Das put forward a proposal suggesting that

the effective magnetic field provided by spin-orbit coupling could be used as a spin polarizer and filter. The specific device they proposed is known as the Datta-Das spin transistor or spin field effect transistor (spin FET) [40]. The key insight is that in a 2D heterostructure such as an InGaAs/InAlAs quantum well, the applied potential difference perpendicular to the confining plane controls the value of the Rashba coupling λ. That means the SOC can be turned on or off with a gate voltage. Returning to the setup for giant magnetoresistance, we can imagine a Rashba 2DEG sandwiched between a ferromagnetic source and drain with aligned moments. Without SOC, the polarized spins will flow from source to drain with minimal magnetoresistance. When the SOC is turned on, the spins will precess around the eigenspinor direction in Eq. (1.24). For example, if one injects a spin polarized in the z direction, travelling in the x direction, e.g. $\psi = e^{ik_x x}(1,0)^T$, with small momentum k_x, this state will evolve according to the approximate time-evolution operator $U \approx \cos(\lambda k_x t)\mathbb{I} + i\sin(\lambda k_x t)\sigma_y$. This produces the time-dependent state $\psi(t) = e^{ik_x x}(\cos(\lambda k_x t), -\sin(\lambda k_x t))^T$. So indeed, the Rashba coupling provides an effective magnetic field with a momentum-dependent "Larmor frequency" $k\lambda$. Because this frequency is roughly controlled by the current and gate voltage, one can arrange for spin to be anti-parallel to the ferromagnets (in this example $\psi \sim (0,1)^T$) precisely when it reaches the drain as shown in Fig. 2.1.

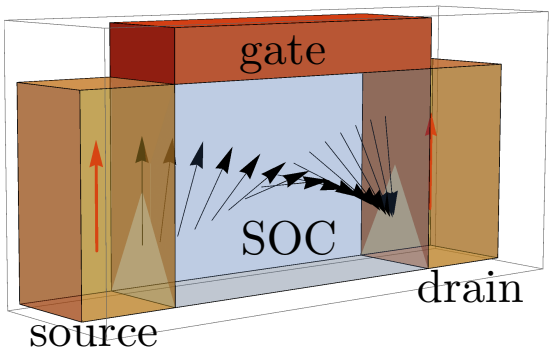

FIGURE 2.1: Schematic of the Datta Das spin transistor proposal. A Rashba 2DEG (e.g. InAlAs/InGaAs quantum well) is sandwiched between a ferromagnetic source and drain. A gate voltage controls the SOC.

Unfortunately, this proposal is fraught with practical difficulties. The spin-FET relies on

the spin coherence of an electric current, and several factors stand in the way of such coherence. For one, if a large portion of the Fermi surface is available for the initial states, then the time-evolved states at the drain will include many undesired spin-orientations in accordance with the spin texture in Fig. 1.1. Another problem is that finite temperature can cause the Fermi surface to smear enough that both helicity bands contribute to the modes in the current. Even if the momentum mode is highly restricted, temperature could cause pollution of a given spin-polarization with its opposite helicity partner. The presence of these two helicity bands (see Fig. 1.1b) is at the heart of perhaps the most significant obstacle, impurity scattering. At low temperatures, impurities can cause significant interband scattering, which is the dominant spin decoherence mechanism [41]. As a result, much theoretical effort has been focused on the energy regime above the Dirac point where both helicity bands are available for elastic scattering processes. Indeed, this is where the Fermi level sits in the majority of Rashba materials. Thus far, the approach has been to formulate circular potential scattering problems at energies $E > 0$ with an emphasis on spin polarization, interference, and coherence of the resulting wavefunctions [42–45]. One such study revealed that a near-field region of the scattering wavefunction exhibits polarization but only in the forward scattering direction [46]. Another showed that backscattering was dominated by the inter-helicity channel [47]. This begs the question: if one helicity band is removed, as is the case for scattering energies $E < 0$, are these backscattering events removed with it? The answer is no, and we will show why this is the case in Chapter 3.

Only very recently (coincident with our work), has a research group paid attention to impurity scattering at low energies [48–50]. In these references, the authors go beyond the scattering problem to investigate transport quantities in Rashba systems with Fermi levels below the Dirac point. While this work reveals some interesting features in the conductivity, it is based on the first Born approximation (to be discussed in section 2.3), which, while valid for conventional scattering problems, breaks down in the ultra-low energy Rashba system. In a sense, Part 1 of this thesis is devoted to understanding this breakdown in detail.

A thorough understanding of the low-energy Rashba physics is more important now than ever, due to recent discoveries of materials with very large Rashba splittings (see e.g. Table 1.1), where this previously ignored low-energy regime is now within experimental reach. Until now, much of the theoretical literature in spintronics has treated Rashba

coupling as a small effect, i.e., in perturbation theory ($E_0 \ll E$), but with the advent of materials with giant Rashba splittling, it is essential to explore the nonperturbative regime where Rashba SOC is the largest energy scale ($E_0 > E$).

2.2 Motivation: interacting systems

There is good reason to study the low energy Rashba scattering problem as it fills a hole in the spintronics scattering literature. However, we should also intuitively expect this regime to be host to some unusual phenomena simply by looking at Fig. 1.2. The presence of a singularity in the density of states leads to an increased phase space for scattering which means that electron-electron interactions become important. In the presence of attractive interactions, this enhances instabilities for Cooper pairing [51], as we will see in Part 2, as well as instabilities for Bose-Einstein condensation of tightly bound fermionic molecules [52]. In the presence of repulsive interactions, there are several expected symmetry-breaking phases as well. At low densities, electrons typically form a Wigner crystal: a phase in which electrons form their own crystalline solid due to interactions [53]. The origin of this crystallization is easily seen from some simple energetic considerations. At zero temperature, the kinetic energy of a Fermi sea in 2D is

$$E \sim V \int_0^{k_F} dk k^3 \sim V k_F^4, \tag{2.1}$$

where V is the system volume. The number of electrons in that Fermi sea is

$$N \sim V \int_0^{k_F} dk k \sim V k_F^2. \tag{2.2}$$

So the kinetic energy per electron is

$$E/N \sim k_F^2 \sim n \sim r^{-2}, \tag{2.3}$$

where n is the electron density and r is the average inter-particle spacing. The same result holds in three dimensions as well. Since the kinetic energy goes like $1/r^2$ and the Coulomb interaction goes like $1/r$, the Coulomb interaction is dominant at low densities and the system minimizes its energy by crystallizing. If we repeat the above analysis for

a low density Rashba system, then we must integrate over a Fermi annulus

$$\begin{aligned} E \sim V \int_{k_<}^{k_>} dk k^3 &\sim V(k_>^4 - k_<^4) && (2.4)\\ &= V(k_> - k_<)(k_> + k_<)(k_>^2 + k_<^2) && (2.5)\\ &= V k_0 (k_> - k_<)^3, && (2.6) \end{aligned}$$

using Eq. (1.28). Meanwhile, the number of electrons is

$$N \sim V \int_{k_<}^{k_>} dk k \sim V(k_> - k_<), \tag{2.7}$$

so the energy per electron is

$$E/N \sim (k_> - k_<)^2 \sim n^2 \sim r^{-4}. \tag{2.8}$$

This means that even interactions of much shorter range than Coulomb will be dominant in the low density limit. Wigner crystals are hard to observe in solid state systems because the Coulomb interaction is screened. The enhancement provided by the Rashba DOS circumvents this issue. Moreover, it is believed that these shorter-range interactions produce a competition between many exotic states including anisotropic Wigner crystals, smectic phases and liquid crystal phases with nematic (invariant under C_2) or ferromagnetic-nematic (invariant under C_2 followed by time-reversal) orders [54–56]. With these examples in mind, it is natural to ask whether there is something fundamentally anisotropic about scattering in the low density Rashba regime that could lead to these symmetry-breaking instabilities. In this part of the thesis, we will only study single-particle (potential) scattering, but much of the formalism we develop could be extended to two-body scattering by working in the center-of-mass frame, allowing one to probe the interacting physics in detail.

2.3 Single-particle scattering formalism in 2D

In the next two chapters we will develop a formalism for single-particle scattering in Rashba systems. Scattering problems in quantum mechanics are full of different quantities: phase shifts, S matrices, T matrices, scattering amplitudes, all expressing the

same information, so it is worth reviewing some basic features and definitions. Details of conventional (spin-degenerate) scattering in 2D can be found in Appendix B.

There are two different but complementary ways of describing potential scattering. The first is a real-space, wavefunction-centered approach. If the potential is simple enough and short-ranged, one can solve for the eigenfunctions of the full Hamiltonian exactly, applying matching conditions as needed. Generally, we are interested in the wavefunction far outside the range of the potential where we can measure observables. In this region, the wavefunction will always be some linear combination of free particle states. This combination is organized into two pieces: an incident wave that is a prepared free-particle eigenstate carrying probability current towards the scattering center, and an outgoing scattered wave carrying probability current away from the scattering centre. It is the relation between these two components that contains all the scattering information. We exclusively consider circularly symmetric potentials, so it is useful to expand the wavefunction in a circular harmonic basis (in polar coordinates) so that each eigenfunction acquires a partial-wave index l: $\psi^l(r,\theta)$.[1] Each partial-wave component of the incident wave is connected to the corresponding component of the outgoing wave via a transformation that encodes the scattering physics. Note that this transformation is diagonal (different partial-waves do not scatter amongst each other) for spin-independent circular potentials, which cannot change the angular momentum. For an elastic scattering process, the possible transformations that can take place are very limited. If energy and angular momentum do not change, then each partial-wave component of the wavefunction can only undergo a *phase shift* δ_l. As we will see, the Rashba system is more subtle because there are two elastic scattering channels, so it makes more sense to work with the partial-wave *S-matrix* S^l. The S-matrix encodes the same information as the phase shift, but with a different definition. Specifically, S^l is the unitary transformation between asymptotic states in the incoming circular basis and the outgoing circular basis. Unitarity of this transformation is guaranteed by conservation of probability.

Another very important scattering quantity for us is the *T-matrix*. Again, it encodes the same information as the other quantities but in a sense is more directly connected to the potential. The outgoing circular waves referred to in the discussion above regarding the S-matrix include contributions from the part of the incident wave that passes by

[1]Note that we do not require the wavefunction to be an eigenfunction of the angular momentum operator L_z. In a Rashba system only the total angular momentum $J_z = L_z + (1/2)\sigma_z$ is conserved.

the potential without scattering. The T^l components remove this portion and may be thought of as the S-matrix minus the identity matrix. Furthermore, the T-matrix is proportional to the *scattering amplitude* $f(\theta)$, which is essentially the angular dependence of the scattered wavefunction [57]. The exact relation between these three quantities will be derived explicitly for the Rashba case in Chapter 4 and Appendix E.

Let us now relate those quantities to physical observables. The two main observables in a scattering experiment are the total and differential cross sections. One defines the effective target area $d\sigma$ for which incident flux is scattered into an angle $d\theta$ (or solid angle $d\Omega$ in 3D). If N_{in} particles pass through an area A in a time dt, then a number of particles

$$N_{\text{sc}} = N_{\text{in}} \frac{d\sigma}{A} \tag{2.9}$$

will pass through the scattering region during dt. In 2D the "area" we are interested in is an arc subtended by $d\theta$ a distance r from the scattering centre. So in terms of flux current densities $\boldsymbol{j}$, we have

$$r \frac{|\boldsymbol{j}_{\text{sc}}|}{|\boldsymbol{j}_{\text{in}}|} = \frac{d\sigma}{d\theta}. \tag{2.10}$$

The differential cross section may be integrated to obtain the total cross section σ.

All of these quantities are defined most naturally from the real-space wavefunction, but it will prove very useful to have an alternative formalism that does not depend explicitly on the Hamiltonian eigenfunctions. Such a formalism is naturally given by the interaction picture where states evolve according to the interaction-picture time-evolution operator $\hat{U}(t, t_0)$ that satisfies the Dyson equation [58]

$$\hat{U}(t, t_0) = 1 - i \int_{t_0}^{t} dt' \hat{V}(t') \hat{U}(t', t_0). \tag{2.11}$$

$\hat{U}$ is related to the Heisenberg-picture evolution operator U via

$$U(t, t_0) = e^{-iH_0 t} \hat{U}(t, t_0) e^{iH_0 t_0}. \tag{2.12}$$

The idea is that if we allow an eigenstate $|i\rangle$ of an unperturbed Hamiltonian H_0 to evolve over a time t during which a perturbation (scattering potential) V acts, then the

probability amplitude of transitioning to a state $|f\rangle$ is

$$\langle f|i(t)\rangle = \langle f|U(t,t_0)|i\rangle = \left(\delta_{fi} - i\int_{t_0}^{t} dt' \langle f|\hat{V}(t')\hat{U}(t',t_0)|i\rangle\right) e^{-iE_f t} e^{iE_0 t_0}. \tag{2.13}$$

To pose a well-defined scattering problem, we assume that the scattering potential was turned on adiabatically and asymptotically far in the past. This is done using the potential $V(t') = Ve^{\epsilon t'}$, where $0 < \epsilon < 1/t$. The later condition ensures that $e^{\epsilon t'}$ stays close to unity throughout $t' > t_0$. At the end we will take $\epsilon \to 0$. Inserting a complete set of states $|m\rangle$ in Eq. (2.13), we have

$$\langle f|i(t)\rangle = \delta_{fi} - i\sum_m \langle f|V|m\rangle \int_{t_0}^{t} dt' e^{i(E_f - E_m)t' + \epsilon t'} \langle m|\hat{U}(t',t_0)|i\rangle. \tag{2.14}$$

If the potential is perturbatively small, we expect the *first Born approximation* to hold:

$$\langle f|i(t)\rangle = \delta_{fi} - i\langle f|V|i\rangle \int_{t_0}^{t} dt' e^{i(E_f - E_m)t' + \epsilon t'}. \tag{2.15}$$

The first Born approximation is a common approximation which is assumed to be valid for low scattering energies. We will see that this is not the case for Rashba systems which diverge from the first Born result as $E \to 0$. We would therefore like to generalize Eq. (2.15) to the non-perturbative statement

$$\langle f|i(t)\rangle = \delta_{fi} - i\langle f|T|i\rangle \int_{t_0}^{t} dt' e^{i(E_f - E_m)t' + \epsilon t'}. \tag{2.16}$$

The operator T that satisfies this expression is called the *T-matrix*.

In scattering problems, we are interested in the time-independent physics that occurs when the observation times are infinitely far apart. In this limit, the amplitude above is simply the S-matrix

$$\begin{aligned} \langle f|i(t)\rangle \to \langle f|S|i\rangle &\equiv \delta_{fi} - i\langle f|T|i\rangle \int_{-\infty}^{\infty} dt' e^{i(E_f - E_m)t'} && (2.17) \\ &= \delta_{fi} - 2\pi i\delta(E_f - E_i)\langle f|T|i\rangle, && (2.18) \end{aligned}$$

where we have taken the limit $\epsilon \to 0$ to ensure that $\epsilon < 1/t$ holds even at long times. Eq. (2.18) is the formal relation between the S and T matrices.

The rate of change of the probability corresponding to this amplitude between different states is the *transition rate*

$$\begin{aligned} w_{i\to f} &\equiv \lim_{t\to\infty}\lim_{\epsilon\to 0}\frac{d}{dt}|\langle f|i(t)\rangle|^2 && (2.19)\\ &= \lim_{t\to\infty}\lim_{\epsilon\to 0}\frac{d}{dt}\left(|\langle f|T|i\rangle|^2\frac{e^{2\epsilon t}}{\epsilon^2+(E_f-E_i)^2})\right) && (2.20)\\ &= |\langle f|T|i\rangle|^2 2\pi\delta(E_f-E_i), && (2.21)\end{aligned}$$

using

$$\delta(x)=\lim_{\epsilon\to 0}\frac{1}{\pi}\frac{\epsilon}{x^2+\epsilon^2}. \tag{2.22}$$

Eq. (2.21) is *Fermi's golden rule*. For a continuous dispersion, we have a continuum of final states and the transition rate must be integrated over a small window of final states. Furthermore, a scattering experiment may have angular resolution as well, so the relevant angle-resolved transition rate is

$$w_{i\to f}d\theta = 2\pi|\langle f|T|i\rangle|^2 g(E)d\theta, \tag{2.23}$$

where $g(E)d\theta$ is the density of final states within an angle $d\theta$ of θ. This result gives us a second expression for the differential cross-section. In a time dt, the number of particles that transition to a final state $|f\rangle$ within an angle $d\theta$ of θ is $w_{i\to f}d\theta dt$, which according to Eq. (2.9) gives

$$\frac{d\sigma}{d\theta}=\frac{w_{i\to f}}{|\boldsymbol{j}_{\rm in}|}. \tag{2.24}$$

Before ending this chapter, we need to develop the T-matrix a little further. While Eq. (2.16) defines the T-matrix, that equation is rarely useful for computing it. However, if we input Eq. (2.16) into the Dyson equation (2.11) (sandwiching between $\langle f|$ and $|i\rangle$), and take the limit $t_0\to-\infty$ as before, we get

$$\langle f|T|i\rangle = \langle f|V|i\rangle - i\sum_m \frac{\langle f|V|m\rangle\langle m|T|i\rangle}{i(E_m-E_i)+\epsilon}. \tag{2.25}$$

Now suppose there exists a state $|\psi^+\rangle$ such that

$$T|i\rangle = V|\psi^+\rangle. \tag{2.26}$$

Plugging this into Eq. (2.25), and using the fact that $|f\rangle$ is arbitary gives

$$|\psi^+\rangle = |i\rangle + \sum_m \frac{|m\rangle\langle m|V|\psi^+\rangle}{E_i - E_m + i\epsilon} \tag{2.27}$$

$$= |i\rangle + \frac{1}{E_i - H_0 + i\epsilon} V|\psi^+\rangle. \tag{2.28}$$

This is the *Lippmann-Schwinger Equation.* If the T-matrix is thought of as the effective interaction including all virtual scatterings, then $|\psi^+\rangle$ should be thought of as an effective state obtained by performing all possible number of scatterings on an incident state $|i\rangle$. This, of course, is just the final outgoing state observed. The fact that it is outgoing is expressed by the infinitesimal $+i\epsilon$ with a positive imaginary part in the denominator, which defines the *retarded unperturbed Green's function*

$$G^R(E) \equiv \frac{1}{E - H_0 + i\epsilon}. \tag{2.29}$$

Finally, if we multiply the Lippmann-Schwinger equation on the left by V, and use Eq. (2.26), we are left with the operator equation

$$T(E_i) = V + VG^R(E_i)T(E_i). \tag{2.30}$$

This is the closed form expression for the *Born series.* In all but the simplest examples, it must treated iteratively to obtain an expression for T:

$$T(E_i) = V + VG^R(E_i)V + VG^R(E_i)VG^R(E_i)V + \ldots. \tag{2.31}$$

Truncating this series to first order in V reproduces the first Born approximation.

All of this scattering formalism will be used explicitly to derive unique properties of low energy Rashba systems in the next three chapters.

Chapter 3

Single-particle Rashba scattering at low energy: simple potentials

In this chapter, we explore the single-particle scattering of Rashba electrons off of two simple potentials for energies $E < E_0$, with a focus on the low-energy limit $E \to 0$. We find peculiar features in the low-energy limit: (1) the S-matrix for a partial wave of angular momentum l approaches a purely off-diagonal form with both off-diagonal elements equal to one, independent of l [Eq. (3.27)]; (2) the differential cross section becomes quasi-1D, with only forward and backward scattering allowed [Eq. (3.37)]; (3) the total cross section exhibits quantized plateaus [Eq. (3.40)]. Remarkably, these results hold for both the infinite barrier (Sec. 3.2) and infinitely thin shell (Sec. 3.3) potentials considered here, with no dependence on the details of the potentials such as range and amplitude. These features contrast severely with both $E > E_0$ scattering in the Rashba case and low-energy scattering in the conventional case without spin-orbit coupling; we conjecture they are universal properties of Rashba scattering in the low-energy limit.

3.1 Low-energy setup

For convenience, we shift the energy spectrum such that the ground state occurs at $E = 0$ and the Dirac point is at $E = E_0 = (1/2)m\lambda^2$, where λ is the Rashba coupling. The dispersion in this regime, where only one helicity band is relevant, is shown in Fig 3.1. This figure highlights the ring of degenerate ground states occurring at the characteristic

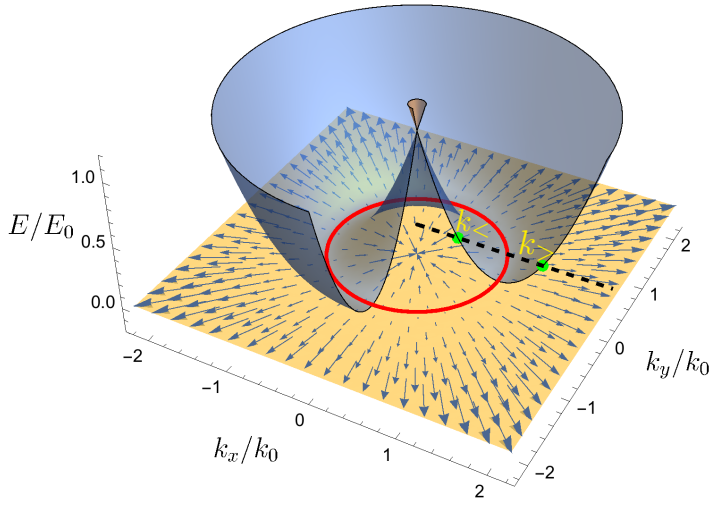

FIGURE 3.1: Lower helicity dispersion $E_-(\boldsymbol{k})$ (in blue). The plane beneath it shows the corresponding group velocity vector field which changes from pointing inward to pointing outward at the band minimum (shown in red). At a generic energy below the Dirac point (dashed line), there are two available rings of states with wavenumbers $k_<$ and $k_>$.

wavenumber $k_0 = m\lambda$. As described in Chapter 1, there are two degenerate rings of states at any given energy with wavenumbers

$$k_{\gtrless} \quad = \quad k_0 \pm \sqrt{2mE}. \tag{3.1}$$

To solve the scattering problem, we require the Hamiltonian in position-space polar coordinates (r, θ):

$$H = \begin{pmatrix} -\frac{1}{2m}(\partial_r^2 + \frac{1}{r}\partial_r + \frac{1}{r^2}\partial_\theta^2) & \lambda e^{-i\theta}(\partial_r - \frac{i}{r}\partial_\theta) \\ -\lambda e^{i\theta}(\partial_r + \frac{i}{r}\partial_\theta) & -\frac{1}{2m}(\partial_r^2 + \frac{1}{r}\partial_r + \frac{1}{r^2}\partial_\theta^2) \end{pmatrix}, \tag{3.2}$$

whose eigenfunctions can be expanded in partial waves as

$$\psi(r,\theta) = \sum_{l=-\infty}^{\infty} e^{il\theta} \begin{pmatrix} R_l(r) \\ e^{i\theta} R_{l+1}(r) \end{pmatrix}. \tag{3.3}$$

The radial functions $R_l(r)$ are linear combinations of incoming and outgoing Hankel functions $H_l^{\pm}(kr)$, defined as $H_l^{\pm}(x) = J_l(x) \pm iN_l(x)$ where $J_l(x)$ and $N_l(x)$ are Bessel functions of the first and second kind (Neumann functions), respectively. The Bessel

functions are regular at the origin while the Neumann functions are singular. We consider elastic scattering where k in the argument of the Hankel functions can take on either value $k_{\gtrless}$ satisfying (3.1). There are four independent solutions to the Schrödinger equation, and an eigenfunction Ψ at energy E for the free-particle problem may be written as the generic linear combination

$$\begin{aligned}\Psi(r,\theta) &= \sum_{l=-\infty}^{\infty} e^{il\theta}\Bigg[a_l \begin{pmatrix} H_l^+(k_< r) \\ -H_{l+1}^+(k_< r)e^{i\theta}\end{pmatrix} + b_l \begin{pmatrix} H_l^-(k_< r) \\ -H_{l+1}^-(k_< r)e^{i\theta}\end{pmatrix} \\ &\quad + c_l \begin{pmatrix} H_l^+(k_> r) \\ -H_{l+1}^+(k_> r)e^{i\theta}\end{pmatrix} + d_l \begin{pmatrix} H_l^-(k_> r) \\ -H_{l+1}^-(k_> r)e^{i\theta}\end{pmatrix}\Bigg],\end{aligned} \tag{3.4}$$

where a_l, b_l, c_l, and d_l are arbitrary coefficients.

3.2 Hard-disk scattering

We now add to the free-particle Hamiltonian (3.2) a scattering potential V. We first consider single-electron scattering off an infinite circular barrier

$$V = \begin{cases} \infty, & r \le R, \\ 0, & r > R, \end{cases} \tag{3.5}$$

as shown in Fig. 3.2. Because the potential vanishes identically for $r > R$, eigenstates of the full Hamiltonian with energy E obey the free-particle expansion (3.4) in that region. In that region, the wave function consists of an incident plane wave $\psi_{\gtrless}^{\text{in}}$ with definite wave vector $k_{\gtrless}\hat{\boldsymbol{x}}$, as well as outgoing scattered waves with each of the allowed wave vectors. In a typical scattering problem, the outgoing states consist of $H^+(kr)$ radial functions. In the asymptotic region,

$$H_l^{\pm}(kr) \approx \sqrt{\frac{2}{\pi kr}} e^{\pm i(kr - l\pi/2 - \pi/4)}. \tag{3.6}$$

It is the combination of the sign in the exponential *and* the group velocity that determines whether the circular wave is outgoing or incoming. In a conventional scattering problem, the group velocity is always directed radially outwards, which is why $H^+(kr)$ gives the outgoing waves. This is a crucial distinction from the Rashba case. In the

Rashba problem the expectation value of the group velocity $\boldsymbol{v}_g = \nabla_{\boldsymbol{k}} H_0(\boldsymbol{k})$ in states of negative helicity is $\langle \boldsymbol{v}_g \rangle = (k - k_0)\hat{\boldsymbol{k}}/m$. This vector field is shown at the bottom of Fig. 3.1. For energies below the Dirac point, the $k_<$ states have group velocity antiparallel to the wave vector. Thus the outgoing $k_<$ states should be accompanied by $H^-(kr)$ radial functions to carry a probability current directed radially outwards. Ultimately, this is due to the presence of an additional term in the Rashba probability current, that is not present in spin-degenerate systems. We will discuss this current in Sec. 3.2.1.

For an incident wave in the $k_>$ state, the wave function for $r > R$ can be written as

$$\psi_>(r,\theta) = \psi_>^{\text{in}}(r,\theta) + \sum_{l=-\infty}^{\infty} e^{il\theta}[\psi_c^l(r,\theta) + \psi_b^l(r,\theta)], \tag{3.7}$$

where

$$\psi_c^l(r,\theta) \equiv \left(c_l - \frac{i^l}{2\sqrt{2}}\right)\begin{pmatrix} H_l^+(k_>r) \\ -H_{l+1}^+(k_>r)e^{i\theta}\end{pmatrix}, \tag{3.8}$$

$$\psi_b^l(r,\theta) \equiv b_l\begin{pmatrix} H_l^-(k_<r) \\ -H_{l+1}^-(k_<r)e^{i\theta}\end{pmatrix}, \tag{3.9}$$

while for an incident wave in the $k_<$ state, we have

$$\psi_<(r,\theta) = \psi_<^{\text{in}}(r,\theta) + \sum_{l=-\infty}^{\infty} e^{il\theta}[\psi_{\tilde{c}}^l(r,\theta) + \psi_{\tilde{b}}^l(r,\theta)], \tag{3.10}$$

where

$$\begin{aligned}\psi_{\tilde{c}_l}^l(r,\theta) &\equiv \tilde{c}_l\begin{pmatrix} H_l^+(k_>r) \\ -H_{l+1}^+(k_>r)e^{i\theta}\end{pmatrix}, \\ \psi_{\tilde{b}_l}^l(r,\theta) &\equiv \left(\tilde{b}_l - \frac{i^l}{2\sqrt{2}}\right)\begin{pmatrix} H_l^-(k_<r) \\ -H_{l+1}^-(k_<r)e^{i\theta}\end{pmatrix}.\end{aligned} \tag{3.11}$$

In these expressions b_l, c_l, $\tilde{b}_l$, and $\tilde{c}_l$ are coefficients to be determined by a solution of the scattering problem.

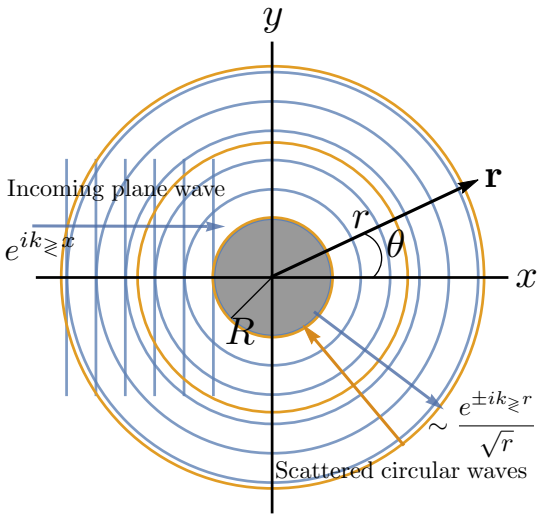

FIGURE 3.2: Plane wave scattering off an infinite circular barrier. There are two circular scattered states (blue and orange) of different wavelengths corresponding to the $k_>$ and $k_<$ states, respectively.

The incident plane wave can itself be decomposed into partial waves using the Jacobi-Anger expansion $e^{ikr\cos\theta} = \sum_{l=-\infty}^{\infty} i^l J_l(kr) e^{il\theta}$:

$$\begin{aligned}\psi^{\text{in}}_{\gtrless}(r,\theta) &= \frac{1}{\sqrt{2}}\begin{pmatrix}1\\ i\end{pmatrix} e^{ik_{\gtrless}x} \\ &= \sum_{l=-\infty}^{\infty} \frac{i^l}{2\sqrt{2}} e^{il\theta}\left[\begin{pmatrix} H_l^+(k_{\gtrless}r)\\ -H_{l+1}^+(k_{\gtrless}r)e^{i\theta}\end{pmatrix} + \begin{pmatrix} H_l^-(k_{\gtrless}r)\\ -H_{l+1}^-(k_{\gtrless}r)e^{i\theta}\end{pmatrix}\right]. \end{aligned} \tag{3.12}$$

The infinite potential barrier (3.5) forces the wave function to vanish at $r = R$,

$$\psi_{\gtrless}(R,\theta) = \begin{pmatrix}0\\ 0\end{pmatrix}. \tag{3.13}$$

Imposing this condition in Eq. (3.7) and (3.10) gives four equations from which we obtain the unknown coefficients b_l, $\tilde{b}_l$, c_l, $\tilde{c}_l$:

$$\begin{aligned} b_l &= \frac{1}{\Delta_l}\Big(H_l^+(k_>R)H_{l+1}^-(k_>R) - H_l^-(k_>R)H_{l+1}^+(k_>R)\Big), \\ c_l &= \frac{1}{\Delta_l}\Big(H_l^-(k_>R)H_{l+1}^-(k_<R) - H_l^-(k_<R)H_{l+1}^-(k_>R)\Big), \\ \tilde{b}_l &= \frac{1}{\Delta_l}\Big(H_l^+(k_>R)H_{l+1}^+(k_<R) - H_l^+(k_<R)H_{l+1}^+(k_>R)\Big), \\ \tilde{c}_l &= \frac{1}{\Delta_l}\Big(H_l^+(k_<R)H_{l+1}^-(k_<R) - H_l^-(k_<R)H_{l+1}^+(k_<R)\Big), \end{aligned}$$

where we have defined

$$\Delta_l \equiv \frac{2\sqrt{2}}{i^l}\Big(H_l^-(k_<R)H_{l+1}^+(k_>R) - H_l^+(k_>R)H_{l+1}^-(k_<R)\Big). \tag{3.14}$$

3.2.1 S-matrix

The four coefficients above determine the S-matrix for this scattering problem. As described in Sec. 2.3, the S-matrix may be written in terms of its l-components which are the unitary transformations that connect asymptotic states in the incoming circular basis ($e^{\mp i(k_\gtrless r - l\pi/2)}/\sqrt{r}$) to asymptotic states in the outgoing circular basis ($e^{\pm i(k_\gtrless r - l\pi/2)}/\sqrt{r}$). Using the asymptotic form of the Hankel functions for large argument (Eq. (3.6)), we obtain the S-matrix in angular momentum channel l,

$$S^l = \begin{pmatrix} S_{>>} & S_{><} \\ S_{<>} & S_{<<} \end{pmatrix} = \frac{2\sqrt{2}}{i^l}\begin{pmatrix} c_l & b_l\sqrt{\frac{k_>}{k_<}} \\ \tilde{c}_l\sqrt{\frac{k_<}{k_>}} & \tilde{b}_l \end{pmatrix}. \tag{3.15}$$

Using the explicit expressions given earlier for the coefficients b_l, $\tilde{b}_l$, c_l, $\tilde{c}_l$, as well as the Wronskian identity

$$H_l^+(z)H_{l+1}^-(z) - H_{l+1}^+(z)H_l^-(z) = \frac{4i}{\pi z}, \tag{3.16}$$

we find that $S^l_{><} = S^l_{<>}$; this is a consequence of time-reversal symmetry combined with reflection symmetry about the x axis (see Appendix C). In this case, there are two independent unitarity conditions on the S-matrix,

$$|c_l|^2 + |b_l|^2\frac{k_>}{k_<} = \frac{1}{8}, \quad b_l\tilde{b}_l^* = -c_l b_l^*, \tag{3.17}$$

which are satisfied by the coefficients given above. Unitarity of the S-matrix should be equivalent to the continuity equation:

$$\frac{d}{dt}\int_A |\psi(\boldsymbol{r},t)|^2 d^2r + \int_A \boldsymbol{\nabla}\cdot\boldsymbol{j}(\boldsymbol{r},t)d^2r = 0, \tag{3.18}$$

which defines the current density $\boldsymbol{j}$. A general expression for the current density is found by taking the above time derivative using the Schrodinger equation to get

$$\boldsymbol{\nabla}\cdot\boldsymbol{j}(\boldsymbol{r},t) = \Big(-i\psi(\boldsymbol{r},t)^\dagger\hat{H}\psi(\boldsymbol{r},t) + i\psi(\boldsymbol{r},t)\hat{H}\psi^\dagger(\boldsymbol{r},t)\Big). \tag{3.19}$$

The flux current density is readily found for the Rashba system to be $\boldsymbol{j}(\boldsymbol{r},t) = \boldsymbol{j}_K + \boldsymbol{j}_R$, where the usual kinetic current density

$$\boldsymbol{j}_K \equiv -\frac{i}{2m}(\psi^\dagger \nabla\psi - \nabla\psi^\dagger\psi) \tag{3.20}$$

is accompanied by a new Rashba current density

$$\boldsymbol{j}_R \equiv -\lambda\psi^\dagger(\boldsymbol{\sigma}\times\hat{\boldsymbol{z}})\psi. \tag{3.21}$$

Because the scattering potential does not alter the angular momentum, we can replace ψ in the above definitions with its partial wave component. For our time-independent scattering problem, the continuity equation becomes

$$\int_A d^2r\,\nabla\cdot\boldsymbol{j}(\boldsymbol{r},t) = \int_0^{2\pi} d\theta\,\boldsymbol{r}\cdot\boldsymbol{j}(\boldsymbol{r},\theta) = 0. \tag{3.22}$$

The integral over the ring in the continuity equation (3.22) is then evaluated for each partial wave. For an incident $k_>$ wave, one obtains

$$\int_0^{2\pi} d\theta\,\boldsymbol{r}\cdot\boldsymbol{j}_K = -\frac{16\lambda}{\sqrt{k_>k_<}}b_l^* d_l \cos[(k_< - k_>)r] + \frac{8}{m}(-|b_l|^2 + |c_l|^2 - 1/8), \tag{3.23}$$

$$\int_0^{2\pi} d\theta\,\boldsymbol{r}\cdot\boldsymbol{j}_R = \frac{16\lambda}{\sqrt{k_>k_<}}b_l^* d_l \cos[(k_< - k_>)r] + 8\lambda\left(\frac{|b_l|^2}{k_<} - \frac{|c_l|^2}{k_>} + \frac{1/8}{k_>}\right). \tag{3.24}$$

The first term in each equation is an interference term between scattered partial wave components of different wave vectors ($k_>$ and $k_<$). Combining the kinetic and Rashba pieces, we see that the interference terms completely cancel giving

$$\int_0^{2\pi} d\theta\,\boldsymbol{r}\cdot\boldsymbol{j} = \sqrt{2mE}\left(\frac{|b_l|^2}{k_<} + \frac{|c_l|^2}{k_>} - \frac{1/8}{k_>}\right), \tag{3.25}$$

so the continuity equation is satisfied by the first unitarity condition in Eq. (3.17). Repeating the above calculation for an incident $k_<$ wave, gives a second continuity equation:

$$|\tilde{b}_l|^2 + |\tilde{c}_l|^2\frac{k_<}{k_>} = \frac{1}{8}, \tag{3.26}$$

which may alternatively be obtained using $S^l_{><} = S^l_{<>}$ in combination with the unitarity conditions (3.17). Unitarity means that we have correctly identified the scattered and incident pieces of the wavefunction.

We may plot transition probabilities from the square modulus of the S-matrix elements in Eq. (3.15). The second equation in (3.17) ensures that $|S_{>>}|^2 = |S_{<<}|^2$, and symmetry requires $|S_{><}|^2 = |S_{<>}|^2$, hence only $|S_{>>}|^2$ and $|S_{><}|^2$ are plotted in Fig. 3.3. The curves are plotted on a log-linear scale with $\delta \equiv \sqrt{|E|/E_0}$ a dimensionless measure of the departure of the energy from the band bottom at $\delta = 0$. As the energy approaches the band bottom, fewer partial waves contribute to the diagonal transition probabilities, while more partial waves contribute to the off-diagonal ones. Exactly at the band bottom, we have $c_l = \tilde{b}_l = 0$ and $b_l = -i^l/2\sqrt{2}$, so that the S-matrix becomes

$$S^l = \begin{pmatrix} 0 & -1 \\ -1 & 0 \end{pmatrix}, \tag{3.27}$$

for all l, independent of the radius of the scatterer R. Scattering is entirely off-diagonal in this limit, and all angular momentum channels contribute equally. As we will see in Sec. 3.4, this is a consequence of destructive interference between $k_<$ and $k_>$ states. Near zero energy, the beating pattern imposed on the wavefunction by these two scattering channels helps the wavefunction to vanish at $r = R$ in accordance with the matching condition. Such destructive interference can not occur within the diagonal scattering channel, hence the off-diagonal form of the S-matrix.

3.2.2 Differential cross section

The differential cross section is the ratio of scattered to incident flux in a particular incoming ($k_{\gtrless}$) channel, which may be computed from (2.10). Using the asymptotic form of the incident and scattered wave functions, the fluxes are given by

$$|\boldsymbol{\jmath}^{\rm sc}_{>}| = \frac{k_> - k_0}{mr}\left(|\Phi_{>>}|^2 + |\Phi_{><}|^2\right), \tag{3.28}$$

$$|\boldsymbol{\jmath}^{\rm sc}_{<}| = \frac{k_> - k_0}{mr}\left(|\Phi_{<>}|^2 + |\Phi_{<<}|^2\right), \tag{3.29}$$

$$\boldsymbol{\jmath}^{\rm in}_{\gtrless} = \pm\frac{1}{m}(k_> - k_0)\hat{x}, \tag{3.30}$$

so that

$$\left(\frac{d\sigma}{d\theta}\right)_> = |\Phi_{>>}|^2 + |\Phi_{><}|^2, \tag{3.31}$$

$$\left(\frac{d\sigma}{d\theta}\right)_< = |\Phi_{<>}|^2 + |\Phi_{<<}|^2. \tag{3.32}$$

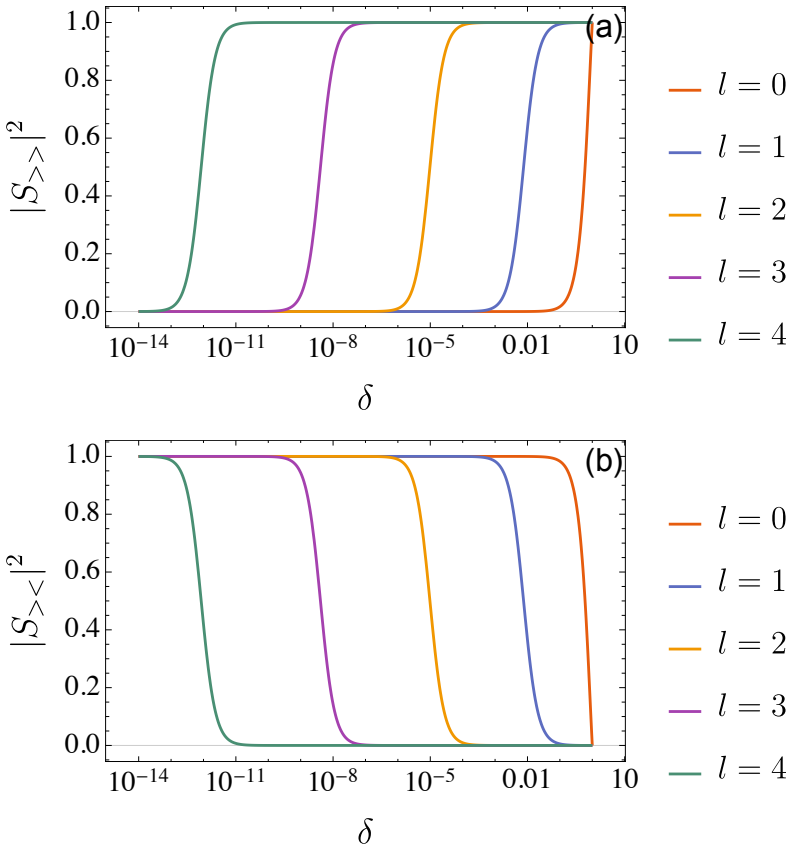

FIGURE 3.3: (a) Diagonal and (b) off-diagonal transition probabilities from the S-matrix elements for partial waves $l = 0, 1, 2, 3, 4$, as a function of $\delta = \sqrt{E/E_0}$. In both plots $k_0 R = 0.1$.

We have defined

$$\Phi_{>>} = \sqrt{\frac{4}{\pi k_>}} \sum_l \left(c_l - \frac{i^l}{2\sqrt{2}} \right) e^{il(\theta - \pi/2)}, \tag{3.33}$$

$$\Phi_{><} = \sqrt{\frac{4}{\pi k_<}} \sum_l b_l e^{il(\theta + \pi/2)}, \tag{3.34}$$

$$\Phi_{<>} = \sqrt{\frac{4}{\pi k_>}} \sum_l \tilde{c}_l e^{il(\theta - \pi/2)}, \tag{3.35}$$

$$\Phi_{<<} = \sqrt{\frac{4}{\pi k_<}} \sum_l \left(\tilde{b}_l - \frac{i^l}{2\sqrt{2}} \right) e^{il(\theta + \pi/2)}, \tag{3.36}$$

where sums over l range from $-\infty$ to ∞.

We plot the differential cross section in units of k_0^{-1} in Fig. 3.4. From panel (c), we see that the differential cross section in the incoming $k_>$ channel ($|\Phi_{>>}|^2 + |\Phi_{><}|^2$) becomes increasingly anisotropic with peaks at $\theta = 0$ (forward scattering) and $\theta = \pi$

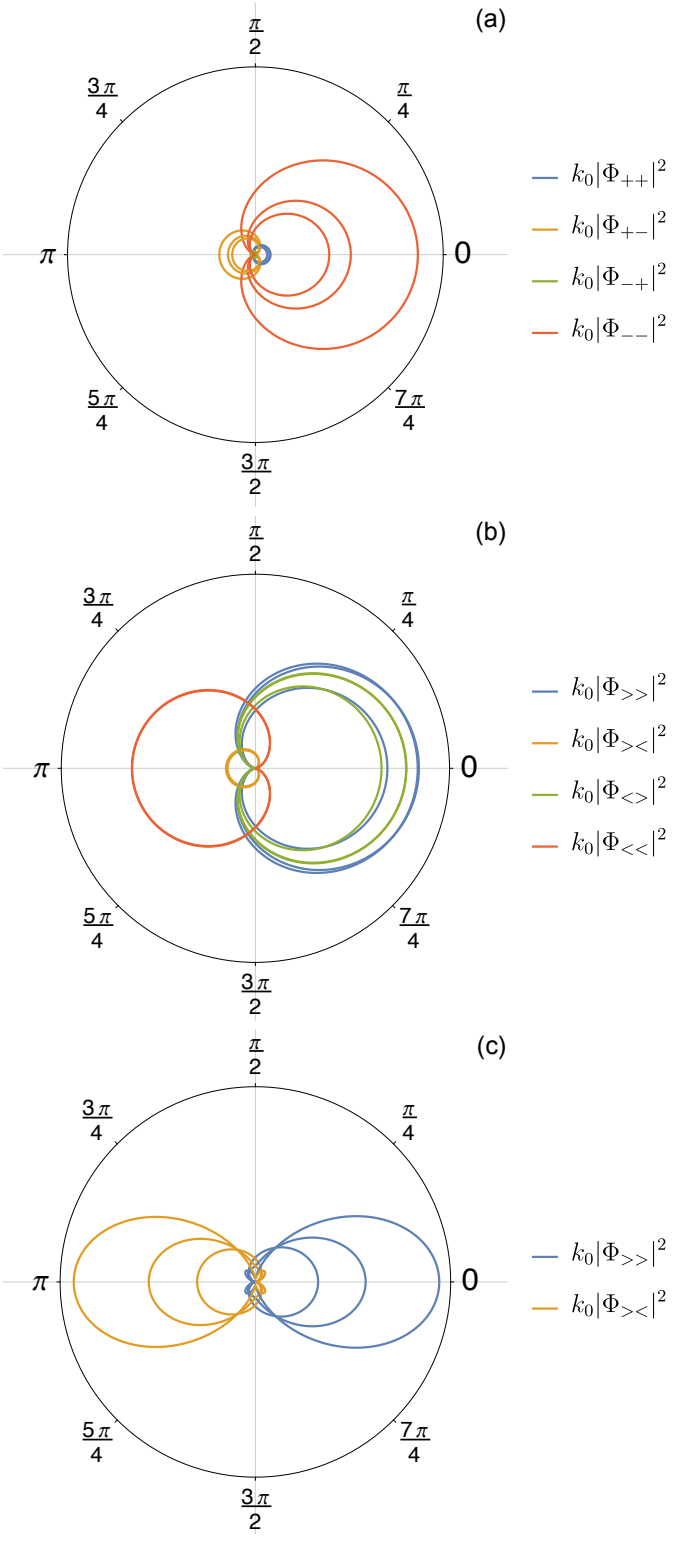

FIGURE 3.4: Polar plots of differential cross section for scattering between: (a) helicity bands at energies above the Dirac point ($E = 3E_0$, $E = 5E_0$, $E = 7E_0$), (b) $k_{\gtrless}$ states at energies below the Dirac point ($E = 0.99E_0$, $E = 0.5E_0$, $E = 0.01E_0$), and (c) $k_{\gtrless}$ states near the band bottom ($E = 0.001E_0$, $E = 0.0001E_0$, $E = 0.00001E_0$). In each plot, k_0R is set to 0.1. The radius of each curve is the magnitude of $k_0|\Phi_{ii}|^2$. In the bottom figure, there is no visible distinction between $|\Phi_{><}|^2$ and $|\Phi_{<<}|^2$, as with $|\Phi_{>>}|^2$ and $|\Phi_{<>}|^2$, so only one of each is plotted.

(backscattering) as E tends to the band bottom. Using the observation that in this limit, $c_l = \tilde{b}_l = 0$ and $\tilde{c}_l = b_l = -i^l/2\sqrt{2}$, the sums over l in Eq. (3.33) and (3.34) can be performed analytically and we find that the differential cross section at the band bottom formally becomes

$$\left(\frac{d\sigma}{d\theta}\right)_{\gtrless}\Bigg|_{E=0} = \frac{2\pi}{k_0}\left[\delta^2(\theta) + \delta^2(\theta - \pi)\right], \tag{3.37}$$

where $\delta(\theta)$ is an angular delta function normalized such that $\int_{-\pi}^{\pi} d\theta\delta(\theta) = 1$. At the band bottom, scattering becomes effectively one-dimensional in that only forward and backward scattering are allowed. No such feature occurs in the $E > E_0$ regime. The non-integrability of the differential cross section at threshold is a common feature of scattering in two dimensions (see Appendix B). Unlike conventional scattering though, the divergence here arises from the contribution of an infinite number of partial waves at the threshold energy. Remarkably, Eq. (3.37) has no R dependence, and is therefore insensitive to the range of the scattering potential. As shown in Appendix B, this is in contrast with scattering of an electron without spin-orbit coupling where the differential cross section near the band bottom depends explicitly on the radius R of the scatterer. In Sec. 3.3 we present further evidence that the details of the impurity potential do not affect this result.

For reference, we show in Fig. 3.4(a) the differential cross section for the $E > E_0$ regime, which was previously worked out by Yeh *et al.* [47]. In this regime $\pm$ refers to the helicity of the band. The anisotropies in the differential cross section can be understood from the fact that the scattering potential is spin-independent. For example, when starting from an incident positive-helicity state, the electron can only forward scatter into a state of the same helicity. Forward scattering to the negative-helicity state would flip the spin. Likewise, the electron can only backward scatter into the negative-helicity state, since scattering to the positive-helicity state would flip the spin. This is why the differential cross sections vanish at $\theta = \pi$ for the blue curves, and $\theta = 0$ for the orange curves. The same reasoning can be applied to scattering between $k_{\gtrless}$ states in the negative-energy regime [Fig. 3.4(b) and (c)]. Here, an incident $k_>$ electron cannot backscatter to another $k_>$ state without flipping its spin. For scattering from $k_>$ to $k_<$, there is a subtlety to this argument. Because the group velocity in the $k_<$ state is directed oppositely to that in the $k_>$ state, the outgoing flux measured in the $k_<$ channel at $\theta = 0$ will correspond to the wave vector $-k_<\hat{\boldsymbol{x}}$. This is a spin-flipped state and will thus have zero contribution to the cross section. Hence, the orange lines in Fig. 3.4 go to zero at $\theta = 0$. Likewise, if

the incident wave vector is $k_<\hat{\boldsymbol{x}}$, then the spin-flipped states would be $-k_<\hat{\boldsymbol{x}}$, detected at $\theta = 0$, and $-k_>\hat{\boldsymbol{x}}$, detected at $\theta = \pi$, corresponding to the zeroes of the differential cross section in those channels (red and green respectively in Fig. 3.4).

3.2.3 Total cross section

Integrating Eq. (3.31) and (3.32) over θ gives the total cross sections $\sigma_{\gtrless}$ for an incident $k_{\gtrless}$ state,

$$\sigma_> = \frac{2}{k_>} \sum_l \left[1 - 8 \,\mathrm{Re} \left(c_l \frac{(-i)^l}{2\sqrt{2}} \right) \right], \tag{3.38}$$

$$\sigma_< = \frac{2}{k_<} \sum_l \left[1 - 8 \,\mathrm{Re} \left(\tilde{b}_l \frac{(-i)^l}{2\sqrt{2}} \right) \right]. \tag{3.39}$$

These are plotted in Fig. 3.5 as a function of the energy. For any value of the dimensionless radius of the scatterer $k_0 R$, there is a singularity in the cross section at the band bottom due to the squared delta functions in Eq. (3.37). Equivalently, from Eq. (3.38) and (3.39) we get the divergent sum $\sigma_{\gtrless} \to (2/k_0) \sum_l 1$ as $E \to 0$. Threshold singularities in the cross section are common to scattering problems in 2D (see Appendix B); however, in the conventional case without spin-orbit coupling such singularities are typically due to a prefactor of $1/k$ which diverges as $k \to 0$ at the bottom of a parabolic band [59]. In the Rashba case, it is the sum over partial waves rather than the prefactor $1/k_0$ that diverges at the band bottom, since in that limit all l channels contribute equally (Fig. 3.3).

In Fig. 3.5(c), we zoom in on the region near the band bottom, and plot the total cross section $\sigma_>$ as a function of $\delta = \sqrt{E/E_0}$ on a log-linear scale. As the energy approaches the band bottom, the cross section increases in discrete steps and displays a series of plateaus that are increasingly flat as δ tends to zero on a logarithmic scale, with the onset of each plateau occurring at the threshold energy where a new l channel contributes to the off-diagonal S-matrix elements [compare with Fig. 3.3(b)]. A similar behavior is found for $\sigma_<$. On these plateaus the total cross section is quantized in units of $4/k_0$,

$$\sigma_{\gtrless} = \frac{4n}{k_0},\ n = 0, 1, 2, \ldots, \tag{3.40}$$

independently of the scatterer radius R. The way $\sigma_{\gtrless}$ approaches infinity as the energy nears the band bottom is thus much more complex than the smooth $1/k \propto 1/\sqrt{E}$ divergence (moderated by a logarithmic factor) found in the case without spin-orbit coupling. In that case, the $l = 0$ partial wave (s-wave) dominates the low-energy behavior [59]. An analogy with Landauer quantization of the conductance in 1D [60–62] may lead one to conjecture that the quantization of the total cross section (3.40) in the low-energy limit is a direct consequence of the emergent 1D behavior in that limit, observed in the extreme anisotropy of the differential cross section (3.37).

3.3 Delta-shell scattering

In the low-energy limit, the S-matrix (3.27) and, consequently, the differential cross section (3.37) as well as the plateau behavior of the total cross section (3.40) were found to be completely independent of the range R of the scattering potential. While this result suggests the form (3.27) of the S-matrix is a universal feature of Rashba scattering in the low-energy limit, at least for spin-independent and rotationally invariant finite-range potentials $V(r)$, the possibility remains that Eq. (3.27) is a special feature of the hard-disk potential (3.5). To further support our conjecture of the universality of the low-energy S-matrix (3.27), we consider the $E < 0$ scattering problem for another scattering potential, the delta-shell potential:

$$V(r) = V_0 \delta(r - R). \tag{3.41}$$

Compared with the hard-disk potential (3.5), this potential has two tunable parameters, V_0 and R. In the region $r > R$, the wave function has the same form as Eq. (3.4). For $r < R$, the Neumann functions $N_l(k_{\gtrless} r)$ must be eliminated for the solution to be regular at $r = 0$. Thus,

$$\Psi_{r<R}(r,\theta) \;=\; \sum_{l=-\infty}^{\infty} e^{il\theta}\left[a_l' \begin{pmatrix} J_l(k_> r) \\ -J_{l+1}(k_> r)e^{i\theta} \end{pmatrix} + b_l' \begin{pmatrix} J_l(k_< r) \\ -J_{l+1}(k_< r)e^{i\theta} \end{pmatrix}\right]. \tag{3.42}$$

Consider an incident $k_>$ state. Then $a_l = 0$, $d_l = \frac{i^l}{2\sqrt{2}}$, and there are four unknown coefficients. Continuity of the wave function at $r = R$ gives two equations (or one spinor

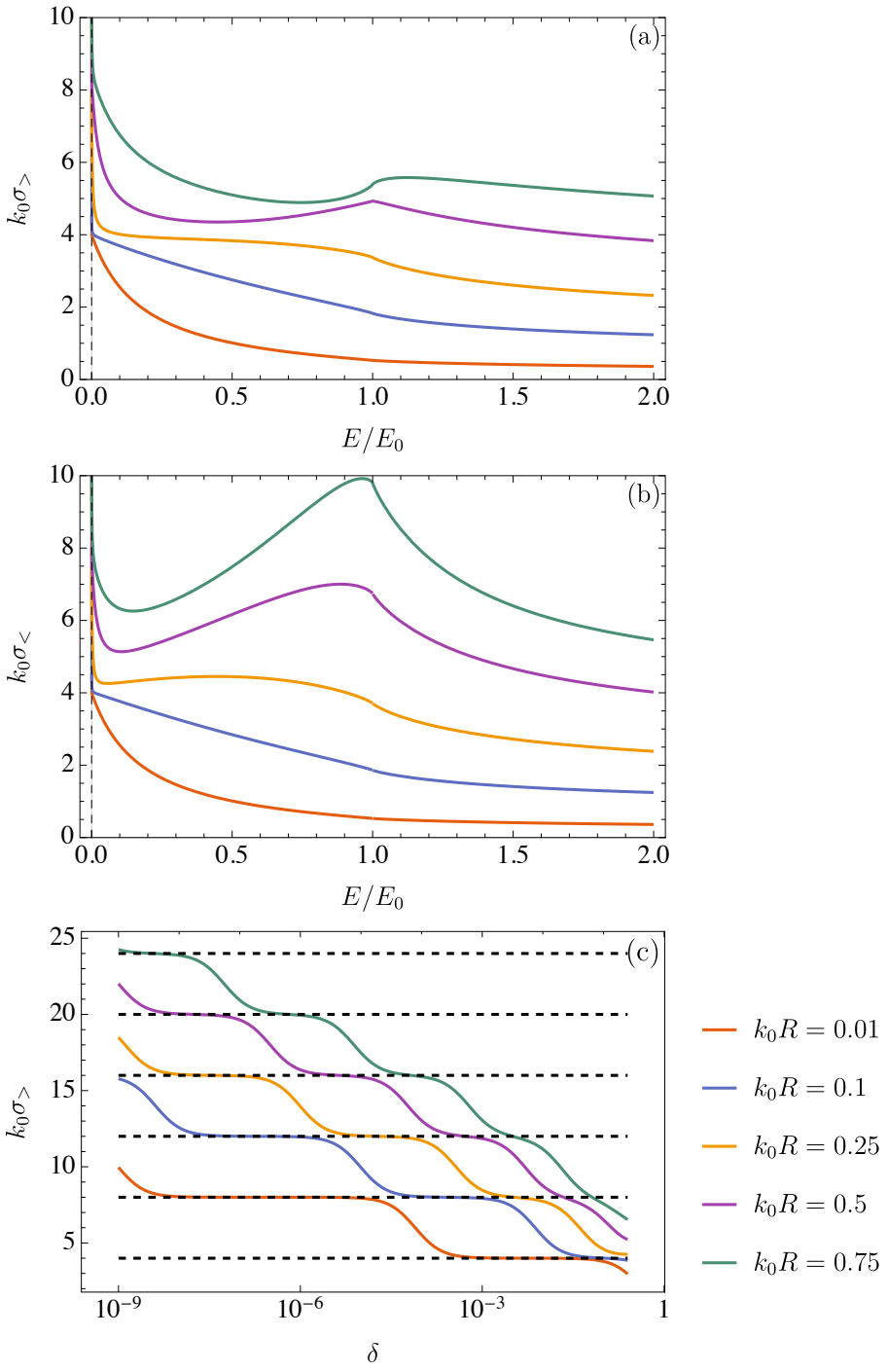

FIGURE 3.5: Total cross section for various values of the dimensionless scatterer radius k_0R: (a) total cross section for incoming $k_>$ state as a function of energy, (b) total cross section for incoming $k_<$ state as a function of energy, (c) total cross section for incoming $k_>$ state as a function of δ on a log-linear scale. In each of (a) and (b), the cross section is also calculated in the $E > E_0$ regime. For $\sigma_<$ ($\sigma_>$), this shows scattering from an incident positive-helicity (negative-helicity) state. The vertical dashed line in (a) and (b) at $E/E_0 = 0$ is a guide to the eye, showing the divergent behavior of all cross sections at the band bottom. The horizontal dashed lines in (c) show the plateaus at $k_0\sigma_> = 4n$, $n = 0, 1, 2, \ldots$

equation),

$$\Psi_{r>R}(R,\theta) = \Psi_{r<R}(R,\theta), \tag{3.43}$$

and integrating the Schrödinger equation along the radial direction from $R-\epsilon$ to $R+\epsilon$ gives two more

$$\partial_r \Psi_{r>R}(R,\theta) - \partial_r \Psi_{r<R}(R,\theta) = 2mV_0\Psi(R,\theta). \tag{3.44}$$

All four coefficients can thus be solved for, but their closed forms are too long to present here. Instead, we focus on the low-energy limit for now (more results for this potential will be shown in Chapter 4). At the band bottom, we have $k_< = k_> = k_0$ and the matching conditions (3.43)-(3.44) may be written as the matrix equation

$$M \begin{pmatrix} a_l' \\ b_l' \\ b_l + \frac{i^l}{2\sqrt{2}} \\ c_l \end{pmatrix} = \begin{pmatrix} 0 \\ 0 \\ 0 \\ 0 \end{pmatrix}, \tag{3.45}$$

where M is a 4×4 matrix containing Bessel and Hankel functions evaluated at k_0R. One can readily verify that $\det M \neq 0$ for any nonzero value of V_0. Thus only the trivial solution $a_l' = b_l' = c_l = 0$, $b_l = -\frac{i^l}{2\sqrt{2}}$ satisfies the matching conditions, which is precisely the result from hard-disk scattering.

The S-matrix (3.27) appears to be a universal feature of low-energy Rashba scattering in that it applies to both hard-disk and delta-shell potentials of any radius R and magnitude V_0. We conjecture that this extends to any circularly symmetric, spin-independent potential of finite radius.

3.4 Discussion

In summary, we have studied the scattering of electrons with Rashba spin-orbit coupling off spin-independent, circularly symmetric potentials in the low-energy regime $E < E_0$, with a focus on the approach to the band bottom $E \to 0$. We find several features in this limit that appear to be insensitive to details of the scattering potential: the S-matrix approaches a purely off-diagonal form with both off-diagonal elements equal to negative one, and all angular momentum channels contribute equally at the band

bottom; the differential cross section is increasingly peaked at forward and backward scattering angles; the total cross section increases by quantized steps as the energy approaches the band bottom. The quasi-1D character of these features supports and further expands Ref. [51]'s interpretation of reduction in effective dimensionality in the low-energy limit of Rashba systems.

Our simple scattering setup results in unusual features in the scattering quantities. The presence of quantized steps in the cross-section is clearly a consequence of new partial-wave scattering channels opening up at progressively lower energies as evidenced by Fig 3.3, but why should these channels contribute at all and what determines the energies at which each channel turns on? To better understand what is happening, we need to note two fundamental ways in which Rashba scattering differs from spin-degenerate scattering. The first is that in the Rashba case there are two distinct scattering channels $k_<$ and $k_>$ and their wavefunctions can interfere *destructively*. The second is that in the zero-energy limit there is an incident wave of finite wavenumber $k = k_0$ as opposed to $k = 0$ in the spin degenerate case. In the spin-degenerate case, the low-energy incident wave consists of Bessel functions that are vanishingly small at $r = R$ for all $l > 0$ and with decreasing magnitude as the energy is lowered (see Appendix B). Meanwhile, the scattered wave consists of Hankel functions which have a singular part. This too must vanish at $r = R$ for $l > 0$, and the only way to do so is if the coefficient (which determines the phase shift) is vanishingly small. So the low-energy limit of the spin-degenerate case is very simple. The only significant contributions to the wavefunction are in the $l = 0$ channel, and forcing this wavefunction to have a node at the potential radius is as simple as applying a single phase shift. What changes in the Rashba system? First, the destructive interference of the scattered waves dramatically reduces the singular part of the Hankel function by an amount that increases as the energy is lowered. This means that below an l-dependent energy, the singular part no longer affects the wavefunction and the corresponding coefficients no longer need to vanish. Second, because k remains finite, higher partial waves contribute significantly at $r = R$. In the limit $E = 0$, the only way for the full wavefunction to vanish at R is if it is extinguished completely: $\psi(r, \theta) = 0$. In other words the scattered wave becomes a plane wave with all partial waves contributing equally. Of course, a zero wavefunction is not normalizable, but this is an artifact of the plane-wave approximation. In a real scattering setup, the wavefunction would be a linear combination of plane waves with a very small bandwidth,

containing some weight up to a finite energy where not all partial waves are involved in the scattering.

The distinction bewteen the spin-degenerate and Rashba wavefunctions is epitomized in the schematic Fig. 3.6. In the top (spin-degenerate) panel we see the singular part of the

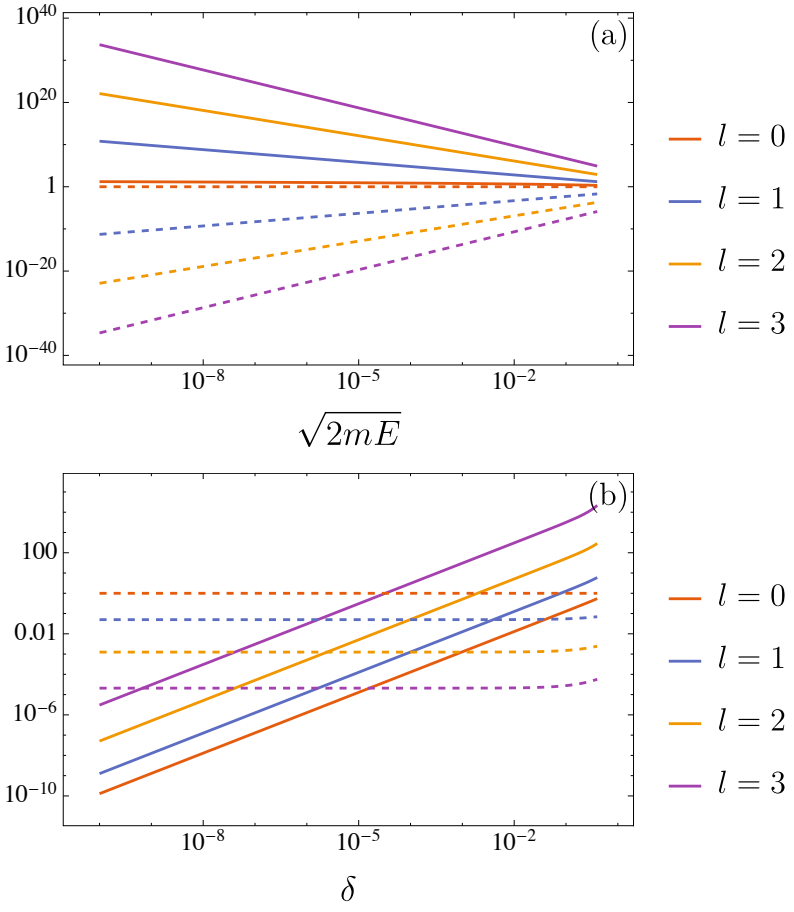

FIGURE 3.6: (a) Spin-degenerate system: magnitude of the singular part of the scattered waveform $H_l^+(kR)$ at the potential radius (solid). Magnitude of the incident waveform $J_l(kR)$ at the potential radius (dashed). (b) Rashba system: magnitude of the singular part of the scattered waveform $H_l^+(k_>R) + H_l^-(k_<R)$ at the potential radius (solid). Magnitude of the incident waveform $J_l(k_>R)$ at the potential radius (dashed).

scattered waveform diverges with increasing l and decreasing energy. These divergences must be cancelled by a vanishing coefficient. The exception is $l = 0$ where the incident (dashed) and scattered parts are similar in magnitude. Contrast this with Rashba scattering in the lower panel where the singular part is suppressed as the energy is lowered. The intersection points between solid lines and their dashed counterparts mark the transition energy where a new partial wave is added (or subtracted) from the S-matrix, and the cross-section increases by a step.

This discussion centers on the fact that the wavefunction vanishes at $r = R$. However, we saw that the low-energy limit of the S-matrix was the same for the delta-shell potential where the wavefunction remains finite and is independent of the potential strength and radius. This suggests that the constraints imposed by any circular potential may be so restrictive as to cause this destructive interference phenomena and the corresponding unusual cross-section. Therefore, we conjecture that the features we have found are indeed universal for spin-independent, circularly symmetric, finite-range potentials. In fact, the next chapter will be devoted to proving this statement. It would be interesting to see if these results extend to a broader class of spin-dependent but otherwise time-reversal-symmetric potentials, but we leave this for future research. We expect some of the features we have discussed could be observed experimentally in low-density, strongly spin-orbit coupled 2D electron gases using scanning gate microscopy techniques, which have been used to image coherent electron flow [63, 64]. Concrete predictions to be compared directly with experiment such as simulated current maps could in principle be derived from the results presented in this chapter, for example by the method discussed in Ref. [43].

Chapter 4

Universality of low-energy Rashba scattering

In the present chapter we establish the result that the peculiar scattering features found in Chapter 3 are a universal property of low-energy scattering in the Rashba system and should hold for arbitrary spin-independent, circularly symmetric, finite-range potentials. This is established via a nonperturbative solution of the Lippmann-Schwinger equation for an arbitrary potential satisfying the requirements listed above. In Sec. 4.1 we formulate the Lippmann-Schwinger equation for the Rashba scattering problem, introduce the T-matrix and establish its relation to the S-matrix, then relate the T and S matrices to the differential and total scattering cross sections, deriving a new optical theorem for low-energy Rashba scattering in the process. In Sec. 4.2 we present a nonperturbative solution of the Lippmann-Schwinger equation, obtaining the T-matrix in the low-energy limit. Our solution relies on the application of a momentum cutoff around the degenerate low-energy Rashba ring of states. As expected, the low-energy T-matrix is universal and exhibits a distinct 1D character. Using the relation between the S and T matrices derived earlier, we obtain the universal off-diagonal S-matrix of Eq. (3.27). Our optical theorem allows us to show that the quantized plateaus seen in the previous chapter for the hard disk potential are indeed a generic feature of the low-energy total cross section, independent of the details of the potential. Finally, in Sec. 4.3 we illustrate these results with a number of example potentials. We conclude in Sec. 4.4, and derive a number of technical results in Appendices D-F.

4.1 Scattering quantities

The presence of Rashba SOC causes the effective potential, which includes many virtual scattering processes, to be altered. We hypothesize that this alteration is universal, for a class of impurity potentials. The resulting effective potential is the T-matrix, and we will focus on this quantity throughout the chapter. As described in Sec. 2.3, the T-matrix is the portion of the S-matrix in which some scattering occurs. Since Rashba scattering involves new subtleties, it is worth deriving the exact relation between these objects in the lower helicity band, elucidating various scattering quantities along the way. The natural starting point is the Lippmann-Schwinger equation (2.28). Written in terms of the wavevector $\boldsymbol{k}$ and spin σ components, it reads

$$\psi_{\boldsymbol{k}\sigma}(\boldsymbol{r};E) \;=\; \psi^{\text{in}}_{\boldsymbol{k}\sigma}(\boldsymbol{r};E) + \sum_{\sigma'}\int d^2\boldsymbol{r}' G^R_{\sigma\sigma'}(\boldsymbol{r},\boldsymbol{r}';E)V(\boldsymbol{r}')\psi_{\boldsymbol{k}\sigma'}(\boldsymbol{r}';E), \tag{4.1}$$

where $G^R_{\sigma\sigma'}(\boldsymbol{r},\boldsymbol{r}';E)$ is the retarded position-space Green's function of the unperturbed Hamiltonian and $V(\boldsymbol{r})$ is the scattering potential. Once again, the incident wavefunction is chosen to be a negative helicity plane wave with wavevector $\boldsymbol{k}$ oriented at an angle $\theta_{\boldsymbol{k}}$ with respect to the x-axis,

$$\psi^{\text{in}}_{\boldsymbol{k}\sigma}(\boldsymbol{r};E) = e^{i\boldsymbol{k}\cdot\boldsymbol{r}}\eta^-_\sigma(\theta_{\boldsymbol{k}}), \tag{4.2}$$

where $\eta^-_\sigma(\theta_{\boldsymbol{k}})$ is the σ component of the $\eta^-(\theta_{\boldsymbol{k}})$ eigenspinor defined in Eq. (1.24). We can relate this to the T-matrix through the defining relation Eq. (2.26): $T|i\rangle = V|\psi\rangle$, where $|i\rangle$ is the initial state, and $|\psi\rangle$ is the scattering state. In terms of wavefunctions, we write

$$V|\psi\rangle = \sum_{\sigma'}\int d^2\boldsymbol{r}' T|\boldsymbol{r}'\sigma'\rangle\psi^{\text{in}}_{\boldsymbol{k}\sigma'}(\boldsymbol{r}';E), \tag{4.3}$$

or equivalently,

$$V(\boldsymbol{r})\psi_{\boldsymbol{k}\sigma}(\boldsymbol{r};E) = \sum_{\sigma'}\int d^2\boldsymbol{r}' T^{\boldsymbol{r}\boldsymbol{r}'}_{\sigma\sigma'}e^{i\boldsymbol{k}\cdot\boldsymbol{r}'}\eta^-_{\sigma'}(\theta_{\boldsymbol{k}}). \tag{4.4}$$

We will need to Fourier transform the T-matrix to momentum-space,

$$T^{\boldsymbol{r}\boldsymbol{r}'}_{\sigma\sigma'} = \int\frac{d^2\boldsymbol{k}'}{(2\pi)^2}\int\frac{d^2\tilde{\boldsymbol{k}}}{(2\pi)^2}T^{\boldsymbol{k}'\tilde{\boldsymbol{k}}}_{\sigma\sigma'}e^{i\boldsymbol{k}'\cdot\boldsymbol{r}}e^{-i\tilde{\boldsymbol{k}}\cdot\boldsymbol{r}'}. \tag{4.5}$$

Substituting (4.5) into (4.4) and (4.4) into (4.1), we obtain a modified Lippman-Schwinger equation,

$$\psi_{\boldsymbol{k}\sigma}(\boldsymbol{r};E) \;=\; \psi^{\rm in}_{\boldsymbol{k}\sigma}(\boldsymbol{r};E) + \sum_{\sigma'\sigma''}\int d^2\boldsymbol{r}' \int \frac{d^2\boldsymbol{k}'}{(2\pi)^2} G^R_{\sigma\sigma'}(\boldsymbol{r},\boldsymbol{r}';E) T^{\boldsymbol{k}'\boldsymbol{k}}_{\sigma'\sigma''} e^{i\boldsymbol{k}'\cdot\boldsymbol{r}'}\eta^-_{\sigma''}(\theta_{\boldsymbol{k}}). \tag{4.6}$$

To proceed any further requires knowing the position-space Green's function. This is derived in Appendix D: see Eq. (D.7) for $\sigma = \sigma'$ and Eq. (D.12) for $\sigma \neq \sigma'$. For a scattering problem, we must consider the asymptotic wavefunction, which for a finite range potential, amounts to imposing $r \gg r'$, $|\boldsymbol{r}-\boldsymbol{r}'| \approx r - \hat{\boldsymbol{r}}\cdot\boldsymbol{r}'$ and $\theta_{\boldsymbol{r}-\boldsymbol{r}'} \approx \theta_{\boldsymbol{r}}$ in the Green's function, where $\hat{\boldsymbol{r}}$ denotes a unit vector in the direction of $\boldsymbol{r}$. Using the asymptotic form of the Hankel function for large argument, Eq. (3.6), we obtain the asymptotic Green's function

$$G^R_{\sigma\sigma'}(\boldsymbol{r},\boldsymbol{r}';E) \approx -\frac{m}{k_+ + k_-}\sqrt{\frac{i}{2\pi r}} \sum_{j=+,-} g^j_{\sigma\sigma'}(\boldsymbol{r}) e^{-i\boldsymbol{k}_j\cdot\boldsymbol{r}'}, \tag{4.7}$$

where $\boldsymbol{k}_j \equiv k_j\hat{\boldsymbol{r}}$ and k_j is given in Eq. (D.3) and (D.4). We have also defined the matrix

$$\begin{aligned} g^j(\boldsymbol{r}) \;&\equiv\; \sqrt{k_j}e^{ik_jr}\begin{pmatrix} 1 & ie^{-i\theta_{\boldsymbol{r}}}j \\ -ie^{i\theta_{\boldsymbol{r}}}j & 1 \end{pmatrix} \\ &=\; 2\sqrt{k_j}e^{ik_jr}\eta^j(\theta_{\boldsymbol{r}})\eta^j(\theta_{\boldsymbol{r}})^\dagger. \end{aligned} \tag{4.8}$$

Since the $\boldsymbol{r}'$ dependence of the Green's function has been isolated, we can now evaluate the integrals in (4.6) to get the asymptotic wavefunction,

$$\psi_{\boldsymbol{k}}(\boldsymbol{r};E) \;\approx\; \psi^{\rm in}_{\boldsymbol{k}}(\boldsymbol{r};E) - \frac{m}{(k_+ + k_-)}\sqrt{\frac{2i}{\pi r}} \sum_{j=+,-} \sqrt{k_j}e^{ik_jr}\eta^j(\theta_{\boldsymbol{r}})\eta^j(\theta_{\boldsymbol{r}})^\dagger T^{\boldsymbol{k}_j\boldsymbol{k}}\eta^-(\theta_{\boldsymbol{k}}). \tag{4.9}$$

At this point we orient the x-axis along the incident wave direction ($\theta_{\boldsymbol{k}} = 0$) and recognize that for any energy below the Dirac point, the magnitude of the corresponding wavevector is either $k_>$ or $k_<$. We write this as $\boldsymbol{k} = k_\mu\hat{\boldsymbol{x}}$, where $\mu = >, <$.

We need a sum over wave vector magnitudes $\nu = >, <$ in (4.9) rather than helicity index $j = +, -$. This is accomplished by noting from $k_{\gtrless} = k_0(1 \pm \delta)$ and $k_\pm = k_0(\delta \mp 1)$, the

mathematical relation

$$k_\pm = \mp k_{\lessgtr}, \tag{4.10}$$

valid for any energy below the Dirac point. Eq. (4.9) then reads

$$\begin{aligned}\psi_\mu(\boldsymbol{r};E) \;\approx\; & \psi_\mu^{\text{in}}(\boldsymbol{r};E) - \frac{m}{2k_0\delta}\sqrt{\frac{2i}{\pi r}}\Big(\sqrt{k_>}e^{ik_>r}\eta^-(\theta_{\boldsymbol{r}})\eta^-(\theta_{\boldsymbol{r}})^\dagger T^{\boldsymbol{k}_>\boldsymbol{k}}\eta^-(0) \\ & + i\sqrt{k_<}e^{-ik_<r}\eta^+(\theta_{\boldsymbol{r}})\eta^+(\theta_{\boldsymbol{r}})^\dagger T^{-\boldsymbol{k}_<\boldsymbol{k}}\eta^-(0)\Big),\end{aligned} \tag{4.11}$$

where $\boldsymbol{k}_{\gtrless} \equiv k_{\gtrless}\hat{\boldsymbol{r}}$.

From Eq. (4.11), we can establish the relation between the T-matrix and S-matrix as well as the scattering amplitude. The result is

$$T_{--}^{\boldsymbol{k}_\nu\boldsymbol{k}_\mu} = \frac{i}{m}\frac{k_0\delta}{\sqrt{k_\mu k_\nu}}\sum_{l=-\infty}^{\infty} e^{il\theta}(S_{\mu\nu}^l - \mathbb{I}_{\mu\nu}), \tag{4.12}$$

and is derived in App. E.

4.1.1 Cross section and optical theorem

As seen in the previous chapter, it is very useful to examine the differential cross section. Beginning with Fermi's golden rule, Eq. (2.23), the transition rate is connected to the T-matrix via

$$w_{\mu\to\nu}d\theta = 2\pi|T_{--}^{\boldsymbol{k}_\mu\boldsymbol{k}_\nu}|^2 g(E_\nu)d\theta, \tag{4.13}$$

where $g(E_\nu)d\theta$ is the density of final states in the channel ν within an angle $d\theta$ of θ:

$$g(E_\nu) = \int_0^\infty \frac{dk\,k}{(2\pi)^2}\delta(E_\nu - E(k)) = \frac{m}{(2\pi)^2}\frac{k_\nu}{k_0\delta}. \tag{4.14}$$

Furthermore, the differential cross section in this channel is simply the transition rate divided by the incident flux [see Eq. (2.24)],

$$\begin{aligned}\left.\frac{d\sigma}{d\theta}\right|_{\mu\nu} &= \frac{w_{\mu\to\nu}}{|\boldsymbol{j}_\mu|} \\ &= \frac{m^2}{2\pi}\frac{k_\nu}{k_0^2\delta^2}|T_{--}^{\boldsymbol{k}_\mu\boldsymbol{k}_\nu}|^2 \\ &= \frac{1}{2\pi k_\mu}\left|\sum_{l=-\infty}^{\infty} e^{il\theta}(S_{\mu\nu}^l - \mathbb{I}_{\mu\nu})\right|^2,\end{aligned} \tag{4.15}$$

using Eq. (4.12). This last expression was denoted $|\phi_{\mu\nu}|^2$ in Chapter 3 [see Eqs (3.31), (3.32)]. Integrating over angles and summing over scattering channels gives the total cross section for an incident k_μ wave,

$$\begin{aligned}
\sigma_\mu &= \int_0^{2\pi} d\theta \sum_\nu \frac{1}{2\pi k_\mu} \left| \sum_{l=-\infty}^{\infty} e^{il\theta}(S^l_{\mu\nu} - \delta_{\mu\nu}) \right|^2 && (4.16)\\
&= \frac{1}{k_\mu} \sum_{l=-\infty}^{\infty} \left(\left| S^l_{\mu\mu} - 1 \right|^2 + \left| S^l_{\mu,-\mu} \right|^2 \right) && (4.17)\\
&= \frac{1}{k_\mu} \sum_{l=-\infty}^{\infty} (2 - (S^l_{\mu\mu} + S^{l*}_{\mu\mu})) && (4.18)\\
&= \frac{2}{k_\mu} \sum_{l=-\infty}^{\infty} (1 - \mathrm{Re}(S^l_{\mu\mu})), && (4.19)
\end{aligned}$$

where $S^l_{\mu,-\mu}$ denotes the off-diagonal component with first index μ, and we used the unitarity condition of the S-matrix ($|S^l_{\mu,-\mu}|^2 = 1 - |S_{\mu\mu}|^2$) in line (4.18). The final form of this cross section makes it clear that the diagonal part of the T-matrix in (4.12) obeys an optical theorem, since

$$\begin{aligned}
\mathrm{Im}\, T^{\boldsymbol{k}_\mu \boldsymbol{k}_\mu}_{--}(\theta = 0) &= -\frac{k_0 \delta}{m k_\mu} \sum_{l=-\infty}^{\infty} (1 - \mathrm{Re}(S^l_{\mu\mu}))\\
&= -\frac{k_0 \delta}{2m} \sigma_\mu. && (4.20)
\end{aligned}$$

Optical theorems are a feature of most scattering problems. They tell us that the cross section may be determined from the forward scattering part of the scattering amplitude (or equivalently the T-matrix). This is a property of wave mechanics. The effective size of a potential is given by the "shadow" cast behind it. For any wave, this shadow is due to destructive interference between the $\theta = 0$ part of the scattered and incident waves.

4.2 Universal Rashba T-matrix

With this scattering formalism at hand, we may compute any scattering observable in a Rashba system with $E < E_0$, provided we know the T-matrix $T^{\boldsymbol{k}_\mu \boldsymbol{k}_\nu}_{--}$. In a conventional 2D system without spin-orbit coupling, the T-matrix takes on a form at low energies that is dominated by the s-wave term, that decays logarithmically with the energy

(see Eq. (B.11)). Before doing any calculation, we can already see that the Rashba T-matrix has a different energy dependence, simply by looking at the Lippmann-Schwinger equation (4.9) or (E.8). Since the coefficient of the scattered wavefunction goes as $1/\delta$ for low energies, the T-matrix must at least be linear in δ in order to keep the probability density finite. We now make this explicit by deriving the low-energy Rashba T-matrix for any circularly symmetric, spin-independent potential of finite range.

First, we impose a momentum cutoff

$$k_0 - \tilde{\Lambda} < k < k_0 + \tilde{\Lambda}, \tag{4.21}$$

to avoid ultraviolet divergences. This amounts to keeping only the low-energy modes in our model, similar to the momentum shell renormalization group approach in the many-body problem [65, 66]. The appropriate dimensionless quantity corresponding to this cutoff is $\Lambda \equiv \tilde{\Lambda}/k_0$, so that we will always enforce the following hierarchy of scales:

$$\delta \ll \Lambda \ll 1. \tag{4.22}$$

This is indicated in the schematic Fig 4.1.

In the helicity basis denoted by i, j, any central spin-independent potential may be written as

$$\begin{aligned} V_{ij}(\boldsymbol{k}, \boldsymbol{k}') &= \int d^2\boldsymbol{r}\, e^{i(\boldsymbol{k}-\boldsymbol{k}')\cdot\boldsymbol{r}} V(\boldsymbol{r}) \eta^i(\theta_{\boldsymbol{k}'})^\dagger \eta^j(\theta_{\boldsymbol{k}}) \\ &= \frac{1}{2}\sum_{l=-\infty}^{\infty} V^l(k,k') e^{il(\theta_{\boldsymbol{k}'}-\theta_{\boldsymbol{k}})} \left(1 + ije^{i(\theta_{\boldsymbol{k}}-\theta_{\boldsymbol{k}'})}\right) \\ &= \frac{1}{2}\sum_{l=-\infty}^{\infty} \left(V^l(k,k') + ijV^{l+1}(k,k')\right) e^{il\theta_{\boldsymbol{k}'-\boldsymbol{k}}}, \end{aligned} \tag{4.23}$$

where $\theta_{\boldsymbol{k}'-\boldsymbol{k}} \equiv \theta_{\boldsymbol{k}'} - \theta_{\boldsymbol{k}}$, and in the second line, we introduced the partial wave component

$$V^l(k,k') = \int_0^{2\pi} \frac{d\theta_{\boldsymbol{k}'-\boldsymbol{k}}}{2\pi} \int_0^\infty dr\, rV(r) J_0(|\boldsymbol{k}-\boldsymbol{k}'|r) e^{il\theta_{\boldsymbol{k}'-\boldsymbol{k}}}, \tag{4.24}$$

where $J_0(|\boldsymbol{k}-\boldsymbol{k}'|r)$ is the zeroth order Bessel function of the first kind.

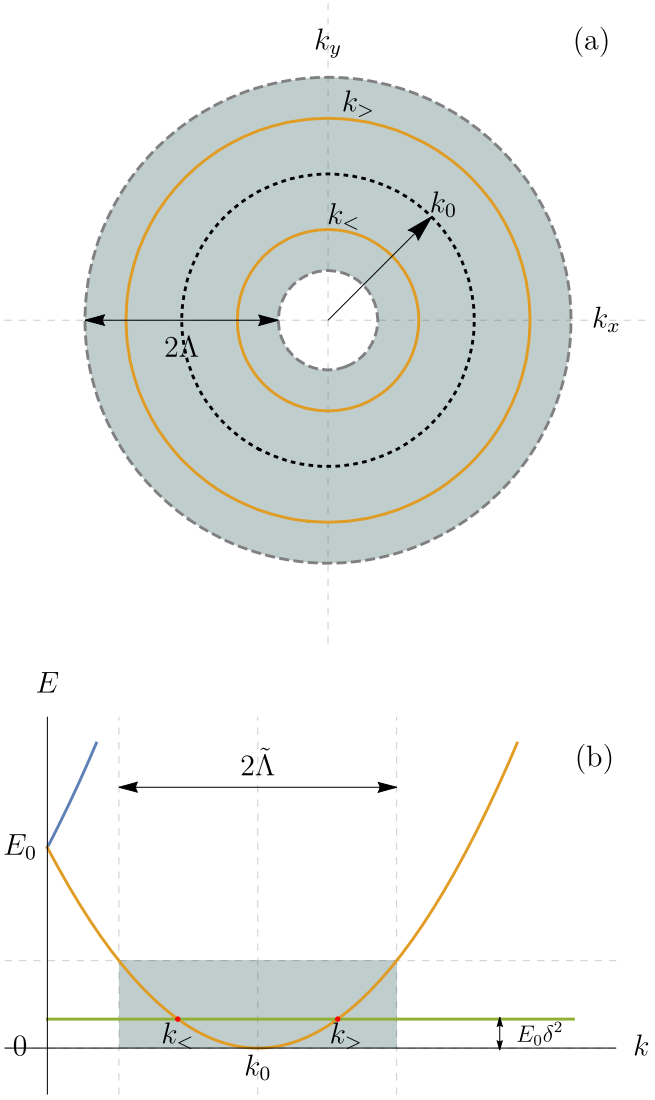

FIGURE 4.1: (a) Constant energy contours in momentum space and (b) low-energy spectrum for a single Rashba electron. The shaded region shows the allowed virtual transitions with $|k - k_0| < \tilde{\Lambda}$ to be incorporated in the T-matrix. The orange lines show the continuum of negative helicity eigenstates. The blue line in (b) is the positive helicity branch.

Now the T-matrix is defined by the Born series Eq. (2.30). We write this in the momentum-helicity basis $|\boldsymbol{k}, i\rangle$ in which the Green's function is diagonal,

$$T_{ji}^{\boldsymbol{k}_\nu \boldsymbol{k}_\mu} = V_{ji}(\boldsymbol{k}_\nu, \boldsymbol{k}_\mu) + \sum_{n=+,-} \int \frac{d^2q}{(2\pi)^2} V_{jn}(\boldsymbol{k}_\nu, \boldsymbol{q}) G_{nn}^R(q) T_{ni}^{\boldsymbol{q}\boldsymbol{k}_\mu}. \tag{4.25}$$

We want to expand the potential about the ground state wavevector k_0. More precisely, let us examine the V^l components given by (4.24). For the on-shell terms $V_{ji}(\boldsymbol{k}_\mu, \boldsymbol{k}_\nu)$ in

(4.25), the argument of this Bessel function is

$$\begin{aligned} |\boldsymbol{k}_\mu - \boldsymbol{k}_\nu| r &= r\sqrt{k_\mu^2 + k_\nu^2 - 2k_\mu k_\nu \cos\theta_{\boldsymbol{k}'-\boldsymbol{k}}} \\ &= \sqrt{2}k_0 r\sqrt{1-\cos\theta_{\boldsymbol{k}'-\boldsymbol{k}}} + \mathcal{O}(\delta). \end{aligned} \tag{4.26}$$

The off-shell components in the integral of (4.25) may also be expanded about $\delta = 0$. The argument of the Bessel function becomes

$$|\boldsymbol{k}_\nu - \boldsymbol{q}| r = \sqrt{2}k_0 r\sqrt{(1+\epsilon)(1-\cos\theta_{\boldsymbol{k}'-\boldsymbol{k}})} + \mathcal{O}(\delta), \tag{4.27}$$

where we have changed the integration variable using $q \equiv k_0(1+\epsilon)$. Thus, to order δ in the potential, we can approximate the on-shell terms as $V_{ji}(\boldsymbol{k}_\nu, \boldsymbol{k}_\mu) \approx V_{ji}(k_0\hat{\boldsymbol{k}}_\nu, k_0\hat{\boldsymbol{k}}_\mu)$, which describe angular scattering within the ground-state ring, and the off-shell terms as $V_{ji}(\boldsymbol{k}_\nu, \boldsymbol{q}) \approx V_{ji}(k_0\hat{\boldsymbol{k}}_\nu, \boldsymbol{q})$. This is a crucial approximation. Since now the right-hand side of (4.25) is independent of the magnitude k_ν, the T-matrix is independent of this magnitude as well:

$$T_{ij}^{\boldsymbol{k}_\nu \boldsymbol{k}_\mu} \approx T_{ij}(\hat{\boldsymbol{k}}_\nu, \boldsymbol{k}_\mu). \tag{4.28}$$

We argue in Appendix F that the error in this approximation is $\mathcal{O}(\delta^2)$. Writing the T-matrix in partial wave components just as we did with the potential, the Born series simplifies to

$$\begin{aligned} \sum_{l=-\infty}^{\infty} T_{ji}^l(k_\mu) e^{il\theta} &= \sum_{l=-\infty}^{\infty} \frac{1}{2}[V^l(k_0,k_0) + ijV^{l+1}(k_0,k_0)]e^{il\theta} \\ &+ \sum_{n=+,-}\sum_{l=-\infty}^{\infty} \int_0^\infty \frac{dq\, q}{4\pi}\Big(V^l(k_0,q) + jnV^{l+1}(k_0,q)\Big) G_{nn}^R(q) T_{ni}^l(k_\mu) e^{il\theta}. \end{aligned} \tag{4.29}$$

Equation (4.29) may be solved algebraically for each partial wave component. Since the diagonal parts of the potential are equal, this equation becomes two pairs of coupled equations. For the lower helicity band, the relevant pair is

$$T_{--}^l(k_\mu) \approx \frac{1}{2}[V^l(k_0,k_0) + V^{l+1}(k_0,k_0)] + I_-^l T_{--}^l(k_\mu) + J_-^l T_{+-}^l(k_\mu), \tag{4.30}$$

$$T_{+-}^l(k_\mu) \approx \frac{1}{2}[V^l(k_0,k_0) - V^{l+1}(k_0,k_0)] + I_+^l T_{--}^l(k_\mu) + J_+^l T_{+-}^l(k_\mu), \tag{4.31}$$

where we have defined the integrals

$$I^l_\pm = \int_0^\infty \frac{dq\, q}{4\pi}[V^l(k_0,q) \mp V^{l+1}(k_0,q)]G^R_{--}(q), \tag{4.32}$$

$$J^l_\pm = \int_0^\infty \frac{dq\, q}{4\pi}[V^l(k_0,q) \pm V^{l+1}(k_0,q)]G^R_{++}(q). \tag{4.33}$$

The $J_\pm$ integrals correspond to transitions between different helicity bands, and these are expected to have a negligible contribution to the low-energy scattering. Indeed, one can show that $J_\pm \sim \Lambda \ll 1$ and so we may solve for T^l_{--} to get

$$T^l_{--} \approx \frac{\delta^*_l/m}{1 - I^l_-}, \tag{4.34}$$

where we have defined a new dimensionless parameter

$$\delta^*_l \equiv \frac{m}{2}\left(V^l(k_0,k_0) + V^{l+1}(k_0,k_0)\right). \tag{4.35}$$

The energy dependence of the T-matrix is entirely determined by the integral I^l_- of Eq. (4.32). We claim that to leading order in δ, this integral is approximated by

$$I^l_- = -\frac{m}{2}\left(\frac{i}{\delta} - \frac{2}{\pi\Lambda}\right)[V^l(k_0,k_0) + V^{l+1}(k_0,k_0)] + \mathcal{O}(\delta) + \mathcal{O}(\Lambda), \tag{4.36}$$

so that the T-matrix is

$$T^l_{--} = \frac{\frac{1}{2}[V^l(k_0,k_0) + V^{l+1}(k_0,k_0)]}{1 + \frac{m}{2}(\frac{i}{\delta} - \frac{2}{\pi\Lambda})[V^l(k_0,k_0) + V^{l+1}(k_0,k_0)]} + \mathcal{O}(\delta^2). \tag{4.37}$$

The detailed derivation of this result is left for Appendix F. To leading order in δ, we can then write the T-matrix as

$$T^l_{--} \approx \frac{1}{m}\frac{\delta^*_l}{1 + i\delta^*_l/\delta} \tag{4.38}$$

$$= -\frac{i\delta}{m} + \mathcal{O}(\delta^2). \tag{4.39}$$

To this order, the low-energy limit of the S-matrix from (4.12) is

$$S^l = \begin{pmatrix} -\delta & -1 \\ -1 & \delta \end{pmatrix}. \tag{4.40}$$

To zeroth order in δ, this is precisely the result that was found for the infinite circular barrier and delta-shell potentials in Chapter 3. Eqs. (4.38) and (4.40) are the main results of this chapter. They establish that the low-energy S-matrix for circularly symmetric potentials in Rashba systems is completely universal, as conjectured in the previous chapter: it is independent of any details of the potential, provided the latter has finite range. Thus all the conclusions drawn in Chapter 3 from the particular form (4.40) of the S-matrix, such as the extreme anisotropy of the differential cross section, are equally universal.

We now draw our attention to the peculiar energy dependence of the T-matrix in Eq. (4.39). Firstly, the T-matrix scales as the square root of the scattering energy, in contrast with the inverse logarithm dependence found in conventional 2D systems (B.11). Furthermore, it does not depend on the details of the potential (its range or strength), as already mentioned. Lastly, the partial wave components of the low-energy T-matrix are independent of partial wave number l. The usual intuition of low-energy physics being dominated by s-wave scattering does not apply to the Rashba system.

The energy dependence in (4.39) is very telling. Suppose we were to look for the universal form of a low-energy T-matrix in a 1D scattering problem with a conventional quadratic dispersion. We could follow the same reasoning used above. A finite-range on-shell potential in momentum space can be approximated by a constant at low energy where the particle wavelength is much larger than the potential size,

$$V(k,k') \approx \lim_{k,k'\to 0} V(k,k') = \int_{-\infty}^{\infty} dx\, V(x) \equiv V. \tag{4.41}$$

The momentum-space T-matrix must again be independent of k' in this approximation, so that

$$\begin{aligned} T^{k'k} &\approx T(k) \\ &= V + \left(\int_{-\infty}^{\infty} dx \int_{-\infty}^{\infty} \frac{dq}{2\pi} \frac{e^{iqx} V(x)}{E - \frac{q^2}{2m} + i\eta} \right) T(k) \\ &= V + \left(\frac{mi}{\sqrt{2mE}} \int_{-\infty}^{\infty} dx\, V(x) e^{i\sqrt{2mE}x} \right) T(k). \end{aligned} \tag{4.42}$$

If we only consider the lowest order terms in E, and make use of the fact that the potential is short-ranged, we get the following approximate solution for T,

$$\begin{aligned} T &\approx \frac{V}{1-\frac{im}{\sqrt{2mE}}\int_{-\infty}^{\infty} dx\, V(x) e^{i\sqrt{2mE}x}} \\ &= \frac{i}{m}\sqrt{2mE} + \mathcal{O}(E). \end{aligned} \tag{4.43}$$

Thus, provided we identify the 1D δ parameter with $\sqrt{2mE}$, we get the same T-matrix as in the low-energy 2D Rashba case.[1] This connection suggests once again that low-energy Rashba scattering has a fundamental 1D character, independent of the details of the potential. Indeed, it was shown in Chapter 3 that Eq. (4.40) implies only forward and backward scattering are allowed at very low energies. In other words, the wavefunction behaves like that of a particle scattering in a 1D system.

One might notice that (4.43) and (4.39) differ by a minus sign. For the Rashba case, this sign ensures that the scattering cross section is positive in the optical theorem (4.20). More importantly, it has interesting implications for the S-matrix. Looking at Eq. (4.12) or (E.11), we see that this sign guarantees that the diagonal part of the S-matrix vanishes as δ approaches zero.

The form of the low-energy T-matrix has interesting consequences for the cross section as well. First note that the total cross section becomes infinite at the threshold energy $E = 0$. As mentioned in the previous chapter, this result is typical of 2D scattering, though the reasons for it are not. Using the optical theorem (4.20), our T-matrix approximation gives a low-energy cross section of

$$\sigma \approx \frac{2}{k_0}\sum_{l=-\infty}^{\infty} \frac{(\delta_l^*/\delta)^2}{1+(\delta_l^*/\delta)^2}. \tag{4.44}$$

Qualitatively speaking, there is a threshold parameter δ_l^* for each partial wave l. As we lower the energy, and thereby δ, we pass through these points one by one. Each time the condition $\delta \lesssim \delta_l^*$ is satisfied an additional two partial waves (one for l and one for $-l$) contribute to the scattering, and the cross section increases by $4/k_0$, tending to infinity stepwise as $\delta \to 0$. This is unlike the conventional 2D case in which the prefactor $1/k$ diverges while the partial wave sum remains finite. Thus there generically is a series of

[1] Unlike the 2D Rashba case, this 1D δ parameter is not dimensionless. This is simply because in two dimensions the momentum-space T-matrix must have units of inverse energy, while in one dimension, it is dimensionless.

jumps and plateaus in the cross section as a function of δ (see, e.g., Fig. 4.6). However, because δ_l^* decays as $|l|$ increases, these plateaus become narrower and narrower as we approach the ground state energy. The precise location of the jumps δ_l^* depends on the details of the potential via Eq. (4.35), but the magnitude $4n/k_0$, $n = 1, 2, 3, \ldots$ of the plateaus in the cross section is universal.

4.3 Example potentials

4.3.1 Delta function potential

The simplest potential we can consider is the delta function

$$V(r) = \frac{V_0}{r}\delta(r)\delta(\theta), \tag{4.45}$$

which has partial wave components $V^l(k, k') = V_0\delta_{l,0}$, from (4.24). Since this is independent of the momenta k and k', the T matrix is as well, and there is no need for an approximation at this level. Instead, the T-matrix exactly satisfies the equations

$$T^0_{--} = \frac{V_0/2}{1 - (I^0 + J^0)} = T_{+-}, \tag{4.46}$$

where we have made use of the fact that $I^l_+ = I^l_- \equiv I^l$, and $J^l_+ = J^l_- \equiv J^l$ for the delta potential. As usual, the integral J^0 may be ignored since (using $q = k_0(1 + \epsilon)$)

$$J^0 = 2mV_0 \int_{-\Lambda}^{\Lambda} \frac{d\epsilon}{4\pi} \frac{1+\epsilon}{\delta^2 - 4(\epsilon+1) - \epsilon^2} \sim \mathcal{O}(\Lambda). \tag{4.47}$$

The other integral evaluates to

$$\begin{aligned} I^0 &= 2mV_0 \int_{-\Lambda}^{\Lambda} \frac{d\epsilon}{4\pi} \frac{1+\epsilon}{\delta^2 - \epsilon^2 + i\eta} \\ &\approx \frac{mV_0}{2\pi}\left(-\frac{i\pi}{\delta} + \frac{2}{\Lambda}\right), \end{aligned} \tag{4.48}$$

so that

$$T^0_{--} = \frac{V_0/2}{1 + \frac{m}{2}(\frac{i}{\delta} - \frac{2}{\pi\Lambda})V_0} \approx \frac{1/m}{\frac{i}{\delta} - \frac{2}{\pi\Lambda}}, \tag{4.49}$$

in agreement with (4.37). We emphasize that the lowest-order contributions in δ are independent of the cutoff scale. This is in stark contrast with the conventional 2D case

where the contact T-matrix satisfies

$$\begin{aligned} T^0 &= V_0 - V_0 \int_0^\Lambda \frac{dk\, k}{\frac{k^2}{2m} - E - i\epsilon} T^0 \\ &= V_0 - \left(m V_0 \ln \left| \frac{\Lambda^2}{2mE} \right| + i\pi m V_0 \right) T^0 \\ &\approx \frac{1/m}{i - \frac{1}{\pi} \ln |\frac{2mE}{\Lambda^2}|}. \end{aligned} \tag{4.50}$$

One can understand this difference on dimensional grounds. Since V_0 is dimensionless, the energy must be compared to the only other scale around. In the conventional 2D case, this is the cutoff scale, which has the physical interpretation of an effective range of the potential (proportional to the scattering length). The process of acquiring this extra scale from what started as a scale-invariant problem is known as dimensional transmutation [67]. In the Rashba system this problem does not exist, since there is always an inherent scale to compare with, set by the spin-orbit coupling.

Note from the optical theorem (4.20), that the low-energy cross section for the delta function potential is finite; $\sigma_\mu = 2/k_0$. This is highly atypical of 2D scattering both with and without Rashba spin-orbit coupling, where the threshold cross section is generally divergent. The fact that only $l = 0$ contributes to the T-matrix for the contact potential is an artifact of the singular nature this potential. Next we will investigate more typical examples where all partial wave components become important at low energies.

4.3.2 Circular barrier potential

Consider the finite circular barrier

$$V(r) = \begin{cases} V_0, & r < R, \\ 0, & r > R. \end{cases} \tag{4.51}$$

The partial wave components

$$V^l(k, k') = V_0 R \int_0^{2\pi} \frac{d\theta_{\boldsymbol{k}'-\boldsymbol{k}}}{2\pi} \frac{e^{il\theta_{\boldsymbol{k}'-\boldsymbol{k}}}}{|\boldsymbol{k} - \boldsymbol{k}'|} J_1(R|\boldsymbol{k} - \boldsymbol{k}'|), \tag{4.52}$$

are evaluated numerically. When $k = k' = k_0$, this is most easily done by summing the first few terms of (F.13). Inserting these components into (4.37) gives the low-energy

T-matrix which is plotted in Fig. 4.2 for a short barrier. Along with our approximation, we plot the results for the first Born approximation $T^l_{--} = (V^l(k,k') + V^{l+1}(k,k'))/2$.

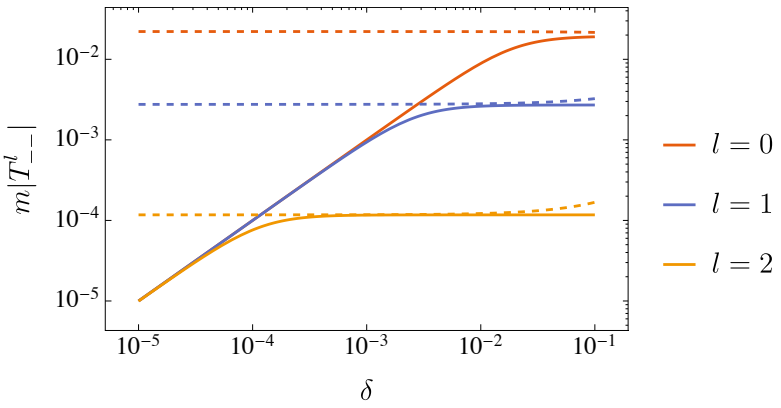

FIGURE 4.2: Absolute value of the lower-helicity T-matrix for the circular barrier as a function of the dimensionless parameter δ, for $l = 0, 1, 2$, obtained from (4.37) (solid), and from the first Born approximation (dashed). The dimensionless parameters used are $mV_0R^2 = 0.1$, $k_0R = 1$, $\Lambda = 0.1$. Note that in the first Born approximation, T^l_{--} is a 2×2 matrix in the $k_{\lessgtr}$ basis. However, these four different components are visually indistinguishable at these energies, so here we just show one of them.

We see that for each l component, there is a threshold energy below which the Born approximation fails to capture the correct energy dependence. The reason is most quickly seen from the asymptotic Green's function in position-space (4.7), which is singular at $\delta = 0$ (recall that $k_+ + k_- = k_> - k_< = 2\delta$). Evidently, it is not enough to require that the potential be perturbatively small to use the Born approximation. Instead we require $mV_0R^2/\delta \ll 1$.

We will see below that this qualitative structure of the T-matrix is reproduced in the delta-shell potential, for which an exact solution is available.

4.3.3 Delta-shell potential

We now consider the potential

$$V(r) = V_0\delta(r - R), \tag{4.53}$$

so that

$$V^l(k,k') = V_0R \int_0^{2\pi} \frac{d\theta_{\boldsymbol{k}'-\boldsymbol{k}}}{2\pi} e^{il\theta_{\boldsymbol{k}'-\boldsymbol{k}}} J_0(|\boldsymbol{k} - \boldsymbol{k}'|). \tag{4.54}$$

Again, we plot the corresponding value of the T-matrix approximation (see Fig. 4.3). With this potential, we are afforded an independent check of our approximation. The S-matrix for the delta-shell potential was computed directly from matching conditions of the wavefunction in Chapter 3 (see Eq. (3.45)). With the aid of (4.12) we may translate this into the corresponding T-matrix (or vice versa using (E.11)) and compare with our approximation.

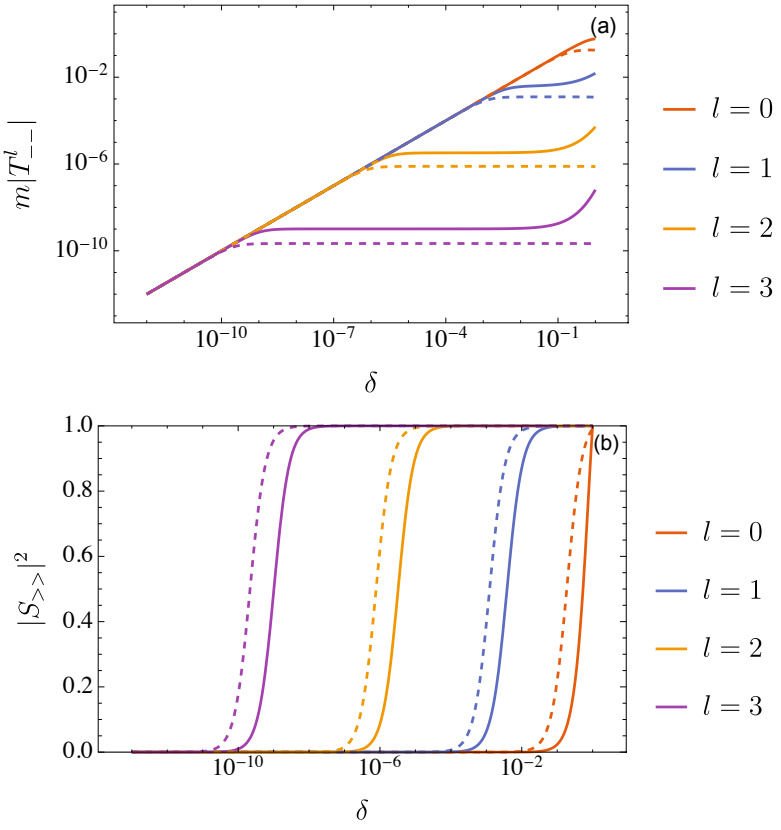

FIGURE 4.3: Absolute value of the lower-helicity T-matrix (a) and diagonal part of the S-matrix (b) for the delta-shell potential as a function of the dimensionless parameter δ for $l = 0, 1, 2, 3$. Curves are obtained from an exact calculation of the wavefunction (solid), and from the approximation (4.37) (dashed). The dimensionless parameters used are $mV_0R = 1$, $k_0R = 0.1$, $\Lambda = 0.1$.

Figure 4.4 shows the real and imaginary parts of the T-matrix. Note that the apparent steps in the imaginary part of the T-matrix translate into quantized steps in the total cross-section upon adding partial waves and using (4.20). The maxima of $-\mathrm{Im}(mT^l_{--})$ provide a useful measure of the value of δ (for each l) below which the first Born approximation fails. From our approximation (4.38), this value turns out to be simply δ^*_l defined in (4.35). In Fig. 4.5, we compare this to the exact value determined from the solution of $\frac{d}{d\delta}\mathrm{Im}(mT^l_{--}) = 0$, computed numerically from the exact T-matrix. Note that

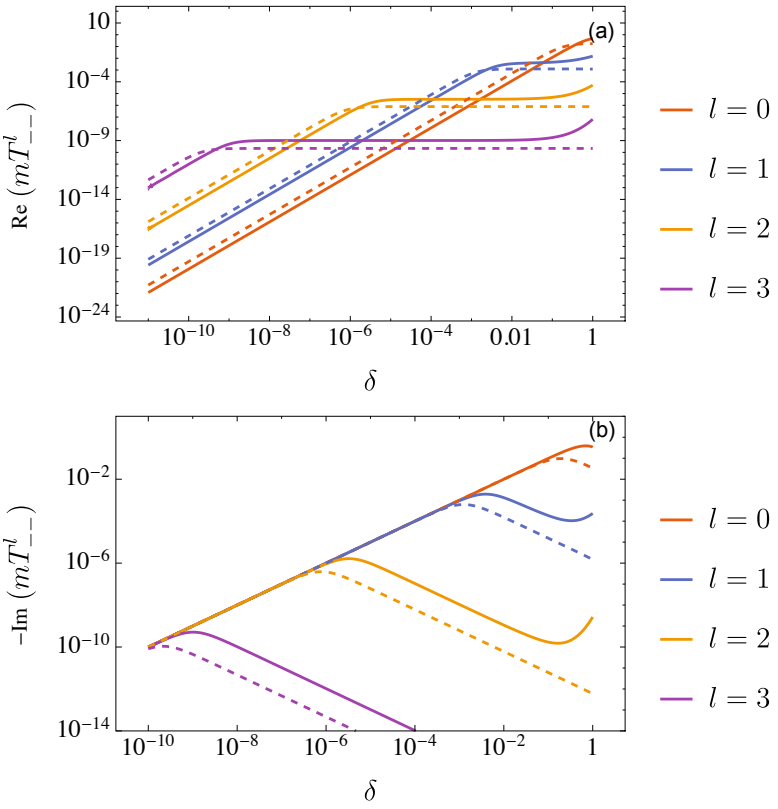

FIGURE 4.4: Real (a) and imaginary (b) parts of the lower-helicity T-matrix for the delta-shell as a function of the dimensionless parameter δ for $l = 0, 1, 2, 3$. Curves are obtained from an exact calculation of the wavefunction (solid), and from the approximation (4.37) (dashed). The dimensionless parameters used are the same as in Fig. 4.3.

the y-axis in Fig. 4.5 has a logarithmic scale: the absolute accuracy of our approximation (4.38) increases exponentially with partial wave number. However, it should be noted that the relative accuracy $(\delta_l^* - \delta_{l,\text{exact}})/\delta_{l,\text{exact}}$ saturates at a fixed value as l increases.

Finally, the delta-shell cross section is shown in Fig. 4.6. We see the generic features discussed in Sec. 4.2, namely the jumps in the cross section corresponding to the points $\delta = \delta_l^*$. Note that the x-axis has a logarithmic scale, so the cross section is indeed divergent at $\delta = 0$. As already mentioned in the previous paragraph, this also implies that the accuracy of the approximation (4.38) for the T-matrix increases exponentially as the energy is lowered towards the band bottom $\delta = 0$.

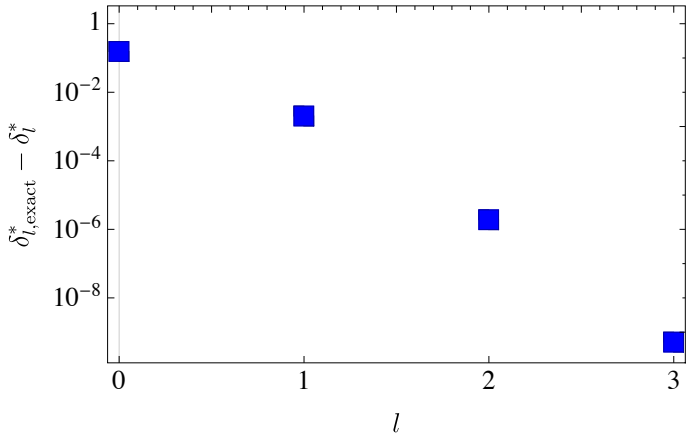

FIGURE 4.5: Difference between the value of δ_l^* computed from the exact solution of the delta-shell T-matrix and the value computed from our approximation, for each partial wave. The dimensionless parameters used are the same as in Fig. 4.3 and 4.4.

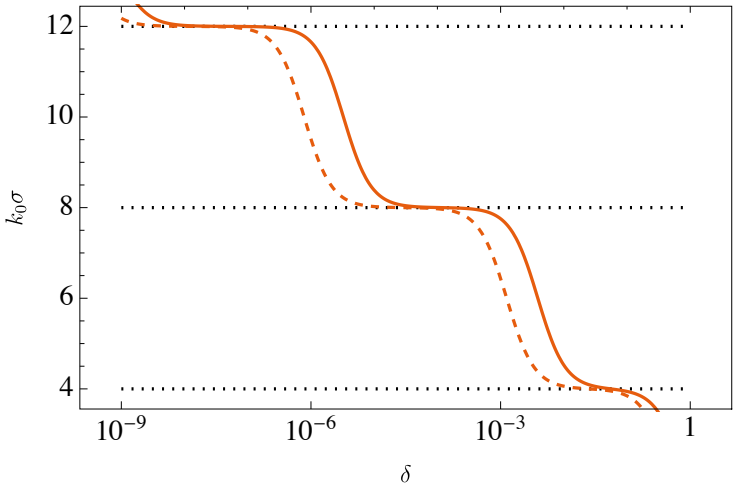

FIGURE 4.6: Total cross section σ as a function of δ for the delta-shell potential. Solid curves show the exact result computed from the optical theorem. Dashed curves are obtained from the approximation (4.44). The dotted black lines are guides to the eye, showing that the cross section increases in steps of $4/k_0$. The dimensionless parameters used are the same as in Fig. 4.3-4.5.

4.4 Discussion

We have shown that in a 2D system with Rashba spin-orbit coupling, the low-energy T-matrix of a particle scattering off of a circular, finite-range, spin-independent potential takes on a universal form given by (4.39). A universal form of the S-matrix was extracted using a complete scattering formalism developed for Rashba scattering below the Dirac point. These results have several important features that generalize the qualitative results of Chapter 3 to a large class of impurity potentials. The T-matrix has a square

root dependence on the difference between the energy of the scattering particle and the ground state energy, with a subleading dependence on the details of the potential. This is unlike the conventional inverse logarithm energy dependence seen in regular 2D systems, but agrees with the energy dependence of a 1D system. Indeed, this feature cannot be recovered via the Born approximation even with a perturbatively small potential, but requires a nonperturbative solution of the Lippmann-Schwinger equation. For each partial wave there exists a threshold energy below which the corresponding component of the T-matrix takes on this nontrivial square-root dependence on the energy. By deriving an optical theorem for Rashba systems below the Dirac point, we found that at these discrete threshold energies the total cross section exhibits quantized jumps of magnitude $4/k_0$, resulting in a plateau structure in the cross section.

In the extreme low-energy limit, the T-matrix becomes independent of partial wave number. This is markedly different from the conventional 2D problem where s-wave scattering dominates in this limit. Evidently, ultra-low-energy scattering in a Rashba system is highly anisotropic, a result which may have interesting consequences for the physics of spontaneous symmetry breaking in interacting 2D Rashba systems described in Sec. 2.2.

Given the ubiquity of these unusual scattering features in Rashba systems, we expect that some remnant of them will appear in the transport properties of a Rashba 2DEG, particularly at low temperatures, where impurity scattering is dominant. Non-magnetic point defects, arising from vacancies, substitutions or interstitial atoms in the crystal fall into the class of potentials considered here, though the detailed form of their potentials may not be known. Fortunately, the T-matrix result derived here is independent of these details and thus provides an ideal input for the transport problem in this regime. The precise manner in which these features are expressed in the low-energy transport properties is the subject of the next chapter.

Chapter 5

Unconventional transport in low-density Rashba systems

In this chapter we focus on how the low-energy scattering properties discussed in Chapters 3-4 affect transport in 2D Rashba materials. It has been recognized that the DC conductivity is a nonlinear function of the density in this regime [48–50]. The purpose of this chapter is to extend the work of these references to include the non-perturbative scattering effects that arise at ultra-low densities. In particular, we will show that the plateaus we found in the scattering cross-section (Fig. 4.6) as a function of the logarithm of the energy are manifest in the conductivity as well. We begin with Sec. 5.1, a calculation of the linear response conductivity using the semiclassical Boltzmann equation. The key difference between this and a standard Boltzmann treatment is the use of the full T-matrix found in Eq. (4.37). We first focus on the zero-temperature DC and AC conductivities (Sec. 5.1.1), before generalizing to finite temperature (Sec. 5.1.2) where we allow the chemical potential to vary through and below the conduction band. Such a treatment describes Rashba semiconductors and allows us to outline a possible experimental realization of the unique conductivity features we uncover in this section. Sec. 5.2 goes beyond the semiclassical Boltzmann approach to include quantum corrections within a self-consistent full Born approximation. Again, the difference between this and previous work is that the self-energy is computed self-consistently from the full T-matrix. We first focus on the single-particle Green's function, self-energy and density of states (Sec. 5.2.1) before employing this approach in a fully quantum-mechanical calculation of the conductivity using the Kubo formula (Sec. 5.2.2).

5.1 Semiclassical Boltzmann transport

We start with a review of the semiclassical Boltzmann equation approach to electronic transport. The initial assumption is that in the absence of an external electric field, electrons are distributed in energy E according to the Fermi function $f(E-\mu)$, where μ is the chemical potential, and that the presence of a small electric field $\boldsymbol{\mathcal{E}}$ (linear response regime) causes this distribution to deviate, but does not destroy the existence of well-defined quasi-particles. We denote this deviation by $n_\mu(\phi_{\boldsymbol{k}}, E)$, where the subscript μ indicates the $>$,$<$ states described in the previous chapters, and $\phi_{\boldsymbol{k}}$ is the angle between the corresponding wavevector $\boldsymbol{k}_\mu$ and the x axis.[1] The deviation distribution must satisfy the translation-invariant Boltzmann equation

$$i\omega n_{\boldsymbol{k}_\mu} + e\boldsymbol{\mathcal{E}}\cdot\boldsymbol{\nabla}_{\boldsymbol{k}_\mu} n^0_{\boldsymbol{k}_\mu} \;=\; n_i \sum_\nu \int_0^{2\pi} d\phi'_{\boldsymbol{k}}\, W_{\mu\nu}^{\phi_{\boldsymbol{k}}\phi'_{\boldsymbol{k}}} [n_\mu(\phi_{\boldsymbol{k}}, E) - n_\nu(\phi'_{\boldsymbol{k}}, E)], \quad (5.1)$$

where ω is the oscillation frequency of the electric field, and n_i is the impurity density. $n^0_{\boldsymbol{k}_\mu}$ is the equilibrium distribution function which is simply the Fermi function:

$$\boldsymbol{\nabla}_{\boldsymbol{k}_\mu} n^0_{\boldsymbol{k}_\mu} = \frac{\partial f}{\partial E}\boldsymbol{\nabla}_{\boldsymbol{k}_\mu}\xi_k = \frac{k_0\delta}{m}\frac{\partial f}{\partial E} s_\mu \hat{k}, \quad (5.2)$$

where $\hat{k} = \boldsymbol{k}/|\boldsymbol{k}|$, $s_\mu \equiv \mathrm{sgn}(k_\mu - k_0) = \pm 1$. Since we are now considering a many-body system, we introduce a chemical potential and work with the lower helicity dispersion $\xi_k = \frac{k^2}{2m} - \lambda k - \mu + E_0$. Furthermore, we redefine the parameter δ to include the chemical potential $\delta \equiv \sqrt{(E+\mu)/E_0}$, so that the band bottom is still at $\delta = 0$. The matrix $n_i W_{\mu\nu}^{\phi_{\boldsymbol{k}}\phi'_{\boldsymbol{k}}}$ is the elastic scattering rate between state $|E, \nu, \phi'_{\boldsymbol{k}}\rangle$ and $|E, \mu, \phi_{\boldsymbol{k}}\rangle$ determined from Fermi's golden rule. The Boltzmann equation (5.1) is a statement of conservation of charge, $\dot{n}_{\boldsymbol{k}_\mu} = 0$, where the rate of change of the distribution function is due both to the applied electric field (left-hand-side of Eq. (5.1)) and a collision term that expresses the rate of change in occupation of a given state due to scattering (right-hand-side of Eq. (5.1)). In order for the number of quasiparticles in each state to be conserved, the quasiparticle lifetime must be sufficiently long. We will justify this assumption in Sec. 5.2.

[1] The single-particle state is specified either by $\boldsymbol{k}$, or by $\{E, \mu, \phi_{\boldsymbol{k}}\}$, but we will often use the redundant notation $\boldsymbol{k}_\mu$ for clarity.

While the left-hand side of Eq. (5.1) contains only classical terms (the second term is Newton's second law), the right-hand side may be made to include quantum effects by using a scattering rate that contains many virtual scattering processes in $W_{\mu\nu}^{\phi_{\boldsymbol{k}}\phi'_{\boldsymbol{k}}}$. For circularly symmetric impurity potentials, this quantity depends only on the difference $\tilde{\phi}_k \equiv \phi_{\boldsymbol{k}} - \phi'_{\boldsymbol{k}}$, and may be expressed in terms of the T-matrix derived in Chapter 4. Starting from Eq. (2.23):

$$W_{\mu\nu}^{\phi_{\boldsymbol{k}}\phi'_{\boldsymbol{k}}} = |T^{\boldsymbol{k}_\mu \boldsymbol{k}_\nu}|^2 g_\nu(E) \tag{5.3}$$

$$= \frac{m}{2\pi\delta}\left|\sum_{l=-\infty}^{\infty} T^l(E) e^{il\tilde{\phi}_k}\right|^2 (1+s_\nu\delta), \tag{5.4}$$

where we have used the density of states in the ν channel,

$$g_\nu(E) = \int \frac{d^2\boldsymbol{k}}{(2\pi)^2}\delta(E-\xi_{k_\nu}) = \frac{m}{2\pi\delta}(1+s_\nu\delta). \tag{5.5}$$

In Appendix C, we show that the scattering rate above satisfies detailed balance. Using our non-perturbative solution for the low-energy T-matrix will allow us to go well beyond the usual perturbative treatments in the Born approximation.

5.1.1 Zero temperature

We will now study transport in the low-density limit, defined as $\mu/E_0 \ll 1$, i.e., where the chemical potential is much below the Dirac point.

5.1.1.1 DC Conductivity

First, we consider the DC conductivity by setting $\omega = 0$ and choosing the following ansatz for the distribution function,

$$n_\mu(\phi_{\boldsymbol{k}}, E) = \sum_\nu \Gamma_{\mu\nu}^{-1} e\boldsymbol{\mathcal{E}} \cdot \boldsymbol{\nabla}_{\boldsymbol{k}_\nu} n^0_{\boldsymbol{k}_\nu}, \tag{5.6}$$

where Γ is a 2×2 matrix to be determined. Substituting this into equation (5.1) and integrating over $\phi_{\boldsymbol{k}}$ gives a matrix equation in the $>, <$ basis,

$$\left[\left(\frac{1}{\tau}\Gamma^{-1} - \mathbb{I}\right) - \frac{(1/\tau - 1/\tau^{\mathrm{tr}})}{2}\begin{pmatrix} 1+\delta & 1-\delta \\ 1+\delta & 1-\delta \end{pmatrix}\Gamma^{-1}\right]\begin{pmatrix} 1 \\ -1 \end{pmatrix} = 0. \tag{5.7}$$

In analogy with the conventional spin-degenerate system, we define the energy-dependent lifetime τ and transport time $\tau^{\rm tr}$ as

$$\frac{1}{\tau} \equiv \frac{n_i m}{\pi\delta}\int_0^{2\pi} d\tilde{\phi}_k \left|\sum_{l=-\infty}^{\infty} T^l(E) e^{il\tilde{\phi}_k}\right|^2, \tag{5.8}$$

$$\frac{1}{\tau^{\rm tr}} \equiv \frac{n_i m}{\pi\delta}\int_0^{2\pi} d\tilde{\phi}_k (1-\cos\tilde{\phi}_k)\left|\sum_{l=-\infty}^{\infty} T^l(E) e^{il\tilde{\phi}_k}\right|^2. \tag{5.9}$$

In Sec. 5.2.1 we will see that Eq. (5.8) is consistent with the lifetime derived from the self-energy. In a conventional transport problem, it is the transport time that governs the conductivity since only backscattering degrades the current.

Equation (5.7) is readily solved by the matrix

$$\Gamma^{-1} = \begin{pmatrix} \tau^{\rm tr} & (1-\delta)(\tau^{\rm tr}-\tau) \\ (1+\delta)(\tau^{\rm tr}-\tau) & \tau^{\rm tr} \end{pmatrix}, \tag{5.10}$$

from which we get the distribution function,

$$n_\mu(\phi_{\boldsymbol{k}}, E) = \frac{k_0\delta}{m}\frac{\partial f}{\partial E} e\boldsymbol{\mathcal{E}}\cdot\hat{k} s_\mu(\tau + s_\mu\delta(\tau^{\rm tr}-\tau)). \tag{5.11}$$

From this result, and using the group velocity $v_{\boldsymbol{k}_\mu} = \boldsymbol{\nabla}_{\boldsymbol{k}_\mu}\xi_k$, we calculate the current,

$$\boldsymbol{J} = -e\sum_\mu \int dE \int \frac{d\phi_{\boldsymbol{k}}}{2\pi} g_\mu(E) n_\mu(\phi_{\boldsymbol{k}}, E)\boldsymbol{\nabla}_{\boldsymbol{k}_\mu}\xi_k \tag{5.12}$$

$$= -\frac{e^2k_0^2}{2\pi m}\int dE\delta\frac{\partial f}{\partial E}(\tau + \delta^2(\tau^{\rm tr}-\tau))\boldsymbol{\mathcal{E}}. \tag{5.13}$$

Taking the zero-temperature limit, we extract the DC longitudinal conductivity from Ohm's law $J_i = \sigma_{\rm DC}\mathcal{E}_i$:

$$\sigma_{\rm DC} = \frac{e^2}{2\pi}\frac{k_0^2\delta}{m}(\tau + \delta^2(\tau^{\rm tr}-\tau)), \tag{5.14}$$

where it is understood that the energies in this expression are evaluated at the Fermi level. We may write this in terms of the electron density using

$$n = \frac{k_0^2}{\pi}\delta, \tag{5.15}$$

which follows from (5.5). Thus,

$$\sigma_{\rm DC} = \frac{e^2}{2}\frac{n}{m}\left[\tau + \left(\frac{n}{n_0}\right)^2(\tau^{\rm tr} - \tau)\right], \tag{5.16}$$

where $n_0 \equiv k_0^2/\pi$ is the density at the Dirac point. This expression is valid for all densities $n < n_0$ below the Dirac point, provided the correct lifetimes τ and $\tau^{\rm tr}$ are used.

There are several important features to note about (5.16). First, recall that τ and $\tau^{\rm tr}$ both depend on the density through δ and $T^l(E_F)$ in (5.8) and (5.9), so the conductivity is a highly non-linear function of the density. Second, it reproduces the Drude conductivity

$$\sigma^{\rm Drude} = \frac{e^2}{2}\frac{n}{m}\tau^{\rm tr}, \tag{5.17}$$

only at the Dirac point where $n \to n_0$, though our low-energy expression for the transport time (5.9) is not accurate in this regime. What is special for transport about the Dirac point is that there is only one channel ($k_>$) with a non-vanishing density of states, and a group velocity parallel to $\boldsymbol{k}$, just as in a typical parabolic dispersion for a single fermion species (giving the 1/2 in the Drude conductivity). In the opposite limit, $n \to 0$, we see that it is the *lifetime*, not the transport time that governs the conductivity

$$\sigma_{\rm DC}(n \to 0) = \frac{e^2}{2}\frac{n}{m}\tau. \tag{5.18}$$

This is because in this limit, one has $k_> \approx k_<$, so that these two channels have approximately the same phase space for scattering. But since they have oppositely directed group velocities, scattering through an angle $\tilde{\phi}_k = \pi$ is just as likely to result in forward scattering as scattering through an angle $\tilde{\phi}_k = 0$ (see the discussion in Sec. 3.2).

We will see shortly that the unusual density dependence of the *full* T-matrix results in novel features in the conductivity. However, we first consider the first Born approximation as was done in Ref. [48], for which the T-matrix is given by a spin-independent constant potential transformed to the helicity basis:

$$\left|\sum_{l=-\infty}^{\infty} T^l(E)e^{il\tilde{\phi}_k}\right|^2 = |v_0\eta_-^\dagger(\phi_{\boldsymbol{k}})\eta_-(\phi_{k'})|^2 \tag{5.19}$$

$$= \frac{v_0^2}{2}(1+\cos\tilde{\phi}_k), \tag{5.20}$$

where $\eta_-(\phi_{\boldsymbol{k}}) = \frac{1}{\sqrt{2}}(1, ie^{i\phi_{\boldsymbol{k}}})^T$ is the negative-helicity eigenspinor of the Rashba Hamiltonian. In this case, the lifetime and transport time become

$$\frac{1}{\tau} = n_i m v_0^2 \frac{n_0}{n} = \frac{2}{\tau^{\rm tr}}, \tag{5.21}$$

and the conductivity is

$$\sigma_{\rm DC}^{\rm 1BA} = \frac{e^2}{2n_i m^2 v_0^2} \frac{n^2}{n_0} \left[1 + \left(\frac{n}{n_0}\right)^2\right], \tag{5.22}$$

in agreement with [48].

In Fig. 5.1, we plot the density dependence of the DC conductivity for the case where the impurity potentials are modeled by δ-function shells $V(r) = v_0 R\delta(r - R)$. The single-impurity Rashba T-matrix is computed from Eqs. (4.38) and (4.35). Recall that the specific choice of impurity potential makes no qualitative difference at low energies, as long as rotational symmetry is maintained. The delta-shell potential contains two independent parameters, the impurity strength v_0 and radius R. Varying these parameters simply changes the overall scales in Fig. 5.1. Increasing the impurity strength decreases the conductivity everywhere, and increasing its radius shifts the plateaus of the bottom panel to higher densities. Indeed, one can find a quantitative estimate of the effect of these parameters for a given potential. In the long-wavelength limit $k_0 R \ll 1$, we have

$$\delta_l^* \approx \frac{m v_0 R^2}{2(|l|!)^2} \left(\frac{(k_0 R)^2}{4}\right)^{|l|} \qquad \text{(delta-shell)} \tag{5.23}$$

$$\delta_l^* \approx \frac{m v_0 R^2}{4|l|!|l+1|!} \left(\frac{(k_0 R)^2}{4}\right)^{|l|} \qquad \text{(finite barrier)}. \tag{5.24}$$

With this in mind, we will maintain the same parameter values throughout this chapter.

Figure 5.1 constitutes the main result of this chapter, so we pause to flesh out the salient observations contained within. First, as seen in the top panel, the conductivity does not go smoothly to zero with decreasing density, unlike the prediction from the first Born approximation.[2] In fact, measurements at low densities might lead one to believe there is a finite residual conductivity as $n \to 0$. This is not physical, and indeed is not the case

[2]Note that the full Born T-matrix approaches the first Born T-matrix only in the limit $\delta \gg \delta_l^*$ for all l. For the choice of potential plotted in Fig. 5.1, the largest δ_l^* is $\delta_0^* \approx 0.5$, so the two conductivity results do not converge below the Dirac point.

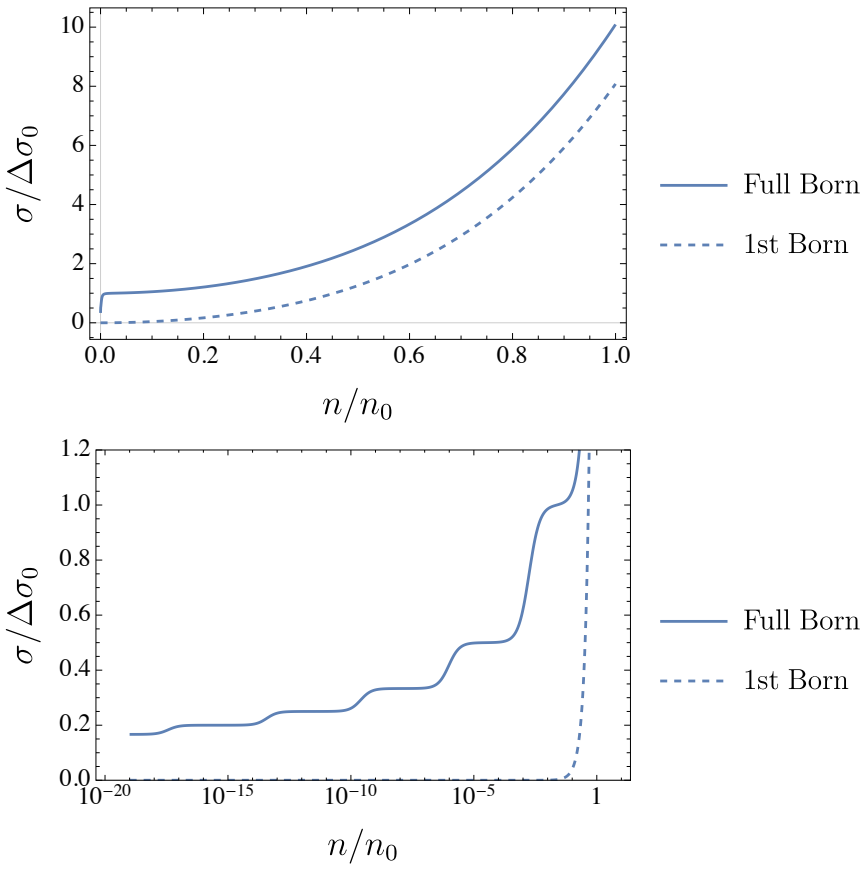

FIGURE 5.1: DC conductivity divided by $\Delta\sigma_0 \equiv \frac{e^2}{8\hbar}\frac{n_0}{n_i}$ vs electron density on a linear (top) and log (bottom) scale. The solid lines indicate the Boltzmann result using the full Born T-matrix. The dashed lines show the corresponding first Born approximation for the conductivity. A delta-shell impurity potential is used with the parameters $mv_0R^2 = 1$ and $R = 0.1/k_0$.

as shown in the lower panel, where we see that the conductivity goes through a series of steps (on a logarithmic scale) to reach zero at $n = 0$. On such a scale, the conductivity is quantized, with plateaus given by the values

$$\sigma_{\mathrm{DC}} = \left(\frac{n_0}{n_i}\right)\frac{e^2}{8\hbar l}, \quad l = 1, 2, 3, \ldots, \tag{5.25}$$

and transitions between plateaus occurring at $n/n_0 \sim \delta_l^*$. Although the conductivity plateaus depend on material parameters such as the impurity concentration and the spin-orbit coupling strength, the ratio of any two conductivity plateaus is a pure rational number, independent of all such parameters. The origin of these plateaus is the energy scale separation of the different circular harmonic contributions to the T-matrix, discussed in the previous chapter. To recap, the destructive interference between the $k_<$ and $k_>$ scattering states causes the scattered wavefunction to become more and more

quasi-one-dimensional as the energy is lowered, resembling a plane wave at the band bottom. This plane wave is composed of equal contributions of all angular momentum components which are turned on at successively lower scattering energies, essentially when $\delta \approx \delta_l^*$. Each time this happens, a new angular momentum channel contributes to the scattering and the conductivity drops by a quantized amount.

5.1.1.2 AC Conductivity

Retaining the frequency dependence in (5.1) allows us to compute the AC conductivity as well. One can readily check that the AC Boltzmann equation is solved by

$$n_\mu(\phi_{\boldsymbol{k}}, E) = \frac{k_0 \delta}{m} \frac{\partial f}{\partial E} e\boldsymbol{\mathcal{E}} \cdot \hat{k} s_\mu \left(\frac{\tau(1 - i\omega\tau^{\mathrm{tr}}) + s_\mu \delta(\tau^{\mathrm{tr}} - \tau)}{(1 - i\omega\tau^{\mathrm{tr}})(1 - i\omega\tau)} \right), \tag{5.26}$$

from which we get the current

$$\boldsymbol{J} = -\frac{e^2 k_0^2}{2\pi m} \int dE \delta \frac{\partial f}{\partial E} \left(\frac{\tau(1 - i\omega\tau^{\mathrm{tr}}) + \delta^2(\tau^{\mathrm{tr}} - \tau)}{(1 - i\omega\tau^{\mathrm{tr}})(1 - i\omega\tau)} \right) \boldsymbol{\mathcal{E}}, \tag{5.27}$$

and the zero-temperature conductivity

$$\sigma(\omega) = \frac{e^2}{2} \frac{n}{m} \left(\frac{\tau(1 - i\omega\tau^{\mathrm{tr}}) + (n/n_0)^2(\tau^{\mathrm{tr}} - \tau)}{(1 - i\omega\tau^{\mathrm{tr}})(1 - i\omega\tau)} \right), \tag{5.28}$$

shown in Fig. 5.2.

As we saw in the DC case, the conductivity takes the Drude form in the two limits $n \to n_0$ and $n \to 0$, dependent on τ^{tr} and τ respectively. As $n \to n_0$,

$$\sigma(\omega) \to \frac{e^2}{2} \frac{n}{m} \frac{\tau^{\mathrm{tr}}}{1 - i\omega\tau^{\mathrm{tr}}} = \sigma^{\mathrm{Drude}}(\omega), \tag{5.29}$$

while in the opposite limit $n \to 0$,

$$\sigma(\omega) \to \frac{e^2}{2} \frac{n}{m} \frac{\tau}{1 - i\omega\tau} = \frac{\tau}{\tau^{\mathrm{tr}}} \sigma^{\mathrm{Drude}}(\omega\tau/\tau^{\mathrm{tr}}). \tag{5.30}$$

Thus, as the density is lowered, the width of the Drude peak decreases from $1/\tau^{\mathrm{tr}}$ to $1/\tau$. At low densities, the height of the peak in the imaginary part of the AC conductivity at

$\omega = 1/\tau$ becomes quantized since

$$\mathrm{Im}\,\sigma(1/\tau) \approx \frac{e^2}{2}\frac{n}{m}\frac{\tau}{2} = \frac{\sigma_{\mathrm{DC}}}{2}, \tag{5.31}$$

where σ_{DC} has the plateaus in (5.25), shown in Fig. 5.3.

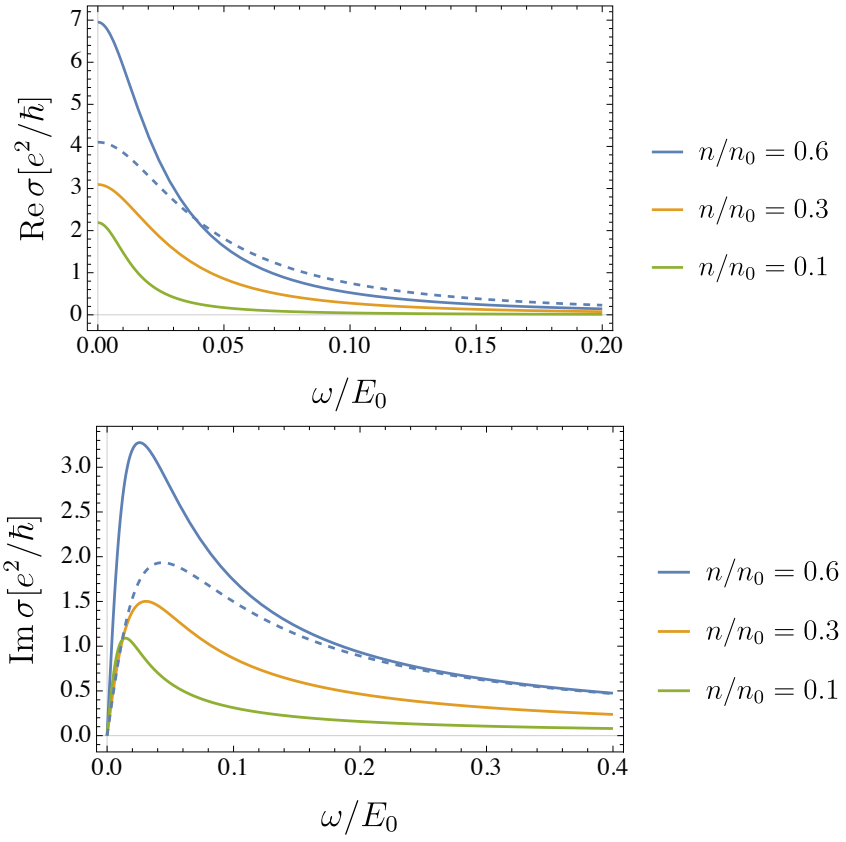

FIGURE 5.2: Real (top) and imaginary (bottom) parts of the semiclassical Boltzmann AC conductivity vs frequency for various values of the electron density with impurity density set to $n_i = 0.06n_0$. The dashed line shows the corresponding ($n = 0.6n_0$) first Born approximation result for the conductivity, found by inserting (5.21) into (5.28).

5.1.2 Finite temperature

We now consider the effect of finite temperature on transport in a Rashba semiconductor. Several materials exist with large Rashba splitting of order $E_0 \sim 0.1$eV, including BiTeI and $CH_3NH_3PbI_3$ (see Table 1.1). For example, BiTeI possesses 2D surface conduction and valence bands with a large Rashba splitting; the Fermi level can be adjusted between these two bands by changing the termination layer [68]. In the following, however, we

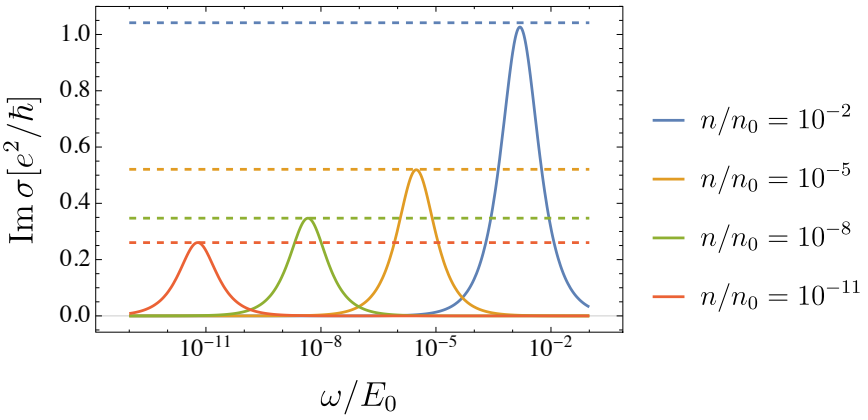

FIGURE 5.3: Imaginary part of the semiclassical Boltzmann AC conductivity vs frequency for various values of the electron density on a log scale with impurity density set to $n_i = 0.06 n_0$. The dashed lines show the quantization of the peaks given by $\frac{n_0}{n_i}(\frac{1}{16l})$ for $l = 1, 2, 3, 4$.

ignore material-specific details and consider a simplified model of a semiconductor with a Fermi level close to the bottom of a 2D Rashba-split conduction band.

Returning to (5.13), we retain the temperature dependence via

$$\frac{\partial f}{\partial E} = -\frac{\beta e^{\beta(E-\mu)}}{(e^{\beta(E-\mu)}+1)^2}. \tag{5.32}$$

Furthermore, we assume that $|E_0 - \mu| \gg k_B T$, so that the upper helicity band contributes negligibly to the integrand. The DC conductivity,

$$\sigma_{\mathrm{DC}} \approx \frac{e^2 k_0^2 \beta}{2\pi m} \int_0^{E_0} dE\, \delta \frac{e^{(E-\mu)\beta}}{(e^{\beta(E-\mu)}+1)^2}(\tau + \delta^2(\tau^{\mathrm{tr}} - \tau)), \tag{5.33}$$

is then computed numerically as a function of the chemical potential. The result is shown in the top panel of Fig. 5.4, where we see that the sharp zero temperature drop that occurs at the band bottom ($\mu = 0$) maintains some weight at finite temperatures. The magnitude of this drop is determined by the impurity density

$$\Delta\sigma(\mu = 0) = \Delta\sigma_0 \equiv \frac{e^2}{8\hbar}\frac{n_0}{n_i}. \tag{5.34}$$

This is in contrast to the prediction from the first Born approximation shown in the bottom panel of Fig. 5.4, which produces a conductivity that smoothly goes to zero as the chemical potential is lowered.

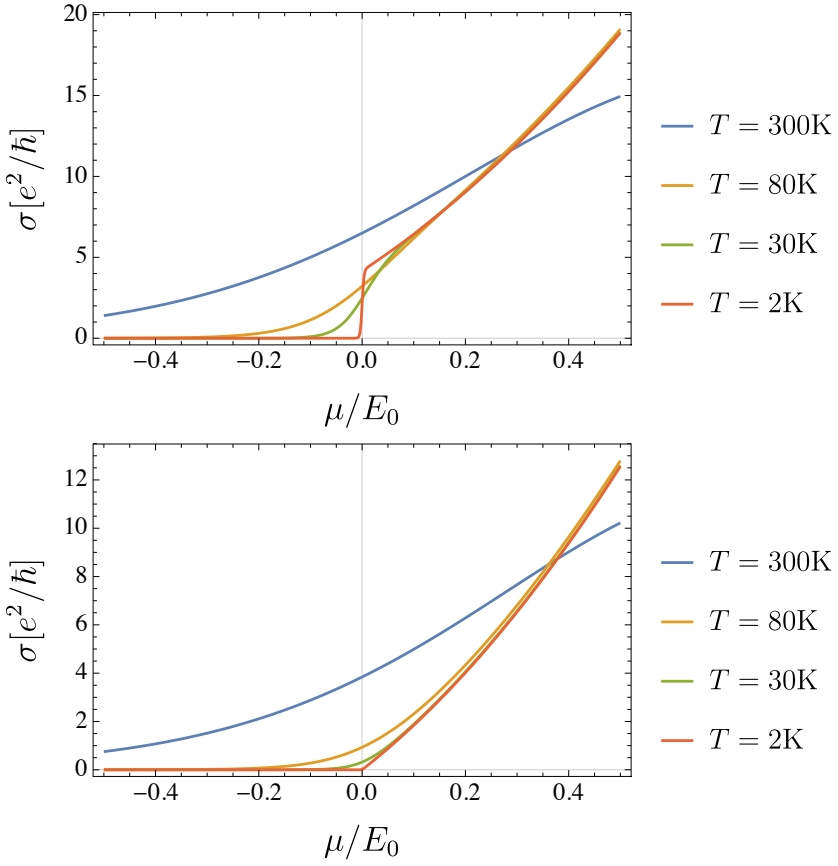

FIGURE 5.4: Semiclassical Boltzmann DC conductivity vs chemical potential for various temperatures, with impurity density set to $n_i = 0.03n_0$. The top panel shows the results computed from the full T-matrix, while the bottom panel shows the first Born approximation.

The conductivity plateaus seen in the zero temperature case are hidden in the sharp drop near $\mu = 0$. In a real material, doping offers crude control over the chemical potential, and one might be skeptical that the quantization seen as a function of the logarithmic changes in the density (or alternatively, the logarithmic changes in the chemical potential) could ever be observed. As one possible means of overcoming this, we propose the use of pump-probe measurements. This technique has been used to study transport properties of systems with large Rashba splitting before [69]. In such an experiment, a (typically THz) pump laser pulse is used to excite carriers from the valence to conduction band. These carriers quickly establish a quasi-equilibrium and a corresponding chemical potential $\mu > 0$, on a time scale ($\sim 10^{-15}$ s) much smaller than the typical recombination time $\tau_n \sim 10^{-9}$ s [70]. The pump pulse is then followed by a probe pulse that can be used to measure the AC conductivity of the new quasi-equilibrium system. To illustrate the potential usefulness of this technique for our purposes, consider a simple

model where the recombination time τ_n is a constant. After a time dt, the number of carriers remaining in the conduction band will be $n_c(t+dt) = (1 - \frac{dt}{\tau_n})n_c(t)$,[3] so that

$$n_c(t) = n_c(0)e^{-t/\tau_n}. \tag{5.35}$$

Thus, the delay time $t \sim \ln(n_c/n_c(0))$ provides an ideal control parameter for observing the quantized behaviour of the conductivity. We may compute the conductivity as a function of delay time using (5.33), where the quasi-equilibrium chemical potential $\mu(t)$ is determined by the number equation

$$n_c(t) = \frac{m}{2\pi}\int_0^{E_0} dE\sqrt{\frac{E_0}{E}}\frac{1}{e^{\beta(E-\mu)}+1} = n_c(0)e^{-t/\tau_n}. \tag{5.36}$$

The result is shown in Fig. 5.5, where the first plateau, now as a function of delay time, is easily visible at sufficiently low temperatures. This plot is for a fixed impurity density. For cleaner systems, one would see more plateaus at a given temperature. This is again in contrast to the first Born approximation result which smoothly decays to zero.

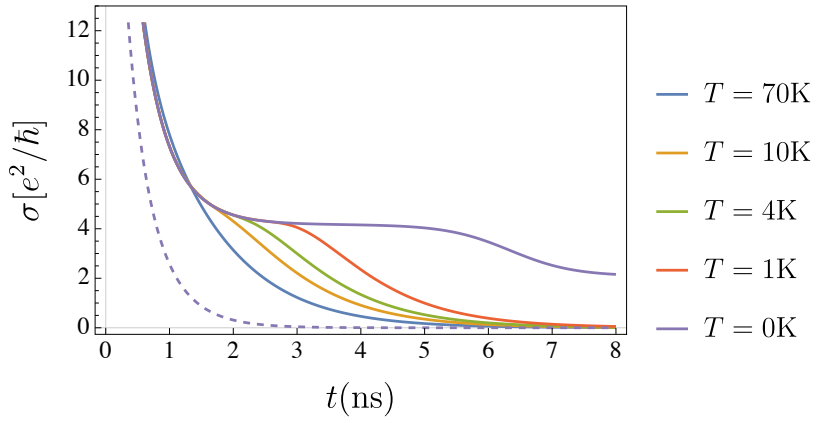

FIGURE 5.5: Semiclassical Boltzmann DC conductivity vs delay time in a pump-probe measurement at various temperatures, with impurity density set to $n_i = 0.03n_0$, and recombination time $\tau_n = 1$ ns. The dashed line shows the $(T = 0)$ prediction from the first Born approximation.

[3]Note that in this very simple picture we have ignored the contribution of the holes to the AC transport properties, as well as any excitonic effects.

5.2 Self-consistent full Born approximation

Until now, we have looked exclusively at the semiclassical transport features of low-density Rashba systems. Given the delicate nature of the dependence of these features on the density, one might be skeptical that they survive a fully quantum treatment. The purpose of this section is to address this question. We will focus exclusively on the zero-temperature limit throughout this section.

5.2.1 Single-particle properties

An appropriate quantum treatment of the transport problem requires acknowledging that the propagation of quasi-particles in the system is modified by a self-energy that depends on the impurity scattering. We will utilize a self-consistent *full* Born approximation (SCFBA) in this regard. Note that this is different from the conventional self-consistent Born approximation (SCBA) used in Ref. [48, 49], in that the self-energy is determined self-consistently from the full T-matrix, and not simply the T-matrix in the first Born approximation. The distinction is illustrated by the Feynman diagrams in Fig. 5.6. In the conventional SCBA, no diagrams in the self-energy have more than two impurity lines attached to a single vertex. In the SCFBA, one includes all non-crossed diagrams, that is, all Feynman diagrams where the interaction lines do not cross. We proceed with standard impurity averaging [71]. We start with N_i uncorrelated impurities located at random positions $\boldsymbol{R}_j$, described by the potential

$$U(\boldsymbol{r}) = \sum_{j=1}^{N_i} V(|\boldsymbol{r} - \boldsymbol{R}_j|). \tag{5.37}$$

The Green's function and self-energy are averaged over impurity positions. In doing so, we assume that there is no coherent scattering off of multiple impurities. In the next section, we will make explicit the conditions for this statement to be true. Since the impurity positions only enter through phase factors $e^{i\boldsymbol{q}\cdot\boldsymbol{R}_j}$ in the Fourier transform of (5.37), the averaging induces a factor n_i and a momentum-conserving delta function at each vertex. The series shown in Fig. 5.6 (b) is precisely the Born series for the T-matrix with the addition of these self-averaging factors. Thus, we take the irreducible retarded

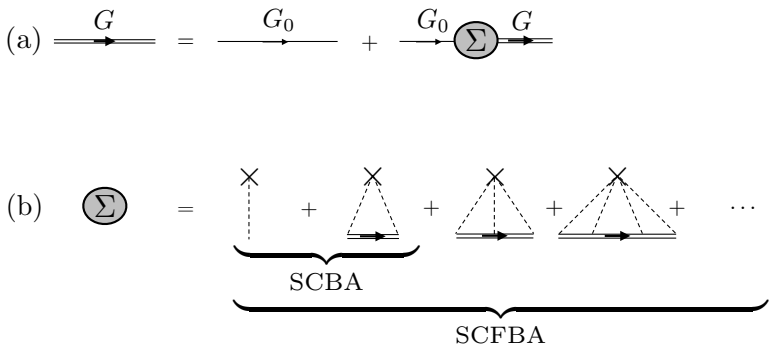

FIGURE 5.6: (a) Dyson equation for the full Green's function G, where G_0 is the bare Green's function and Σ is the irreducible self-energy; (b) Diagrammatic expansion of the irreducible self-energy Σ for impurity scattering, showing the truncation made in SCBA. Each vertex comes with an impurity density n_i and dashed lines indicate an electron-impurity interaction.

self-energy in the helicity basis to be

$$\Sigma_{\alpha\beta}(\boldsymbol{k}, E) = n_i T_{\alpha\beta}^{\boldsymbol{k},\boldsymbol{k}}(E). \tag{5.38}$$

The T-matrix satisfies the Born series,

$$T_{\alpha\beta}^{\boldsymbol{k},\boldsymbol{k}'}(E) = V_{\alpha\beta}(\boldsymbol{k},\boldsymbol{k}') + \sum_{\lambda\gamma}\int\frac{d^2\boldsymbol{q}}{(2\pi)^2}\int\frac{d^2\boldsymbol{q}'}{(2\pi)^2}V_{\alpha\lambda}(\boldsymbol{k},\boldsymbol{q})G^R_{\lambda\gamma}(\boldsymbol{q},\boldsymbol{q}';E)T_{\gamma\beta}^{\boldsymbol{q}',\boldsymbol{k}'}(E), \tag{5.39}$$

where $V_{\alpha\beta}(\boldsymbol{k},\boldsymbol{k}')$ is the matrix element of $V(\boldsymbol{r})$ in the momentum-helicity basis. The difference between this Born series and the one in Eq. (4.25), is that G^R now represents the *full* retarded Green's function in this basis, which obeys the Dyson equation,

$$G^R_{\alpha\beta}(\boldsymbol{k}, E) \;=\; G^0_{\alpha\alpha}(\boldsymbol{k}, E)\delta_{\alpha\beta} + \sum_{\gamma} G^0_{\alpha\alpha}(\boldsymbol{k}, E)\Sigma_{\alpha\gamma}(\boldsymbol{k}, E)G^R_{\gamma\beta}(\boldsymbol{k}, E). \tag{5.40}$$

Note that the impurity averaging procedure restores translation invariance, so that the Green's function is diagonal in momentum. For circularly symmetric potentials, which

have angular components given by Eq. (4.24), the low-energy T-matrix in the negative-helicity sector is independent of the magnitude of the momenta:

$$T^{\boldsymbol{k}\boldsymbol{k}'}_{--} = \sum_{l=-\infty}^{\infty} T^l(E) e^{il(\theta_{\boldsymbol{k}}-\theta_{\boldsymbol{k}'})}. \tag{5.41}$$

This follows from the arguments made in Chapter 4, which also hold for the SCFBA Green's function. This guarantees that the self-energy is independent of momentum in the same limit: $\Sigma_{--}(\boldsymbol{k}, E) \equiv \Sigma(E)$. By (5.40), this also means that the Green's function is independent of θ_k. The full Born series (5.39) is then solved by

$$T^l(E) = \frac{1}{2}\left(\frac{V^l(k_0,k_0)(1-J^l_+ + J^l_-)}{1-I^l_- - J^l_+ + I^l_- J^l_+ - I^l_+ J^l_-} + \frac{V^{l+1}(k_0,k_0)(1-J^l_+ - J^l_-)}{1-I^l_- - J^l_+ + I^l_- J^l_+ - I^l_+ J^l_-}\right), \tag{5.42}$$

where $I^l_\pm$ and $J^l_\pm$ are the integral contributions of the lower and upper helicity Green's functions, respectively, defined by Eqs. (4.32), (4.33).

In the low-energy regime of interest to us, the integrand of $J^l_\pm$ is far from its poles in q and we expect $J^l_\pm$ to be negligible. More precisely, let us impose a momentum cutoff $k_0\Lambda$, as in Fig. 4.1, around the ring of degenerate states such that $\Lambda \ll 1$, and then integrate from $k_0(1-\Lambda)$ to $k_0(1+\Lambda)$. In this range, $|J^l_\pm| \sim \Lambda \ll 1$. As in the previous chapter, the T-matrix is then determined entirely by the integral I^l_-, and is given by the expression Eq. (4.34), only now, the integral I^l_- depends on the Green's function component that satisfies the Dyson equation

$$G^R_{--}(k,E) = \left(G^0_{--}(k,E)^{-1} - \Sigma_{--}(E) - \frac{\Sigma_{-+}(E)G^0_{++}(k,E)\Sigma_{+-}(E)}{1-G^0_{++}(k,E)\Sigma_{++}(E)}\right)^{-1}. \tag{5.43}$$

The last term, containing the off-diagonal parts, is second order in the impurity density and will be ignored from now on. I^l_- is derived in Appendix F to be

$$I^l_- \approx -i\frac{\delta^*_l}{z} + \frac{2\delta^*_l}{\pi\Lambda}, \tag{5.44}$$

where

$$z \equiv \sqrt{(E+\mu)/E_0 - \Sigma(E)/E_0}. \tag{5.45}$$

We thus have the following self-consistency condition for the self-energy,

$$\Sigma(E) = \frac{n_i}{m} \sum_{l=-\infty}^{\infty} \frac{\delta_l^*}{1 + i\delta_l^*/z - \frac{2\delta_l^*}{\pi\Lambda}}. \tag{5.46}$$

Note that by expanding to lowest order in n_i, we get the self-energy corresponding to the full Born approximation as expected,

$$\Sigma(E) \approx \frac{n_i}{m} \sum_{l=-\infty}^{\infty} \frac{\delta_l^*}{1 + i\delta_l^*[(E+\mu)/E_0]^{-1/2} - \frac{2\delta_l^*}{\pi\Lambda}}. \tag{5.47}$$

It is conventional to absorb the lowest order self-energy term into the chemical potential. This amounts to redefining

$$\tilde{\Sigma}(E) \equiv \Sigma(E) - n_i V_{--}(k_0, k_0) \tag{5.48}$$

$$\tilde{\mu} \equiv \mu + n_i V_{--}(k_0, k_0). \tag{5.49}$$

The resulting self-energy is shown in Fig. 5.7.

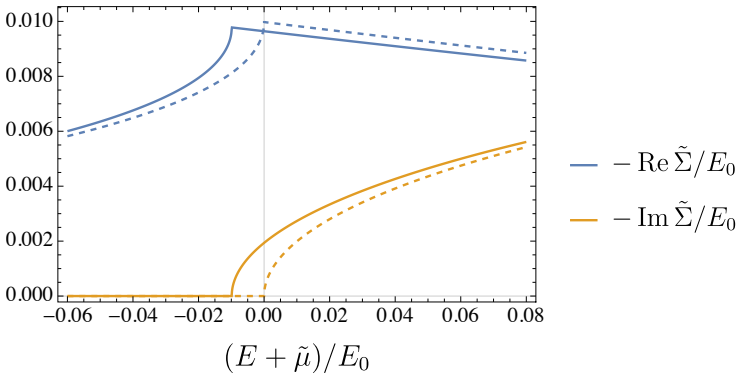

FIGURE 5.7: Real and imaginary parts of the self-energy for the SCFBA (solid lines) and the full Born approximation (dashed lines). The two coincide in the clean limit. Here, the impurity density was chosen to be $n_i/n_0 = 0.016$. A cutoff of $\Lambda = 0.5$ was used, although the self-energy in this regime is largely independent of this choice.

From (5.43) we may compute the spectral function $A(\boldsymbol{k}, E) = -2\operatorname{Im} G_{--}(\boldsymbol{k}, E)$. It is a Lorentzian, which means our quasi-particle assumption is correct. The width of this Lorentzian gives the quasi-particle lifetime, which in this case is energy-dependent:

$$1/\tau(E) = -2\operatorname{Im}\Sigma(E) = n_i \sum_l \operatorname{Im} T^l(E). \tag{5.50}$$

This is equivalent to the definition of the lifetime used in the Boltzmann description (5.8) due to the optical theorem for the low-energy T-matrix derived in Sec. 4.1.1:

$$\operatorname{Im} T^{\boldsymbol{k}\boldsymbol{k}'}_{--}(\theta = 0) = -\frac{m}{2\pi}\int_0^{2\pi} d\theta \, |T^{\boldsymbol{k}\boldsymbol{k}'}_{--}|^2, \tag{5.51}$$

where θ is the angle between $\boldsymbol{k}$ and $\boldsymbol{k}'$.

We integrate the spectral function to obtain the density of states

$$g(E) \;=\; -\frac{\operatorname{Im}\Sigma}{2\pi^2}\int_{k_0(1-\Lambda)}^{k_0(1+\Lambda)} \frac{dk\; k}{(E-\xi_k^- - \operatorname{Re}\Sigma)^2 + (\operatorname{Im}\Sigma)^2}, \tag{5.52}$$

applying the same cutoff as before. This integral is similar to I^l_- and is derived in Appendix F. The result is

$$g(E) = \frac{m}{\pi}\operatorname{Re}\left(\sqrt{\frac{E_0}{E+\tilde{\mu}-\tilde{\Sigma}(E)}}\right). \tag{5.53}$$

Note that in the clean limit, $\tilde{\Sigma}(E) \to 0$, $\tilde{\mu} \to \mu$, and we recover the non-interacting density of states (5.5). Integrating this up to the Fermi level gives the density, which we invert to obtain $g(n)$ as shown in Fig. 5.8. As expected, disorder rounds the van Hove singularity in the density of states.

A similar rounding of the density of states was found in the study of a 2D Rashba electron gas with delta-function impurities, for which an asymptotically exact solution is available in the low-energy limit [72]. Here we are considering a more general situation making use of the universal behaviour of the T-matrix for arbitrary circularly symmetric, finite-range potentials (4.34).

5.2.2 Kubo conductivity

Using the Green's function and T-matrix derived in the previous subsection, we now look at the conductivity within linear response theory. In linear response theory, a perturbation $H'(t)$ due to an external field is added to the Hamiltonian. For any operator $A(t)$ in the Heisenberg picture, the deviation of its expectation value from equilibrium

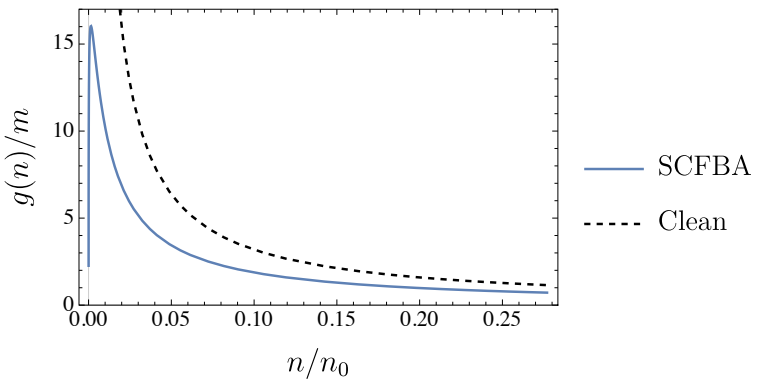

FIGURE 5.8: Density of states as a function of electron density computed from the SCFBA for an impurity density of $n_i/n_0 = 0.016$, compared to the clean limit.

is then determined by the retarded correlation function $-i\theta(t-t')\langle[A(t), H'(t')]\rangle_0$, evaluated in equilibrium. To compute the conductivity, we take $A(t)$ to be the current density operator in the x direction, $J_x(t)$, which also appears in $H'(t)$, so that the longitudinal conductivity is determined from the retarded current-current correlator $\Pi_{\rm ret}(t-t') = -i\theta(t-t')\langle[J_x(t), J_x(t')]\rangle_0$. Specifically, the DC conductivity is given by the Kubo formula

$$\sigma^{\rm DC} = -e^2 \lim_{\omega\to 0}\left(\frac{\mathrm{Im}\,\Pi_{\rm ret}(\omega)}{\omega}\right), \tag{5.54}$$

where $\Pi_{\rm ret}(\omega)$ is the Fourier-transformed retarded current-current correlator shown diagrammatically in Fig. 5.9(a). This reduces to the standard expression [71]

$$\sigma^{\rm DC} = \frac{e^2}{2\pi}\int_{-\infty}^{\infty} dE\left(-\frac{\partial f}{\partial E}\right)\Big[P^{\rm AR}(E) - \mathrm{Re}\,P^{\rm RR}(E)\Big], \tag{5.55}$$

where we have defined the advanced-retarded ($P^{\rm AR}(E)$) and retarded-retarded ($P^{\rm RR}(E)$) response functions via

$$P^{\rm XR}(E) \equiv \int \frac{d^2\boldsymbol{p}}{(2\pi)^2}\,\mathrm{Tr}\,G^{\rm X}(p,E)\Gamma_0(\boldsymbol{p})G^{\rm R}(p,E)\Gamma^{\rm XR}(\boldsymbol{p},E), \tag{5.56}$$

with $X \in \{R, A\}$. Here, $G^{\rm R}$ and $G^{\rm A}$ are the retarded and advanced low-energy Green's functions:

$$G^R(p,E) = \frac{1}{E - \xi_p - \Sigma(E)} = G^A(p,E)^*. \tag{5.57}$$

Since we are only interested in energies near the band bottom, we may neglect the contribution from the upper-helicity component of the Green's functions as they do not have any poles near those energies. $\Gamma^{\rm RR}(\boldsymbol{p},E)$, and $\Gamma^{\rm AR}(\boldsymbol{p},E)$ are the retarded-retarded

and advanced-retarded vertex parts, which satisfy the integral equation shown in Fig. 5.9(b). Lastly, $\Gamma_0(\boldsymbol{p}) \equiv \frac{\partial H}{\partial p_x}$ is the bare vertex. In the helicity basis, it is given by

$$\Gamma_0(\boldsymbol{p}) = \frac{p_x}{m}\mathbb{I} - \lambda\cos\theta_{\boldsymbol{p}}\sigma_z - \lambda\sin\theta_{\boldsymbol{p}}\sigma_y. \tag{5.58}$$

Isotropy of the system allows us to just consider the x-component of the vertex part, corresponding to the longitudinal conductivity $\sigma_{xx}^{\mathrm{DC}}$. The integral equation for the vertex part in this basis is, in matrix notation,

$$\Gamma^{\mathrm{XR}}(\boldsymbol{p}, E) \;=\; \Gamma_0(\boldsymbol{p}) + \int \frac{d^2\boldsymbol{k}}{(2\pi)^2} T^{\boldsymbol{pk}}(E) G^{\mathrm{X}}(k, E)\Gamma^{\mathrm{XR}}(\boldsymbol{k}, E) G^{\mathrm{R}}(k, E) T^{\boldsymbol{kp}}(E). \tag{5.59}$$

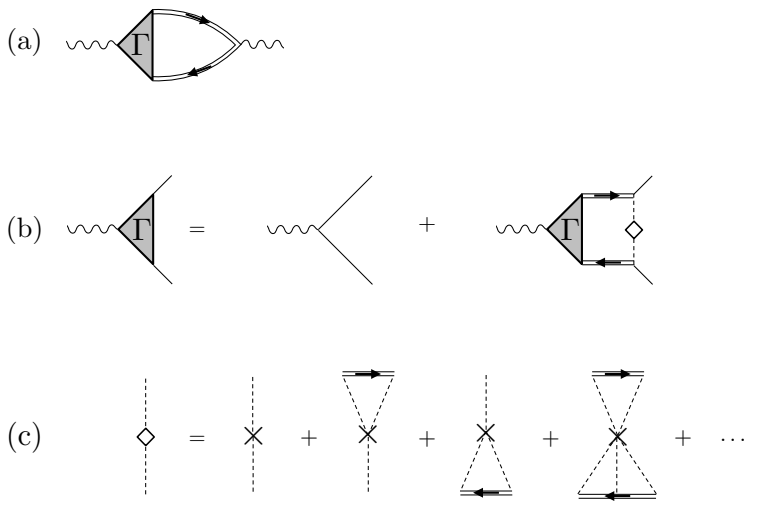

FIGURE 5.9: (a) Conductivity bubble; squiggly lines connected to two Green's function lines represent the current operator. Shown in the conductivity bubble is the vertex part that includes all possible interaction lines consistent with the bubble diagram. (b) Integral equation for the vertex part Γ^{XR}. Here, the upper double line corresponds the Green's function G^{X}, and the lower one corresponds to G^{R}, while the diamond with interaction lines represents a product of T-matrices. (c) Born series for the T-matrix product. Double lines represent the SCFBA Green's function.

Eq. (5.59) is a scalar equation in the lower-helicity sector. In this sector, $\Gamma_0(\boldsymbol{p}) = \frac{p_x}{m} - \lambda\cos\theta_{\boldsymbol{p}}$, which motivates us to use the following ansatz for the renormalized vertex,

$$\Gamma^{\mathrm{XR}}(\boldsymbol{p}, E) = \frac{p_x}{m} - \tilde{\lambda}^{\mathrm{XR}}(E)\cos\theta_{\boldsymbol{p}}. \tag{5.60}$$

We have anticipated a renormalized Rashba coupling $\tilde{\lambda}^{\rm XR}(E)$ independent of momentum. The mass cannot be renormalized because the only term on the right-hand side of (5.59) that depends on the magnitude of $\boldsymbol{p}$ is the bare vertex. Expanding the T-matrix in circular harmonics again, Eq. (5.59) reads

$$\begin{aligned}\tilde{\lambda}^{\rm XR}(E) &= \lambda - \frac{n_i}{2\pi}\sum_{ll'} T^l(E-i\delta)T^{l'}(E+i\delta)\int_0^{2\pi}\frac{d\phi}{2\pi}e^{i(l-l')\phi}(\cos\phi - \sin\phi\tan\theta_{\boldsymbol{p}}) \\ &\quad\times\int_{k_0(1-\Lambda)}^{k_0(1+\Lambda)} dk\; k\left(\frac{k}{m}-\tilde{\lambda}^{\rm XR}(E)\right)G^{\rm X}(k,E)G^{\rm R}(k,E).\end{aligned} \tag{5.61}$$

Our ansatz for the vertex part works because the mirror symmetry of the T-matrix [see Eq.(C.26)] guarantees that

$$\sum_{ll'} T^l(E-i\delta)T^{l'}(E+i\delta)\int_0^{2\pi}\frac{d\phi}{2\pi}e^{i(l-l')\phi}\sin\phi = 0, \tag{5.62}$$

so that the $\theta_{\boldsymbol{p}}$ dependence in (5.61) disappears. Using the lifetimes defined in (5.8) and (5.9), the renormalized coupling is

$$\frac{\tilde{\lambda}^{\rm XR}(E)}{\lambda} = \frac{1+\frac{\delta}{4\pi k_0}(\frac{1}{\tau^{\rm tr}}-\frac{1}{\tau})P_2^{\rm XR}}{1+\frac{\delta}{4\pi m}(\frac{1}{\tau^{\rm tr}}-\frac{1}{\tau})P_1^{\rm XR}}, \tag{5.63}$$

where

$$P_1^{\rm XR} \equiv \int_{k_0(1-\Lambda)}^{k_0(1+\Lambda)} dp\; pG^{\rm X}(p,E)G^{\rm R}(p,E), \tag{5.64}$$

$$P_2^{\rm XR} \equiv \int_{k_0(1-\Lambda)}^{k_0(1+\Lambda)} dp\; \frac{p^2}{m}G^{\rm X}(p,E)G^{\rm R}(p,E). \tag{5.65}$$

The integrals for the advanced-retarded part may be computed analytically as shown in Appendix F [Eqs. (F.37), (F.41)]. The result is shown as a function of density in Fig. 5.10. At low density, the Rashba coupling renormalization is minimal.

Having obtained the renormalized coupling, we may evaluate the response function,

$$\begin{aligned}P^{\rm XR}(E) &= \frac{1}{4\pi}\bigg(\int dp\;\frac{p^3}{m^2}G^{\rm X}(p,E)G^{\rm R}(p,E) - (\lambda+\tilde{\lambda}(E))\int dp\;\frac{p^2}{m}G^{\rm X}(p,E)G^{\rm R}(p,E) \\ &\quad +\lambda\tilde{\lambda}(E)\int dp\; pG^{\rm X}(p,E)G^{\rm R}(p,E)\bigg).\end{aligned} \tag{5.66}$$

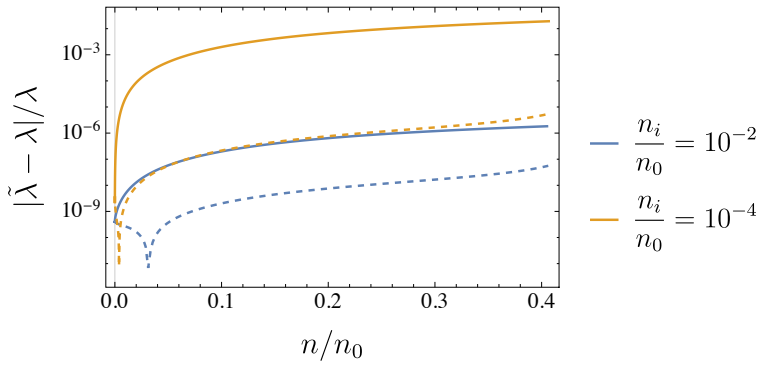

FIGURE 5.10: Renormalized Rashba couplings $\tilde{\lambda}^{AR}$ (solid) and $\tilde{\lambda}^{RR}$ (dashed) relative to the bare coupling for two different impurity densities. The advanced-retarded coupling is slightly smaller than the bare coupling. The cusp seen in the retarded-retarded coupling occurs at $n \approx n_i$ and corresponds to a change in sign of $\tilde{\lambda}^{RR} - \lambda$. This coupling is slightly smaller than the bare value at electron densities below the impurity density, but becomes larger than the bare coupling above the impurity density.

Once again, the advanced-retarded integrals are evaluated analytically in Appendix F; we obtain

$$P^{\mathrm{AR}}(E) = \frac{1}{\pi}\left(\frac{\tilde{\lambda}^{\mathrm{AR}}}{\lambda} - 2\right)\left(\frac{2}{\Lambda} + \frac{\pi}{\operatorname{Im}\tilde{\Sigma}} \operatorname{Re}\sqrt{E_0[E + \tilde{\mu} - \tilde{\Sigma}(E)]}\right). \tag{5.67}$$

It should be noted that the retarded-retarded part $P^{\mathrm{RR}}(E)$ only becomes important for electron densities below the impurity density. Above this density, the zero-temperature conductivity is well-approximated by

$$\sigma^{\mathrm{DC}} \approx \frac{e^2}{2\pi} P^{\mathrm{AR}}(E). \tag{5.68}$$

Using (5.67), one can show that this reduces to the Boltzmann result in the limit $n_0 \gg n \gg n_i$. This is also clearly seen numerically in Fig. 5.11, where the conductivity is computed from the full expression (5.55) at zero temperature. We see that the prominent features of the DC conductivity found in the Boltzmann calculation (the drop near zero density, and the quantization on a log scale) survive in the fully quantum Kubo formula calculation as long as $n_i < n$. Note that this regime is consistent with the implicit assumption in the impurity-averaging process, namely that there is enough inelastic scattering (e.g., from electron-electron or electron-phonon interactions) to cause decoherence between impurity-scattering events.

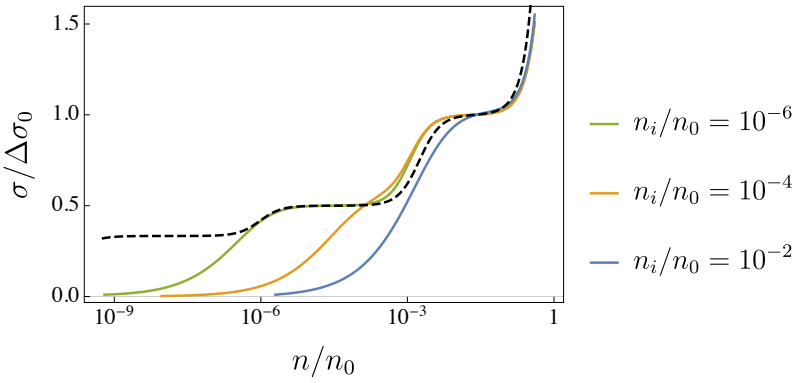

FIGURE 5.11: Zero-temperature DC conductivity as a function of electron density computed numerically from the SCFBA for different impurity densities. We have normalized each curve by the impurity-density-dependent factor $\Delta\sigma_0 \equiv \frac{e^2}{8\hbar}\frac{n_0}{n_i}$ [Eq. (5.34)]. For comparison, the Boltzmann result is shown with a dashed line. As shown in the text, the neglected crossing diagrams may become important for $n < n_i$. Thus the range of validity of these curves is: $n/n_0 > 10^{-2}$ for the blue curve, $n/n_0 > 10^{-4}$ for the orange curve, and $n/n_0 > 10^{-6}$ for the green curve. In these ranges we see good agreement with the Boltzmann result.

One might be skeptical about trusting the SCFBA in such a low-density regime. First, Fermi liquid theory (validating the quasiparticle assumption in the Boltzmann description) typically breaks down at ultra-low densities [58]. For another, the rapid drop seen in the conductivity as the density is lowered indicates a diverging scattering rate, and one might think that this could lead to interimpurity interference effects, such as weak antilocalization [73]. As it turns out however, this is not the case, provided we focus on $n_i \ll n$, which is precisely the Boltzmann limit. To see this, recall that the only diagrams excluded from the SCFBA are the crossed diagrams, which give rise to quantum interference effects. An example of such a crossed diagram is shown in Fig. 5.12, compared to a non-crossed diagram of the same order. We know that the SCFBA spectral function is a Lorentzian with a width $1/\tau$ given in Eq. (5.50). At the Fermi level E_F, this corresponds to a smearing (Δk) in momentum space that satisfies

$$\frac{[k_F \pm (\Delta k)]^2}{2m} - \lambda[k_F \pm (\Delta k)] \sim E_F + 1/\tau, \tag{5.69}$$

where $+$ and $-$ correspond to the $>$ and $<$ states respectively. As shown in Ref. [72], the condition for crossed diagrams to be negligible is that $(\Delta k) \ll k_0$. We include this argument here for completeness. The result of Eq. (5.69) is that

$$(\Delta k) \sim k_0\delta\left(-1 + \sqrt{1 + \frac{2m}{(k_0\delta)^2}(1/\tau)}\right). \tag{5.70}$$

Returning to the diagrams in Fig. 5.12, we see that the internal momenta in the non-crossed diagram are independent, so that the phase space for this diagram is

$$\Omega_{\mathrm{NC}} = [(2\pi k_< + 2\pi k_>)(\Delta k)]^2 = [4\pi k_0(\Delta k)]^2. \tag{5.71}$$

On the other hand, crossing diagrams have the restriction $|\boldsymbol{k}_2 + \boldsymbol{k} - \boldsymbol{k}_1| \in [k - (\Delta k), k + (\Delta k)]$, which means that once one momentum is fixed, the other is restricted to the intersection of four annuli. One possibility is shown in the bottom right of Fig. 5.12 with two intersections, but there are three other cases with four, six and eight intersections as well. Regardless, the phase space will be

$$\Omega_{\mathrm{C}} \sim 8\pi k_0(\Delta k)^3. \tag{5.72}$$

So we can neglect crossing diagrams (at least at this order), provided that

$$\frac{\Omega_{\mathrm{C}}}{\Omega_{\mathrm{NC}}} \sim \frac{(\Delta k)}{2\pi k_0} \ll 1. \tag{5.73}$$

In the low-energy regime, this means that

$$\frac{1}{E_0\tau} \ll 4\pi^2. \tag{5.74}$$

Let us now see if the SCFBA scattering rate meets this criterion. To be consistent with impurity averaging and the low-density approximations we have made, we should focus on

$$\frac{n_i}{n_0} \ll \frac{n}{n_0} \ll 1. \tag{5.75}$$

In this case, we have seen that the scattering rate is well approximated by the low-density Boltzmann result. From (5.18), we have

$$\frac{1}{E_0\tau} = \frac{e^2}{\pi}\left(\frac{n}{n_0}\right)\frac{1}{\sigma_{\mathrm{DC}}}. \tag{5.76}$$

If the conductivity drops to zero too rapidly as the electron density is lowered, one is not able to satisfy (5.74). But using Eq. (5.25), as the index l of the plateau increases, the conductivity decreases at a rate of

$$\frac{d\sigma_{\mathrm{DC}}}{dl} \sim -\frac{n_0}{n_i}\frac{e^2}{8l^2}, \tag{5.77}$$

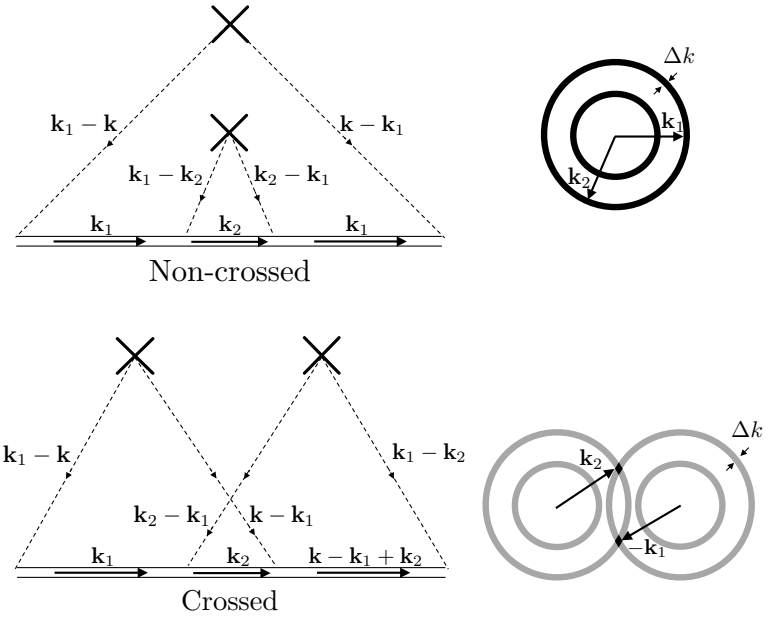

FIGURE 5.12: Top: example of a non-crossed Feynman diagram that contributes to the irreducible part of the SCFBA self-energy and the corresponding phase space for internal momenta. Both $\mathbf{k}_1$ and $\mathbf{k}_2$ can lie anywhere within the two black annuli defined by the Fermi surface. Bottom: a crossed diagram of the same order (second order in n_i, fourth order in the interaction), and one example of the corresponding phase space. Once $\boldsymbol{k}_2$ is fixed, $-\boldsymbol{k}_1$ is restricted to lie within the black diamonds.

treating l as a continuous variable and ignoring the detailed non-linear behaviour. Likewise, the density at each plateau transition is given by $n/n_0 \approx \delta_l^*$, which for δ-shell impurities (5.23) means

$$\ln(n/n_0) = \ln\left(\frac{(k_0R)^2}{4}\right)l - 2\ln(|l|!) + c, \tag{5.78}$$

and

$$\frac{d(n/n_0)}{dl} = \frac{n}{n_0}\left[\ln\left(\frac{(k_0R)^2}{4}\right) - 2\psi(|l|+1)\right], \tag{5.79}$$

where $c = \ln(mv_0R^2/2)$ and $\psi(x)$ is the digamma function. Now if l is large, the conductivity will decay slowly according to (5.77), and the n/n_0 pre-factor in (5.76) will ensure that the crossed diagrams are negligible. The only concern therefore is when l is small. But in this case, $\psi(|l|+1) \approx -\gamma$, and $\ln(|l|!) \approx -\gamma l$, where γ is the Euler-Mascheroni constant. The result is

$$l^2 = \left(\frac{\ln(n/n_0) - c}{\ln[\frac{(k_0R)^2}{4}] + 2\gamma}\right)^2, \tag{5.80}$$

and

$$\frac{d\sigma_{\rm DC}}{d(n/n_0)} = \frac{d\sigma_{\rm DC}}{dl}\frac{dl}{d(n/n_0)} \sim \frac{n_0/n_i}{n/n_0[\ln(n/n_0) - c]^2}. \tag{5.81}$$

Integrating with respect to n/n_0, we see that, roughly speaking, the conductivity changes with the density according to

$$\sigma_{\rm DC} \sim \frac{n_0/n_i}{\ln(n/n_0)}, \tag{5.82}$$

so that

$$\begin{aligned} \frac{1}{E_0\tau} &\sim (n/n_0)(n_i/n_0)\ln(n/n_0) && (5.83)\\ &\ll (n/n_0)^2\ln(n/n_0) && (5.84)\\ &\ll 1. && (5.85) \end{aligned}$$

Thus we can trust the SCFBA result in the regime where the conductivity quantization is observed.

5.3 Discussion

This chapter demonstrated that the low-density conductivity due to impurity scattering in a 2D Rashba system takes a highly non-linear form that exhibits quantization as a function of the logarithm of the electron density. This unusual behaviour arises from the full non-perturbative low-energy T-matrix discussed in Chapter 4, which describes electron-impurity scattering near the ring minimum at the bottom of the Rashba conduction band.

It is clear that this highly degenerate band minimum is responsible for many unusual characteristics of low-energy transport. For one thing, the Fermi surface consists of two concentric circles with group velocities in opposite directions. At zero temperature, in the low-density limit, this produces an unconventional Drude-like expression for the conductivity that is controlled by the electron lifetime, as opposed to the usual transport time that appears in the conventional Drude formula. The transition from conventional to unconventional Drude transport as the density is lowered results in a non-linear conductivity as a function of density. This behaviour was first pointed out in Ref. [48]. The focus of this chapter has been on the *ultra*-low density regime, where the unconventional

Drude conductivity becomes quantized. We showed this quantization within a semiclassical Boltzmann treatment (provided the full T-matrix is used in the scattering rate), as well as a fully quantum Kubo formula treatment, provided the electron density remains larger than the impurity density.

The most important distinction between our research and previous work is the use of the non-perturbative T-matrix in calculations. A T-matrix limited to the first Born approximation (or even a self-consistent first Born approximation) leads to qualitatively different transport phenomena. In particular, the first Born conductivity goes smoothly to zero with decreasing electron density, while the full T-matrix leads to a seemingly abrupt drop at zero density. For a Rashba semiconductor, we showed that this translates to a sharp drop in conductivity as the chemical potential passes through the band bottom, and that this drop retains significant weight at finite temperature.

We recognize that experimentally it is difficult to control the electron density with enough precision to access these ultra-low-density features. We have outlined a brief proposal of one way to overcome this difficulty in Rashba semiconductors. Namely, one could use a pump-probe approach in which the conductivity is measured as function of delay time between the two pulses. Such an approach allows one to use the logarithm of the carrier density as a control parameter. Of course, many technical issues would need to be addressed for such an experiment. One would need to carefully choose a 2D Rashba system with large splitting and Fermi level in the gap. The experiment would have to be done at very low ($\lesssim$ 10K) temperatures. Furthermore, the effects of hole carriers and excitons have not been addressed.

Our analysis is restricted to non-interacting systems. We recognize that at the low densities we are considering here, the effect of electron-electron interactions is enhanced; as a result, one might expect Wigner crystallization to occur. The electron-electron scattering process is dependent on a T-matrix that would likely contain unusual features similar to the impurity-scattering T-matrix considered here. Such a T-matrix may enhance or suppress the transport properties described in this chapter or produce unique signals of its own. To say more would require explicit calculations that are beyond the scope of this thesis. Instead, we can look for cases where we expect Fermi liquid theory to hold, outside the Wigner crystal regime. For one, it should be noted that many examples of Rashba 2D electron gases occur within gated samples. The presence of a

metallic gate is expected to screen the Coulomb interaction, and the resulting short-range interaction may be insufficient to cause crystallization. Without knowing the details of the interaction it is hard to say more, though the unique low-energy density of states of the Rashba system may allow liquid crystal or anisotropic Wigner crystal phases to exist even for short-range interactions as described in Sec. 2.2. However, the stability of these phases to disorder must be considered as well. Perhaps the simplest way to avoid the crystalline phase is to focus on temperatures above the melting point of the Wigner crystal. This occurs at a critical value of the dimensionless parameter $\Gamma = e^2\sqrt{\pi n}/(4\pi\epsilon_0 k_B T)$, the ratio of potential and kinetic energies of a classical gas of electrons. In two dimensions, the melting point occurs around $\Gamma \approx 130$ [74, 75]. Using this number, we see that at the ultra-low densities considered in this paper, the Wigner crystal should melt at very low temperatures. For example, the density corresponding to the first plateau in Fig. 5.11 at $n/n_0 \sim 10^{-2}$ would be within the Fermi liquid phase for $T \gtrsim 2$K. The second plateau at $n/n_0 \sim 10^{-5}$ corresponds to a melting temperature of $T \sim 0.07$K. Now of course our SCFBA analysis was performed at zero temperature, but given the robustness of the non-perturbative transport effects to finite temperature in the Boltzmann treatment (Figs. 5.4, 5.5), it is reasonable to assume that at least the first plateau would be observable at temperatures above the Wigner crystal melting point.

It is likely that these unusual transport features are not unique to Rashba systems. It would be interesting to determine exactly what aspects of this Hamiltonian are responsible for such non-linear behaviour. If the key aspect is the degenerate ring minimum in the band structure, then such features could also be observed in materials with pure Dresselhaus spin-orbit coupling [22]. If the key aspect is the topology of the Fermi sea, then these features could appear in higher dimensional systems as well. Indeed, if the same quantization occurs in three-dimensional systems, then the group of candidate materials for experimental observation would be enlarged significantly.

Part II

BCS superconductivity

Chapter 6

Introduction

In Part 1 of this thesis, we considered a non-interacting gas of electrons, and showed how changing the single-particle dispersion, by breaking inversion symmetry, can drastically affect the propagation of electrons in a disordered system. Yet even these drastic changes were captured by Fermi liquid theory. Part 2 of this thesis focuses on a different regime where the electron-electron interaction destabilizes the Fermi liquid. In particular, we exclusively consider interactions that lead to Cooper pairing, resulting in a superconducting state. We probe the thermodynamics of this state for different variations of the Hubbard model. Many other fascinating ordered phases such as charge and spin density waves exist with and without spin-orbit coupling [76], but these will not be considered here.

6.1 BCS theory and tight-binding

From its discovery in 1911 [77], until 1957, the theory of superconductivity consisted of several phenomenological models that lacked a microscopic basis. A few of the requirements for such a microscopic theory were clear. Both the complete lack of electrical resistance, and the Meissner-Ochsenfeld effect [78] could be explained by a thermodynamic transition at a critical temperature T_c to a phase where electrons formed a macroscopic phase-coherent state. Phase coherence is a crucial property since the presence of current in zero field requires a macroscopic gradient in the phase of the many-body wavefunction, not its amplitude, which can be understood from Eq. (3.20). Such a

state can be considered as a superfluid condensate of paired electrons [79], much like a Bose-Einstein condensate in momentum-space. One roadblock in progressing the theory was to understand why two electrons obeying Pauli exclusion with a repulsive Coulomb interaction should pair together. Two-body bound states in three dimensions do not exist unless the attraction exceeds a critical value [80].[1] Thus even a weak attraction would not be enough for electrons to pair in real space. A major insight in this regard was provided by Leon Cooper in 1956 who pointed out that an arbitrarily weak attraction amongst electrons would cause pairing in momentum-space, precisely because of the presence of a Fermi sea [81]. In other words, the Femi sea is unstable to electron-electron attraction. The origin of this attractive interaction in most conventional superconductors is a phonon-mediated electron-electron interaction. A word of caution is needed here. The distinction between *conventional* and *unconventional* superconductivity is not universally defined [82]. In some of the literature, the term conventional is taken to mean superconductors that are well described by BCS theory. In other cases, it means superconductors with a phonon origin of pairing. In this thesis, we will define conventional superconductors as ones whose order parameter has the highest symmetry consistent with the normal state (above T_c). This distinction only became important in the 1980's with the discovery of heavy fermion [83], and high-T_c cuprate (CuO) superconductors [84], whose order-parameter symmetry and underlying pairing mechanism are much more elusive than those of conventional superconductors. Indeed, for many of these materials, both the symmetry and pairing mechanism are still under debate [85]. We will have more to say on this in Sec. 6.3.

Fortunately, knowledge of the origin of the interaction was not necessary to formulate a detailed theory of superconductivity. For Cooper, it was taken to be an attractive constant $-V < 0$ within a small window of the Fermi energy and zero elsewhere. In Chapter 7 we will see how superconductivity can arise from repulsive interactions. A year after Cooper's discovery, Bardeen, Cooper and Schrieffer published a complete theory (BCS theory) of the superconducting state including the ground state many-body wavefunction [86]. This theory, expressed as a mean-field theory, will be our primary tool for understanding the superconducting phase of a variety of models in this thesis. Mean-field theory allows us to decouple electron-electron interactions by treating the electrons as if they interact with an effective mean field whose form is chosen based in the

[1] This is not true in one and two dimensions where attractive potentials always produce at least one bound state.

instability we are interested in probing (in this case a superconducting instability), and whose value is determined self-consistently. The key component of BCS theory that we retain throughout this work is that the only important interactions for superconductivity are interactions in the Cooper channel, and furthermore, that electron pairs have zero total momentum. The absence of a center-of-mass momentum is due to a phase-space argument. Cooper pairs scatter within a narrow shell around the Fermi surface. If they have a finite center-of-mass momentum, then conservation of momentum will severely restrict the available scattering states within this shell. However, if the two electrons in the pair have opposite momenta $\boldsymbol{k}$ and $-\boldsymbol{k}$ they may scatter to states all over the shell.[2] In addition, BCS theory consists of spin singlet pairs; an electron with spin up is paired with an electron with spin down. This is a consequence of the choice of isotropic interaction which is reflected in the symmetry of the pair wavefunction. Since the wavefunction is symmetric in $\boldsymbol{k} \to -\boldsymbol{k}$, it must be antisymmetric in spin indices to preserve the right exchange statistics. In the following chapters, we will relax this condition by allowing more general interactions for which there may be spin triplet pairing.

In this part of the thesis will will consider superconductivity in several tight-binding models related to the Hubbard model [89]. The tight-binding paradigm is one in which models describe electrons hopping between ionic sites on a lattice [31]. More formally, we begin with a Bloch wavefunction of an electron in a lattice potential $\psi_{\boldsymbol{k}\sigma}(\boldsymbol{x}) = \sum_i e^{i\boldsymbol{k}\cdot\boldsymbol{x}_i}\phi_{i\sigma}(\boldsymbol{x})$ where i is a site index, σ is a spin index, and $\phi_{i\sigma}(\boldsymbol{x})$ is a Wannier function centered at site i. In the atomic limit, the Wannier functions correspond to localized electronic wavefunctions on the atom located at site i. In the tight-binding approximation, we imagine starting from this limit, bringing N atoms closer together until a small overlap between neighbouring wavefunctions forms. As this overlap grows, the N-fold degeneracy of a single atomic level is split, forming a band. The tight-binding approximation therefore best describes narrow-band materials. In such materials, the Wannier functions may be approximated by linear combinations of atomic orbitals. For now, it will suffice to consider a single orbital. The second-quantized field operators expanded on the basis of these Wannier functions are $\hat{\psi}^\dagger_\sigma(\boldsymbol{x}) = \sum_i \phi^*_{i\sigma}(\boldsymbol{x})c^\dagger_{i\sigma}$. The many-body Hamiltonian (without phonons) consists of a Bloch Hamiltonian term, which includes the kinetic and electron-ion interaction terms as well as an electron-electron

[2]The exception to this is the Fulde-Ferrell-Larkin-Ovchinnikov phase which is predicted to occur at strong magnetic fields and low temperatures [87, 88].

interaction term:

$$\begin{aligned} H &= \sum_{ij\sigma} \int d\boldsymbol{x} \phi_i^*(\boldsymbol{x}) H_{\text{Bloch}} \phi_j(\boldsymbol{x}) c_{i\sigma}^\dagger c_{j\sigma} \\ &+ \sum_{ijmn\sigma\sigma'} \int d\boldsymbol{x} \int d\boldsymbol{x'} \phi_i^*(\boldsymbol{x}) \phi_j^*(\boldsymbol{x'}) V_{\text{e-e}} \phi_m(\boldsymbol{x'}) \phi_n(\boldsymbol{x}) c_{i\sigma}^\dagger c_{j\sigma'}^\dagger c_{m\sigma'} c_{n\sigma}. \end{aligned} \tag{6.1}$$

We define the hopping amplitude t_{ij} from the (negative of the) first integral and the interaction U_{ijmn} from the second double integral so that

$$H = -\sum_{ij\sigma} t_{ij} c_{i\sigma}^\dagger c_{j\sigma} + \sum_{ijmn\sigma\sigma'} U_{ijmn} c_{i\sigma}^\dagger c_{j\sigma'}^\dagger c_{m\sigma'} c_{n\sigma}. \tag{6.2}$$

This Hamiltonian is still far from tractable; in any tight-binding model we can only retain the most important terms in these summations. In most cases, these are interactions involving two nearest-neighbour sites i and j. From now on we will only consider hopping between nearest neighbours with $t_{ij} = t$. If we enumerate all interaction terms that involve these two sites, neglecting spin-flip hopping terms (which contribute to the Heisenberg interaction), we get Table 6.1, where we have made use of the number operator $n_{i\sigma}$ and $\langle ij \rangle$ indicates nearest neighbour sites. Note, for example, that Pauli exclusion prevents terms like $c_{i\sigma}^\dagger c_{j\sigma} n_{i\sigma}$. Similarly, a term like $n_{i\sigma} n_{i\sigma}$ is the same as a one-body term since $n_{i\sigma}^2 = n_{i\sigma}$.

Name	Coupling	Interaction term
Hubbard U	$U_{iiii} \equiv U/2$	$U \sum_i n_{i\uparrow} n_{i\downarrow}$
Correlated hopping	$U_{iiij} \equiv \Delta t$	$\Delta t \sum_{\langle ij \rangle \sigma} (c_{i\sigma}^\dagger c_{j\sigma} + c_{j\sigma}^\dagger c_{i\sigma})(n_{i-\sigma} + n_{j-\sigma})$
Extended term	$U_{ijij} \equiv V$	$V \sum_{\langle ij \rangle \sigma} n_{i\sigma} n_{j\sigma}$
Exchange term	$U_{ijji} \equiv -J$	$J \sum_{\langle ij \rangle \sigma} n_{i\sigma} n_{j-\sigma}$

TABLE 6.1: Non-trivial couplings for nearest-neighbour tight-binding models. Here $-\sigma$ means the spin opposite of σ.

Including just the first term in Table 6.1 gives us the Hubbard model. It has a superconducting instability for all negative values of U, with an isotropic order parameter in momentum-space. Half filling (average density $n = 1$) is an exceptional case. Here particle-hole symmetry ensures that superconductivity can coexist with charge-density-wave order, potentially forming a supersolid phase [90].

The attractive local interaction between electrons may originate from a variety of different sources, including electron-phonon coupling (attraction between polarons), density

oscillations of itinerant electrons (plasmons), or even spin fluctuations [91, 92]. The second term in Table 6.1 stands out. Unlike the others, it is not a diagonal density-density interaction but looks rather like the hopping term, only modulated by the number of electrons on the sites involved in each hop. This term will be discussed in detail in Chapter 7. The third term will be discussed in Chapter 8. For the same reasons as U, this extended term may also be attractive, leading to superconductivity as well. We will not consider the exchange coupling in this thesis, though it is important for understanding the magnetic properties of many materials.

These interactions are more complicated than the simple potential considered in BCS theory, and can lead to momentum-dependent interactions $V(\boldsymbol{k}, \boldsymbol{k}')$ and therefore order parameters that are also momentum-dependent. Nonetheless, we may still follow the same framework as BCS theory, namely, deleting components of the interaction that do not connect Cooper pairs, and doing mean-field theory on the resulting Hamiltonian for the superconducting order parameter. For example, in this procedure, the order parameter for singlet pairing takes the form

$$\Delta_k \equiv -\frac{1}{N}\sum_{\boldsymbol{k}'} V(\boldsymbol{k}, \boldsymbol{k}') \left\langle c_{-\boldsymbol{k}'\downarrow} c_{\boldsymbol{k}'\uparrow} \right\rangle . \tag{6.3}$$

This quantity is also known as the gap function because its magnitude is half the energy gap for excitations. The details of the mean-field approach are found in Appendix G.

6.2 Spin-orbit coupling and superconductivity

In the years following its publication, BCS theory succeeded in a myriad of experimental tests, but failed with regards to the so-called *Knight shift*. Due to hyperfine coupling, the nuclear spins in a crystal are sensitive to the spin magnetic moments of conduction electrons. In a nuclear magnetic resonance measurement, the nuclear spin precesses at a Larmor frequency that is shifted by the presence of these conduction electrons. This shift is the Knight shift. In BCS theory, the singlet pairing ensures that the zero-temperature electronic spin susceptibility is zero, unless the applied magnetic field is strong enough to break Cooper pairs. Thus the low field Knight shift in a superconductor was expected to be zero. However, many superconductors that were otherwise well-described by conventional BCS theory (e.g. Mercury, Tin), exhibited a Knight shift

similar to their normal state value [93, 94]. Shortly after, Anderson, Abrikosov, and Gor'kov suggested that since these Knight shift measurements were carried out on very small samples, spin-orbit coupling at the surface was important, and that this could partially restore the Knight shift [95, 96]. This discussion was revived as superconductors with crystal structure that lacked a centre of inversion became more common [97]. In 2001, Rashba and Gor'kov computed the spin susceptibility for continuum Rashba pairs [98], motivated by observed superconductivity on the surface of WO_3, which has strong near-surface electric fields (and therefore strong Rashba SOC). In the Rashba dispersion, zero center-of-mass momentum pairing near the Fermi surface requires both electrons to be in the same helicity band, and therefore not in a singlet state like a Cooper pair. The result is that each pair is a mixture of singlet and triplet, and the triplet part prevents the spin-susceptibility from vanishing at zero temperature.

Superconductivity has been observed in many other non-centrosymmetric materials including $CePt_3Si$, $SrAuSi_3$, $LaNiC_2$, and UIr, as well as the $LaAlO_3/SrTiO_3$ interface with strong Rashba SOC [99–103]. Much effort has gone into understanding the nature of the pairing in these unconventional superconductors. It should be noted that Rashba superconductivity may be more pervasive than the specialized examples above. One has to remember that Rashba spin-splitting is due to inversion asymmetry in the *local* environment of an electron [30], and thus is present in quasi-2D materials where there is polar asymmetry within each plane. This is particularly relevant for some cuprate superconductors, where pairing occurs entirely within copper-oxide planes that have a local inversion asymmetry. Indeed $YBa_2Cu_3O_7$ was the motivation for some of the early theoretical work on non-centrosymmetric superconductivity [97].

While the above references identified the mixed singlet-triplet state, which was implicit all along since spin had been identified in the early work as *not* a good quantum number, the impact on thermodynamic properties (including the superconducting critical temperature, T_c) was not really considered. In principle a large enhancement in T_c could occur [51], because of the enhancement in the electronic density of states in the low density region, due to the effective "dimensionality reduction" evidenced in Part 1 of this thesis. However, as we saw earlier, this region is a rather narrow window of electron densities, and the corresponding T_c enhancement is not likely to be found in a typical Rashba superconductor. We will demonstrate this explicitly in Chapter 7, and also see that the overall scale of T_c is low for a weakly coupled system.

An interesting general question remains, which is the impact of the Rashba spin-orbit interaction on superconducting T_c in the presence of different types of pairing interactions. Some calculations have been recently performed in Ref. [104] for the extended Hubbard model (including the first and third terms in Table 6.1) and will be verified in Chapters 7 and 8. The generic short-range attractive interaction (e.g., the attractive Hubbard model) already results in a mixed singlet-triplet state due to the spin-orbit interaction. However, as we will show (and also found in Ref. [104]), in that case the spin-orbit interaction suppresses superconductivity. In Chapter 7 we will see how this is drastically modified when we include correlated hopping in the interaction, previously considered in the context of cuprate superconductivity [105].

6.3 Symmetry of the gap function

Symmetry breaking is a crucial part of superconductivity. The existence of a non-zero superconducting order parameter is a hallmark of broken $U(1)$ symmetry. But the order parameter is also a function of momentum (see e.g. Eq. (6.3)). If the interaction is a constant, as in standard BCS theory and the attractive Hubbard model, then the gap function is a constant, having the same magnitude all over the Fermi surface. Such a gap is referred as an (isotropic) s-wave gap. If the gap function is non-trivial, it may indicate breaking of the point-group symmetry inherited by the lattice. In this part of the thesis, we exclusively consider the square lattice, whose point group D_4 is shown in Table A.7. The gap functions that transform under the irreps A_1, B_1, B_2, and E are labelled in the same manner as atomic orbitals: s, $d_{x^2-y^2}$, d_{xy} and p-wave respectively. The appearance of these additional functions in the order parameter is allowed by the presence of an extended interaction (e.g. extended term in Table 6.1). Some important physical distinctions between these types include the fact that d-wave gaps have nodes and p-wave gaps are antisymmetric under inversion, corresponding to triplet pairing. The presence of Rashba spin-orbit coupling makes this even richer. As discussed in the previous section, when spin is not a good quantum number, pairing generally includes a mixture of singlet and triplet. The argument for zero center-of-mass momentum pairing in this case leads to pairing within a Rashba helicity band s. As shown in Chapter 7 and Appendix G, intra-band Rashba pairing induces a complex $\boldsymbol{k}$-dependent phase, so

that the gap function may be written as

$$\Delta_{\boldsymbol{k}s} = s e^{-i\theta(\boldsymbol{k})} \bar{\Delta}_{\boldsymbol{k}s}, \tag{6.4}$$

where

$$e^{i\theta(\boldsymbol{k})} \equiv \frac{\sin k_y - i \sin k_x}{\sqrt{\sin^2 k_x + \sin^2 k_y}}. \tag{6.5}$$

The function $\bar{\Delta}_{\boldsymbol{k}s}$ transforms under the irreps of D_4. In the presence of both extended interactions and Rashba SOC, we are left with three possible symmetries of the gap function shown in Fig. 6.1. We see that, $\bar{\Delta}_{\boldsymbol{k}s}$ can have s-wave, $d_{x^2-y^2}$, and d_{xy} symmetry.

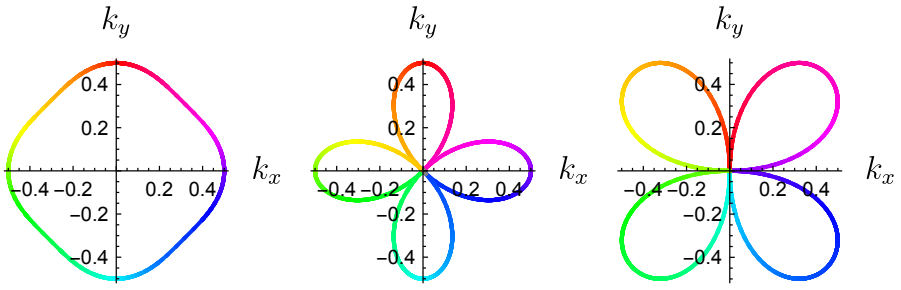

FIGURE 6.1: Polar plots of the intra-band gap function with Rashba SOC at fixed $|\boldsymbol{k}| = \pi/2$, where $\bar{\Delta}_{\boldsymbol{k}s}$ has s-wave symmetry (left), $d_{x^2-y^2}$ symmetry (center), and d_{xy} symmetry (right). The hue indicates the complex phase of the gap.

Knowledge of the symmetry of the gap function produces constraints on the possible pair-interactions and therefore constraints on the underlying microscopic model; an invaluable asset for so many superconductors where the pairing mechanism is still under debate. Thus as more and more unconventional superconductors are discovered, the question of the symmetry of the superconducting order parameter has moved to the forefront as one of the most immediate and important questions to answer about any new material. Experimentally, it is a difficult question to answer, as the arduous history of the cuprates provides testament for, which, through several years of experimental effort, settled on d-wave superconductivity [106]. The resolution of this question has been aided, in part, by phase-sensitive tunnelling measurements, which have been particularly useful in uncovering the gap symmetry of the heavy-fermion compound UPt_3 [107]. Like ^{3}He, UPt_3 has an A and a B phase over different temperature ranges differentiated by different symmetries of the order parameter [108]. A variety of models have been proposed to describe the nature of this gap and its symmetry transition [109]. It is possible

that the separation of these phases is due to magnetic moments lowering the symmetry of the hexagonal lattice, but this is not the only explanation. As we point out in Chapter 8, many exotic superconducting symmetries can emerge from a normal state that retains the point group symmetry of the lattice. Irrespective of its origin, the lesson to take from UPt_3 is that in general, the superconducting order parameter does not necessarily retain a fixed symmetry below T_c. Similarly, recent observations in $LaAlO_3/SrTiO_3$ suggest that a second component of the gap function develops below T_c [110]. One might consider these to be unusual circumstances. Indeed, $LaAlO_3/SrTiO_3$ has strong Rashba coupling; UPt_3 has time-reversal symmetry breaking, with significant spin-orbit coupling and a complex order parameter in the B phase. However, we will point out that such exotic conditions are not a requirement for a superconductor to have a rich phase diagram below T_c. In fact, in Chapter 8 we illustrate that symmetry transitions occur as a function of temperature in one of the simplest and most studied models for superconductivity, the extended Hubbard model.

With this expanding collection of unconventional superconductors, one might ask what symmetries can exist in a generic superconductor. The answer is well established within Landau-Ginzburg theory. In Landau-Ginzburg theory, the free energy is expanded in powers of the unknown order parameter which develops from zero at T_c [31]. The gap function is segmented into pieces that transform under irreps of the normal state symmetry group. Any of these individual pieces could form the superconducting state at T_c, but cannot be mixed at this temperature. However, at lower temperatures, when the magnitude of the order parameter is no longer small, higher order terms in the Landau free energy become important, and mixing can occur [111]. As we will see, the phases below T_c can be described by bifurcations of critical points of the free energy. Such mixing and bifurcations have been predicted before in the context of anisotropic tight-binding models [112–114]. We will illustrate these ideas within a case study of the simplest model that has competing symmetry phases: the two-dimensional (2D) extended Hubbard model on a square lattice, relevant for some layered high-temperature superconductors. We will then examine the symmetry phases that occur at the onset of superconductivity when SOC is included.

Chapter 7

Enhancement of superconducting T_c due to the spin-orbit interaction

In this chapter we will introduce a tight-binding model with both Rashba spin-orbit coupling and correlated hopping. Working within the Rashba helicity basis, we follow the usual BCS description for the pairing state; this leads to a simple parameterization of the wavevector dependence of the order parameter, in the presence of spin-orbit coupling. We then present results for T_c as a function of the various interaction strengths and as a function of the electron density. In general, with the correlated hopping interaction present, spin-orbit coupling leads to a significant enhancement of superconducting T_c.

7.1 Correlated hopping

In principle, the Coulomb interaction, being long range, contains all elements of Table 6.1, including the correlated hopping. Typically, this term is ignored because in the tight-binding limit, where ions are well separated, the on-site Hubbard U interaction is dominant. However, the correlated hopping term can also originate from another phenomenon that should not be ignored. This is the modification of the on-site electron wavefunction when a second electron occupies a site, due to Coulomb repulsion. Essentially, this is a failure of single-band (or even few-band) models. When there are

few electrons in a system, such models are appropriate; the picture of itinerant electrons hopping between valence orbitals works. However, when the electron density is high, this picture breaks down. When two electrons occupy the same site, the minimal description of this configuration is as a three-body system (two electrons, one ion), which does *not* have hydrogenic-like eigenstates, yet we are attempting to describe this configuration with a single hydrogenic band. Hydrogenic eigenstates (including the continuum states) form a complete basis, so an infinite number of them would be required to capture the electron configuration. A quantitative estimate of the importance of these additional states is given for the case of a helium atom in Ref. [115], where it was found that the ground state of helium contains significant contributions from all excited hydrogenic orbitals as well as ionized states. On the other hand, we do not wish to give up the computational simplicity of a single band model. The compromise is to include the effect of higher orbitals in a phenomenological term. Note that this effect is not captured by the on-site Hubbard U term which penalizes double occupation (for $U > 0$). In fact, the effect we wish to account for reduces this penalty by allowing an effective orbital expansion for doubly occupied sites which is described by the 'dynamic Hubbard model' [116]. In a many-electron system, this orbital expansion is a dynamic quantity. The dynamic Hubbard model describes this via a harmonic oscillator coordinate q_i. One could think of this coordinate in terms of the effective on-site electron separation, but it is convenient to take it to be the displacement of the effective Hubbard U value

$$U(q_i) = U + \alpha q_i. \tag{7.1}$$

The oscillator part of the Hamiltonian

$$H_i = \frac{p_i^2}{2M} + \frac{1}{2}Kq_i^2 + (U + \alpha q_i)\, n_{i\uparrow} n_{i\downarrow}, \tag{7.2}$$

produces the occupation-dependent equilibrium value of this coordinate:

$$q_i = \begin{cases} 0 & n_i = 0, 1 \\ -\alpha/K & n_i = 2. \end{cases} \tag{7.3}$$

In second quantization, the oscillator coordinate is upgraded to a bosonic field a_i, and Eq. (7.2) becomes

$$H_i = \omega a_i^\dagger a_i + \left[U + g\omega\left(a_i^\dagger + a_i\right)\right] n_{i\uparrow} n_{i\downarrow}, \tag{7.4}$$

where $\omega = \sqrt{K/M}$, and $g = \alpha/\sqrt{2K\omega}$.

A generalized Lang-Firsov transformation [116, 117]

$$c_{i\sigma} = e^{g(a_i^\dagger - a_i)\tilde{n}_{i,-\sigma}} \tilde{c}_{i\sigma} \equiv X_{i\sigma}\tilde{c}_{i\sigma} \tag{7.5}$$

relates the original fermion operators $c_{i\sigma}$ to new fermion quasiparticle operators $\tilde{c}_{i\sigma}$ that both destroy the electron at the site and change the state of the boson so that the boson field follows the fermion motion. Since $X_{i\sigma}^\dagger = X_{i\sigma}^{-1}$, the transformation preserves fermion anticommutation relations. To obtain a low-energy effective Hamiltonian we replace the boson field with its ground state expectation value, and in this approximation the relation Eq. (7.5) becomes [116]

$$c_{i\sigma}^\dagger = [1 - (1-S)\tilde{n}_{i,-\sigma}]\tilde{c}_{i\sigma}^\dagger, \tag{7.6}$$

where $S = e^{-g^2/2}$ increases with the ionic charge. The on-site repulsion U is lowered to $U_{eff} = U - \omega g^2$, and bilinear terms in fermion operators at different sites transform as follows:

$$c_{i\sigma}^\dagger c_{j\sigma'} \quad = \quad \tilde{c}_{i\sigma}^\dagger \tilde{c}_{j\sigma'}[1 - (1-S)(\tilde{n}_{i,-\sigma} + \tilde{n}_{j,-\sigma'}) + (1-S)^2 \tilde{n}_{i,-\sigma}\tilde{n}_{j,-\sigma'}]. \tag{7.7}$$

We will be interested in the regime where the band is close to full for which terms like $(1 - \tilde{n}_{i,-\sigma})(1 - \tilde{n}_{j,-\sigma})$ are negligible. In this case, the coefficient in the square brackets above becomes

$$S(2-S) + S(S-1)(\tilde{n}_{i,-\sigma} + \tilde{n}_{j,-\sigma}). \tag{7.8}$$

Replacing the bare operators $c_{i\sigma}$ by the quasiparticle operators $\tilde{c}_{i\sigma}$ in the hopping term $-t_0 \sum_{\substack{\langle ij \rangle \\ \sigma}} (c_{i\sigma}^\dagger c_{j\sigma} + c_{j\sigma}^\dagger c_{i\sigma})$, and renaming the quasiparticle operators $\tilde{c}_{i\sigma} \to c_{i\sigma}$ gives the correlated hopping Hamiltonian

$$H_{\text{Corr}} = -t' \sum_{\substack{\langle ij \rangle \\ \sigma}} (c_{i\sigma}^\dagger c_{j\sigma} + c_{j\sigma}^\dagger c_{i\sigma}) + U \sum_i n_{i\uparrow} n_{i\downarrow} + \Delta t \sum_{\substack{\langle ij \rangle \\ \sigma}} \big(c_{i\sigma}^\dagger c_{j\sigma} + c_{j\sigma}^\dagger c_{i\sigma}\big)\big(n_{i-\sigma} + n_{j-\sigma}\big), \tag{7.9}$$

where $t' \equiv t_0 S(2-S)$ and $\Delta t \equiv -t_0 S(S-1)$. The t' term is renormalized by a Hartree-Fock contribution coming from the new correlated hopping term: $t' \to t \equiv t' - n\Delta t$, where n is the density of electrons. In the high electron density regime, we have $t \approx 0.1t'$. All energies in this chapter will be measured with respect to the renormalized value t.

We now add spin-orbit coupling to this tight-binding model. Recall that the Rashba term on a lattice is given by Eq. (1.34). The bilinears in this term are modified by the transformation (7.7) just as the regular hopping term was. The resulting spin-orbit coupling term is

$$\begin{aligned} H_{\mathrm{SO}} &= -iV_{\mathrm{SO}} \sum_{i,\alpha\beta} \Big(c^{\dagger}_{i,\alpha} \sigma_x^{\alpha\beta} c_{i+\hat{y},\beta} [1 - \frac{\Delta t}{t}(n_{i,\beta} + n_{i+\hat{y},\alpha})] \\ &\quad - c^{\dagger}_{i,\alpha} \sigma_y^{\alpha\beta} c_{i+\hat{x},\beta} [1 - \frac{\Delta t}{t}(n_{i,\beta} + n_{i+\hat{x},\alpha})] \Big) + h.c., \end{aligned} \tag{7.10}$$

so that the full Hamiltonian of our model is $H = H_{\mathrm{Corr}} + H_{\mathrm{SO}} - \mu \sum_{i,\sigma} n_{i\sigma}$, where μ is the chemical potential.

The non-interacting part of this Hamiltonian is diagonalized in the $s = \pm 1$ helicity basis to produce the dispersion Eq. (1.37), with corresponding eigenvectors

$$c^{\dagger}_{\mathbf{k}s} = \frac{1}{\sqrt{2}}(c^{\dagger}_{\mathbf{k}\uparrow} + s e^{i\theta(\mathbf{k})} c^{\dagger}_{\mathbf{k}\downarrow}). \tag{7.11}$$

Here we have made use of the phase factor defined in Eq. (6.5), which governs the mixing of spin-up and spin-down components for eigenstates of the non-interacting Hamiltonian. This mixing ensures that pairs are always formed in a mixed singlet-triplet state.

In the conventional BCS programme, the next step would be to restrict the Hamiltonian to interactions between singlet pairs. In view of the Rashba spin-mixing, however, it is clear that this would not capture the right pairing physics and that it is natural to consider pairs within the same helicity band at zero total momentum. At zero magnetic field, the pairing is expected to be intraband [118, 119]. This is in line with the prescription of time-reversed pairing due to Anderson [120], who suggested that even in non-magnetic disordered systems with broken translation symmetry, one can carry out BCS theory using pairs formed from time-reversed eigenstates. In our case, it is spin rather than momentum that is not a good quantum number, but the same reasoning applies such that $c_{\mathbf{k}s}$ should be matched with its time-reversed partner $-s e^{i\theta(\boldsymbol{k})} c_{-\mathbf{k}s}$. We then carry out BCS theory on the corresponding mean field $b_{\boldsymbol{k}s} \equiv s e^{i\theta(\boldsymbol{k})} \langle c_{-\boldsymbol{k}s} c_{\boldsymbol{k}s} \rangle$

in Appendix G.2, which results in the gap equation

$$\Delta_{\boldsymbol{k}s} = -\frac{1}{2N}\sum_{\boldsymbol{k}'s'} V_{ss'}(\boldsymbol{k},\boldsymbol{k}')\Delta_{\boldsymbol{k}'s'} g_{\boldsymbol{k}s}, \tag{7.12}$$

where $g_{\boldsymbol{k}s} \equiv \frac{1}{2E_{\boldsymbol{k}s}}(1-f(E_{\boldsymbol{k}s}))$, $f(E)$ is the Fermi function, and the interaction $V_{ss'}(\boldsymbol{k},\boldsymbol{k}')$ is given in Eq. (G.32).

7.2 Gap equations

The self-consistency condition (7.12) determines the ansatz for $\bar{\Delta}_{\boldsymbol{k}s} \equiv se^{i\theta(\boldsymbol{k})}\Delta_{\boldsymbol{k}s}$:

$$\bar{\Delta}_{\boldsymbol{k}s} = \Delta^0 + \Delta^s s_{\boldsymbol{k}} + \Delta^{x-y} s\sqrt{\sin^2 k_x + \sin^2 k_y}, \tag{7.13}$$

where $s_{\boldsymbol{k}} \equiv \frac{1}{2}(\cos k_x + \cos k_y)$ denotes the extended s-wave part of the gap. Note that while the gap parameter definitively has the full s-wave symmetry of the lattice, it will always be mixed singlet-triplet, unlike in conventional BCS theory. With this ansatz, the self-consistency condition yields three coupled equations:

$$\Delta^0 = -\frac{1}{2N}\sum_{\boldsymbol{k}'s'}\left(U + 8\Delta t s_{\boldsymbol{k}'} - 4\frac{\Delta t}{t}V_{\mathrm{SO}}s'\sqrt{\sin^2 k'_x + \sin^2 k'_y}\right) g_{\boldsymbol{k}'s'}\bar{\Delta}_{\boldsymbol{k}'s'} \tag{7.14}$$

$$\Delta^s = -\frac{1}{2N}\sum_{\boldsymbol{k}'s'} 8\Delta t g_{\boldsymbol{k}'s'}\bar{\Delta}_{\boldsymbol{k}'s'} \tag{7.15}$$

$$\Delta^{x-y} = \frac{1}{2N}\sum_{\boldsymbol{k}'s'} 4\frac{\Delta t}{t}V_{\mathrm{SO}} g_{\boldsymbol{k}'s'}\bar{\Delta}_{\boldsymbol{k}'s'}. \tag{7.16}$$

Equations (7.15) and (7.16) reveal that there are in fact only two independent parameters since

$$\Delta^{x-y} = -\frac{V_{\mathrm{SO}}}{2t}\Delta^s. \tag{7.17}$$

This also means that the gap function is a linear function of the kinetic energy, since

$$\bar{\Delta}_{\boldsymbol{k}s} = \Delta^0 + \Delta^s\left(s_{\boldsymbol{k}} - \frac{sV_{\mathrm{SO}}}{2t}\sqrt{\sin^2 k_x + \sin^2 k_y}\right) \tag{7.18}$$

$$= \Delta^0 - \Delta^s\epsilon_{\boldsymbol{k}s}/(4t), \tag{7.19}$$

where $\epsilon_{\boldsymbol{k}s} \equiv -2t(\cos k_x + \cos k_y) + 2sV_{\rm SO}\sqrt{\sin^2 k_x + \sin^2 k_y}$ is the single-particle energy in the normal state. This energy dependence is in stark contrast with that of the constant gap found in conventional BCS theory. In the context of electron tunnelling, it will cause an energy dependence in the conductance, independent of the density of states. This is seen as an asymmetry in the tunnelling current for bias voltages of different sign [105, 121]. This asymmetry would be slightly enhanced by spin-orbit coupling, though the enhancement should diminish with increasing U, according to Fig. 7.1. We can check this prediction through a simple model of tunnelling from a normal Rashba metal (N) to Rashba superconductor (SC) through an insulating barrier. Assuming a constant tunnelling probability $|T|^2$, the tunnelling current as a function of bias voltage V (defined by the difference between the chemical potential of the metal and that of the superconductor) is given by

$$I = -e\sum_{\boldsymbol{k}s}\sum_{\boldsymbol{k}'s'}|T|^2\int_{-\infty}^{\infty}\frac{d\omega}{2\pi}A_s^{\rm N}(\boldsymbol{k},\omega)A_{s'}^{\rm SC}(\boldsymbol{k}',\omega+eV)[f(\omega+eV)-f(\omega)], \tag{7.20}$$

where $A_s^{\rm N}(\boldsymbol{k},\omega)$ is the spectral function of the normal Rashba metal and $A_s^{\rm SC}(\boldsymbol{k},\omega)$ is the spectral function of the superconductor. Let us assume that the density of states has an approximately constant value g at the Fermi level of the metal, which is a good approximation away from half-filling and the band edges (see Fig. 1.4). In that case, the tunneling current is

$$I = -2\pi e|T|^2 g^2 \mathcal{V}^{\rm N}\mathcal{V}^{\rm SC}\int_{-\infty}^{\infty}d\omega\frac{N^{\rm SC}(\omega)}{g}[f(\omega+eV)-f(\omega)], \tag{7.21}$$

where $\mathcal{V}^{\rm N}$ and $\mathcal{V}^{\rm SC}$ are the volumes of the metal and superconductor respectively. The superconducting density of states $N^{\rm SC}(\omega)$, is derived in Appendix G. This gives the differential conductance

$$\frac{dI}{dV} \propto \frac{e^2}{\hbar}\int_{-\infty}^{\infty}d\omega\frac{N^{\rm SC}(\omega)}{g}\frac{df(\omega+eV)}{d(eV)}, \tag{7.22}$$

where we have ignored the dimensionless proportionality constant $-2\pi|T|^2 g^2\mathcal{V}^{\rm N}\mathcal{V}^{\rm SC}$, and restored $\hbar$. The integral may be computed numerically.

The linearized version (small gap function) of the self-consistency equations is a 3×3 determinant equation that determines the critical temperature. Due to the presence of the chemical potential in the Fermi function we fix the density and simultaneously solve

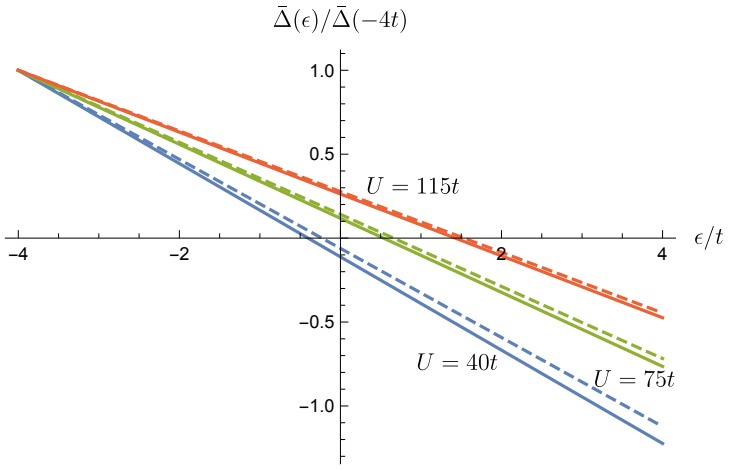

FIGURE 7.1: Low temperature gap dependence on kinetic energy for various values of U. Recall that U is measured with respect to the renormalized hopping ($t \sim 0.1t'$ in the high electron density regime), which is why we consider such large values. Here we have set $\Delta t = 4.5t$, $n = 1.875$, $k_B T = 0.01t$. The solid lines correspond to $V_{\mathrm{SO}} = 0.5t$. The dashed lines show the result for $V_{\mathrm{SO}} = 0$. A slightly larger value for the absolute value of the slope indicates that V_{SO} increases the asymmetry around the Fermi level.

the number equation

$$n = 1 - \frac{1}{2N} \sum_{\boldsymbol{k}'s'} \frac{(\epsilon_{\boldsymbol{k}'s'} - \mu)}{E_{\boldsymbol{k}'s'}} \tanh(\beta E_{\boldsymbol{k}'s'}/2). \tag{7.23}$$

Note that in the absence of spin-orbit coupling, Δ^{x-y} vanishes, and this problem reduces to three coupled equations which have been solved in Ref. [105]. The determinant and number equations are solved together iteratively. That is, we iterate over temperatures until the determinant equation is satisfied, and for each temperature, the chemical potential is found from the number equation. The same strategy can be used to solve for the gap function below T_c.

7.3 Results

Fig. 7.2 shows the critical temperature T_c as a function of electron density for the attractive Hubbard model with correlated hopping turned off ($U < 0$, $\Delta t = 0$). We see that except at very low ($n \to 0$) and high ($n \to 2$) densities where the singular density of states becomes important, increasing the spin-orbit coupling has the effect of decreasing the critical temperature. This is understood by noting that the available phase space for intra-band pairs is reduced by the presence of spin-orbit coupling except at the bottom

and top of the band where all states are of the same helicity and the density of states becomes singular. Recall that the density of states is lower for the $s = -$ ($s = +$) band in the electron (hole) doped part of the band. Indeed, half-filling, which would have the highest T_c in the absence of spin-orbit coupling, shows a dip due to the minimum (see Fig. 1.4) in the density of states.

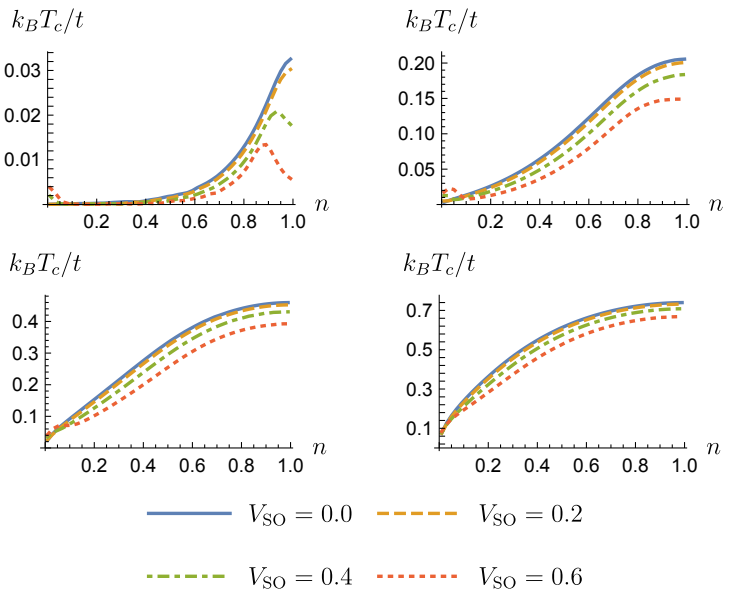

FIGURE 7.2: Critical temperature as a function of electron density for various values of the spin-orbit coupling measured in units of t with $\Delta t = 0$. $U = -t$ (top left), $U = -2t$ (top right), $U = -3t$ (bottom left), and $U = -4t$ (bottom right). By particle-hole symmetry, the plot above half-filling is a reflection of this plot, i.e. $T_c(2 - n) = T_c(n)$ for $0 < n < 1$.

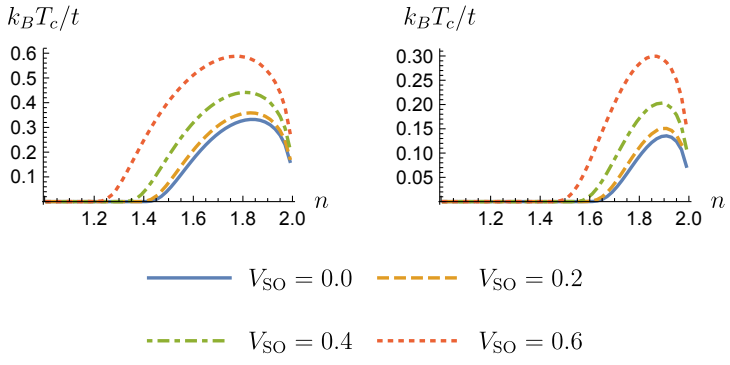

FIGURE 7.3: Critical temperature as a function of electron density for various values of the spin-orbit coupling measured in units of t with $\Delta t = 4.5t$. $U = 90t$ (left), $U = 115t$ (right).

Figs. 7.3 and 7.4 show a very different effect. Here correlated hopping has been turned on

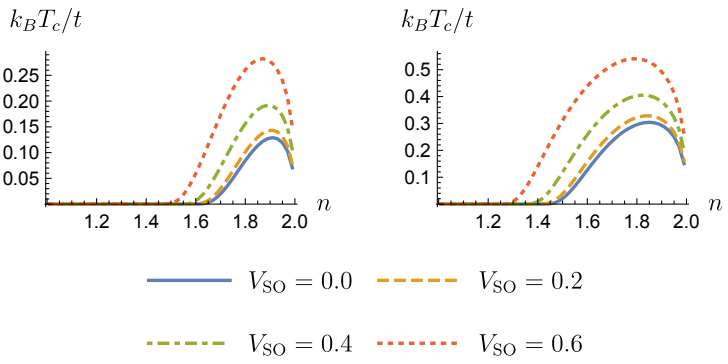

FIGURE 7.4: Critical temperature as a function of electron density for various values of the spin-orbit coupling with $U = 75t$. $\Delta t = 3.5t$ (left), $\Delta t = 4t$ (right).

and we now consider repulsive interactions ($U > 0$, $\Delta t \neq 0$). The presence of correlated hopping is crucial to get superconductivity with a repulsive U. The superconducting instability in this case is primarily driven by kinetic energy instead of local attraction since the order parameter increases with kinetic energy. A non-zero Δt breaks particle-hole symmetry, and we see that the Rashba spin-orbit coupling and correlated hopping cooperate to enhance the critical temperature in the high electron (low hole) density regime. This too follows from the single-particle density of states. The spin-orbit coupling and correlated hopping couple to produce an effective interaction whose sign is opposite the sign of the helicity band [see the last line of Eq. (G.32)]. At high electron densities, the $s = -$ density of states is suppressed, and the $s = +$ density of states increases towards the singularity at the top of the band. Thus, the pair interaction becomes dominantly attractive and its magnitude increases with V_{SO} and Δt. In fact the maximum value of the critical temperature shows a quadratic dependence on the spin-orbit coupling as seen in Fig. 7.5.

The gap and number equations are solved at finite temperature as well. Temperature profiles of the gap components are shown in Figs. 7.6, 7.7 without and with correlated hopping respectively. We can check the ratio of the quasiparticle energy gap to the critical temperature as well. Due to the energy dependence of the gap, it is more appropriate to use the minimum value of the excitation energy. This occurs when

$$\epsilon_{\boldsymbol{k}s} = \frac{\mu + \Delta^0 \frac{\Delta^s}{4t}}{1 + (\frac{\Delta^s}{4t})^2}, \tag{7.24}$$

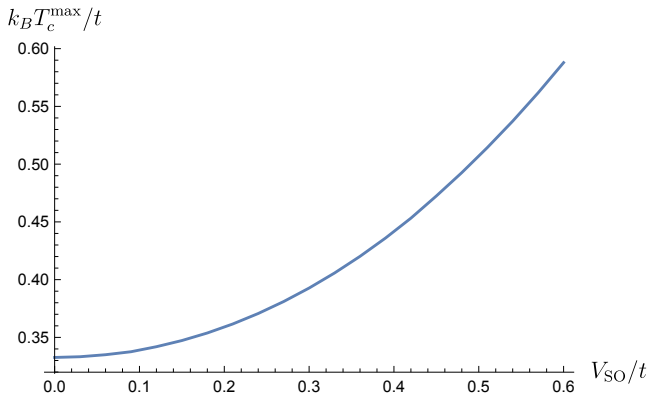

FIGURE 7.5: Maximum critical temperature as a function of spin-orbit coupling with $U = 90t$, $\Delta t = 4.5t$.

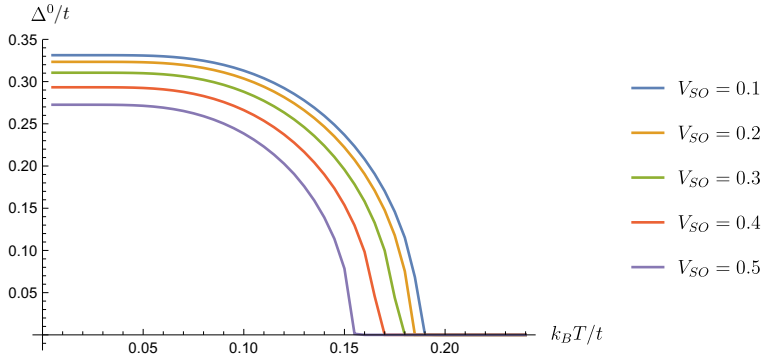

FIGURE 7.6: Gap function vs temperature for different values of the Rashba coupling. Here $U = -2t$, $\Delta t = 0$, and $n = 0.8$.

Recall that the chemical potential is renormalized by the gap via Eq. (7.23). Here we consider weak coupling where μ remains within the band. For strong coupling, μ can move outside the band. In that case one should take ϵ_{ks} to be the value at the band edge.

The excitation energy evaluated at (7.24) is

$$E_{\min} = \frac{|\Delta^0 - \mu \frac{\Delta^s}{4t}|}{\sqrt{1 + (\frac{\Delta^s}{4t})^2}}. \tag{7.25}$$

This value is plotted in Fig. 7.8 along with the gap ratio. We see that for these parameter values, the spin-orbit coupling introduces very little deviation from the BCS gap ratio value of 3.52 [86].

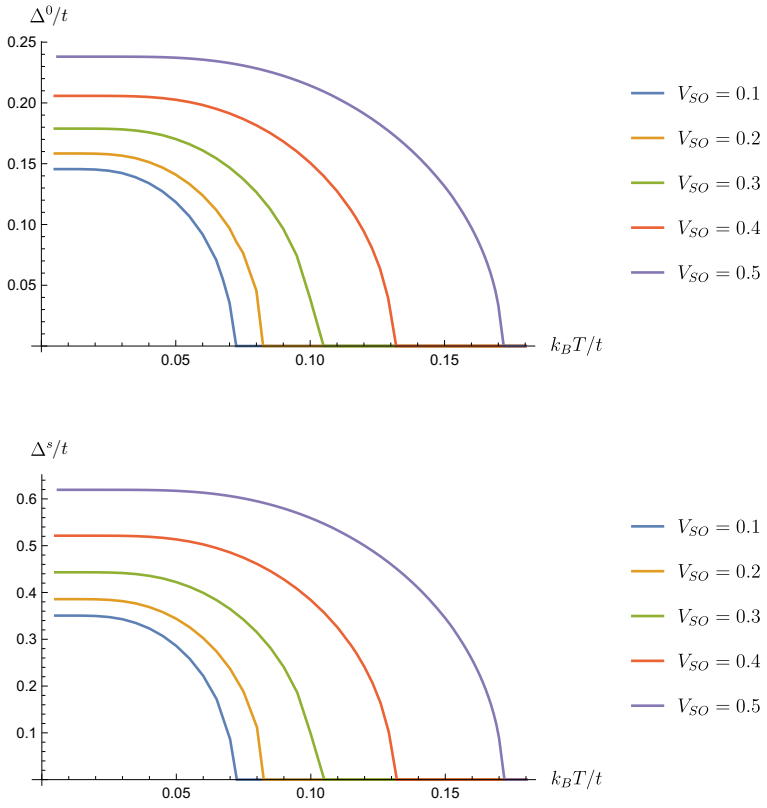

FIGURE 7.7: Δ_0 (top) and Δ_s (bottom) components of the gap function vs temperature for different values of the Rashba coupling in units of t. Here $U = 115t$, $\Delta t = 4.3t$, and $n = 1.85$.

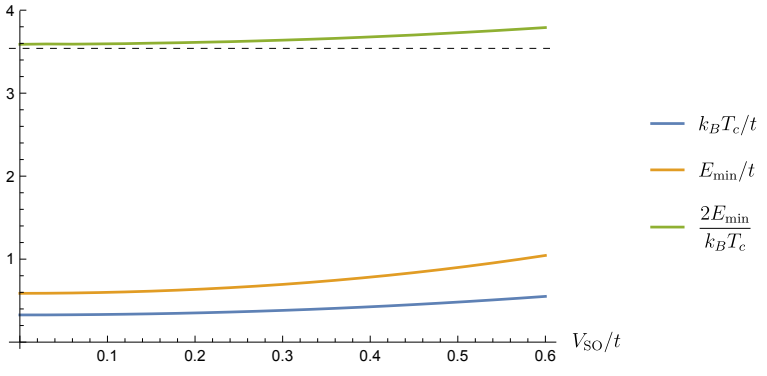

FIGURE 7.8: Critical temperature, $E_{\min}$, and the corresponding gap ratio at low temperature as a function of spin-orbit coupling. Here we have set $U = 90t$, $\Delta t = 4.5t$, $n = 1.875$, $k_BT = 0.01t$. The dashed line shows the conventional BCS value.

Finally, we compute the voltage-dependence of the differential conductance, i.e., the right-hand-side of Eq. (7.22), approximating the normal-state density of states as a constant g within the band : $g(\omega) = g[\Theta(\omega + 4t) - \Theta(\omega - 4t)]$, where $\Theta(\omega)$ is the Heaviside-theta function. The full energy-dependent density of states will induce additional asymmetries, but here we just wish to see the effect of the kinetic-energy dependent gap function, so we focus on the regime away from the van Hove singularities, where this approximation is valid. The result is shown in Fig. 7.9 as a function of bias voltage V. We see a significant asymmetry, both in the magnitude of the energy gap on either side of $V = 0$ and in the coherence peaks. These asymmetries increase with the spin-orbit coupling as predicted.

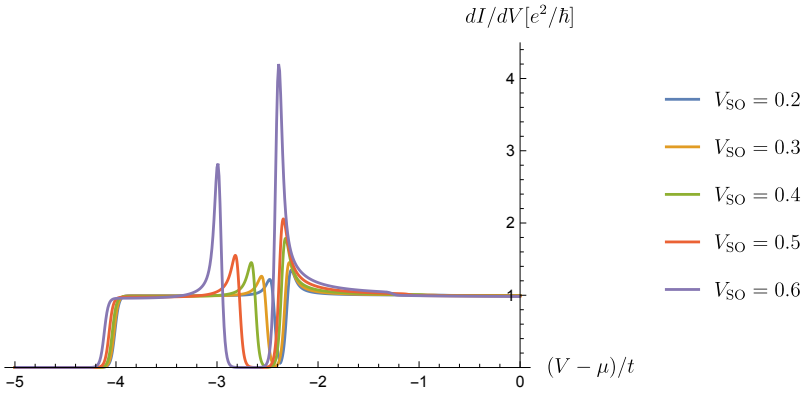

FIGURE 7.9: Dependence of the differential conductance (normalized as in Eq. (7.22)) on bias voltage for a metal-superconductor junction for different values of the Rashba coupling in units of t. Here $U = 105t$, $\Delta t = 4.3t$, $n = 1.7$, and the temperature is $k_B T = 0.02t$. At small Rashba coupling, the conductance does not appear to reach zero. This is simply because the fixed temperature used in this plot becomes a significant fraction of T_c at low Rashba coupling.

7.4 Discussion

We have shown that within a 2D tight-binding model on a square lattice, correlated hopping and Rashba spin-orbit coupling work together to enhance the critical temperature of superconductivity even with significant repulsive on-site interactions. This may explain the experimental findings of Ref. [110, 122] where the authors report that the strength of the spin-orbit interaction in the $LaAlO_3/SrTiO_3$ interface tracks the magnitude of T_c across the superconducting dome. This behaviour is in contrast to the Rashba model with attractive on-site interactions and no correlated hopping, where the

spin-orbit coupling inhibits superconductivity. Thus, correlated hopping may play an important role in this system. Our analysis was done within a mean-field treatment of the model assuming Cooper pairs to form within the same helicity band of the non-interacting Rashba spectrum.

The enhancement is strongest in the high electron-density regime. This is relevant for the cuprates at low hole doping, where the oxygen p-band is nearly full. Rashba spin-splitting is expected to be present in many cuprates, though its magnitude is likely much smaller than the values considered in this chapter.

The superconducting gap for this model is thermodynamically similar to the gap in conventional BCS theory in the sense that the ratio of the minimum quasiparticle energy to T_c is very close to the BCS value. However, the broken particle-hole symmetry of our model will produce a spin-orbit-coupling dependent tunnelling asymmetry in a metal-superconductor junction not seen in conventional BCS theory [105, 121].

In this chapter, we have focused on the magnitude of the superconducting gap, as this correlates with the critical temperature. However, it is interesting to look at the symmetry of the gap function as well. This will be the focus of the next chapter. The gap in the model presented here has an extended s-wave symmetry, but if one considers a model with nearest-neighbour interaction, the gap symmetries will be enriched by the presence of additional d-wave phases (see Fig. 6.1). These are not the symmetries of the full gap function, but rather the part that transforms under irreps of the lattice point group ($\bar{\Delta}_{\boldsymbol{k}s}$). In particular, the gap carries an additional complex phase ($se^{-i\theta(\boldsymbol{k})}$) due to the spin-orbit coupling. It is an important open question as to whether this phase is observable, though it has been shown that it will not contribute to the Josephson effect [123].

Chapter 8

Superconducting order parameter symmetry

In this chapter, we focus on superconductivity within tight-binding models that include a nearest-neighbour interaction (third term in Table 6.1). In reality, the Coulomb interaction is long-range (though this range is reduced by screening). As a result, the Hubbard model with only on-site interaction may not be a qualitatively accurate description of most materials. For example, the addition of an interaction that is not on-site has important consequences because it allows the gap function to have symmetries beyond s-wave, such as d-wave and triplet p-wave. Indeed, the fact that so many unconventional superconductors have been observed is an indication that we need to understand the impact of electron-electron interactions that go beyond the on-site model [82]. As we will see, the landscape below T_c becomes even more rich as a result, with order parameters that include mixtures of different symmetries.

8.1 Extended Hubbard model critical temperature

In this chapter we drop the correlated hopping term and study the extended Hubbard model:

$$H = -t \sum_{\substack{\langle i,j \rangle \\ \sigma}} \left(c^\dagger_{i\sigma} c_{j\sigma} + c^\dagger_{j\sigma} c_{i\sigma} \right) + U \sum_i n_{i\uparrow} n_{i\downarrow} + V \sum_{\substack{\langle ij \rangle \\ \sigma,\sigma'}} n_{i\sigma} n_{j\sigma'} - \mu \sum_{i,\sigma} n_{i\sigma}. \tag{8.1}$$

Pairing can occur within any spin channel, so the order parameter is a 2×2 matrix $\Delta_{\alpha\beta}$, which we will express in terms of singlet and triplet components (see Eqs. (G.23), (G.24), (G.25), (G.26)). Within mean-field theory, this model produces the following self-consistent gap equations derived in Appendix G:

$$\Delta_{\boldsymbol{k}}^{\text{sing}} = -\frac{1}{N}\sum_{\boldsymbol{k}'}[U + 4V(s_{\boldsymbol{k}}s_{\boldsymbol{k}'} + d_{\boldsymbol{k}}d_{\boldsymbol{k}'})]\Delta_{\boldsymbol{k}'}^{\text{sing}} g_{\boldsymbol{k}'}, \tag{8.2}$$

$$\Delta_{\boldsymbol{k}}^{\lambda} = -\frac{1}{N}\sum_{\boldsymbol{k}'} 2V(\sin k_x \sin k_x' + \sin k_y \sin k_y')\Delta_{\boldsymbol{k}'}^{\lambda} g_{\boldsymbol{k}'}. \tag{8.3}$$

Here $\Delta_{\boldsymbol{k}}^{\text{sing}}$ represents the gap function involving pairing in the singlet channel, $\Delta_{\boldsymbol{k}}^{\lambda}$ (with $\lambda = x, y, z$) involve pairing in the triplet channels, and we have used the s-wave and d-wave basis functions $s_{\boldsymbol{k}} \equiv \frac{1}{2}(\cos k_x + \cos k_y)$, $d_{\boldsymbol{k}} \equiv \frac{1}{2}(\cos k_x - \cos k_y)$. As in the previous chapter, we have defined $g_{\boldsymbol{k}} \equiv \frac{1}{2E_{\boldsymbol{k}}}(1 - 2f(E_{\boldsymbol{k}}))$ and the quasi-particle spectrum is $E_{\boldsymbol{k}} = \sqrt{\xi_{\boldsymbol{k}}^2 + |\Delta_{\boldsymbol{k}}|^2}$, where $|\Delta_{\boldsymbol{k}}|^2 = |\Delta_{\boldsymbol{k}}^{\text{sing}}|^2 + \sum_\lambda |\Delta_{\boldsymbol{k}}^{\lambda}|^2$.

The $\boldsymbol{k}$-dependence of Eqs. (8.2) and (8.3) determines the appropriate ansatz for the gap functions:

$$\Delta_{\boldsymbol{k}}^{\text{sing}} = \Delta_0 + \Delta_s s_{\boldsymbol{k}} + \Delta_d d_{\boldsymbol{k}}, \tag{8.4}$$

$$\Delta_{\boldsymbol{k}}^{\lambda} = \Delta_x^{\lambda} \sin k_x + \Delta_y^{\lambda} \sin k_y. \tag{8.5}$$

These components satisfy the following gap equations:

$$\Delta_0 = -\frac{U}{N}\sum_{\boldsymbol{k}'} g_{\boldsymbol{k}'}(\Delta_0 + \Delta_s s_{\boldsymbol{k}'} + \Delta_d d_{\boldsymbol{k}'}), \tag{8.6}$$

$$\Delta_s = -\frac{4V}{N}\sum_{\boldsymbol{k}'} s_{\boldsymbol{k}'} g_{\boldsymbol{k}'}(\Delta_0 + \Delta_s s_{\boldsymbol{k}'} + \Delta_d d_{\boldsymbol{k}'}), \tag{8.7}$$

$$\Delta_d = -\frac{4V}{N}\sum_{\boldsymbol{k}'} d_{\boldsymbol{k}'} g_{\boldsymbol{k}'}(\Delta_0 + \Delta_s s_{\boldsymbol{k}'} + \Delta_d d_{\boldsymbol{k}'}), \tag{8.8}$$

$$\Delta_x^{\lambda} = -\frac{2V}{N}\sum_{\boldsymbol{k}'} \sin k_x'(\Delta_x^{\lambda} \sin k_x' + \Delta_y^{\lambda} \sin k_y') g_{\boldsymbol{k}'}, \tag{8.9}$$

$$\Delta_y^{\lambda} = -\frac{2V}{N}\sum_{\boldsymbol{k}'} \sin k_y'(\Delta_x^{\lambda} \sin k_x' + \Delta_y^{\lambda} \sin k_y') g_{\boldsymbol{k}'}. \tag{8.10}$$

First we consider the situation near T_c where all gap components are small. If we linearize the above equations about $\Delta = 0$, then the function $g_{\boldsymbol{k}'}$ no longer depends on the gap, and the symmetry of the lattice ensures that most of these equations decouple

$$\Delta_0 = -\frac{U}{N}\sum_{\boldsymbol{k}'} g_{\boldsymbol{k}'}(\Delta_0 + \Delta_s s_{\boldsymbol{k}'}), \tag{8.11}$$

$$\Delta_s = -\frac{4V}{N}\sum_{\boldsymbol{k}'} s_{\boldsymbol{k}'} g_{\boldsymbol{k}'}(\Delta_0 + \Delta_s s_{\boldsymbol{k}'}), \tag{8.12}$$

$$1 = -\frac{4V}{N}\sum_{\boldsymbol{k}'} d^2_{\boldsymbol{k}'} g_{\boldsymbol{k}'}, \tag{8.13}$$

$$1 = -\frac{2V}{N}\sum_{\boldsymbol{k}'} \sin^2 k'_x g_{\boldsymbol{k}'} = -\frac{2V}{N}\sum_{\boldsymbol{k}'} \sin^2 k'_y g_{\boldsymbol{k}'}. \tag{8.14}$$

We see that the gap equations decouple into three different sets of equations that correspond to the s-wave, d-wave and p-wave phases (Eqs. (8.11) + (8.12), Eq. (8.13), and Eq. (8.14) respectively). In general, each irrep of the lattice point group will have a corresponding T_c equation provided there is a part of the interaction that transforms under this irrep.

Unlike the d-wave case, the linearized s-wave gap equations can have two eigenvalues in some parts of the parameter space and therefore two critical temperatures. In Fig. 8.1, we show the phase diagram in the U-V plane based solely on the critical temperatures determined by solving the linearized gap equations. In the positive U regime, there is competing spin-density wave order that we do not consider here [91]. The p-wave (triplet) portion of the phase diagram only exists at small $|V|$ and this region diminishes with increasing electron density, vanishing at half-filling. Often, this diagram is taken to give the symmetry of the order parameter below T_c. However, we will see that the true phase diagram is much richer when we take into account the temperature dependence of the gap.

For the sake of generality, we may rewrite the gap function as

$$\Delta^{\text{sing}}_{\boldsymbol{k}} = \sum_{i\in\{0,s,d\}} \Delta_i x^i_{\boldsymbol{k}}; \quad \Delta^{\lambda}_{\boldsymbol{k}} = \sum_{i\in\{x,y\}} \Delta^{\lambda}_i x^i_{\boldsymbol{k}} \tag{8.15}$$

where the basis functions $x^i_{\boldsymbol{k}}$ are: $x^0_{\boldsymbol{k}} = 1$, $x^s_{\boldsymbol{k}} = s_{\boldsymbol{k}}$, $x^d_{\boldsymbol{k}} = d_{\boldsymbol{k}}$, $x^x_{\boldsymbol{k}} = \sin k_x$, $x^y_{\boldsymbol{k}} = \sin k_y$. Such a decomposition can be made for any separable interaction and makes the expressions in the next section valid for many models beyond the extended Hubbard

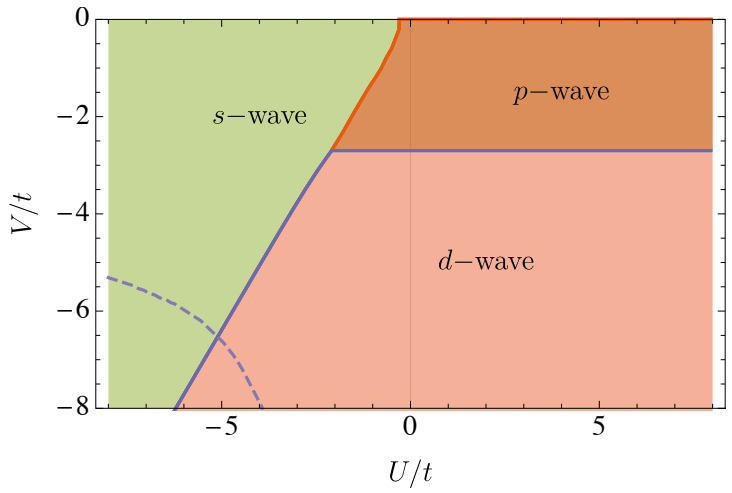

FIGURE 8.1: Phase diagram based on T_c for electron density $n = 0.5$. There are two s-wave solutions to the lower left of the dashed purple line, and one s-wave solution to the upper right.

model. From Table A.7, note that $x^0_{\boldsymbol{k}}$ and $x^s_{\boldsymbol{k}}$ belong to one irrep of the square lattice point group (A_1), while $x^d_{\boldsymbol{k}}$ belongs to B_1 and ($x^x_{\boldsymbol{k}}$, $x^y_{\boldsymbol{k}}$) belong to E. For the singlet part, this means that Eqs. (8.6) and (8.7) decouple from (8.8) whenever $\Delta_d = 0$ or $\Delta_0 = \Delta_s = 0$. We refer to such solutions as pure solutions, and reserve "mixed solutions" for any case where components from multiple *different* irreps are non-zero.

8.2 Free energy

This model has several components of the gap function with different symmetries. The natural question to ask is which of these symmetries would be observed for a given value of the parameters U, V [1] and electron density n? The answer is whatever minimizes the Helmholtz free energy density. Note that we defined the Hamiltonian in the grand canonical ensemble, but we will work exclusively at fixed electron density. Therefore it is the free energy density $f = \Omega/N + \mu n$ and not the grand potential density Ω/N that must be minimized. Within mean-field theory, this value is easily determined. Combining the quasi-particle energy density with the ground state energy density (see

[1] Originally, we had imagined altering the values of U and V as a function of temperature, so that the symmetry choice at T_c would almost certainly be overturned as the temperature was lowered. Such temperature-dependent coupling parameters could be argued to occur for a variety of physical reasons. In any event, as we discovered, these transitions occur even if U and V are held constant as a function of temperature.

Eqs. (G.17), (G.19)) yields the internal energy density:

$$u = \frac{2}{N}\sum_{\mathbf{k}} E_{\mathbf{k}} f(E_{\boldsymbol{k}}) + \frac{1}{N}\sum_{\mathbf{k}}\left(\xi_{\mathbf{k}} - E_{\mathbf{k}} + \frac{|\Delta_{\mathbf{k}}|^2}{2E_{\mathbf{k}}}\left(1 - 2f\left(E_{\mathbf{k}}\right)\right)\right) + \mu n. \tag{8.16}$$

In mean field theory, the entropy density is that of a free Fermi gas:

$$s = -\frac{2k_B}{N}\sum_{\mathbf{k}}\left[\left(1 - f(E_{\boldsymbol{k}})\right)\ln\left(1 - f(E_{\boldsymbol{k}})\right) + f(E_{\boldsymbol{k}})\ln f(E_{\boldsymbol{k}})\right]. \tag{8.17}$$

Combining these produces the mean-field free energy density $f_{\mathrm{MF}} = u - Ts$:

$$f_{\mathrm{MF}} \;=\; \frac{1}{N}\sum_{\boldsymbol{k}}\left(\xi_{\boldsymbol{k}} - E_{\boldsymbol{k}} + |\Delta_{\boldsymbol{k}}|^2 g_{\boldsymbol{k}}\right) + \frac{2k_{\mathrm{B}}T}{N}\sum_{\boldsymbol{k}}\ln(1 - f(E_{\boldsymbol{k}})) + \mu n. \tag{8.18}$$

f_{MF} gives the correct value of the free energy at the solutions to the gap equation, i.e. its critical points, but it is not the correct functional to minimize in order to obtain these critical points. That functional comes from the finite temperature variational theorem [124]

$$f \leq f[\Delta_{\boldsymbol{k}}] \equiv f_{\mathrm{MF}} + \langle H - H_{\mathrm{MF}}\rangle_{\mathrm{MF}}, \tag{8.19}$$

where the mean-field Hamiltonian H_{MF} is given in Eq. (G.7). Of course, if we know the solutions to the gap equation, we can simply plug them into f_{MF} and compare the resulting free energies, but it will prove fruitful to work with the variational free energy $f[\Delta_{\boldsymbol{k}}]$. Here, the mean-field expectation of an operator X is given by

$$\langle X\rangle_{\mathrm{MF}} \equiv \frac{1}{Z_{\mathrm{MF}}}\operatorname{Tr} e^{-\beta H_{\mathrm{MF}}} X. \tag{8.20}$$

We must compute

$$\langle H - H_{\mathrm{MF}}\rangle_{\mathrm{MF}} \;=\; \frac{1}{2N}\sum_{\boldsymbol{k}\boldsymbol{k}'}\sum_{\alpha\beta\gamma\delta} V_{\alpha\beta\gamma\delta}(\boldsymbol{k},\boldsymbol{k}')\langle c^\dagger_{\boldsymbol{k}\alpha} c^\dagger_{-\boldsymbol{k}\beta} c_{-\boldsymbol{k}'\gamma} c_{\boldsymbol{k}'\delta}\rangle_{\mathrm{MF}} + \frac{1}{N}\sum_{\boldsymbol{k}}|\Delta_{\boldsymbol{k}}|^2 g_{\boldsymbol{k}}. \tag{8.21}$$

The trace of the quartic term is readily evaluated in the eigenbasis of H_{MF}. Using Wick's theorem and the fact that the occupation number distribution of the quasi-particles $\langle\gamma^\dagger_{\boldsymbol{k}\alpha}\gamma_{\boldsymbol{k}\alpha}\rangle$ is the Fermi function $f(E_{\boldsymbol{k}})$, we obtain the identity

$$\langle\gamma^\dagger_{\boldsymbol{k}\alpha}\gamma_{\boldsymbol{k}\beta}\gamma^\dagger_{\boldsymbol{k}'\gamma}\gamma_{\boldsymbol{k}'\delta}\rangle_{\mathrm{MF}} = \delta_{\alpha\beta}\delta_{\gamma\delta} f(E_{\boldsymbol{k}}) f(E_{\boldsymbol{k}'}), \tag{8.22}$$

Applying the Bogoliubov transformation (G.20), (G.21) and using this identity, we can evaluate the quartic term

$$\langle c^\dagger_{\boldsymbol{k}\alpha} c^\dagger_{-\boldsymbol{k}\beta} c_{-\boldsymbol{k}'\gamma} c_{\boldsymbol{k}'\delta}\rangle_{\mathrm{MF}} = \Delta^*_{\boldsymbol{k}\alpha\beta}\Delta_{\boldsymbol{k}'\delta\gamma} g_{\boldsymbol{k}} g_{\boldsymbol{k}'}. \tag{8.23}$$

The free energy functional follows from this,

$$\begin{aligned} f[\Delta_{\boldsymbol{k}}] &= \frac{2k_BT}{N}\sum_{\boldsymbol{k}} \ln(1-f(E_{\boldsymbol{k}})) + \frac{1}{N^2}\sum_{\boldsymbol{k}\boldsymbol{k}'} V^{\mathrm{sing}}(\boldsymbol{k},\boldsymbol{k}')\Delta^{\mathrm{sing}*}_{\boldsymbol{k}}\Delta^{\mathrm{sing}}_{\boldsymbol{k}'} g_{\boldsymbol{k}} g_{\boldsymbol{k}'} \\ &\quad + \frac{1}{N^2}\sum_{\boldsymbol{k}\boldsymbol{k}'}\sum_{\lambda} V^{\mathrm{trip}}(\boldsymbol{k},\boldsymbol{k}')\Delta^{\lambda *}_{\boldsymbol{k}}\Delta^{\lambda}_{\boldsymbol{k}'} g_{\boldsymbol{k}} g_{\boldsymbol{k}'} + \frac{1}{N}\sum_{\boldsymbol{k}}(\xi_{\boldsymbol{k}} - E_{\boldsymbol{k}} + 2|\Delta_{\boldsymbol{k}}|^2 g_{\boldsymbol{k}}) + \mu n, \end{aligned} \tag{8.24}$$

where we have separated the interaction into its parity-even and odd parts:

$$V^{\mathrm{sing}}(\boldsymbol{k},\boldsymbol{k}') = U + 4V(s_{\boldsymbol{k}}s_{\boldsymbol{k}'} + d_{\boldsymbol{k}}d_{\boldsymbol{k}'}), \tag{8.25}$$

$$V^{\mathrm{trip}}(\boldsymbol{k},\boldsymbol{k}') = 2V(\sin k_x \sin k'_x + \sin k_y \sin k'_y). \tag{8.26}$$

Minimization of the free energy is an important problem that requires strict numerical control. The free energy is a nonlinear function of the gap components in a large-dimensional parameter space.[2] Ensuring that one has obtained the *global* minimum of this function is numerically difficult in a brute-force approach. In this regard, we have made use of the theory of Morse functions [125, 126, 126] to aid our numerical search for the global minimum. These details are included in Appendix H.

8.3 Extended Hubbard model at finite temperature

In this section, we focus on real, singlet order parameters to get an idea of the temperature-dependent behaviour of solutions to the gap equation. Coincident with this work, the authors of Ref. [127] studied the low-temperature phase diagram of this model including complex and triplet order parameters, and found significant regions in which either $p_x + ip_y$ (where the phase of Δ^λ_x and Δ^λ_y differ by $\pi/2$) dominates or $s + id$ (where the phase of Δ_s and Δ_d differ by $\pi/2$) dominates. It appears that only relative phases of 0 and $\pi/2$ between different gap components play any significant role. Indeed, looking at

[2] By "parameter space" we refer to the vector space spanned by the Δ_i components, not to be confused with the material parameters $\{U, V, n, T\}$.

Eqs. (8.6)-(8.8), we see that the Δ_0, Δ_s equations decouple from the Δ_d equation if the relative phase between these two sets of components is $\pi/2$. Likewise, Eqs. (8.9) and (8.10) decouple for $p_x + ip_y$. The advantage of our formulation is that we do not need to discretize the parameter space in order to find the global minimum of the free energy.

Regardless of which order parameters are considered, the most important feature one finds upon minimizing Eq. (8.24) is that there are regions of the phase diagram where a mixed solution takes over below T_c. An example of such a point is shown in Fig. 8.2. We find that for these parameters, the system starts as a d-wave superconductor at T_c^d, but attains a lower free energy upon the emergence of s-wave components at a lower temperature.

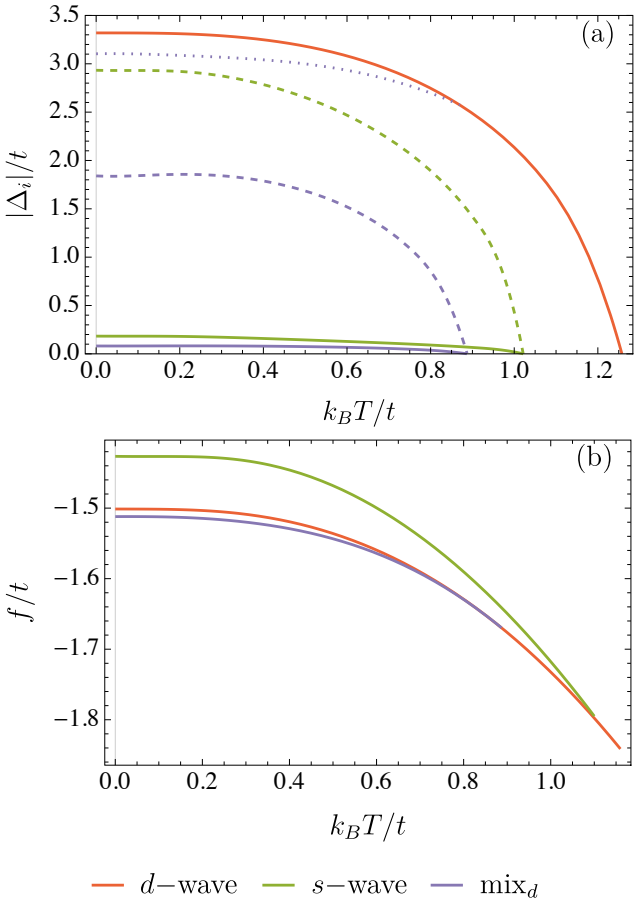

FIGURE 8.2: (a) Temperature dependence of the gap components for solutions at $U = -1.5$, $V = -6$, $n = 0.5$. The solid red line shows $|\Delta_d|/t$ for the d-wave solution. The s-wave solution (green) and the mixed solution (purple) have multiple components. In both cases, the solid lines show $|\Delta_0|/t$, the dashed lines show $|\Delta_s|/t$ and the dotted line shows $|\Delta_d|/t$. The label mix$_d$ denotes the fact that the mixed solution $(\Delta_0 + \Delta_s s_{\boldsymbol{k}} + \Delta_d d_{\boldsymbol{k}})$ emerges from the d-wave solution. (b) Free energy density computed from (8.18) for the same parameters and solutions.

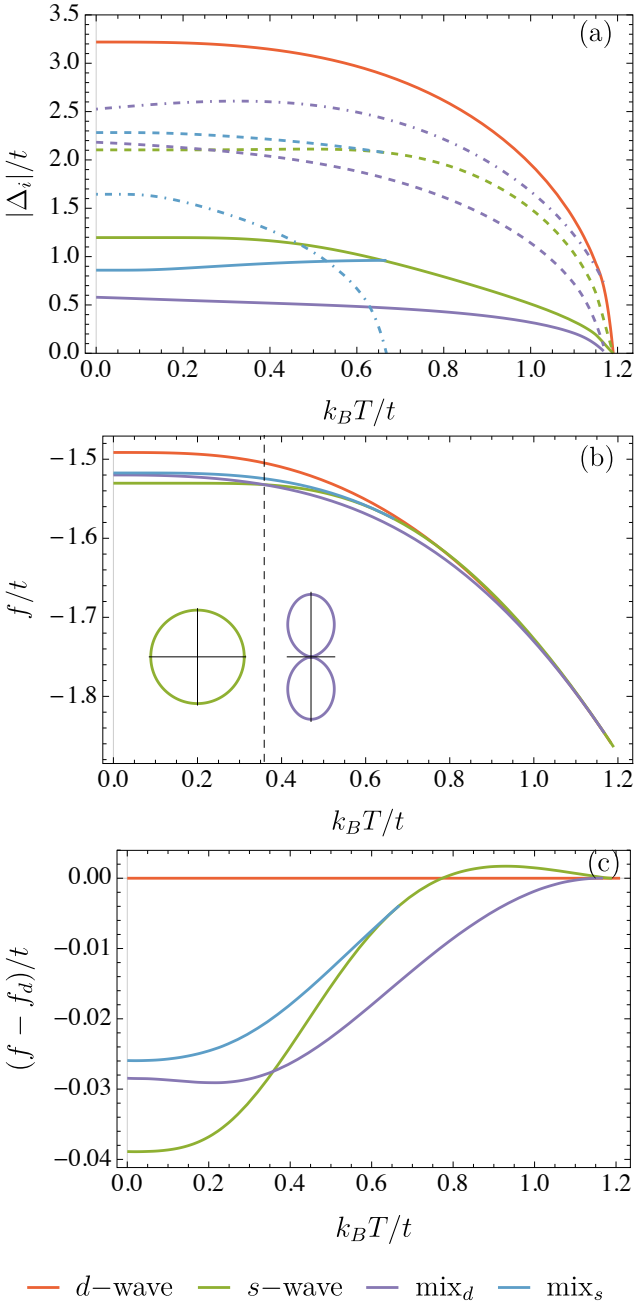

FIGURE 8.3: (a) Temperature dependence of the gap components for solutions at $U = -4.5$, $V = -5.85$, $n = 0.5$. The solid red line shows $|\Delta_d|/t$ for the d-wave solution. The s-wave solution (green) and the mixed solutions (purple and blue) have multiple components. In each case, the solid lines show $|\Delta_0|/t$, the dashed lines show $|\Delta_s|/t$ and the dot-dashed line shows $|\Delta_d|/t$. The label mix$_d$ denotes the fact that the mixed solution $(\Delta_0 + \Delta_s s_{\boldsymbol{k}} + \Delta_d d_{\boldsymbol{k}})$ emerges from the d-wave solution, while mix$_s$ means that mixed solution emerges from the s-wave solution. (b) Free energy density for the same parameters and solutions. The dashed line indicates the transition temperature between mix$_d$ and pure s-wave phases. The insets are polar plots of the gap on the fermi surface (defined by $\xi_{\boldsymbol{k}} = 0$) before and after the transition. (c) Free energy density measured with respect to the d-wave free energy density.

Fig. 8.3 shows a more unusual situation near the $T_c^s = T_c^d$ line. Here we see the development of two mixed solutions below T_c (purple and blue). The second mixed solution (mix_s) is a saddle point. Its emergence from the s-wave critical point allows the pure s-wave solution to become a minimum in accordance with the bifurcation rules discussed in Appendix H. Ultimately, this minimum has a lower free energy than the mix_d minimum at zero temperature. The inset of Fig. 8.3 (b) shows the angular dependence of the gap evaluated on the Fermi surface. In general, mixed gap functions can have zero, two, or four nodes depending on the Fermi level and the relative magnitude of the Δ_i's. In the particular case shown here, the mixed state appears p-wave like in that there are two nodes on the Fermi surface. However it is actually predominantly of extended s-wave type because there is no sign change around the Fermi surface. Note that the mixed state is four-fold degenerate, corresponding to the parameters $\pm(\Delta_0 + \Delta_s) \pm \Delta_d$, while here we only show one of the four possible states (the other polar plots are found by rotating this by $\pi/2$ and multiplying by a sign).

If these symmetry transitions occur in superconductors, they will have observable consequences. The specific heat per unit volume, $c_v = -T\frac{\partial^2 f_{\min}}{\partial T^2}$, will have an additional discontinuity below T_c due to the development of a mixed minimum in the free energy. In the case of a transition to a new pure state, as in Fig. 8.3, the specific heat would exhibit a singularity consistent with a first-order phase transition. This is shown in Fig. 8.4 with the parameter values corresponding to Fig. 8.3. The singularity is infinitesimally thin, but may be broadened by fluctuations and impurities [128].

With these examples, we see that the full temperature-dependent phase diagram is quite complicated. In general, there will be a large region in the $U - V$ plane where the superconductor starts with one pure symmetry at its critical temperature and undergoes a transition to a different symmetry at a lower temperature.

The density-dependence of these transitions is interesting as well. Half-filling is a special case. For $n = 1$, $\mu = 0$, the number equation (H.3) ensures that $\frac{1}{N}\sum_{\boldsymbol{k}} s_{\boldsymbol{k}} g_{\boldsymbol{k}} = 0$. As a result, the Δ_0 and Δ_s gap equations (8.6), (8.7) decouple for pure solutions, and the s-wave critical points move to the Δ_0 and Δ_s axes. There are then three pure solutions: on-site s-wave, nodal extended s-wave, and d-wave, while the mixed solutions are confined to the Δ_0-Δ_d and Δ_s-Δ_d planes.

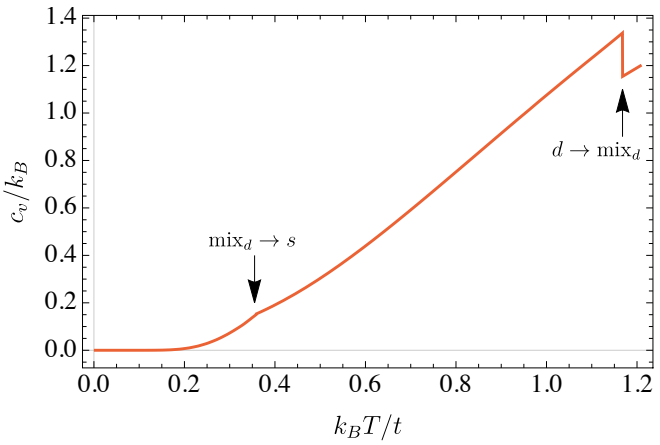

FIGURE 8.4: Temperature dependence of the specific heat at $U = -4.5$, $V = -5.85$, $n = 0.5$. There is a discontinuity (second-order transition) when the mixed state takes over from the d-wave state, and a singularity (first-order transition) when the s-wave state takes over from the mixed state. The singularity is a discontinuity in the entropy. Intriguingly, the derivative of the entropy is the same for both states at this temperature, so the singularity appears as a cusp in the specific heat.

8.4 Extended Rashba-Hubbard model critical temperature

Let us consider what happens when SOC is added to the extended Hubbard model:

$$\begin{aligned} H &= -t\sum_{\substack{\langle i,j\rangle \\ \sigma}}\left(c^\dagger_{i\sigma}c_{j\sigma}+c^\dagger_{j\sigma}c_{i\sigma}\right)+U\sum_i n_{i\uparrow}n_{i\downarrow}+V\sum_{\substack{\langle ij\rangle \\ \sigma,\sigma'}}n_{i\sigma}n_{j\sigma'}-\mu\sum_{i,\sigma}n_{i\sigma} \\ &\quad -\left[iV_{\text{SO}}\sum_{i,\alpha\beta}(c^\dagger_{i,\alpha}\sigma_x^{\alpha\beta}c_{i+\hat{y},\beta}-c^\dagger_{i,\alpha}\sigma_y^{\alpha\beta}c_{i+\hat{x},\beta})+h.c.\right]. \end{aligned} \tag{8.27}$$

As in Chapter 7, we will work in the Rashba basis and consider only intraband pairing, so that the order parameter is labeled by a single helicity index s. The derivation of the gap equation in mean-field theory proceeds exactly as in Appendix G, only with a modified interaction. We once again obtain the gap equation

$$\Delta_{\boldsymbol{k}s} = -\frac{1}{2N}\sum_{s'\boldsymbol{k}'}V_{ss'}(\boldsymbol{k},\boldsymbol{k}')\Delta_{\boldsymbol{k}'s'}g_{\boldsymbol{k}'s'}, \tag{8.28}$$

but now with

$$V_{ss'}(\boldsymbol{k},\boldsymbol{k}') \equiv ss'e^{i\theta(\boldsymbol{k}')}e^{-i\theta(\boldsymbol{k})}\Big[U+4V(s_{\boldsymbol{k}}s_{\boldsymbol{k}'}+d_{\boldsymbol{k}}d_{\boldsymbol{k}'}) +2Vss'\Big(\frac{(\sin k_x \sin k'_x+\sin k_y \sin k'_y)^2}{\sqrt{\sin^2 k_x+\sin^2 k_y}\sqrt{\sin^2 k'_x+\sin^2 k'_y}}\Big)\Big]. \tag{8.29}$$

The dependence on $\boldsymbol{k}$ and s determine the ansatz for the gap function:

$$\Delta_{\boldsymbol{k}s} \equiv se^{-i\theta(\boldsymbol{k})}\bar{\Delta}_{\boldsymbol{k}s}, \tag{8.30}$$

$$\bar{\Delta}_{\boldsymbol{k}s} = \sum_i \Delta_i x^i_{\boldsymbol{k}s}, \tag{8.31}$$

with the basis functions

$$x^0_{\boldsymbol{k}s} \equiv 1, \tag{8.32}$$

$$x^s_{\boldsymbol{k}s} \equiv s_{\boldsymbol{k}}, \tag{8.33}$$

$$x^{x-y}_{\boldsymbol{k}s} \equiv s\sqrt{\sin^2 k_x+\sin^2 k_y}, \tag{8.34}$$

$$x^d_{\boldsymbol{k}s} \equiv d_{\boldsymbol{k}}, \tag{8.35}$$

$$x^{x+y}_{\boldsymbol{k}s} \equiv s\frac{(\sin^2 k_x-\sin^2 k_y)}{\sqrt{\sin^2 k_x+\sin^2 k_y}}, \tag{8.36}$$

$$x^{xy}_{\boldsymbol{k}s} \equiv s\frac{\sin k_x \sin k_y}{\sqrt{\sin^2 k_x+\sin^2 k_y}}. \tag{8.37}$$

The first three basis functions are invariant under all operations of the square lattice point group D_4 and so represent the s-wave portion of the gap. The next two transform under the B_1 irrep and represent the $d_{x^2-y^2}$ portion. The last one, which was not seen in the absence of SOC transforms under B_2 and represents the d_{xy} portion of the gap.

The corresponding six gap equations are

$$\Delta_0 = -\frac{1}{2N}\sum_{\boldsymbol{k}'s'} U\Delta_{\boldsymbol{k}'s'}g_{\boldsymbol{k}'s'}, \tag{8.38}$$

$$\Delta_s = -\frac{1}{2N}\sum_{\boldsymbol{k}'s'} 4Vs_{\boldsymbol{k}'}\Delta_{\boldsymbol{k}'s'}g_{\boldsymbol{k}'s'}, \tag{8.39}$$

$$\Delta_{x-y} = -\frac{1}{2N}\sum_{\boldsymbol{k}'s'} Vs'\sqrt{\sin^2 k'_x + \sin^2 k'_y}\Delta_{\boldsymbol{k}'s'}g_{\boldsymbol{k}'s'}, \tag{8.40}$$

$$\Delta_d = -\frac{1}{2N}\sum_{\boldsymbol{k}'s'} 4Vd_{\boldsymbol{k}'}\Delta_{\boldsymbol{k}'s'}g_{\boldsymbol{k}'s'}, \tag{8.41}$$

$$\Delta_{x+y} = -\frac{1}{2N}\sum_{\boldsymbol{k}'s'} Vs'\left(\frac{\sin^2 k'_x - \sin^2 k'_y}{\sqrt{\sin^2 k'_x + \sin^2 k'_y}}\right)\Delta_{\boldsymbol{k}'s'}g_{\boldsymbol{k}'s'}, \tag{8.42}$$

$$\Delta_{xy} = -\frac{1}{2N}\sum_{\boldsymbol{k}'s'} 4Vs'\left(\frac{\sin k'_x \sin k'_y}{\sqrt{\sin^2 k'_x + \sin^2 k'_y}}\right)\Delta_{\boldsymbol{k}'s'}g_{\boldsymbol{k}'s'}. \tag{8.43}$$

$$\tag{8.44}$$

The linearized versions of these equations decouple into s, $d_{x^2-y^2}$ and d_{xy} eigenvalue equations for T_c. Defining $I_{i,j} \equiv \frac{1}{2N}\sum_{\boldsymbol{k}'s'} x^i_{\boldsymbol{k}'s'}x^j_{\boldsymbol{k}'s'}g_{\boldsymbol{k}'s'}$, we have for the s-wave sector,

$$\det\begin{pmatrix} 1+UI_{0,0} & UI_{0,s} & UI_{0,x-y} \\ 4VI_{0s} & 1+4VI_{ss} & 4VI_{s,x-y} \\ VI_{0,x-y} & VI_{s,x-y} & 1+VI_{x-y,x-y} \end{pmatrix} = 0, \tag{8.45}$$

while for the $d_{x^2-y^2}$ sector,

$$\det\begin{pmatrix} 1+4VI_{d,d} & 4VI_{d,x+y} \\ VI_{d,x+y} & 1+VI_{x+y,x+y} \end{pmatrix} = 0, \tag{8.46}$$

and for the d_{xy} sector,

$$1 + 4VI_{xy,xy} = 0. \tag{8.47}$$

Note that if we take the zero SOC limit, $g_{\boldsymbol{k}s}$ becomes independent of s, and the sums $I_{0,x-y}$, $I_{s,x-y}$, $I_{d,x+y}$ all vanish. In this case, the T_c equations further decouple into singlet and triplet sectors. The singlet s and d-wave T_c equations are exactly what we found for the extended Hubbard model without SOC (Eqs. (8.11), (8.12), (8.13)).

However, the triplet equations are no longer degenerate. They are given by

$$1 + VI_{x-y,x-y} = 0 \tag{8.48}$$

$$1 + VI_{x+y,x+y} = 0 \tag{8.49}$$

$$1 + VI_{xy,xy} = 0. \tag{8.50}$$

The first equation is formally the same as Eq. (8.14), while the second two are new. The situation at $V_{SO} = 0$ is summarized in Fig. 8.5, which is representative of the T_c's for all weak SOC strengths (i.e. this plot looks the same for all $V_{SO} \lesssim 0.2$). Note that the new

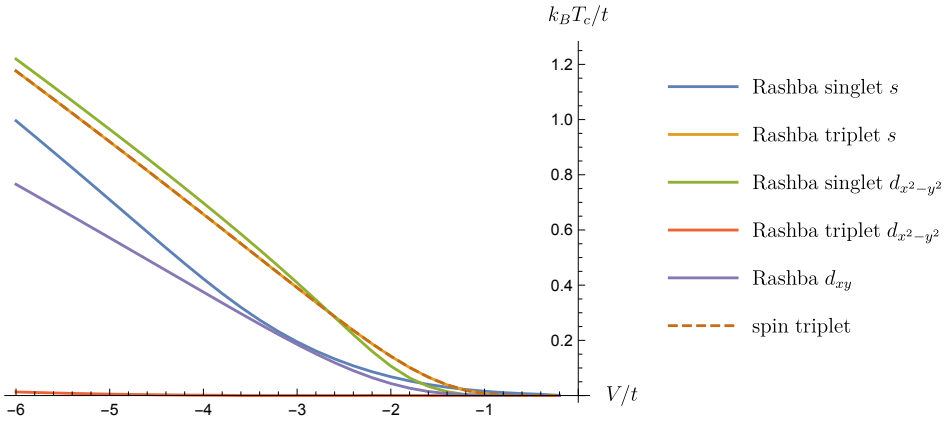

FIGURE 8.5: Critical temperatures as a function of nearest-neighbour attraction V for electron density $n = 0.5$, $U/t = -1$, $V_{SO} = 0$. Here the "Rashba" T_c's are computed in the helicity basis and have been separated into their singlet and triplet contributions. For comparison, we show the triplet T_c computed in the spin basis from Eq. (8.14) (dashed).

triplet T_c's (coming from the d-wave parts) are lower than all the other T_c's. Evidently, we do not lose anything by restricting to intraband pairing, since even in the limit of no spin splitting, we accurately capture the phases of the extended Hubbard model (at least near the onset of superconductivity). In this limit, the linear combination of intraband pairs $(c^\dagger_{\boldsymbol{k}+} c^\dagger_{-\boldsymbol{k}+}|0\rangle + c^\dagger_{\boldsymbol{k}-} c^\dagger_{-\boldsymbol{k}-}|0\rangle)$ corresponds to a triplet pair in the spin basis, while $(c^\dagger_{\boldsymbol{k}+} c^\dagger_{-\boldsymbol{k}+}|0\rangle - c^\dagger_{\boldsymbol{k}-} c^\dagger_{-\boldsymbol{k}-}|0\rangle)$ corresponds to a singlet pair in the spin basis.

If we increase the SOC, the phase diagram will change. Fig. 8.6 shows the SOC dependence of T_c for each phase. As in the attractive Hubbard model without correlated hopping, studied in Chapter 7 and in agreement with Ref. [104], T_c decreases with V_{SO} for all phases. However, the high s-wave T_c decreases more gradually and eventually displaces the $d_{x^2-y^2}$ solution as the highest T_c. Fig. 8.7 shows the phases as determined

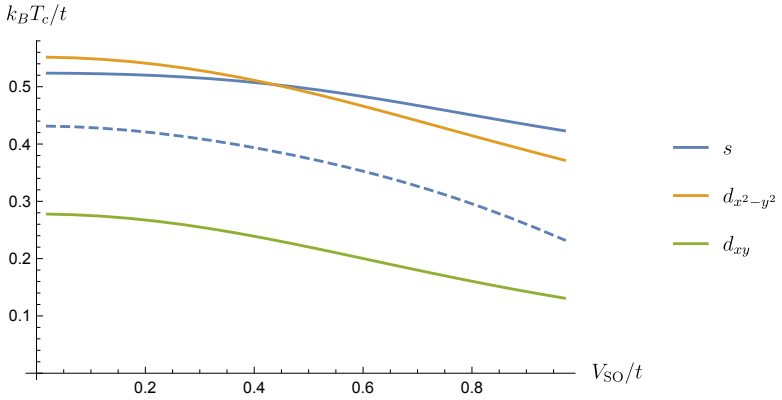

FIGURE 8.6: Critical temperatures as a function of spin-orbit coupling for electron density $n = 0.5$, $U/t = -2$, $V/t = -3.5$. Note that for these parameters, s and $d_{x^2-y^2}$ phases have two critical temperatures. The lower s-wave T_c is given by the dashed blue line. The lower $d_{x^2-y^2}$ T_c is not shown because it is visibly indistinguishable from zero.

by the highest T_c for various values of V_{SO}. Recall that for non-zero SOC, the s-wave phase includes a component that reduces to the p-wave triplet part as $V_{SO} \to 0$. We see that as V_{SO} increases, the stability of the $d_{x^2-y^2}$ phase is pushed to lower V and higher U. In this parameter range the d_{xy} phase never has the highest T_c. The situation is different close to half filling. For $n = 0.7$, the range of the $d_{x^2-y^2}$ phase is much larger.

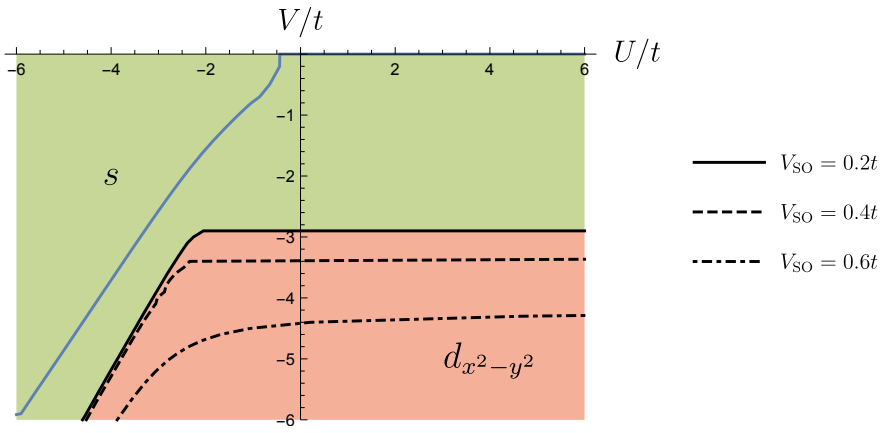

FIGURE 8.7: Phase diagram based on critical temperatures for different values of the spin-orbit coupling. The black curves show the transition for $n = 0.5$. The solid blue curve shows the transition for $n = 0.7$, which is qualitatively independent of the spin-orbit coupling (here we chose $V_{SO} = 0.2t$). To the upper-left of each curve the s-wave T_c is the highest. To the lower right, $d_{x^2-y^2}$-wave T_c is the highest.

8.5 Discussion

In this chapter, we have studied the symmetry of the superconducting gap in the 2D extended Hubbard and extended Rashba-Hubbard models, focusing on the regime of attractive nearest neighbour interaction ($V < 0$). We used a mean-field approach to determine the gap equations that set the allowed symmetries of the gap.

The precise symmetry of the gap for given material parameters (U, V, n, T) is determined by the minimum of the free energy. This can be considered as a critical point of a Morse function in a multi-dimensional parameter space of order-parameter components. This perspective, outlined in Appendix H, has conceptual and technical advantages that scale well to other models where the gap function can have a more complicated $\boldsymbol{k}$-dependence.

We discovered that even within the simple extended Hubbard model, there is a rich variety of symmetry phase transitions that occur as a function of temperature; these are observable through the specific heat. In particular, we expect there is a significant portion of the phase diagram where there is a different symmetry at $T = T_c$ and $T = 0$, with a first or second-order transition at some finite temperature in-between. This may explain the experimental difficulty in determining the symmetry of some superconducting materials. Recent observations of very underdoped cuprates indicate precisely this kind of transition, with a gap opening at the $d_{x^2-y^2}$-wave nodes as the temperature is lowered [129]. The cuprates are often described by the extended Hubbard model. Thus, it is entirely possible that this is an observation of an s-wave gap component turning on below T_c. Our results show that such a scenario is more common than not in the extended Hubbard model.

A word about the interaction parameter ranges in this chapter is warranted. We focused mainly on strong coupling, and found that in this regime, the range of symmetry transitions is significant. Such transitions may also occur at weak coupling, but in this regime the free energies of different phases are so similar that it is difficult to discern the transition. Therefore it would be easiest to observe this phenomenon for large $|U/t|$ and $|V/t|$. One promising avenue to explore this is in the context of ultra-cold atoms, where U/t is controlled via the optical lattice potential, n and T are controlled via evaporative cooling, and V can be included through dipolar interactions [130, 131].

We also point out that the phase diagram is highly dependent on the symmetries of the normal state. The addition of particle-hole symmetry (half-filling) alters the allowed symmetry phases and transitions below T_c. In the same regard, we expect models with more exotic symmetries of the normal state to have different symmetry transitions below T_c. One example is a model in which a Rashba term breaks inversion symmetry. Motivated by this, we studied the critical temperature of the extended Rashba-Hubbard model, and showed that SOC alters the allowed symmetry phases. All phases are a mixture of spin-singlet and spin-triplet and may be classified into s, $d_{x^2-y^2}$, and d_{xy} symmetries in momentum-space. The robustness of the s phase increases with spin-orbit coupling. At weak coupling, the phases map onto those of the extended Hubbard model without SOC. This is surprising because the assumption underlying this result is that pairs form in the same helicity band. For $k_BT \gtrsim V_{\mathrm{SO}}$ the two helicity bands are effectively degenerate. Nonetheless, we still need only consider intraband pairing. The reason is that in the helicity basis, the one singlet and three triplet pairing types are divided such that intraband pairing contains the singlet and one triplet, while interband pairing contains the other two triplets. This can be seen by representing the intra and inter-band pairs in the spin basis:

$$c_{-\boldsymbol{k}s}c_{\boldsymbol{k}s} = \frac{se^{i\theta(\boldsymbol{k})}}{2}[s(e^{i\theta(\boldsymbol{k})}c_{-\boldsymbol{k}\uparrow}c_{\boldsymbol{k}\uparrow} - e^{-i\theta(\boldsymbol{k})}c_{-\boldsymbol{k}\downarrow}c_{\boldsymbol{k}\downarrow}) + (c_{-\boldsymbol{k}\uparrow}c_{\boldsymbol{k}\downarrow} - c_{-\boldsymbol{k}\downarrow}c_{\boldsymbol{k}\uparrow})], \tag{8.51}$$

$$c_{-\boldsymbol{k}s}c_{\boldsymbol{k}-s} = \frac{se^{i\theta(\boldsymbol{k})}}{2}[s(e^{i\theta(\boldsymbol{k})}c_{-\boldsymbol{k}\uparrow}c_{\boldsymbol{k}\uparrow} + e^{-i\theta(\boldsymbol{k})}c_{-\boldsymbol{k}\downarrow}c_{\boldsymbol{k}\downarrow}) - (c_{-\boldsymbol{k}\uparrow}c_{\boldsymbol{k}\downarrow} + c_{-\boldsymbol{k}\downarrow}c_{\boldsymbol{k}\uparrow})]. \tag{8.52}$$

Since all triplet phases are degenerate at T_c, it suffices to consider just intraband pairing.

With this in mind, the interband pairing may become important at low temperatures (but not lower than the spin splitting). Indeed, we expect the full temperature-dependent phase diagram to be quite rich. It would be interesting to see what happens to the symmetry transitions we found in Section 8.3 when the SOC is turned on. The free energy minimization method developed in this chapter can be applied to this case as well, with the advantage that the computation time scales, albeit exponentially, with the dimension of the largest pure subspace of parameters (three), rather than the dimension of the full parameter space (six) as in previously used methods [127].

Chapter 9

Conclusion

In this thesis, we have endeavoured to provide theoretical descriptions for a variety of phenomena associated with electronic systems where spin-orbit coupling plays an important role. In particular, we have focused on systems with broken inversion symmetry in two dimensions where the spin-orbit coupling takes the Rashba form. The class of materials with some amount of inversion asymmetry is vast, and the Rashba term must be accounted for in all of these cases. The primary consequence of this, is that the dispersion is dramatically altered from the conventional parabolic (in continuum) or cosine (on a square lattice) band structure. Throughout this dissertation, we have shown that the effects of this drastic alteration can be amplified in a many-electron system and cause observable consequences on a macrosopic scale. In Part 1, this amplification occurred because we focused on a range of electron densities for which the assumptions of Fermi liquid theory held and therefore the relevant excitations qualitatively followed the single-particle properties of the system. In Part 2, this amplification occurred because we focused on situations where the pairing instability occurred within channels demarcated by the single-particle bands.

In Chapter 3 we exactly solved the low-energy single-particle impurity scattering problem for a set of simple impurity potentials and showed that the S-matrix and cross section exhibited unconventional behaviour. Recognizing that these features were independent of the details of the impurity, we derived a universal expression for the T-matrix (and therefore all scattering quantities) of a low-energy Rashba system in Chapter 4. This equipped us with the necessary tools to compute non-perturbative transport quantities

in the many-body system in Chapter 5. The most striking result of these calculations was the existence of quantized steps in the DC conductivity as a function of the logarithm of the electron density, a feature we predict to be observable in a pump-probe experiment.

Several open questions remain on this topic. One is whether or not this phenomenon appears outside the context of Rashba spin-orbit coupling. In other words, is it a consequence of the spin dynamics of these systems, or is it present for all dispersions with highly degenerate minima? Steps towards answering this question would include determining if 2D Dresselhaus systems (same dispersion, different spin texture) exhibit similar phenomena, and whether there is a generalization of these results to 3D Rashba dispersions that have a toroidal ground state manifold [51]. Perhaps it is only the topology of the low-energy Fermi sea that matters in this regard. The other question is how these scattering properties manifest themselves in two-particle scattering. We carefully avoided electron-electron interactions in the first part of this thesis, but it is predicted that these interactions cause liquid and Wigner crystal phases with unusual symmetries in the Rashba system [54–56]. We expect that one could elucidate the origin of these phases by applying the low-energy scattering theory developed here to two or few-body problems.

In the second part of the thesis, we studied superconductivity within the BCS mean-field formalism. Here too, we follow the consequences of the altered Rashba dispersion to the many-body problem by considering the thermodynamics of Cooper pairs formed within the same helicity band of this dispersion. Chapter 7 revealed that while Rashba coupling suppresses the superconducting instability in the Hubbard model, it enhances this instability upon the addition of correlated hopping, and furthermore causes an increased asymmetry in the gap and coherence peaks with respect to the bias voltage of a tunnelling setup. In Chapter 8 we discussed the symmetry of the superconducting order parameter in the extended Hubbard model both with and without spin-orbit coupling. We pointed out that even in the simple extended Hubbard model, the phase diagram is very exotic, particularly if one considers temperatures below T_c, where the order parameter can have components from multiple irreps of the lattice point group. We developed an algorithm to find these phases via global minimization of the free energy. In the case with a Rashba term, our discussion was limited to the phases near T_c, but there we saw that spin-orbit coupling caused a suppression in states with d-wave symmetry.

The natural next step would be to complete a finite temperature analysis of the phases of the extended Rashba-Hubbard model. While the techniques we developed in Chapter 7 are suitable for this, one may need to reformulate the mean-field problem to account for interband pairing. Furthermore, it is known that phases with complex order parameters exist in the extended Hubbard model, such as $s + id$ [127]. In the Rashba case, it is not clear what the relative phase between order-parameter components should be. One can also speculate about the extended Rashba-Hubbard model with correlated hopping. Our results from Chapter 7 revealed that in the presence of correlated hopping, spin-orbit coupling causes an enhancement in the (extended) s-wave part of the gap. Thus, we expect that in the extended Rashba-Hubbard model, a finite Δt would cause a further preference of s over d-wave symmetry.

It is truly striking that spin-orbit coupling, a small relativistic correction to atomic spectra, could produce such dramatic and diverse consequences as quantized conductivity, tunable superconducting T_c, or even a spin transistor. What began as an effort to more accurately compute the band structure of zinc blende and Wurtzite crystals over 60 years ago has formed the basis of a rich set of phenomenology. This has been aided by the discovery of metals, semiconductors, and superconductors with ever larger spin splittings. As this trend continues, more materials are found where spin-orbit coupling plays a dominant role in macroscopic thermodynamic and transport features. It is therefore vital for theorists and experimentalists to continue to map out the possible phenomena associated with this effect. We believe that such investigations will build new bridges between the atomic and macroscopic worlds in future discoveries and technologies.

Bibliography

[1] Joel Hutchinson and Joseph Maciejko. Rashba scattering in the low-energy limit. *Physical Review B*, 93(24):245309, Mar 2016. doi: 10.1103/PhysRevB.93.245309.

[2] Joel Hutchinson and Joseph Maciejko. Erratum: Rashba scattering in the low-energy limit [Phys. Rev. B **93**, 245309 (2016)]. *Phys. Rev. B*, 95(3):039902(E), Jan 2017. doi: 10.1103/PhysRevB.95.039902.

[3] Joel Hutchinson and Joseph Maciejko. Universality of low-energy Rashba scattering. *Phys. Rev. B*, 96:125304, Sep 2017. doi: 10.1103/PhysRevB.96.125304.

[4] Joel Hutchinson, J. E. Hirsch, and Frank Marsiglio. Enhancement of superconducting T_c due to the spin-orbit interaction. *Phys. Rev. B*, 97:184513, May 2018. doi: 10.1103/PhysRevB.97.184513.

[5] Joel Hutchinson and Joseph Maciejko. Unconventional transport in low-density two-dimensional Rashba systems. *Phys. Rev. B*, 98:195305, Nov 2018. doi: 10.1103/PhysRevB.98.195305.

[6] Paul Adrien Maurice Dirac and Ralph Howard Fowler. The quantum theory of the electron. *Proceedings of the Royal Society of London. Series A, Containing Papers of a Mathematical and Physical Character*, 117(778):610–624, Feb 1928. doi: 10.1098/rspa.1928.0023.

[7] L.J. Cui, Y.P. Zeng, Y. Zhang, W.Z. Zhou, L.Y. Shang, T. Lin, and J.H. Chu. Beating patterns in the Shubnikov-de Haas oscillations originated from spin splitting in $In_{0.52}Al_{0.48}As/In_{0.65}Ga_{0.35}As$ heterostructures: Experiment and calculation. *Physica E: Low-dimensional Systems and Nanostructures*, 83:114 – 118, Sep 2016. ISSN 1386-9477. doi: 10.1016/j.physe.2016.04.028.

[8] S. LaShell, B. A. McDougall, and E. Jensen. Spin splitting of an Au(111) surface state band observed with angle resolved photoelectron spectroscopy. *Phys. Rev. Lett.*, 77:3419–3422, Oct 1996. doi: 10.1103/PhysRevLett.77.3419.

[9] Junsaku Nitta, Tatsushi Akazaki, Hideaki Takayanagi, and Takatomo Enoki. Gate control of spin-orbit interaction in an inverted $In_{0.53}Ga_{0.47}As/In_{0.52}Al_{0.48}As$ heterostructure. *Phys. Rev. Lett.*, 78:1335–1338, Feb 1997. doi: 10.1103/PhysRevLett.78.1335.

[10] Friedrich Reinert. Spin-orbit interaction in the photoemission spectra of noble metal surface states. *J. Phys. Condens. Matter*, 15(5):S693–S705, Feb 2003. doi: 10.1088/0953-8984/15/5/321.

[11] X. C. Zhang, A. Pfeuffer-Jeschke, K. Ortner, V. Hock, H. Buhmann, C. R. Becker, and G. Landwehr. Rashba splitting in n-type modulation-doped HgTe quantum wells with an inverted band structure. *Phys. Rev. B*, 63:245305, May 2001. doi: 10.1103/PhysRevB.63.245305.

[12] Yu. M. Koroteev, G. Bihlmayer, J. E. Gayone, E. V. Chulkov, S. Blügel, P. M. Echenique, and Ph. Hofmann. Strong spin-orbit splitting on Bi surfaces. *Phys. Rev. Lett.*, 93:046403, Jul 2004. doi: 10.1103/PhysRevLett.93.046403.

[13] D. Popović, F. Reinert, S. Hüfner, V. G. Grigoryan, M. Springborg, H. Cercellier, Y. Fagot-Revurat, B. Kierren, and D. Malterre. High-resolution photoemission on Ag/Au(111): Spin-orbit splitting and electronic localization of the surface state. *Phys. Rev. B*, 72:045419, Jul 2005. doi: 10.1103/PhysRevB.72.045419.

[14] I. Gierz, T. Suzuki, E. Frantzeskakis, S. Pons, S. Ostanin, A. Ernst, J. Henk, M. Grioni, K. Kern, and C. R. Ast. Silicon Surface with Giant Spin Splitting. *Phys. Rev. Lett.*, 103(4):046803, Jul 2009. doi: 10.1103/PhysRevLett.103.046803.

[15] Christian R. Ast, Jürgen Henk, Arthur Ernst, Luca Moreschini, Mihaela C. Falub, Daniela Pacilé, Patrick Bruno, Klaus Kern, and Marco Grioni. Giant Spin Splitting through Surface Alloying. *Phys. Rev. Lett.*, 98(18):186807, May 2007. doi: 10.1103/PhysRevLett.98.186807.

[16] A. Varykhalov, D. Marchenko, M. R. Scholz, E. D. L. Rienks, T. K. Kim, G. Bihlmayer, J. Sánchez-Barriga, and O. Rader. Ir(111) surface state with giant

Rashba splitting persists under graphene in air. *Phys. Rev. Lett.*, 108:066804, Feb 2012. doi: 10.1103/PhysRevLett.108.066804.

[17] Daniel Niesner, Max Wilhelm, Ievgen Levchuk, Andres Osvet, Shreetu Shrestha, Miroslaw Batentschuk, Christoph Brabec, and Thomas Fauster. Giant Rashba splitting in $CH_3NH_3PbBr_3$ organic-inorganic perovskite. *Phys. Rev. Lett.*, 117: 126401, Sep 2016. doi: 10.1103/PhysRevLett.117.126401.

[18] Mohammad Saeed Bahramy and Naoki Ogawa. Bulk Rashba semiconductors and related quantum phenomena. *Adv. Mater.*, 29(25):1605911, Mar 2017. doi: 10.1002/adma.201605911.

[19] Roland Winkler. *Spin-Orbit Coupling Effects in Two-Dimensional Electron and Hole Systems*. Springer, Berlin, 2003.

[20] A. Zee. *Group Theory in a Nutshell for Physicists*. Princeton University Press, Princeton, 2016.

[21] Russell S Drago. *Physical methods in chemistry*. Philadelphia : Saunders, [2d ed.] edition, 1977. ISBN 0721631843. Published in 1965 under title: Physical methods in inorganic chemistry.

[22] Gene Dresselhaus. Spin-orbit coupling effects in zinc blende structures. *Physical Review*, 100(2):580, Oct 1955. doi: 10.1103/PhysRev.100.580.

[23] EI Rashba and VI Sheka. Symmetry of energy bands in crystals of wurtzite type. II. Symmetry of bands with spin-orbit interaction included. *Fiz. Tverd. Tela: Collected Papers*, 2:162–76, 1959.

[24] G Bihlmayer, O Rader, and R Winkler. Focus on the Rashba effect. *New Journal of Physics*, 17(5):050202, May 2015. doi: 10.1088/1367-2630/17/5/050202.

[25] Fusayoshi J. Ohkawa and Yasutada Uemura. Quantized surface states of a narrow-gap semiconductor. *J. Phys. Soc. Jpn.*, 37(5):1325–1333, Nov 1974. doi: 10.1143/JPSJ.37.1325.

[26] Yu A Bychkov and EI Rashba. Properties of a 2D electron gas with lifted spectral degeneracy. *JETP Lett.*, 39(2):78, Jan 1984.

[27] MI D'yakonov. Spin relaxation of two-dimensional electrons in non-centrosymmetric semiconductors. *Sov. Phys. Semicond.*, 20(1):110–112, 1986.

[28] B. Andrei Bernevig, J. Orenstein, and Shou-Cheng Zhang. Exact SU(2) symmetry and persistent spin helix in a spin-orbit coupled system. *Phys. Rev. Lett.*, 97: 236601, Dec 2006. doi: 10.1103/PhysRevLett.97.236601.

[29] Shanchao Zhang and Gyu-Boong Jo. Recent advances in spin-orbit coupled quantum gases. *J. Phys. Chem. Solids*, 128:75–86, May 2019. ISSN 0022-3697. doi: 10.1016/j.jpcs.2018.04.033.

[30] Xiuwen Zhang, Qihang Liu, Jun-Wei Luo, Arthur J. Freeman, and Alex Zunger. Hidden spin polarization in inversion-symmetric bulk crystals. *Nat Phys*, 10(5): 387–393, May 2014. doi: 10.1038/nphys2933.

[31] N.W. Ashcroft and N.D. Mermin. *Solid State Physics*. Saunders College, Philadelphia, 1976.

[32] Yi Li, Xiangfa Zhou, and Congjun Wu. Two- and three-dimensional topological insulators with isotropic and parity-breaking Landau levels. *Phys. Rev. B*, 85(12): 125122, Mar 2012. doi: 10.1103/PhysRevB.85.125122.

[33] Zhou Li, L. Covaci, and F. Marsiglio. Impact of Dresselhaus versus Rashba spin-orbit coupling on the Holstein polaron. *Phys. Rev. B*, 85:205112, May 2012. doi: 10.1103/PhysRevB.85.205112.

[34] Huaxiang Fu. Tunability of giant Rashba spin splitting in BiTeI. *Phys. Rev. B*, 87:075139, Feb 2013. doi: 10.1103/PhysRevB.87.075139.

[35] M. Johnson and R. H. Silsbee. Interfacial charge-spin coupling: Injection and detection of spin magnetization in metals. *Physical Review Letters*, 55:1790–1793, Oct 1985. doi: 10.1103/PhysRevLett.55.1790.

[36] M. N. Baibich, J. M. Broto, A. Fert, F. Nguyen van Dau, F. Petroff, P. Etienne, G. Creuzet, A. Friederich, and J. Chazelas. Giant magnetoresistance of (001)Fe/(001)Cr magnetic superlattices. *Physical Review Letters*, 61:2472–2475, Nov 1988. doi: 10.1103/PhysRevLett.61.2472.

[37] G. Binasch, P. Grünberg, F. Saurenbach, and W. Zinn. Enhanced magnetoresistance in layered magnetic structures with antiferromagnetic interlayer exchange. *Phys. Rev. B*, 39:4828–4830, Mar 1989. doi: 10.1103/PhysRevB.39.4828.

[38] Mark D. Stiles and Jacques Miltat. *Spin-Transfer Torque and Dynamics*, pages 225–308. Springer Berlin Heidelberg, Berlin, Heidelberg, 2006. ISBN 978-3-540-39842-4. doi: 10.1007/10938171_7.

[39] Sabpreet Bhatti, Rachid Sbiaa, Atsufumi Hirohata, Hideo Ohno, Shunsuke Fukami, and S.N. Piramanayagam. Spintronics based random access memory: a review. *Materials Today*, 20(9):530–548, Nov 2017. ISSN 1369-7021. doi: 10.1016/j.mattod.2017.07.007.

[40] Supriyo Datta and Biswajit Das. Electronic analog of the electro-optic modulator. *Applied Physics Letters*, 56(7):665–667, 1990.

[41] Alexander Khaetskii. Nonexistence of intrinsic spin currents. *Phys. Rev. Lett.*, 96: 056602, Feb 2006. doi: 10.1103/PhysRevLett.96.056602.

[42] J. Cserti, A. Csordás, and U. Zülicke. Electronic and spin properties of Rashba billiards. *Phys. Rev. B*, 70(23):233307, Dec 2004. doi: 10.1103/PhysRevB.70.233307.

[43] Jamie D Walls, Jian Huang, Robert M Westervelt, and Eric J Heller. Multiple-scattering theory for two-dimensional electron gases in the presence of spin-orbit coupling. *Phys. Rev. B.*, 73(3):035325, Jan 2006. doi: 10.1103/PhysRevB.73.035325.

[44] A. Csordás, J. Cserti, A. Pályi, and U. Zülicke. Rashba billiards. *Eur. Phys. J. B*, 54(2):189, Dec 2006. ISSN 1434-6028, 1434-6036. doi: 10.1140/epjb/e2006-00445-9.

[45] A. Pályi and J. Cserti. Skew scattering due to intrinsic spin-orbit coupling in a two-dimensional electron gas. *Phys. Rev. B*, 76(3):035331, Jul 2007. doi: 10.1103/PhysRevB.76.035331.

[46] András Pályi, Csaba Péterfalvi, and József Cserti. Two-dimensional electron scattering in regions of nonuniform spin-orbit coupling. *Phys. Rev. B*, 74(7):073305, Aug 2006. doi: 10.1103/PhysRevB.74.073305.

[47] Jr-Yu Yeh, Ming-Che Chang, and Chung-Yu Mou. Electron scattering from a mesoscopic disk in a Rashba system. *Phys. Rev. B*, 73(3):035313, Jan 2006. doi: 10.1103/PhysRevB.73.035313.

[48] Valentina Brosco, Lara Benfatto, Emmanuele Cappelluti, and Claudio Grimaldi. Unconventional dc transport in Rashba electron gases. *Phys. Rev. Lett.*, 116(16): 166602, Apr 2016. doi: 10.1103/PhysRevLett.116.166602.

[49] Valentina Brosco and Claudio Grimaldi. Anisotropy of transport in bulk Rashba metals. *Phys. Rev. B*, 95:195164, May 2017. doi: 10.1103/PhysRevB.95.195164.

[50] Valentina Brosco, Claudio Grimaldi, Emmanuele Cappelluti, and Lara Benfatto. Two-dimensional Rashba metals: Unconventional low-temperature transport properties. *J. Phys. Chem. Solids*, 128:152 – 160, May 2019. ISSN 0022-3697. doi: 10.1016/j.jpcs.2017.10.040.

[51] E. Cappelluti, C. Grimaldi, and F. Marsiglio. Topological Change of the Fermi Surface in Low-Density Rashba Gases: Application to Superconductivity. *Phys. Rev. Lett.*, 98(16):167002, Apr 2007. doi: 10.1103/PhysRevLett.98.167002.

[52] So Takei, Chien-Hung Lin, Brandon M. Anderson, and Victor Galitski. Low-density molecular gas of tightly bound Rashba-Dresselhaus fermions. *Phy. Rev. A*, 85(2):023626, Feb 2012. doi: 10.1103/PhysRevA.85.023626.

[53] E. Wigner. On the interaction of electrons in metals. *Phys. Rev.*, 46:1002–1011, Dec 1934. doi: 10.1103/PhysRev.46.1002.

[54] Erez Berg, Mark S Rudner, and Steven A Kivelson. Electronic liquid crystalline phases in a spin-orbit coupled two-dimensional electron gas. *Phys. Rev. B*, 85(3): 035116, Jan 2012. doi: 10.1103/PhysRevB.85.035116.

[55] PG Silvestrov and O Entin-Wohlman. Wigner crystal of a two-dimensional electron gas with a strong spin-orbit interaction. *Phys. Rev. B*, 89(15):155103, Apr 2014. doi: 10.1103/PhysRevB.89.155103.

[56] Jonathan Ruhman and Erez Berg. Ferromagnetic and nematic non-fermi liquids in spin-orbit-coupled two-dimensional fermi gases. *Phys. Rev. B*, 90(23):235119, 2014. doi: 10.1103/PhysRevB.90.235119.

[57] Sadhan K. Adhikari. Quantum scattering in two dimensions. *Am. J. Phys.*, 54(4): 362–367, Apr 1986. ISSN 0002-9505. doi: 10.1119/1.14623.

[58] Henrik Bruus and Karsten Flensberg. *Many-Body Quantum Theory in Condensed Matter Physics: an Introduction.* Oxford University Press, 2004.

[59] Harald Friedrich. *Scattering Theory.* Springer, Berlin, 2013.

[60] R. Landauer. Spatial Variation of Currents and Fields Due to Localized Scatterers in Metallic Conduction. *IBM J. Res. Dev.*, 1(3):223, Jul 1957. ISSN 0018-8646. doi: 10.1147/rd.13.0223.

[61] B. J. van Wees, H. van Houten, C. W. J. Beenakker, J. G. Williamson, L. P. Kouwenhoven, D. van der Marel, and C. T. Foxon. Quantized conductance of point contacts in a two-dimensional electron gas. *Phys. Rev. Lett.*, 60(9):848, Feb 1988. doi: 10.1103/PhysRevLett.60.848.

[62] D. A. Wharam, T. J. Thornton, R. Newbury, M. Pepper, H. Ahmed, J. E. F. Frost, D. G. Hasko, D. C. Peacock, D. A. Ritchie, and G. A. C. Jones. One-dimensional transport and the quantisation of the ballistic resistance. *J. Phys. C*, 21(8):L209, Mar 1988. ISSN 0022-3719. doi: 10.1088/0022-3719/21/8/002.

[63] M. A. Topinka, B. J. LeRoy, S. E. J. Shaw, E. J. Heller, R. M. Westervelt, K. D. Maranowski, and A. C. Gossard. Imaging Coherent Electron Flow from a Quantum Point Contact. *Science*, 289(5488):2323, Sep 2000. ISSN 0036-8075, 1095-9203. doi: 10.1126/science.289.5488.2323.

[64] M. A. Topinka, B. J. LeRoy, R. M. Westervelt, S. E. J. Shaw, R. Fleischmann, E. J. Heller, K. D. Maranowski, and A. C. Gossard. Coherent branched flow in a two-dimensional electron gas. *Nature*, 410(6825):183, March 2001. ISSN 0028-0836. doi: 10.1038/35065553.

[65] R. Shankar. Renormalization-group approach to interacting fermions. *Rev. Mod. Phys.*, 66(1):129–192, Jan 1994. doi: 10.1103/RevModPhys.66.129.

[66] Kun Yang and Subir Sachdev. Quantum Criticality of a Fermi Gas with a Spherical Dispersion Minimum. *Phys. Rev. Lett.*, 96(18):187001, May 2006. doi: 10.1103/PhysRevLett.96.187001.

[67] Horacio E. Camblong, Luis N. Epele, Huner Fanchiotti, and Carlos A. García Canal. Dimensional Transmutation and Dimensional Regularization in Quantum Mechanics. *Ann. Phys. (N. Y.)*, 287(1):14–56, Jan 2001. ISSN 0003-4916. doi: 10.1006/aphy.2000.6092.

[68] A Crepaldi, LAGT Moreschini, G Autès, C Tournier-Colletta, S Moser, N Virk, H Berger, Ph Bugnon, YJ Chang, K Kern, et al. Giant ambipolar rashba effect in the semiconductor BiTeI. *Phys. Rev. Lett.*, 109(9):096803, Aug 2012. doi: 10.1103/PhysRevLett.109.096803.

[69] David A. Valverde-Chavez, Carlito S. Ponseca, Constantinos C. Stoumpos, Arkady Yartsev, Mercouri G. Kanatzidis, Villy Sundstrom, and David G. Cooke. Intrinsic femtosecond charge generation dynamics in single crystal $CH_3NH_3PbI_3$. *Energy Environ. Sci.*, 8:3700–3707, Oct 2015. doi: 10.1039/C5EE02503F.

[70] Alessio Filippetti, Pietro Delugas, and Alessandro Mattoni. Radiative recombination and photoconversion of methylammonium lead iodide perovskite by first principles: Properties of an inorganic semiconductor within a hybrid body. *J. Phys. Chem. C*, 118(43):24843–24853, Oct 2014. doi: 10.1021/jp507430x.

[71] Gerald D Mahan. *Many-Particle Physics*. Kluwer Academic/Plenum Publishers, New York, 3rd edition, 2000.

[72] A. G. Galstyan and M. E. Raikh. Disorder-induced broadening of the density of states for two-dimensional electrons with strong spin-orbit coupling. *Phys. Rev. B*, 58:6736–6739, Sep 1998. doi: 10.1103/PhysRevB.58.6736.

[73] L. E. Golub, I. V. Gornyi, and V. Yu. Kachorovskii. Weak antilocalization in two-dimensional systems with large Rashba splitting. *Phys. Rev. B*, 93:245306, Jun 2016. doi: 10.1103/PhysRevB.93.245306.

[74] C. C. Grimes and G. Adams. Evidence for a liquid-to-crystal phase transition in a classical, two-dimensional sheet of electrons. *Phys. Rev. Lett.*, 42:795–798, Mar 1979. doi: 10.1103/PhysRevLett.42.795.

[75] Bryan K. Clark, Michele Casula, and D. M. Ceperley. Hexatic and mesoscopic phases in a 2D quantum Coulomb system. *Phys. Rev. Lett.*, 103:055701, Jul 2009. doi: 10.1103/PhysRevLett.103.055701.

[76] George E. Simion and Gabriele F. Giuliani. *Chirality, charge and spin-density wave instabilities of a two-dimensional electron gas in the presence of Rashba spin-orbit coupling*, pages 125–146. Scuola Normale Superiore, Pisa, 2016. ISBN 978-88-7642-536-3. doi: 10.1007/978-88-7642-536-3_10.

[77] H Kamerlingh Onnes. Further experiments with liquid helium. C. on the change of electric resistance of pure metals at very low temperatures, etc. IV. the resistance of pure mercury at helium temperatures. *Comm. Phys. Lab. Univ. Leiden*, 119: 120–122, 1911.

[78] Walther Meissner and Robert Ochsenfeld. Ein neuer Eeffekt bei Eintritt der Supraleitfähigkeit. *Naturwissenschaften*, 21(44):787–788, 1933.

[79] C.J. Gorter. Chapter I the two fluid model for superconductors and helium II. volume 1 of *Progress in Low Temperature Physics*, pages 1 – 16. Elsevier, 1955. doi: 10.1016/S0079-6417(08)60076-1.

[80] Carl Kocher. Criteria for bound-state solutions in quantum mechanics. *Am. J. Phys.*, 45:71–74, 01 1977. doi: 10.1119/1.10913.

[81] Leon N. Cooper. Bound electron pairs in a degenerate Fermi gas. *Phys. Rev.*, 104: 1189–1190, Nov 1956. doi: 10.1103/PhysRev.104.1189.

[82] J.E. Hirsch, M.B. Maple, and F. Marsiglio. Superconducting materials classes: Introduction and overview. *Physica C: Superconductivity and its Applications*, 514:1 – 8, Jul 2015. doi: 10.1016/j.physc.2015.03.002.

[83] F. Steglich, J. Aarts, C. D. Bredl, W. Lieke, D. Meschede, W. Franz, and H. Schäfer. Superconductivity in the Presence of Strong Pauli Paramagnetism: $CeCu_2Si_2$. *Phys. Rev. Lett.*, 43:1892–1896, Dec 1979. doi: 10.1103/PhysRevLett.43.1892.

[84] J. G. Bednorz and K. A. Müller. Possible high Tc superconductivity in the Ba-La-Cu-O system. *Zeitschrift für Physik B Condensed Matter*, 64(2):189–193, Jun 1986. ISSN 1431-584X. doi: 10.1007/BF01303701.

[85] Yu Li, Min Liu, Zhaoming Fu, Xiangrong Chen, Fan Yang, and Yi-feng Yang. Gap symmetry of the heavy fermion superconductor $CeCu_2Si_2$ at ambient pressure. *Phys. Rev. Lett.*, 120:217001, May 2018. doi: 10.1103/PhysRevLett.120.217001.

[86] John Bardeen, Leon N Cooper, and John Robert Schrieffer. Theory of superconductivity. *Phys. Rev.*, 108(5):1175, Dec 1957. doi: 10.1103/PhysRev.108.1175.

[87] Peter Fulde and Richard A. Ferrell. Superconductivity in a strong spin-exchange field. *Phys. Rev.*, 135:A550–A563, Aug 1964. doi: 10.1103/PhysRev.135.A550.

[88] AI Larkin and Yu N Ovchinnikov. Nonuniform state of superconductors. *Sov. Phys. JETP*, 20(3):762–762, 1965.

[89] J. Hubbard. Electron correlations in narrow energy bands. *Proceedings of the Royal Society of London A: Mathematical, Physical and Engineering Sciences*, 276(1365):238–257, 1963. ISSN 0080-4630. doi: 10.1098/rspa.1963.0204.

[90] Shun-Qing Shen and X C Xie. Pseudospin SU(2)-symmetry breaking, charge-density waves and superconductivity in the Hubbard model. *J. Phys. Condens. Matter*, 8(26):4805–4812, Jun 1996. doi: 10.1088/0953-8984/8/26/012.

[91] R. Micnas, J. Ranninger, and S. Robaszkiewicz. Superconductivity in narrow-band systems with local nonretarded attractive interactions. *Rev. Mod. Phys.*, 62: 113–171, Jan 1990. doi: 10.1103/RevModPhys.62.113.

[92] T. Hattori, Y. Ihara, Y. Nakai, K. Ishida, Y. Tada, S. Fujimoto, N. Kawakami, E. Osaki, K. Deguchi, N. K. Sato, and I. Satoh. Superconductivity induced by longitudinal ferromagnetic fluctuations in UCoGe. *Phys. Rev. Lett.*, 108:066403, Feb 2012. doi: 10.1103/PhysRevLett.108.066403.

[93] F Reif. Study of superconducting Hg by nuclear magnetic resonance techniques. *Phys. Rev.*, 106(2):208, Apr 1957. doi: 10.1103/PhysRev.106.208.

[94] Gaylord Marvin Androes and WD Knight. Nuclear magnetic resonance in superconducting tin. *Phys. Rev. Lett.*, 2(9):386, Feb 1959. doi: 10.1103/PhysRev.121.779.

[95] PW Anderson. Knight shift in superconductors. *Phys. Rev. Lett.*, 3(7):325, Oct 1959. doi: 10.1103/PhysRevLett.3.325.

[96] AA Abrikosov and LP Gor'kov. Spin-orbit interaction and the Knight shift in superconductors. *Sov. Phys. JETP*, 15:752, 1962.

[97] VM Edel'shtein. Characteristics of the Cooper pairing in two-dimensional noncentrosymmetric electron systems. *Sov. Phys. JETP (English Translation)*, 68(6): 1244–1249, 1989.

[98] Lev P. Gor'kov and Emmanuel I. Rashba. Superconducting 2D system with lifted spin degeneracy: Mixed singlet-triplet state. *Phys. Rev. Lett.*, 87:037004, Jul 2001. doi: 10.1103/PhysRevLett.87.037004.

[99] Ernst Bauer, Gerfried Hilscher, Herwig Michor, Ch Paul, EW Scheidt, A Gribanov, Yu Seropegin, H Noël, M Sigrist, and Peter Rogl. Heavy fermion superconductivity and magnetic order in noncentrosymmetric $CePt_3Si$. *Phys. Rev. Lett.*, 92(2): 027003, Jan 2004. doi: 10.1103/PhysRevLett.92.027003.

[100] Nicolas Reyren, S Thiel, AD Caviglia, L Fitting Kourkoutis, G Hammerl, C Richter, CW Schneider, T Kopp, A-S Rüetschi, Didier Jaccard, et al. Superconducting interfaces between insulating oxides. *Science*, 317(5842):1196–1199, Aug 2007. doi: 10.1126/science.1146006.

[101] Masaaki Isobe, Masao Arai, and Naoki Shirakawa. Superconductivity in noncentrosymmetric $SrAuSi_3$. *Phys. Rev. B*, 93:054519, Feb 2016. doi: 10.1103/PhysRevB.93.054519.

[102] Soumya P. Mukherjee and Stephanie H. Curnoe. Superconductivity in noncentrosymmetric $LaNiC_2$. *Physica C: Superconductivity*, 499:6 – 8, Apr 2014. ISSN 0921-4534. doi: 10.1016/j.physc.2014.01.008.

[103] T Akazawa, H Hidaka, T Fujiwara, TC Kobayashi, E Yamamoto, Y Haga, R Settai, and Y Ōnuki. Pressure-induced superconductivity in ferromagnetic UIr without inversion symmetry. *J. Phys. Condens. Matter*, 16(4):L29, Jan 2004. doi: 10.1088/0953-8984/16/4/L02.

[104] Andrzej Ptok, Karen Rodríguez, and Konrad Jerzy Kapcia. Superconducting monolayer deposited on substrate: Effects of the spin-orbit coupling induced by proximity effects. *Phys. Rev. Materials*, 2:024801, Feb 2018. doi: 10.1103/PhysRevMaterials.2.024801.

[105] JE Hirsch and F Marsiglio. Superconducting state in an oxygen hole metal. *Phys. Rev. B*, 39(16):11515, Jun 1989. doi: 10.1103/PhysRevB.39.11515.

[106] J. F. Annett, N. Goldenfeld, and A. J. Leggett. *Experimental Constraints on the Pairing State of the Cuprate Superconductors: An Emerging Consensus*, pages 375–461. World Scientific Publishing Co, 1996. doi: 10.1142/9789814261289_0006.

[107] J. D. Strand, D. J. Van Harlingen, J. B. Kycia, and W. P. Halperin. Evidence for complex superconducting order parameter symmetry in the low-temperature phase of UPt_3 from Josephson interferometry. *Phys. Rev. Lett.*, 103:197002, Nov 2009. doi: 10.1103/PhysRevLett.103.197002.

[108] M. R. Norman. The challenge of unconventional superconductivity. *Science*, 332 6026:196–200, Apr 2011. doi: 10.1126/science.1200181.

[109] Robert Joynt and Louis Taillefer. The superconducting phases of UPt_3. *Rev. Mod. Phys.*, 74:235–294, Mar 2002. doi: 10.1103/RevModPhys.74.235.

[110] D. Stornaiuolo, D. Massarotti, R. Di Capua, P. Lucignano, G. P. Pepe, M. Salluzzo, and F. Tafuri. Signatures of unconventional superconductivity in the $LaAlO_3/SrTiO_3$ two-dimensional system. *Phys. Rev. B*, 95:140502, Apr 2017. doi: 10.1103/PhysRevB.95.140502.

[111] James F. Annett. Symmetry of the order parameter for high-temperature superconductivity. *Advances in Physics*, 39(2):83–126, 1990. ISSN 14606976. doi: 10.1080/00018739000101481.

[112] M. P. Sörensen, T. Schneider, and M. Frick. *Nonlinear Properties of the BCS Gap Equation*, pages 315–327. Springer US, Boston, MA, 1991. ISBN 978-1-4684-5961-6. doi: 10.1007/978-1-4684-5961-6_33.

[113] Mads Peter Soerensen. Bifurcations and nonlinear properties of the BCS gap equation. In *Nonlinear Superconductive Electronics and Josephson Devices*, pages 427–436. Springer, 1991.

[114] Giuseppe G. N. Angilella, Renato Pucci, Fabio Siringo, and Asle Sudbø. Sharp k-space features in the order parameter within the interlayer pair-tunneling mechanism of high-T_c superconductivity. *Phys. Rev. B*, 59:1339–1353, Jan 1999. doi: 10.1103/PhysRevB.59.1339.

[115] Joel Hutchinson, Marc Baker, and Frank Marsiglio. The spectral decomposition of the helium atom two-electron configuration in terms of hydrogenic orbitals.

European Journal of Physics, 34(1):111–128, Nov 2012. doi: 10.1088/0143-0807/34/1/111.

[116] J. E. Hirsch. Dynamic Hubbard model. *Phys. Rev. Lett.*, 87:206402, Oct 2001. doi: 10.1103/PhysRevLett.87.206402.

[117] IG Lang and Yu A Firsov. Kinetic theory of semiconductors with low mobility. *Sov. Phys. JETP*, 16(5):1301, 1963.

[118] Florian Loder, Arno P Kampf, and Thilo Kopp. Superconductivity with Rashba spin–orbit coupling and magnetic field. *J. Phys. Condens. Matter*, 25(36):362201, Aug 2013. doi: 10.1088/0953-8984/25/36/362201.

[119] Ke-Chuan Weng and CD Hu. The p-wave superconductivity in the presence of Rashba interaction in 2DEG. *Scientific reports*, 6:29919, Jul 2016. doi: 10.1038/srep29919.

[120] Philip W Anderson. Theory of dirty superconductors. *J. Phys. Chem. Solids*, 11 (1-2):26–30, Sep 1959. doi: 10.1016/0022-3697(59)90036-8.

[121] F. Marsiglio and J.E. Hirsch. Tunneling asymmetry: A test of superconductivity mechanisms. *Physica C: Superconductivity*, 159(3):157 – 160, Jun 1989. ISSN 0921-4534. doi: 10.1016/0921-4534(89)90363-8.

[122] P. K. Rout, E. Maniv, and Y. Dagan. Link between the superconducting dome and spin-orbit interaction in the (111) $LaAlO_3/SrTiO_3$ interface. *Phys. Rev. Lett.*, 119:237002, Dec 2017. doi: 10.1103/PhysRevLett.119.237002.

[123] I. A. Sergienko and S. H. Curnoe. Order parameter in superconductors with nondegenerate bands. *Phys. Rev. B*, 70:214510, Dec 2004. doi: 10.1103/PhysRevB.70.214510.

[124] R. P. Feynman. Slow electrons in a polar crystal. *Phys. Rev.*, 97:660–665, Feb 1955. doi: 10.1103/PhysRev.97.660.

[125] Richard S Palais. Morse theory on Hilbert manifolds. *Topology*, 2(4):299–340, 1963. doi: 10.1016/0040-9383(63)90013-2.

[126] M. Morse. *The Calculus of Variations in the Large.* Number v. 18 in American Mathematical Society. American Mathematical Society, 1934. ISBN 9780821810187.

[127] Swagatam Nayak and Sanjeev Kumar. Exotic superconducting states in the extended attractive Hubbard model. *J. Phys. Condens. Matter*, 30(13):135601, Mar 2018. doi: 10.1088/1361-648X/aaaefe.

[128] Yoseph Imry and Michael Wortis. Influence of quenched impurities on first-order phase transitions. *Phys. Rev. B*, 19:3580–3585, Apr 1979. doi: 10.1103/PhysRevB.19.3580.

[129] E. Razzoli, G. Drachuck, A. Keren, M. Radovic, N. C. Plumb, J. Chang, Y.-B. Huang, H. Ding, J. Mesot, and M. Shi. Evolution from a nodeless gap to $d_{x^2-y^2}$-wave in underdoped $La_{2-x}Sr_xCuO_4$. *Phys. Rev. Lett.*, 110(4):047004, Jan 2013. doi: 110.047004.

[130] Leticia Tarruell and Laurent Sanchez-Palencia. Quantum simulation of the Hubbard model with ultracold fermions in optical lattices. *Comptes Rendus Physique*, 19(6):365 – 393, Sep 2018. ISSN 1631-0705. doi: 10.1016/j.crhy.2018.10.013.

[131] C. Menotti, M. Lewenstein, T. Lahaye, and T. Pfau. Dipolar interaction in ultracold atomic gases. *AIP Conference Proceedings*, 970(1):332–361, 2008. doi: 10.1063/1.2839130.

[132] Mohit Randeria, Ji-Min Duan, and Lih-Yir Shieh. Superconductivity in a two-dimensional Fermi gas: Evolution from Cooper pairing to Bose condensation. *Phys. Rev. B*, 41(1):327, Jan 1990. doi: 10.1103/PhysRevB.41.327.

[133] DLMF Eq.10.23.1. *NIST Digital Library of Mathematical Functions*. http://dlmf.nist.gov/, Release 1.0.14 of 2016-12-21. URL http://dlmf.nist.gov/. F. W. J. Olver, A. B. Olde Daalhuis, D. W. Lozier, B. I. Schneider, R. F. Boisvert, C. W. Clark, B. R. Miller and B. V. Saunders, eds.

[134] Manfred Sigrist. Introduction to unconventional superconductivity. *AIP Conference Proceedings*, 789(1):165–243, 2005. doi: 10.1063/1.2080350.

[135] G. Rickayzen. *Theory of superconductivity*. Number v. 14 in Interscience monographs and texts in physics and astronomy. Interscience Publishers, 1965.

[136] A. Vansevenant. The gap equation in superconductivity theory. *Physica D: Nonlinear Phenomena*, 17(3):339 – 344, Dec 1985. ISSN 0167-2789. doi: 10.1016/0167-2789(85)90217-9.

Appendix A

Character tables of some relevant point groups

For convenience, we reproduce a selection of character tables for some important point groups in this thesis. The last few columns in each table indicate the low order polynomials and pseudovectors $\boldsymbol{R}$ that transform under the corresponding irrep.

$\boldsymbol{C_{2v}}$	E	C_2(z)	σ_v(xz)	σ_v(yz)	linear	quadratic
A_1	$+1$	$+1$	$+1$	$+1$	z	x^2, y^2, z^2
A_2	$+1$	$+1$	-1	-1	R_z	xy
B_1	$+1$	-1	$+1$	-1	x, R_y	xz
B_2	$+1$	-1	-1	$+1$	y, R_x	yz

TABLE A.1: Character table for C_{2v}

$\boldsymbol{C_{4v}}$	E	$2C_4(z)$	C_2	$2\sigma_v$	$2\sigma_d$	linear	quadratic
A_1	$+1$	$+1$	$+1$	$+1$	$+1$	z	x^2+y^2, z^2
A_2	$+1$	$+1$	$+1$	-1	-1	R_z	
B_1	$+1$	-1	$+1$	$+1$	-1		x^2-y^2
B_2	$+1$	-1	$+1$	-1	$+1$		xy
E	$+2$	0	-2	0	0	$(x,y),(R_x,R_y)$	(xz,yz)

TABLE A.2: Character table for C_{4v}.

$\boldsymbol{C_{6v}}$	E	$2C_6(z)$	$2C_3$(z)	C_2(z)	$3\sigma_v$	$3\sigma_d$	linear	quadratic
A_1	+1	+1	+1	+1	+1	+1	z	x^2+y^2, z^2
A_2	+1	+1	+1	+1	−1	−1	R_z	
B_1	+1	−1	+1	−1	+1	−1		
B_2	+1	−1	+1	−1	−1	+1		
E_1	+2	+1	−1	−2	0	0	$(x,y),(R_x,R_y)$	(xz,yz)
E_2	+2	−1	−1	+2	0	0		(x^2-y^2,xy)

TABLE A.3: Character table for C_{6v}.

$\boldsymbol{C_{8v}}$	E	$2C_8$	$2C_4$	$2(C_8)^3$	C_2	$4\sigma_v$	$4\sigma_d$	linear	quadratic
A_1	+1	+1	+1	+1	+1	+1	1	z	x^2+y^2, z^2
A_2	+1	+1	+1	+1	+1	−1	−1	R_z	
B_1	+1	−1	+1	−1	+1	+1	−1		
B_2	+1	−1	+1	−1	+1	−1	+1		
E_1	+2	$+\sqrt{2}$	0	$-\sqrt{2}$	−2	0	0	$(x,y),(R_x,R_y)$	(xz,yz)
E_2	+2	0	−2	0	+2	0	0		(x^2-y^2,xy)
E_3	+2	$-\sqrt{2}$	0	$+\sqrt{2}$	−2	0	0		

TABLE A.4: Character table for C_{8v}.

$\boldsymbol{T_d}$	E	$8C_3$	$3C_2$	$6S_4$	$6\sigma_d$	linear	quadratic	cubic
A_1	+1	+1	+1	+1	+1		$x^2+y^2+z^2$	xyz
A_2	+1	+1	+1	−1	−1			
E	+2	−1	+2	0	0		$\boldsymbol{g}(\boldsymbol{x})$	
T_1	+3	0	−1	+1	−1	(R_x,R_y,R_z)		$\boldsymbol{f}^1(\boldsymbol{x})$
T_2	+3	0	−1	−1	+1	(x,y,z)	(xy,xz,yz)	$\boldsymbol{f}^{2a}(\boldsymbol{x})$, $\boldsymbol{f}^{2b}(\boldsymbol{x})$

TABLE A.5: Character table for T_d. The quadratic polynomial is $\boldsymbol{g}(\boldsymbol{x}) = (2z^2-x^2-y^2, x^2-y^2)$. Here we have included cubic order polynomials in order to see the SOC terms relevant for bulk Dresselhaus systems: $\boldsymbol{f}^1(\boldsymbol{x}) \equiv (x[z^2-y^2], y[z^2-x^2], z[x^2-y^2])$, $\boldsymbol{f}^{2a} \equiv (x^3, y^3, z^3)$ and $\boldsymbol{f}^{2b}(\boldsymbol{x}) \equiv (x[z^2+y^2], y[z^2+x^2], z[x^2+y^2])$.

$\boldsymbol{D_{2d}}$	E	$2S_4$	C_2(z)	$2C_2'$(z)	$2\sigma_d$	linear	quadratic
A_1	+1	+1	+1	+1	+1		x^2+y^2, z^2
A_2	+1	+1	+1	−1	−1	R_z	
B_1	+1	−1	+1	+1	−1		x^2-y^2
B_2	+1	−1	+1	−1	+1	z	xy
E	+2	0	−2	0	0	$(x,y),(R_x,R_y)$	(xz,yz)

TABLE A.6: Character table for D_{2d}.

$\boldsymbol{D_4}$	E	$2C_4(z)$	C_2(z)	$2C_2'$(z)	$2C_2''$	linear	quadratic
A_1	+1	+1	+1	+1	+1		x^2+y^2, z^2
A_2	+1	+1	+1	−1	−1	z, R_z	
B_1	+1	−1	+1	+1	−1		x^2-y^2
B_2	+1	−1	+1	−1	+1		xy
E	+2	0	−2	0	0	$(x,y),(R_x,R_y)$	(xz,yz)

TABLE A.7: Character table for D_4, the point group of a square lattice. Here C_2' and C_2'' are reflections in the axes and diagonals respectively.

Appendix B

Spin-degenerate scattering

It is useful to explicitly compare the Rashba hard disk scattering results in Chapter 3 to that a spin-degenerate system. Once again we consider the potential

$$V(r) = \begin{cases} \infty & r < R \\ 0 & r > R \end{cases} \tag{B.1}$$

in 2D but without spin-orbit coupling. In this case, the wave function in the scattering region $r > R$ may be written as a linear combination of an incident plane wave and outgoing Hankel functions

$$\Psi(r,\theta) = \left(\frac{1}{\sqrt{2}}e^{ikx} + \sum_{l=-\infty}^{\infty} a_l e^{il\theta} H_l^+(kr)\right)\eta, \tag{B.2}$$

where η is an arbitrary spinor, and there is only a single wave vector $k = \sqrt{2mE}$ for each incident energy E. The matching condition $\Psi(R,\theta) = 0$ gives two degenerate equations (due to the two spinor components) that determine the only unknown coefficient

$$a_l = -\frac{i^l}{\sqrt{2}} \frac{J_l(kR)}{H_l^+(kR)}. \tag{B.3}$$

The incident and scattered current densities have magnitudes $|\vec{j}_{\text{in}}| = \frac{k}{2m}$ and $|\vec{j}_{\text{sc}}| = \frac{2}{\pi m r}|\sum_{l=-\infty}^{\infty} a_l e^{i(\theta-\pi/2)l}|^2$ respectively. Equation (2.10) then gives the differential cross section

$$\frac{d\sigma}{d\theta} = \frac{4}{\pi k}\left|\sum_{l=-\infty}^{\infty} a_l e^{i(\theta-\pi/2)l}\right|^2, \tag{B.4}$$

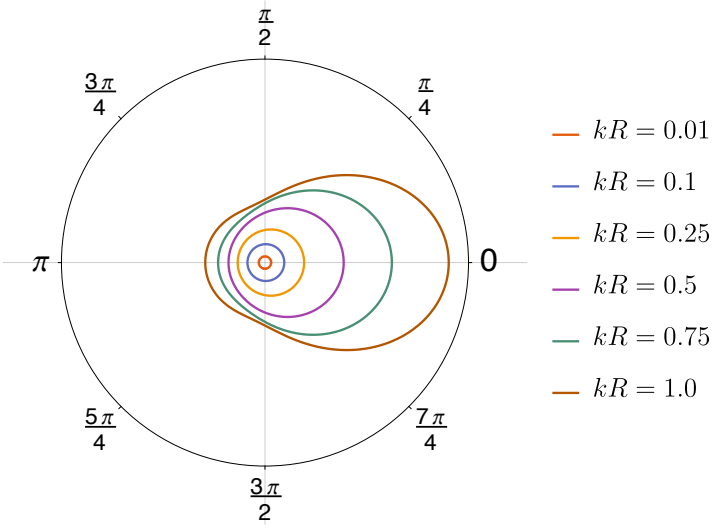

FIGURE B.1: Polar plot of differential cross section for the spin-degenerate problem with various values of kR. The radius of each curve represents the magnitude of $d\sigma/d\theta$ in units of $1/k$.

which is plotted in Fig. B.1. The cross section is isotropic in the long-wavelength limit, and forward scattering is enhanced as the wavelength is decreased.

In the long-wavelength limit, one may use the small-argument form of the Bessel functions,

$$J_l(kr) \approx \frac{\epsilon_l}{|l|!}\left(\frac{kr}{2}\right)^{|l|}, \tag{B.5}$$

$$N_l(kr) \approx \begin{cases} -\dfrac{\epsilon_l(|l|-1)!}{\pi}\left(\dfrac{2}{kr}\right)^{|l|}, & l \neq 0, \\ \dfrac{2}{\pi}\left[\ln\left(\dfrac{kr}{2}\right)+\gamma\right], & l = 0, \end{cases} \tag{B.6}$$

where γ is Euler's constant and

$$\epsilon_l = \begin{cases} 1, & l > 0, \\ (-1)^l, & l < 0. \end{cases} \tag{B.7}$$

In this limit, the coefficient (B.3) is

$$a_l \approx \begin{cases} -\dfrac{i^l}{\sqrt{2}}\left[1 - \dfrac{i}{\pi}(|l|-1)!|l|!\,(kR/2)^{2|l|}\right]^{-1}, & l \neq 0, \\ -\dfrac{1}{\sqrt{2}}\left(1 + i\dfrac{2}{\pi}\left[\ln(kR/2)+\gamma\right]\right)^{-1}, & l = 0. \end{cases} \tag{B.8}$$

The S-matrix partial-wave components are found by dividing the outgoing $H^+(kr)$ coefficients of the wavefunction by the ingoing $H^-(kr)$ coefficients:

$$S^l = 1 + \frac{a^l}{i^l/(2\sqrt{2})}. \tag{B.9}$$

From this, we may also write down the T-matrix:

$$T^l = \frac{i}{m}(S^l - 1) = \frac{ia^l}{mi^l/(2\sqrt{2})}. \tag{B.10}$$

In the low energy $k \to 0$ limit, the $l = 0$ part of Eq. (B.8) dominates and we have

$$T^{\boldsymbol{k}\boldsymbol{k}'} \approx T^0 \sim \frac{1/m}{i - \frac{1}{\pi}\ln(E/E_a)}, \tag{B.11}$$

where in this case $E_a = \frac{mR^2}{2e^{2\gamma}}$ is a parameter related to the scattering length (see, e.g., Ref. [59, 132]).

It is more common to write scattering quantities in terms of the phase shift δ_l (which is more ambiguous in the Rashba case where there are multiple scattering channels) [59]. In terms of the phase shift, the differential cross section (B.4) is written as

$$\frac{d\sigma}{d\theta} = \frac{2}{\pi k}\left| \sum_{l=-\infty}^{\infty} \sin\delta_l e^{i(l\theta+\delta_l)} \right|^2. \tag{B.12}$$

Comparison with Eq. (B.4) and (B.8) gives the phase shifts

$$\cot\delta_l = \begin{cases} -\dfrac{1}{\pi}(|l|-1)!|l|!\left(\dfrac{2}{kR}\right)^{2|l|}, & l \neq 0, \\ \dfrac{2}{\pi}\left[\ln\left(\dfrac{kR}{2}\right) + \gamma\right], & l = 0. \end{cases} \tag{B.13}$$

Note that even in the low-energy limit, the differential cross section and phase shift retain a dependence on R in contrast to the case with spin-orbit coupling. However, the singularity in the cross section at threshold due to the $1/k$ pre-factor in Eq. (B.12) is a common feature of scattering in 2D [59].

Appendix C

Symmetries of the Rashba S and T matrices

C.1 Symmetry of the S-matrix

Here we show that the symmetry of the S-matrix $S^l = (S^l)^T$ for each angular momentum component l is a consequence of the combination of two symmetries: time-reversal symmetry, and a symmetry under reflection about the x axis, i.e., symmetry under $y \to -y$.

The action of the time-reversal operator T on an arbitrary spinor $\psi(\boldsymbol{r}) = \psi_\uparrow(\boldsymbol{r})|\uparrow\rangle + \psi_\downarrow(\boldsymbol{r})|\downarrow\rangle$ (with $|\uparrow\rangle = (1,0)$ and $|\downarrow\rangle = (0,1)$ the eigenvectors of σ_z) is given by

$$T\psi(\boldsymbol{r}) = \psi_\uparrow^*(\boldsymbol{r})|\downarrow\rangle - \psi_\downarrow^*(\boldsymbol{r})|\uparrow\rangle = -i\sigma_y\psi^*(\boldsymbol{r}). \tag{C.1}$$

One can check by explicit calculation that the Hamiltonian (3.2) obeys the relation

$$\sigma_y H(r,\theta)\sigma_y = H^*(r,\theta), \tag{C.2}$$

which is a statement of time-reversal symmetry. Thus if $\psi_E(r,\theta)$ is an eigenstate of $H(r,\theta)$ with energy E, the state $T\psi_E(r,\theta) = -i\sigma_y\psi_E^*(r,\theta)$ is also an eigenstate of $H(r,\theta)$ at the same energy. Likewise, the Hamiltonian obeys the relation

$$\sigma_y H(r,\theta)\sigma_y = H(r,-\theta), \tag{C.3}$$

which is a statement of reflection symmetry about the x axis (i.e., $y \to -y$ or $\theta \to -\theta$). Indeed, because the incident plane wave propagates in the x direction and the scattering potential is rotationally symmetric, this is a symmetry of the scattering geometry (Fig. 3.2). If $\psi_E(r,\theta)$ is an eigenstate of $H(r,\theta)$ with energy E, the state $\sigma_y \psi_E(r,-\theta)$ is also an eigenstate of $H(r,\theta)$ at the same energy [47]. Combining these two symmetries, we find that $\psi_E^*(r,-\theta)$ is an eigenstate of $H(r,\theta)$ with energy E if $\psi_E(r,\theta)$ is.

We can use the fact we have just derived to constrain the form of the S-matrix. Because the scattering states (3.7) and (3.10) described by the S-matrix S^l are eigenstates of the Hamiltonian with energy E, the states $\psi_>^*(r,-\theta)$ and $\psi_<^*(r,-\theta)$ are also eigenstates of the Hamiltonian with the same energy, and should thus be described by the same S-matrix. We first introduce the notation

$$\phi_{\gtrless}^{\text{in}}(r,\theta) = \sqrt{k_{\gtrless}} \begin{pmatrix} H_l^{\mp}(k_{\gtrless} r) \\ -H_{l+1}^{\mp}(k_{\gtrless} r) e^{i\theta} \end{pmatrix}, \tag{C.4}$$

$$\phi_{\gtrless}^{\text{out}}(r,\theta) = \sqrt{k_{\gtrless}} \begin{pmatrix} H_l^{\pm}(k_{\gtrless} r) \\ -H_{l+1}^{\pm}(k_{\gtrless} r) e^{i\theta} \end{pmatrix}. \tag{C.5}$$

Because the combined action of complex conjugation and reversing the sign of θ leaves the angular factor $e^{il\theta}$ invariant, we can consider one l component at a time. Ignoring a constant multiplicative factor, for a given l and in the asymptotic region $k_{\gtrless} r \gg 1$ one has

$$\psi_>(r,\theta) \sim \phi_>^{\text{in}} + S_{>>}^l \phi_>^{\text{out}} + S_{><}^l \phi_<^{\text{out}}, \tag{C.6}$$

$$\psi_<(r,\theta) \sim \phi_<^{\text{in}} + S_{<>}^l \phi_>^{\text{out}} + S_{<<}^l \phi_<^{\text{out}}. \tag{C.7}$$

The combined action of complex conjugation and reversing the sign of θ interchanges incoming and outgoing circular waves,

$$\phi_{\gtrless}^{\text{in}}(r,-\theta)^* = \phi_{\gtrless}^{\text{out}}(r,\theta), \tag{C.8}$$

such that for a given l one has

$$\psi_>^*(r,-\theta) \sim \phi_>^{\text{out}} + (S_{>>}^l)^* \phi_>^{\text{in}} + (S_{><}^l)^* \phi_<^{\text{in}}, \tag{C.9}$$

$$\psi_<^*(r,-\theta) \sim \phi_<^{\text{out}} + (S_{<>}^l)^* \phi_>^{\text{in}} + (S_{<<}^l)^* \phi_<^{\text{in}}. \tag{C.10}$$

Because the scattering states (C.9) and (C.10) are degenerate, an arbitrary linear superposition of those two states is also a valid scattering state at the same energy. In particular, we can construct linear superpositions $\tilde{\psi}_{>}(r,\theta)$ and $\tilde{\psi}_{<}(r,\theta)$ that take the standard form (C.6)-(C.7) of an incoming circular wave $\phi^{\text{in}}_{\gtrless}$ plus outgoing circular waves $\phi^{\text{out}}_{\gtrless}$ multiplied by appropriate coefficients,

$$\tilde{\psi}_{>}(r,\theta) \sim \phi^{\text{in}}_{>} + \left(\frac{S^l_{<<}}{\det S^l}\right)^* \phi^{\text{out}}_{>} - \left(\frac{S^l_{><}}{\det S^l}\right)^* \phi^{\text{out}}_{<}, \tag{C.11}$$

$$\tilde{\psi}_{<}(r,\theta) \sim \phi^{\text{in}}_{<} - \left(\frac{S^l_{<>}}{\det S^l}\right)^* \phi^{\text{out}}_{>} + \left(\frac{S^l_{>>}}{\det S^l}\right)^* \phi^{\text{out}}_{<}. \tag{C.12}$$

Comparing with Eq. (C.6)-(C.7), we obtain the relations

$$\begin{aligned} S^l_{>>} &= \left(\frac{S^l_{<<}}{\det S^l}\right)^*, \quad S^l_{><} = -\left(\frac{S^l_{><}}{\det S^l}\right)^*, \\ S^l_{<>} &= -\left(\frac{S^l_{<>}}{\det S^l}\right)^*, \quad S^l_{<<} = \left(\frac{S^l_{>>}}{\det S^l}\right)^*. \end{aligned} \tag{C.13}$$

Using the inverse of the S-matrix

$$(S^l)^{-1} = \frac{1}{\det S^l}\begin{pmatrix} S^l_{<<} & -S^l_{><} \\ -S^l_{<>} & S^l_{>>} \end{pmatrix}, \tag{C.14}$$

as well as its unitarity $(S^l)^{-1}_{\alpha\beta} = S^*_{\beta\alpha}$, the first and fourth relations in (C.13) are trivial and the second and third give

$$S^l_{><} = S^l_{<>}, \tag{C.15}$$

i.e., $S^l = (S^l)^T$.

C.2 Symmetry of the T-matrix

Besides rotation symmetry, which allows us to expand the T-matrix in circular harmonics with coefficients $T^l(E)$, the Rashba T-matrix for circular impurity potentials is also symmetric under reflections in the $y-z$ plane. In the spin basis, this means

$$\sigma_x T(M_x(\boldsymbol{k},\boldsymbol{k}'))\sigma_x = T(\boldsymbol{k},\boldsymbol{k}'), \tag{C.16}$$

where M_x maps k_x to $-k_x$. Transforming to the helicity basis, this condition becomes

$$(-ie^{-i\phi_{\boldsymbol{k}}}\sigma_z)T(M_x(\boldsymbol{k},\boldsymbol{k}'))(ie^{i\phi_{\boldsymbol{k}'}}\sigma_z) = T(\boldsymbol{k},\boldsymbol{k}'), \tag{C.17}$$

where $\phi_{\boldsymbol{k}}$ is the in-plane angle associated with $\boldsymbol{k}$. Both sides may be expanded in circular harmonics,

$$\sum_l e^{-i(l+1)(\phi_{\boldsymbol{k}}-\phi_{\boldsymbol{k}'})}\sigma_z T^l(E)\sigma_z = \sum_l e^{il(\phi_{\boldsymbol{k}}-\phi_{\boldsymbol{k}'})}T^l(E). \tag{C.18}$$

Shifting $l \to -l-1$ on the left side, we get

$$\sigma_z T^{-l-1}(E)\sigma_z = T^{-l}(E). \tag{C.19}$$

For the lower helicity component T_{--}, this means

$$T^{l-1}(E) = T^{-l}(E). \tag{C.20}$$

Note that this condition guarantees detailed balance in the Boltzmann scattering rate (5.3), since

$$\begin{aligned}
|T^{\boldsymbol{k}'\boldsymbol{k}}|^2 &= \left|\sum_l T^l(E)e^{il(\phi_{\boldsymbol{k}'}-\phi_{\boldsymbol{k}})}\right|^2 && \text{(C.21)}\\
&= \left|\sum_l T^{-l}(E)e^{il(\phi_{\boldsymbol{k}}-\phi_{\boldsymbol{k}'})}\right|^2 && \text{(C.22)}\\
&= \left|\sum_l T^{l-1}(E)e^{il(\phi_{\boldsymbol{k}}-\phi_{\boldsymbol{k}'})}\right|^2 && \text{(C.23)}\\
&= \left|\sum_l T^{l}(E)e^{il(\phi_{\boldsymbol{k}}-\phi_{\boldsymbol{k}'})}\right|^2 |e^{i(\phi_{\boldsymbol{k}}-\phi_{\boldsymbol{k}'})}|^2 && \text{(C.24)}\\
&= |T^{\boldsymbol{k}\boldsymbol{k}'}|^2. && \text{(C.25)}
\end{aligned}$$

Another important consequence of this symmetry is the identity

$$\int_0^{2\pi}\frac{d\phi}{2\pi}\sin\phi|T^{\boldsymbol{k}\boldsymbol{k}'}|^2 = 0, \tag{C.26}$$

where ϕ is the angle between $\boldsymbol{k}$ and $\boldsymbol{k}'$. This follows from expanding the left-hand side in circular harmonics to get

$$\begin{aligned} & \frac{1}{2i}\sum_l \left(T^l(E)^* T^{l-1}(E) - T^l(E)^* T^{l+1}(E) \right) \\ = \; & \frac{1}{2i}\sum_l \left(T^{-l}(E)^* T^l(E) - T^{-l}(E)^* T^l(E) \right) \qquad \text{(C.27)} \\ = \; & 0, \qquad \text{(C.28)} \end{aligned}$$

where we used mirror symmetry and shifted the summation index in each term.

Appendix D

Rashba Green's function

Here we derive the retarded position-space Green's function. A similar derivation can be found in Ref. [43], but we include it here for completeness and to standardize the notation.

We may write the Green's function as a 2×2 matrix in spin-space,

$$G^R(\boldsymbol{r},\boldsymbol{r}';E) = \int \frac{d^2\boldsymbol{k}}{4\pi^2} \frac{e^{i\boldsymbol{k}\cdot(\boldsymbol{r}-\boldsymbol{r}')}}{(E-E_0-\frac{k^2}{2m})^2-(\lambda k)^2+i\epsilon} \begin{pmatrix} E-E_0-\frac{k^2}{2m} & i\lambda k e^{-i\theta_{\boldsymbol{k}}} \\ -i\lambda k e^{i\theta_{\boldsymbol{k}}} & E-E_0-\frac{k^2}{2m} \end{pmatrix}. \tag{D.1}$$

The angular integral is easily evaluated in terms of Bessel functions. For the diagonal part, one finds

$$\begin{aligned} G^R_{\sigma\sigma}(\boldsymbol{r},\boldsymbol{r}';E) &= -\frac{m}{2\pi}\int_0^\infty dk\, J_0(k|\boldsymbol{r}-\boldsymbol{r}'|) \\ &\quad \times\left(\frac{k}{(k+k_0)^2-2mE-i\epsilon}+\frac{k}{(k-k_0)^2-2mE-i\epsilon}\right). \end{aligned} \tag{D.2}$$

For any energy E, we designate the on-shell upper and lower helicity wave vectors by

$$k_\pm = \mp m\lambda+\sqrt{2mE} \tag{D.3}$$

$$= k_0(\delta\mp 1). \tag{D.4}$$

These determine the poles of the Green's function, which are seen from (D.2) by partial fraction decomposition,

$$\begin{aligned} G^R_{\sigma\sigma}(\boldsymbol{r},\boldsymbol{r}';E) &= -\frac{m}{2\pi}\int_0^\infty dk \frac{J_0(k|\boldsymbol{r}-\boldsymbol{r}'|)}{k_- + k_+} \\ &\quad \times\left(\frac{k_+}{k-k_+-i\epsilon}+\frac{k_-}{k+k_-+i\epsilon}+\frac{k_-}{k-k_--i\epsilon}+\frac{k_+}{k+k_++i\epsilon}\right). \end{aligned}$$

The first and last terms may be combined, as well as the second and third to give

$$\begin{aligned} G^R_{\sigma\sigma}(\boldsymbol{r},\boldsymbol{r}';E) &= -\frac{m}{\pi(k_-+k_+)}\left(k_+\int_0^\infty dk \frac{kJ_0(k|\boldsymbol{r}-\boldsymbol{r}'|)}{k^2-(k_++i\epsilon)^2}\right. \\ &\quad \left. +k_-\int_0^\infty dk\frac{kJ_0(k|\boldsymbol{r}-\boldsymbol{r}'|)}{k^2-(k_-+i\epsilon)^2}\right). \end{aligned} \tag{D.5}$$

These last integrals may be evaluated with a useful identity,

$$\int_0^\infty dt\, J_\nu(at)\frac{t}{t^2-z^2} = \frac{\pi i}{2}H^+_\nu(az), \tag{D.6}$$

valid for $a>0$, $\mathrm{Im}\, z>0$. Thus,

$$G^R_{\sigma\sigma}(\boldsymbol{r},\boldsymbol{r}';E) = -\frac{im}{2(k_-+k_+)}\left(k_+H^+_0(k_+|\boldsymbol{r}-\boldsymbol{r}'|)+k_-H^+_0(k_-|\boldsymbol{r}-\boldsymbol{r}'|)\right). \tag{D.7}$$

Next we evaluate the off-diagonal components. The angular integral again gives a Bessel function

$$G^R_{\sigma\sigma'}(\boldsymbol{r},\boldsymbol{r}';E) = \mp\frac{1}{2\pi}\int_0^\infty dk \frac{\lambda k^2 J_1(k|\boldsymbol{r}-\boldsymbol{r}'|)e^{\mp i\theta_{\boldsymbol{r}-\boldsymbol{r}'}}}{(E-E_0-\frac{k^2}{2m})^2-(\lambda k)^2+i\epsilon}. \tag{D.8}$$

Here the top sign is for $\sigma=\uparrow,\sigma'=\downarrow$, and the bottom is for $\sigma=\downarrow,\sigma'=\uparrow$. Proceeding with the radial integral as before, we obtain

$$\begin{aligned} G^R_{\sigma\sigma'}(\boldsymbol{r},\boldsymbol{r}';E) &= \pm\frac{m}{2\pi}e^{\mp i\theta_{\boldsymbol{r}-\boldsymbol{r}'}}\int_0^\infty dk\, k\frac{J_1(k|\boldsymbol{r}-\boldsymbol{r}'|)}{k_-+k_+} \\ &\quad \times\left(\frac{1}{k-k_+-i\epsilon}-\frac{1}{k+k_-+i\epsilon}-\frac{1}{k-k_--i\epsilon}+\frac{1}{k+k_++i\epsilon}\right). \end{aligned} \tag{D.9}$$

Both Bessel and Hankel functions satisfy the differential relation

$$\frac{\partial}{\partial a} f_0(ax) = -x f_1(ax), \tag{D.10}$$

so upon combining the first and last terms as well as the second and third terms in (D.9), we may write

$$\begin{aligned} G^R_{\sigma\sigma'}(\boldsymbol{r},\boldsymbol{r}';E) &= \mp\frac{m}{\pi(k_+ + k_-)} e^{\mp i\theta_{\boldsymbol{r}-\boldsymbol{r}'}} \\ &\times \frac{\partial}{\partial|\boldsymbol{r}-\boldsymbol{r}'|}\int_0^\infty dk\, J_0(k|\boldsymbol{r}-\boldsymbol{r}'|)\left(\frac{-k}{k^2-(k_- + i\epsilon)^2} + \frac{k}{k^2-(k_+ + i\epsilon)^2}\right). \end{aligned} \tag{D.11}$$

Using (D.6), we arrive at

$$G^R_{\sigma\sigma'}(\boldsymbol{r},\boldsymbol{r}';E) = \mp\frac{im}{2(k_- + k_+)}\left(k_- H_1^+(k_-|\boldsymbol{r}-\boldsymbol{r}'|) - k_+ H_1^+(k_+|\boldsymbol{r}-\boldsymbol{r}'|)\right) e^{\mp i\theta_{\boldsymbol{r}-\boldsymbol{r}'}}. \tag{D.12}$$

Appendix E

Derivation of the Rashba S and T matrix relation

In this appendix we derive the relation between the Rashba S and T matrices for energies $E < E_0$ using two different approaches.

E.1 First derivation

Our first approach will be to write down the Lippmann-Schwinger equation in terms of the S-matrix, then in terms of the T-matrix (as done in Chapter 4), and then compare the two to read off the relation between S and T.

We start by using the definition of the S-matrix as the unitary transformation from asymptotic incoming to asymptotic outgoing states. Schematically, in the $k_{\gtrless}$ basis,

$$\psi_{>}(\boldsymbol{r};E) \sim \psi_{>}^{\text{in}} + S_{>>}\phi_{>}^{\text{out}} + S_{<>}\phi_{<}^{\text{out}}, \tag{E.1}$$

$$\psi_{<}(\boldsymbol{r};E) \sim \psi_{<}^{\text{in}} + S_{><}\phi_{>}^{\text{out}} + S_{<<}\phi_{<}^{\text{out}}. \tag{E.2}$$

In Eqs. (3.7), (3.10), the form of the S-matrix for lower-helicity scattering off of a finite range, circularly symmetric potential was obtained. Using a slightly modified notation, we summarize these results by writing the asymptotic wavefunction outside

such a potential as

$$\psi_\mu(\boldsymbol{r};E) \approx \psi_\mu^{\text{in}}(\boldsymbol{r};E) + 2m\sqrt{\frac{i}{k_\mu}}\sum_{\nu=>,<} f_{\mu\nu}(\theta_{\boldsymbol{r}})\frac{e^{is_\nu k_\nu r}}{\sqrt{r}}\eta^{s_\nu}(\theta_{\boldsymbol{r}}). \tag{E.3}$$

Here, the indices μ,ν indicate the magnitude of the wavevector $k_{\gtrless}$ as discussed above, $s_\mu \equiv \text{sgn}(k_\mu - k_0)$, and $\psi_\mu(\boldsymbol{r};E) \equiv \psi_{\boldsymbol{k}}(\boldsymbol{r})|_{\boldsymbol{k}=k_\mu\hat{\boldsymbol{x}}}$. The common spinor factor $\eta^{s_\mu}(\theta)$ is formally equivalent to the definition (1.24) due to the fact that the group velocity for the $<$ and $>$ states are oppositely directed as discussed in Chapter 3. The factor of $2m\sqrt{i/k_\mu}$ in front of the sum is chosen to make $f_{\mu\nu}$ consistent with the conventional *scattering amplitude* in two dimensions [57]. With these conventions, the scattering amplitude has the following relation to the S-matrix expanded in partial waves,

$$f_{\mu\nu}(\theta_{\boldsymbol{r}}) = \frac{e^{-\frac{i\pi}{4}(1+s_\nu)}}{4m}\sqrt{\frac{2}{\pi}}\sum_{l=-\infty}^{\infty} e^{il(\theta_{\boldsymbol{r}}+\frac{\pi}{2}(1-s_\nu))}(S^l_{\mu\nu} - \mathbb{I}_{\mu\nu}). \tag{E.4}$$

The strategy now is to simply equate (4.11) and (E.3). For the $k_>$ term in Eq. (4.11), we note that since $\theta_{\boldsymbol{k}_>} = \theta_{\boldsymbol{r}}$ and $\theta_{\boldsymbol{k}} = 0$,

$$\eta^-(\theta_{\boldsymbol{r}})^\dagger T^{\boldsymbol{k}_>\boldsymbol{k}}\eta^-(0) = T^{\boldsymbol{k}_>\boldsymbol{k}}_{--}, \tag{E.5}$$

which is the component of the helicity transform of T involving only transitions within the negative helicity state. For the $k_<$ term, we use the fact that $\theta_{-\boldsymbol{k}_<} = \theta_{\boldsymbol{r}} + \pi$ to write the eigenspinors as

$$\eta^+(\theta_{\boldsymbol{r}}) = \frac{1}{\sqrt{2}}\begin{pmatrix}1\\ -ie^{i\theta_{\boldsymbol{r}}}\end{pmatrix} = \frac{1}{\sqrt{2}}\begin{pmatrix}1\\ ie^{i(\theta_{\boldsymbol{r}}+\pi)}\end{pmatrix} = \eta^-(\theta_{-\boldsymbol{k}_<}), \tag{E.6}$$

which makes it clear that

$$\eta^+(\theta_{\boldsymbol{r}})^\dagger T^{-\boldsymbol{k}_<\boldsymbol{k}}\eta^-(0) = T^{-\boldsymbol{k}_<\boldsymbol{k}}_{--}. \tag{E.7}$$

The Lippman-Schwinger equation finally reads

$$\psi_\mu(\boldsymbol{r};E) \approx \psi_\mu^{\text{in}}(\boldsymbol{r};E) + \frac{me^{-\frac{i\pi}{4}}}{k_< - k_>}\sqrt{\frac{2i}{\pi r}}\sum_\nu \sqrt{k_\nu}e^{is_\nu(k_\nu r+1)}T^{s_\nu\boldsymbol{k}_\nu\boldsymbol{k}_\mu}_{--}\eta^{s_\nu}(\theta_{\boldsymbol{r}})e^{-\frac{i\pi}{4}s_\nu}. \tag{E.8}$$

Comparing (E.8) to (E.3), we may simply read off the relation between the T-matrix and scattering amplitude:

$$T_{--}^{s_\nu \boldsymbol{k}_\nu \boldsymbol{k}_\mu} = \sqrt{2\pi}\frac{(k_< - k_>)}{\sqrt{k_\mu k_\nu}} e^{-\frac{i\pi}{4}(1+s_\nu)} f_{\mu\nu}(\theta_{\boldsymbol{r}}), \tag{E.9}$$

or, in terms of the S-matrix written in (E.4),

$$T_{--}^{\boldsymbol{k}_\nu \boldsymbol{k}_\mu} = \frac{i}{m}\frac{k_0\delta}{\sqrt{k_\mu k_\nu}} \sum_{l=-\infty}^{\infty} e^{il\theta}(S_{\mu\nu}^l - \mathbb{I}_{\mu\nu}), \tag{E.10}$$

using $k_> - k_< = 2k_0\delta$, and letting $\theta \equiv \theta_{\boldsymbol{r}} = \theta_{\boldsymbol{k}_\nu} - \theta_{\boldsymbol{k}_\mu}$. We may expand the T-matrix in partial wave components as well, which allows us to invert (E.10) to get

$$S_{\mu\nu}^l = \mathbb{I}_{\mu\nu} - \frac{im}{k_0\delta}\sqrt{k_\mu k_\nu} T^l(k_\nu, k_\mu), \tag{E.11}$$

where $T_{--}^{\boldsymbol{k}_\nu \boldsymbol{k}_\mu} = \sum_{l=-\infty}^{\infty} T^l(k_\nu, k_\mu) e^{il\theta}$.

E.2 Second derivation

The above approach was based on an expression for the wavefunction, but we know that scattering quantities can be derived independent of the wavefunction. Our second approach will be to express the formal relation between S and T, Eq. (2.18), in the low-energy Rashba basis.

Any state with energy $E < E_0$ in this system is completely characterized by three quantum numbers: energy, angular momentum, and channel index $s_\mu = \mathrm{sgn}(k_\mu - k_0)$;

$$|\psi\rangle = |E, l, s_\mu\rangle. \tag{E.12}$$

Since these are eigenstates of the unperturbed Hamiltonian, we must have

$$\begin{aligned} 0 &= (H_0 - E)|E, l, s_\mu\rangle \\ &= \left(\frac{k^2}{2m} - \lambda k - E\right)\langle \boldsymbol{k}, -|E, l, s_\mu\rangle, \end{aligned} \tag{E.13}$$

where we have used the fact that H_0 is diagonal in the helicity basis $|\boldsymbol{k}, \pm\rangle$. The overlap above is nontrivial only if

$$\langle \boldsymbol{k}, -|E, l, s_\mu\rangle \propto \delta\left(\frac{k^2}{2m} - \lambda k - E\right). \tag{E.14}$$

The constant of proportionality is chosen to satisfy the orthonormality conditions

$$\langle E', l', s_\nu|E, l, s_\mu\rangle = \delta_{ll'}\delta_{\mu\nu}\delta(E - E'), \tag{E.15}$$

$$\langle \boldsymbol{k}', -|\boldsymbol{k}, -\rangle = (2\pi)^2\delta(\boldsymbol{k} - \boldsymbol{k}'). \tag{E.16}$$

One can check that the appropriate change of basis is given by

$$\langle \boldsymbol{k}, -|E, l, s_\mu\rangle = \sqrt{\frac{2\pi|k_0 - k|}{mk}} e^{il\theta_{\boldsymbol{k}}}\delta_{s_\mu, s(k)}\delta\left(\frac{k^2}{2m} - \lambda k - E\right), \tag{E.17}$$

where $s(k) \equiv \mathrm{sgn}(k - k_0)$.

This conversion allows us to write the momentum-space T-matrix starting with the S-matrix in the E, l, s_μ basis. From (2.18),

$$T^{\boldsymbol{k}\boldsymbol{k}'}_{--}\delta(E(k) - E'(k')) = \frac{i}{2\pi}(S - \mathbb{I})_{\boldsymbol{k}\boldsymbol{k}'} \tag{E.18}$$

$$\begin{aligned} &= i\sum_{s_\nu, s_\rho}\sum_{l=-\infty}^{\infty}\int dE\sqrt{\frac{|k_0 - k|}{mk}}\delta\left(\frac{k^2}{2m} - \lambda k - E\right)e^{il\theta_{\boldsymbol{k}}}\delta_{s(k), s_\nu} \\ &\quad \times(S^l_{\nu\rho}(E) - \delta_{\nu\rho})\sqrt{\frac{|k_0 - k'|}{mk'}}\delta\left(\frac{k'^2}{2m} - \lambda k' - E\right)e^{-il\theta_{\boldsymbol{k}'}}\delta_{s_\rho, s(k')}, \end{aligned} \tag{E.19}$$

where we used the fact that the S-matrix is diagonal in l and E. Thus we finally have

$$T^{\boldsymbol{k}\boldsymbol{k}'}_{--}(E) = \frac{i}{m}\sqrt{\frac{|k_0 - k||k_0 - k'|}{kk'}}\sum_{l=-\infty}^{\infty} e^{il\theta}\left(S^l_{s(k)s(k')} - \delta_{s(k)s(k')}\right). \tag{E.20}$$

Letting $k = k_\nu$, $k' = k_\mu$, and noting that $|k_0 - k_\nu| = |k_0 - k_\mu| = k_0\delta$, we recover (E.10).

Appendix F

Derivations of important integrals

In this appendix we go through the technical derivations of all the important integrals that enter the low-energy Rashba scattering and transport quantities of Part 1.

F.1 The full Born integral I_l^-

We start with the proof of (4.36). Beginning from the definition of the integral I_l^- (4.32), we proceed by making the following substitutions: first, recall that $q = k_0(1+\epsilon)$, so that

$$I_-^l = \frac{m}{2\pi}\int_{-\Lambda}^{\Lambda} d\epsilon \frac{(1+\epsilon)[V^l(k_0,q)+V^{l+1}(k_0,q)]}{\delta^2-\epsilon^2+i\eta}. \tag{F.1}$$

Then, let $x = \delta^2 - \epsilon^2$. This requires splitting the integration region into $\epsilon = \sqrt{\delta^2-x} > 0$ and $\epsilon = -\sqrt{\delta^2-x} < 0$:

$$\begin{aligned} I_-^l &= \frac{m}{4\pi}\int_{\delta^2-\Lambda^2}^{\delta^2} dx \frac{(1+\sqrt{\delta^2-x})[V_+^l+V_+^{l+1}]}{(x+i\eta)\sqrt{\delta^2-x}} \\ &\quad + \frac{m}{4\pi}\int_{\delta^2-\Lambda^2}^{\delta^2} dx \frac{(1-\sqrt{\delta^2-x})[V_-^l+V_-^{l+1}]}{(x+i\eta)\sqrt{\delta^2-x}}, \end{aligned} \tag{F.2}$$

where we have defined $V_\pm^l \equiv V^l(k_0, k_0(1\pm\sqrt{\delta^2-x}))$. We separate these integrals into a principal part and an imaginary part using $\lim_{\epsilon\to 0}\int_a^b \frac{f(x)}{x\pm i\epsilon}dx = \mathcal{P}\int_a^b \frac{f(x)}{x}dx \mp i\pi f(0)$ (where $a < 0 < b$ and $\mathcal{P}$ indicates the principal value). The imaginary part of these

integrals is then simply,

$$\mathrm{Im}\, I_-^l = -\frac{m}{4\delta}\Big((1+\delta)[V_+^l + V_+^{l+1}] + (1-\delta)[V_-^l + V_-^{l+1}]\Big)\Big|_{x=0}. \tag{F.3}$$

Expanding about $\delta = 0$ gives

$$\mathrm{Im}\, I_-^l = -\frac{m}{2\delta}[V^l(k_0,k_0) + V^{l+1}(k_0,k_0)] + \mathcal{O}(\delta). \tag{F.4}$$

Note that the interference between virtual states with $q < k_0$ and $q > k_0$ causes the cancellation of the $\mathcal{O}(1)$ term in (F.4).

The only thing left is to consider the real (or principal) part of (F.2). We will show that this term gives the cutoff-dependent corrections to the T-matrix (4.37). The trick is to isolate the momentum dependence of the potential by making use of the following multiplication theorem for Bessel functions [133],

$$J_\nu(\lambda z) = \lambda^\nu \sum_{k=0}^{\infty} \frac{(-1)^k(\lambda^2-1)^k(z/2)^k}{k!} J_{\nu+k}(z). \tag{F.5}$$

We may apply this to (4.24) to first isolate the angular dependence,

$$\begin{aligned} V^l(k_0,q) &= \sum_{k=0}^{\infty}\frac{1}{k!}\int_0^{2\pi}\frac{d\theta}{2\pi}2^{-k}(e^{i\theta}+e^{-i\theta})^k e^{il\theta} \\ &\quad\times\int_0^\infty dr\, rV(r)\left(\frac{k_0 r}{\sqrt{2}}\sqrt{1+\epsilon}\right)^k J_k(\sqrt{2}k_0 r\sqrt{1+\epsilon}), \end{aligned} \tag{F.6}$$

where convergence of the infinite series allows us to take it outside the integral. The θ integral is easily evaluated with the binomial theorem,

$$V^l(k_0,q) = \sum_{k=0}^{\infty}\frac{2^{-k}}{k!}\sum_{n=0}^{k}\binom{k}{n}\delta_{n,\frac{k+l}{2}}\int_0^\infty dr\, rV(r)\left(\frac{k_0 r}{\sqrt{2}}\sqrt{1+\epsilon}\right)^k J_k(\sqrt{2}k_0 r\sqrt{1+\epsilon}). \tag{F.7}$$

Making a change of summation variables $k \to |l| + 2k$, and applying the same multiplication theorem to the remaining Bessel function, we get

$$\begin{aligned} V^l(k_0, q) &= \sum_{k=0}^{\infty} \frac{2^{-\frac{3}{2}(|l|+2k)}}{(k+|l|)!k!}(1+\epsilon)^{|l|+2k} \sum_{n=0}^{\infty} \frac{(-1)^n \epsilon^n}{n!} \\ &\quad \times \int_0^{\infty} dr\, rV(r) \frac{(k_0 r)^{|l|+2k+n}}{2^{n/2}} J_{|l|+2k+n}(\sqrt{2}k_0 r), \end{aligned} \tag{F.8}$$

or equivalently,

$$V_{\pm}^l = \sum_{n=0}^{\infty}\sum_{k=0}^{\infty} f_{nk|l|} \left(1 \pm \sqrt{\delta^2 - x}\right)^{|l|+2k} \left(\pm\sqrt{\delta^2 - x}\right)^n, \tag{F.9}$$

where he have defined

$$f_{nk|l|} \equiv \frac{2^{-\frac{3}{2}(|l|+2k+n/3)}}{(k+|l|)!k!} \frac{(-1)^n}{n!} \int_0^{\infty} dr\, rV(r)(k_0 r)^{|l|+2k+n} J_{|l|+2k+n}(\sqrt{2}k_0 r). \tag{F.10}$$

Inserting this into (F.2) gives

$$\begin{aligned} \mathrm{Re}\, I_-^l &= \frac{m}{4\pi} \sum_{n=0}^{\infty}\sum_{k=0}^{\infty} f_{nk|l|} \mathcal{P} \int_{\delta^2-\Lambda^2}^{\delta^2} \frac{dx}{x\sqrt{\delta^2 - x}} \Big[(\sqrt{\delta^2 - x})^n (1 + \sqrt{\delta^2 - x})^{|l|+2k+1} \\ &\quad + (-1)^n (\sqrt{\delta^2 - x})^n (1 - \sqrt{\delta^2 - x})^{|l|+2k+1} \Big] + (l \to l+1), \end{aligned} \tag{F.11}$$

where the last line means we add the previous lines with l replaced by $l+1$. These integrals may be solved exactly, but here we only consider the lowest-order terms in the small parameter $\sqrt{\delta^2 - x} < \Lambda \ll 1$. The square brackets above may be expanded in this parameter to give $\delta_{n,0} + \mathcal{O}(\delta^2 - x)$. The fact that no terms of order $\sqrt{\delta^2 - x}$ appear in these brackets is due to the interference between $q < k_0$ and $q > k_0$ states. It is these absent terms that would have yielded the logarithmic dependence $\ln(\delta/\Lambda)$ were this conventional 2D scattering. With this approximation, the integrals are readily evaluated as

$$\mathrm{Re}\, I_-^l \approx \frac{m}{2\pi} \sum_{k=0}^{\infty} \frac{2}{\Lambda} \left(f_{0k|l|} + f_{0k|l+1|}\right), \tag{F.12}$$

where the terms neglected in this approximation are $\mathcal{O}(\Lambda)$. Noting that

$$\sum_{k=0}^{\infty} f_{0k|l|} = V^l(k_0, k_0), \tag{F.13}$$

we summarize this result as

$$\mathrm{Re}\, I_-^l \approx \frac{m}{\pi\Lambda}\left(V^l(k_0,k_0) + V^{l+1}(k_0,k_0)\right). \tag{F.14}$$

Thus we can approximate the T-matrix by

$$T_{--}^l \approx \frac{\frac{1}{2}[V^l(k_0,k_0) + V^{l+1}(k_0,k_0)]}{1 + \frac{m}{2}(\frac{i}{\delta} - \frac{2}{\pi\Lambda})[V^l(k_0,k_0) + V^{l+1}(k_0,k_0)]}, \tag{F.15}$$

which is linear in δ to leading order, with a $\mathcal{O}(\delta^2)$ correction to subleading order. The correction to the approximation I_-^l contributes to $\mathcal{O}(\delta^3)$. Now one might make the following objection. The first approximation we made in Sec. 4.2 was $V_{ji}(\boldsymbol{k}_\nu, \boldsymbol{k}_\mu) = V_{ji}(k_0\hat{\boldsymbol{k}}_\nu, k_0\hat{\boldsymbol{k}}_\mu) + \mathcal{O}(\delta)$ and $V_{ji}(\boldsymbol{k}_\nu, \boldsymbol{q}) = V_{ji}(k_0\hat{\boldsymbol{k}}_\nu, \boldsymbol{q}) + \mathcal{O}(\delta)$. A glance at the Born series (4.25) suggests that there will be corrections to the T-matrix of order δ as well. However, this is not the case because of the nonperturbative nature of the Born series. To be specific, let T' be the corrections in the T-matrix due to the $\mathcal{O}(\delta)$ corrections in the potential,

$$T = T^0 + T', \qquad V = V^0 + \delta V', \tag{F.16}$$

where T^0 is the leading-order T-matrix approximation that was just derived. In terms of operators, the Born series now reads

$$T' = \delta V'(1 + G^+T^0) + (V^0 + \delta V')G^+T'. \tag{F.17}$$

We can then apply the same arguments as before. In terms of helicity and momentum-space components, the right-hand side of this equation is independent of $\boldsymbol{k}_\nu$, and so T' is as well. Expanding in partial waves and ignoring interband scattering gives

$$\begin{aligned}\sum_{l=-\infty}^{\infty} T'^l_{--}(k_\mu)e^{il\theta} &= \sum_{l=-\infty}^{\infty} e^{il\theta}\left\{\frac{\delta}{2}\left([V'^l(k_0,k_0) + V'^{l+1}(k_0,k_0)] + 2I_-^l T_{--}^{0l}(k_\mu)\right)\right. \\ &+ \left. T'^l_{--}(k_\mu)\left[I_-^l + \delta\int\frac{dq}{2\pi}q\left(V'^l(k_0,q) + V'^{l+1}(k_0,q)\right)G_{--}^+(q)\right]\right\}.\end{aligned} \tag{F.18}$$

Defining

$$I'^{l}_{-} \equiv \int \frac{dq\, q}{4\pi}(V'^{l}(k_0,q) + V'^{l+1}(k_0,q))G^{+}_{--}(q), \tag{F.19}$$

and solving for T'^{l}_{--} gives

$$T'^{l}_{--} = \delta \frac{\frac{1}{2}(V'^{l}(k_0,k_0) + V'^{l+1}(k_0,k_0)) + T^{0l}_{--} I^{l}_{-}}{1 - I^{l}_{-} - \delta I'^{l}_{-}}. \tag{F.20}$$

However, we know that to lowest order, $I^{l}_{-} \sim 1/\delta$ and $T^{0l}_{--} \sim \delta$, so the numerator above is constant. Meanwhile, the derivation of I^{l}_{-} did not depend on the details of the potential components $V^{l}(k_0,q)$ and so applies equally to I'^{l}_{-}, giving $I'^{l}_{-} \sim 1/\delta$. The denominator is therefore dominated by the I^{l}_{-} term so that

$$T'^{l}_{--} \sim \delta^2. \tag{F.21}$$

Hence our approximation T^{0l}_{--} is valid to order δ^2 (with an additional $\mathcal{O}(\Lambda)$ coming from the real part).

F.2 The self-consistent full Born integral I^{l}_{-}

We now derive the low-energy form of I^{l}_{-} [equation (4.32)], where G^{+}_{--} is the *full* self-consistent Green's function used in Chapter 5. Since the Green's function now depends on an unknown self-energy, we must take a different tactic than was used in the previous section. This integral governs the energy dependence of the T-matrix and therefore the self-energy via

$$\Sigma(E) = \frac{n_i}{m} \sum_{l=-\infty}^{\infty} \frac{\delta^{*}_{l}}{1 - I^{l}_{-}} \tag{F.22}$$

(see Eqs. (5.38) and (4.34)). We use the same cutoff scheme as before: $k_0(1-\Lambda) < k < k_0(1+\Lambda)$ with $\Lambda \ll 1$. Letting $\epsilon = (q - k_0)/k_0$, we have

$$I^{l}_{-} = \frac{m}{2\pi} \int_{-\Lambda}^{\Lambda} d\epsilon f(\epsilon; E), \tag{F.23}$$

where

$$f(\epsilon; E) \equiv \frac{(1+\epsilon)[V^{l}(k_0, k_0(1+\epsilon)) + V^{l+1}(k_0, k_0(1+\epsilon))]}{(E+\mu)/E_0 - \epsilon^2 - \Sigma(E)/E_0}. \tag{F.24}$$

The integrand $f(\epsilon; E)$ has two poles located at $\epsilon = \pm z$, where

$$z \equiv \sqrt{(E+\mu)/E_0 - \Sigma(E)/E_0}. \tag{F.25}$$

The presence of the unknown function $\Sigma(E)$ in the denominator of Eq. (F.24) is what makes this integral more complicated than the one computed in Appendix F.1. Nonetheless, we can proceed by considering a semicircular contour of radius Λ through the upper half-plane, so that

$$I_-^l = mi \operatorname*{Res}_{\epsilon=z} f(\epsilon; E) - \frac{mi\Lambda}{2\pi} \int_0^\pi d\phi \, e^{i\phi} f(\Lambda e^{i\phi}; E). \tag{F.26}$$

Keeping terms in the numerator of $f(\Lambda e^{i\phi}; E)$ at lowest order in Λ, we have

$$I_-^l = mi \operatorname*{Res}_{\epsilon=z} f(\epsilon; E) - \frac{i\Lambda\delta_l^*}{\pi} \int_0^\pi \frac{d\phi \, e^{i\phi}}{z^2 - \Lambda^2 e^{2i\phi}}, \tag{F.27}$$

where we have discarded the $\mathcal{O}(\Lambda)$ terms in the expansion of $V^l(k_0, k_0(1+\Lambda e^{i\phi}))$ since these are suppressed by an additional factor of $k_0 R$ that we take to be small. Each pole is located a distance z from the origin. We choose our cutoff to be sufficiently large such that $|z| < \Lambda$, which ensures that the self-energy has no cutoff dependence to leading order. Of course, we must also make sure that $\Lambda \ll 1$ so that the lower-helicity-band approximation holds. Whether these two statements are consistent depends on the low-energy behaviour of $\Sigma(E)$ to be derived. Note that the prefactor in Eq. (F.22) must satisfy $n_i/m \ll \Lambda^2 E_0$ so that the average impurity spacing is much larger than the inverse of the momentum cutoff scale. So as long as the T-matrix does not diverge at low energy, we may safely choose $|z| < \Lambda \ll 1$. Thus, z lies within our semicircular contour and contributes a residue to the integral.

We will make use of the following identity:

$$\int_0^\pi \frac{d\phi \, e^{i\phi}}{z^2 - \Lambda^2 e^{2i\phi}} = \frac{2i}{z\Lambda} \operatorname{Arctanh}\left(\frac{z}{\Lambda}\right), \tag{F.28}$$

valid for $\Lambda > |z|$, with $\operatorname{Arctanh}(x)$ being the principal value of $\operatorname{arctanh}(x)$. This gives

$$\begin{aligned} I_-^l &\approx -\frac{i\delta_l^*}{z} - \frac{i\Lambda\delta_l^*}{\pi}\left(\frac{2i}{z\Lambda}\operatorname{Arctanh}(z/\Lambda)\right) \\ &= -i\frac{\delta_l^*}{z} + \frac{2\delta_l^*}{\pi\Lambda} + \mathcal{O}(|z|^2/\Lambda^3). \end{aligned} \tag{F.29}$$

This results in the self-energy (5.46), which indeed satisfies $|z| < \Lambda \ll 1$.

F.3 Density of states

We may apply the same semicircle contour from the previous section to evaluate the integral in the density of states. From (5.52),

$$g(E) = -\frac{m}{\pi^2}\,\mathrm{Im}\,\tilde{\Sigma}/E_0 \int_{-\Lambda}^{\Lambda} \frac{d\epsilon(\epsilon+1)}{[(E+\tilde{\mu}-\mathrm{Re}\,\tilde{\Sigma})/E_0-\epsilon^2]^2+(\mathrm{Im}\,\tilde{\Sigma}/E_0)^2}. \tag{F.30}$$

The ϵ term in the numerator is odd, so we need only evaluate the integral

$$g(E) = -\frac{m}{\pi^2}\frac{\mathrm{Im}\,\tilde{\Sigma}}{E_0}\int_{-\Lambda}^{\Lambda}\frac{d\epsilon}{(a-\epsilon^2)^2+b^2}, \tag{F.31}$$

where $a \equiv (E+\tilde{\mu}-\mathrm{Re}\,\tilde{\Sigma})/E_0$ and $b \equiv \mathrm{Im}\,\tilde{\Sigma}/E_0$. The integrand now has two poles in the upper half-plane, $\epsilon = \mp z_\pm \equiv \mp\sqrt{a \pm ib}$, both with magnitude $(a^2+b^2)^{1/4}$. By the same reasoning as before, these poles are contained within the semicircle of radius Λ and therefore contribute residues to the integral. The integral over the semicircle is given by

$$\begin{aligned} & i\Lambda\int_0^\pi \frac{d\phi\, e^{i\phi}}{(a-\Lambda^2 e^{2i\phi})^2+b^2} \\ = \;& \frac{-\Lambda}{2b}\left(\int_0^\pi \frac{d\phi\, e^{i\phi}}{z_+^2-\Lambda^2e^{2i\phi}} - \int_0^\pi \frac{d\phi\, e^{i\phi}}{z_-^2-\Lambda^2e^{2i\phi}}\right) \qquad \text{(F.32)} \\ = \;& -\frac{i}{b}\left[\frac{1}{z_+}\,\mathrm{Arctanh}(z_+/\Lambda) - \frac{1}{z_-}\,\mathrm{Arctanh}(z_-/\Lambda)\right], \qquad \text{(F.33)} \end{aligned}$$

using (F.28) again. The result is zero to order $|z|^2/\Lambda^3$. Thus we are just left with the residue contribution,

$$\begin{aligned} g(E) &= \frac{m}{\pi^2}\frac{\mathrm{Im}\,\tilde{\Sigma}}{E_0}\frac{\pi}{2b}\left(\frac{1}{\sqrt{a+ib}}+\frac{1}{\sqrt{a-ib}}\right) && \text{(F.34)} \\ &= \frac{m}{\pi}\,\mathrm{Re}\left(\sqrt{\frac{E_0}{E+\tilde{\mu}-\tilde{\Sigma}(E)}}\right). && \text{(F.35)} \end{aligned}$$

F.4 Advanced-retarded integrals

It turns out that all the integrals that enter the advanced-retarded part of the conductivity are simply higher moments of the density of states integral and can be solved analogously. We will look at the first three moments, denoted P_1, P_2, P_3. From (5.52) and (5.57), we immediately see that

$$P_1 \equiv \int_{k_0(1-\Lambda)}^{k_0(1+\Lambda)} dp\; pG^A(p,E)G^R(p,E) \tag{F.36}$$

$$= \frac{-2\pi^2}{E_0 \operatorname{Im}\tilde{\Sigma}} g(E). \tag{F.37}$$

Likewise,

$$P_2 \equiv \int_{k_0(1-\Lambda)}^{k_0(1+\Lambda)} dp\; \frac{p^2}{m} G^A(p,E)G^R(p,E) \tag{F.38}$$

$$= \frac{k_0^3}{mE_0^2} \int_{-\Lambda}^{\Lambda} \frac{d\epsilon \epsilon^2}{(a-\epsilon^2)^2+b^2} + \lambda P_1. \tag{F.39}$$

This time the integration over the semicircle gives

$$\begin{aligned} & i\Lambda^3 \int_0^\pi \frac{d\phi\; e^{3i\phi}}{(a-\Lambda^2 e^{2i\phi})^2+b^2} \\ = \;& \frac{i}{b}[z_- \operatorname{Arctanh}(z_-/\Lambda) - z_+ \operatorname{Arctanh}(z_+/\Lambda)] \\ \approx \;& 2/\Lambda. \end{aligned} \tag{F.40}$$

Adding the residue contribution gives

$$P_2 = \lambda P_1 - \frac{4}{\lambda}\left(\frac{2}{\Lambda} + \frac{\pi}{\operatorname{Im}\tilde{\Sigma}} \operatorname{Re}\left(\sqrt{(E+\tilde{\mu})/E_0 - \tilde{\Sigma}(E)}\right)\right). \tag{F.41}$$

Lastly, the third moment can be obtained from the first two:

$$P_3 \equiv \int_{k_0(1-\Lambda)}^{k_0(1+\Lambda)} dp\; \frac{p^3}{m^2} G^A(p,E)G^R(p,E) \tag{F.42}$$

$$= 4\int_{-\Lambda}^{\Lambda} \frac{d\epsilon(\epsilon+1)^3}{(1-\epsilon^2)^2+b^2} \tag{F.43}$$

$$= \lambda(3P_2 - 2\lambda P_1). \tag{F.44}$$

Appendix G

Mean-field theory for superconductivity in tight-binding models

Here we derive the BCS gap equations for the models discussed in Chapters 7 and 8.

G.1 Extended Hubbard model without spin-orbit coupling

The Fourier transform of the extended Hubbard model reads

$$\begin{aligned} H &= \sum_{\mathbf{k},\sigma} \xi_{\mathbf{k}} c^{\dagger}_{\mathbf{k}\sigma} c_{\mathbf{k}\sigma} + \frac{1}{N} \sum_{\mathbf{k}\mathbf{k}'\mathbf{q}} U c^{\dagger}_{\mathbf{k}\uparrow} c^{\dagger}_{\mathbf{q}\downarrow} c_{\boldsymbol{k}'\downarrow} c_{\boldsymbol{k}-\boldsymbol{k}'+\boldsymbol{q}\uparrow} \\ &\quad -\frac{1}{N} \sum_{\sigma\sigma'} \sum_{\boldsymbol{k}\boldsymbol{k}'\boldsymbol{q}} V[\cos(k_x - k'_x) + \cos(k_y - k'_y)] c^{\dagger}_{\mathbf{k}\sigma} c^{\dagger}_{\mathbf{q}\sigma'} c_{\boldsymbol{k}'\sigma} c_{\boldsymbol{k}-\boldsymbol{k}'+\boldsymbol{q}\sigma'}, \end{aligned} \tag{G.1}$$

where $\xi_{\mathbf{k}} = -2t(\cos k_x + \cos k_y) - \mu$, and N is the total number of sites in the lattice.

A reduced Hamiltonian containing only interactions between pairs of opposite momenta may be written as

$$H = \sum_{\mathbf{k},\sigma} \xi_{\mathbf{k}} c^{\dagger}_{\mathbf{k}\sigma} c_{\mathbf{k}\sigma} + \frac{1}{2N} \sum_{\boldsymbol{k}\boldsymbol{k}'} \sum_{\alpha\beta\gamma\delta} V_{\alpha\beta\gamma\delta}(\boldsymbol{k}, \boldsymbol{k}') c^{\dagger}_{\boldsymbol{k}\alpha} c^{\dagger}_{-\boldsymbol{k}\beta} c_{-\boldsymbol{k}'\gamma} c_{\boldsymbol{k}'\delta}, \tag{G.2}$$

where the non-zero components of the interaction are

$$V_{\uparrow\downarrow\downarrow\uparrow} = V_{\downarrow\uparrow\uparrow\downarrow} = \frac{1}{2}[U + 4V(s_{\boldsymbol{k}}s_{\boldsymbol{k}'} + d_{\boldsymbol{k}}d_{\boldsymbol{k}'}) + 2V(\sin k_x \sin k'_x + \sin k_y \sin k'_y)] \tag{G.3}$$

$$V_{\uparrow\downarrow\uparrow\downarrow} = V_{\downarrow\uparrow\downarrow\uparrow} = \frac{1}{2}[-U - 4V(s_{\boldsymbol{k}}s_{\boldsymbol{k}'} + d_{\boldsymbol{k}}d_{\boldsymbol{k}'}) + 2V(\sin k_x \sin k'_x + \sin k_y \sin k'_y)] \tag{G.4}$$

$$V_{\uparrow\uparrow\uparrow\uparrow} = V_{\downarrow\downarrow\downarrow\downarrow} = 4V(s_{\boldsymbol{k}}s_{\boldsymbol{k}'} + d_{\boldsymbol{k}}d_{\boldsymbol{k}'}) + 2V(\sin k_x \sin k'_x + \sin k_y \sin k'_y)], \tag{G.5}$$

here $s_{\boldsymbol{k}} \equiv \frac{1}{2}(\cos k_x + \cos k_y)$, and $d_{\boldsymbol{k}} \equiv \frac{1}{2}(\cos k_x - \cos k_y)$.

We now use mean-field theory, following Ref. [134]. Including all anomalous pairing mean fields,[1] the generic four-fermion interaction (suppressing momentum labels for now) becomes

$$c^\dagger_\nu c^\dagger_\mu c_{\mu'} c_{\nu'} \approx \langle c^\dagger_\nu c^\dagger_\mu \rangle c_{\mu'} c_{\nu'} + c^\dagger_\nu c^\dagger_\mu \langle c_{\mu'} c_{\nu'} \rangle - \langle c^\dagger_\nu c^\dagger_\mu \rangle \langle c_{\mu'} c_{\nu'} \rangle, \tag{G.6}$$

where we have removed terms of order $(c_\sigma c_{\sigma'} - \langle c_\sigma c_{\sigma'} \rangle)^2$ and their hermitian conjugates.

The result is a Hamiltonian with only fermion bilinears:

$$H_{\rm MF} = \sum_{\mathbf{k},\sigma} \xi_{\mathbf{k}} c^\dagger_{\mathbf{k}\sigma} c_{\mathbf{k}\sigma} - \frac{1}{2} \sum_{\boldsymbol{k}\sigma\sigma'} \Delta_{\boldsymbol{k}\sigma\sigma'} c^\dagger_{\boldsymbol{k}\sigma} c^\dagger_{-\boldsymbol{k}\sigma'} - \frac{1}{2} \sum_{\boldsymbol{k}\sigma\sigma'} \Delta^*_{\boldsymbol{k}\sigma\sigma'} c_{\boldsymbol{k}\sigma} c_{-\boldsymbol{k}\sigma'} + E_{\rm MF}, \tag{G.7}$$

where we have defined the gap function

$$\Delta_{\boldsymbol{k}\sigma\sigma'} \equiv -\frac{1}{N} \sum_{\boldsymbol{k}'\tau\tau'} V_{\sigma\sigma'\tau\tau'}(\boldsymbol{k}, \boldsymbol{k}') \langle c_{-\boldsymbol{k}'\tau} c_{\boldsymbol{k}'\tau'} \rangle, \tag{G.8}$$

and the energy due to the product of mean fields

$$E_{\rm MF} \equiv -\frac{1}{2N} \sum_{\boldsymbol{k}\boldsymbol{k}'} \sum_{\sigma\sigma'\tau\tau'} V_{\sigma\sigma'\tau\tau'}(\boldsymbol{k}, \boldsymbol{k}') \langle c^\dagger_{\boldsymbol{k}\sigma} c^\dagger_{-\boldsymbol{k}\sigma'} \rangle \langle c_{-\boldsymbol{k}'\tau} c_{\boldsymbol{k}'\tau'} \rangle. \tag{G.9}$$

[1] We ignore Hartree-Fock terms here. These terms will renormalize the bandwidth and the chemical potential, but will not qualitatively change our results [91].

This may be compactly written as

$$H_{\rm MF} = \sum_{\boldsymbol{k}} (\psi^\dagger_{\boldsymbol{k}} h_{\boldsymbol{k}} \psi_{\boldsymbol{k}} + \xi_{\boldsymbol{k}}) + E_{\rm MF}, \tag{G.10}$$

where

$$\psi_{\boldsymbol{k}} \equiv \begin{pmatrix} c_{\boldsymbol{k}\uparrow} \\ c_{\boldsymbol{k}\downarrow} \\ c^\dagger_{-\boldsymbol{k}\uparrow} \\ c^\dagger_{-\boldsymbol{k}\downarrow} \end{pmatrix}; \quad h_{\boldsymbol{k}} = \frac{1}{2} \begin{pmatrix} \xi_{\boldsymbol{k}} \mathbb{I} & \Delta_{\boldsymbol{k}} \\ \Delta^\dagger_{\boldsymbol{k}} & -\xi_{\boldsymbol{k}} \mathbb{I} \end{pmatrix}. \tag{G.11}$$

Here $\mathbb{I}$ is the 2×2 identity matrix, and $\Delta_{\boldsymbol{k}}$ is the 2×2 matrix with components $\Delta_{\boldsymbol{k}'\sigma\sigma'}$. We will exclusively consider gap functions that are unitary: $\Delta^\dagger_{\boldsymbol{k}}\Delta_{\boldsymbol{k}} = |\Delta_{\boldsymbol{k}}|^2\mathbb{I}$, where $|\Delta_{\boldsymbol{k}}|^2 \equiv \frac{1}{2}\,\mathrm{Tr}\,\Delta^\dagger_{\boldsymbol{k}}\Delta_{\boldsymbol{k}}$. A non-unitary gap allows for spin-polarized mean fields ($\Delta_{\uparrow\uparrow}$ and $\Delta_{\downarrow\downarrow}$) to be arbitrary, and are only warranted in proximity to a ferromagnetic instability [134]. In particular, all superconductors that preserve time-reversal symmetry are unitary, as seen by the operation of time-reversal on the gap function $\Delta_{\boldsymbol{k}} \to \sigma_y \Delta^*_{\boldsymbol{k}} \sigma_y$. Moreover, some time-reversal symmetry-broken phases are unitary, including the so-called $s + id$ phase mentioned in Chapter 8.

$h_{\boldsymbol{k}}$ is diagonalized by the Bogoliubov transformation

$$U_{\boldsymbol{k}} = \begin{pmatrix} u_{\boldsymbol{k}} & v_{\boldsymbol{k}} \\ v^*_{-\boldsymbol{k}} & u^*_{-\boldsymbol{k}} \end{pmatrix}, \tag{G.12}$$

where

$$u_{\boldsymbol{k}} \equiv \frac{E_{\boldsymbol{k}} + \xi_{\boldsymbol{k}}}{\sqrt{2E_{\boldsymbol{k}}(E_{\boldsymbol{k}} + \xi_{\boldsymbol{k}})}}\mathbb{I} \tag{G.13}$$

$$v_{\boldsymbol{k}} \equiv \frac{-1}{\sqrt{2E_{\boldsymbol{k}}(E_{\boldsymbol{k}} + \xi_{\boldsymbol{k}})}}\Delta_{\boldsymbol{k}} \tag{G.14}$$

$$E_{\boldsymbol{k}} \equiv \sqrt{\xi^2_{\boldsymbol{k}} + |\Delta_{\boldsymbol{k}}|^2}. \tag{G.15}$$

The Hamiltonian transforms to

$$H_{\rm MF} = \sum_{\boldsymbol{k}} \Gamma^\dagger_{\boldsymbol{k}} U^\dagger_{\boldsymbol{k}} h_{\boldsymbol{k}} U_{\boldsymbol{k}} \Gamma_{\boldsymbol{k}} + E_g \tag{G.16}$$

$$= \frac{1}{2}\sum_{\boldsymbol{k}} \Gamma^\dagger_{\boldsymbol{k}} \begin{pmatrix} E_{\boldsymbol{k}}\mathbb{I} & 0 \\ 0 & -E_{\boldsymbol{k}}\mathbb{I} \end{pmatrix} \Gamma_{\boldsymbol{k}} + E_g. \tag{G.17}$$

Here we have used the fact that antisymmetry of $\Delta_{\boldsymbol{k}}$ requires that $v^T_{-\boldsymbol{k}} = -v_{\boldsymbol{k}}$ and $v^*_{-\boldsymbol{k}} = -v^\dagger_{\boldsymbol{k}}$ and we have defined the quasi-particle spinors

$$\Gamma_{\boldsymbol{k}} = \begin{pmatrix} \gamma_{\boldsymbol{k}\uparrow} \\ \gamma_{\boldsymbol{k}\downarrow} \\ \gamma^\dagger_{-\boldsymbol{k}\uparrow} \\ \gamma^\dagger_{-\boldsymbol{k}\downarrow} \end{pmatrix} \tag{G.18}$$

via $\psi_{\boldsymbol{k}} = U_{\boldsymbol{k}}\Gamma_{\boldsymbol{k}}$. We have also identified the ground state energy

$$E_g = E_{\mathrm{MF}} + \sum_{\boldsymbol{k}} (\xi_{\boldsymbol{k}} - E_{\boldsymbol{k}}). \tag{G.19}$$

In terms of these quasi-particle operators, we have

$$c_{\boldsymbol{k}\sigma} = u_{\boldsymbol{k}\sigma\sigma}\gamma_{\boldsymbol{k}\sigma} + \sum_{\sigma'} v_{\boldsymbol{k}\sigma\sigma'}\gamma^\dagger_{-\boldsymbol{k}\sigma'} \tag{G.20}$$

$$c_{-\boldsymbol{k}\sigma} = u_{\boldsymbol{k}\sigma\sigma}\gamma_{-\boldsymbol{k}\sigma} - \sum_{\sigma'} v_{\boldsymbol{k}\sigma'\sigma}\gamma^\dagger_{\boldsymbol{k}\sigma'}. \tag{G.21}$$

This allows us to evaluate the mean-field expectation value $\langle c_{-\boldsymbol{k}\tau}c_{\boldsymbol{k}\tau}\rangle$ since the $\gamma_{\boldsymbol{k}}$ operators satisfy the fermion anticommutation relations and therefore have the occupation number distribution $\langle\gamma^\dagger_{\boldsymbol{k}\sigma}\gamma_{\boldsymbol{k}\sigma}\rangle = f(E_{\boldsymbol{k}})$, where $f(E)$ is the Fermi function. The defining gap equation (G.8) then becomes the self-consistency condition

$$\Delta_{\boldsymbol{k}\sigma\sigma'} = -\frac{1}{N}\sum_{\boldsymbol{k}\tau\tau'} V_{\sigma\sigma'\tau\tau'}(\boldsymbol{k},\boldsymbol{k'})\Delta_{\boldsymbol{k'}\tau'\tau}g_{\boldsymbol{k'}}, \tag{G.22}$$

where we have defined $g_{\boldsymbol{k}} \equiv \frac{1}{2E_{\boldsymbol{k}}}(1 - 2f(E_{\boldsymbol{k}}))$.

It is conventional to separate the gap matrix into its singlet and triplet contributions:

$$\Delta^{\mathrm{sing}}_{\boldsymbol{k}} \equiv \frac{1}{2}(\Delta_{\boldsymbol{k}\uparrow\downarrow} - \Delta_{\boldsymbol{k}\downarrow\uparrow}) \tag{G.23}$$

$$\Delta^x_{\boldsymbol{k}} \equiv \frac{1}{2}(\Delta_{\boldsymbol{k}\downarrow\downarrow} - \Delta_{\boldsymbol{k}\uparrow\uparrow}) \tag{G.24}$$

$$\Delta^y_{\boldsymbol{k}} \equiv \frac{-i}{2}(\Delta_{\boldsymbol{k}\downarrow\downarrow} + \Delta_{\boldsymbol{k}\uparrow\uparrow}) \tag{G.25}$$

$$\Delta^z_{\boldsymbol{k}} \equiv \frac{1}{2}(\Delta_{\boldsymbol{k}\uparrow\downarrow} + \Delta_{\boldsymbol{k}\downarrow\uparrow}) \tag{G.26}$$

Since $\Delta_{-\boldsymbol{k}} = -\Delta_{\boldsymbol{k}}^T$, and $g_{\boldsymbol{k}} = g_{-\boldsymbol{k}}$, the singlet gap equation only contains contributions from the part of the interaction that is parity-even.

$$\Delta_{\boldsymbol{k}}^{\text{sing}} = -\frac{1}{2N}\sum_{\boldsymbol{k}'}[(V_{\uparrow\downarrow\downarrow\uparrow} - V_{\downarrow\uparrow\downarrow\uparrow})\Delta_{\boldsymbol{k}'\uparrow\downarrow} + (V_{\uparrow\downarrow\uparrow\downarrow} - V_{\downarrow\uparrow\uparrow\downarrow})\Delta_{\boldsymbol{k}'\downarrow\uparrow}]g_{\boldsymbol{k}'} \tag{G.27}$$

$$= -\frac{1}{N}\sum_{\boldsymbol{k}'}[U + 4V(s_{\boldsymbol{k}}s_{\boldsymbol{k}'} + d_{\boldsymbol{k}}d_{\boldsymbol{k}'})]\Delta_{\boldsymbol{k}'}^{\text{sing}}g_{\boldsymbol{k}'}. \tag{G.28}$$

Likewise, the triplet parts only contain contributions from the part of the interaction that is parity-odd. In fact, in this model all triplet components satisfy the same gap equation

$$\Delta_{\boldsymbol{k}}^{\lambda} = -\frac{1}{N}\sum_{\boldsymbol{k}'} 2V(\sin k_x \sin k_x' + \sin k_y \sin k_y')\Delta_{\boldsymbol{k}'}^{\lambda}g_{\boldsymbol{k}'}, \tag{G.29}$$

for $\lambda = x, y, z$.

G.2 Rashba model with correlated hopping

In the spin basis, we Fourier transform the model considered in Chapter 7, keeping only interactions between pairs of zero total momentum:

$$\begin{aligned} H = & \sum_{\boldsymbol{k},\sigma}(\epsilon_{\boldsymbol{k}} - \mu)c_{\boldsymbol{k}\sigma}^\dagger c_{\boldsymbol{k}\sigma} \\ & +2V_{\text{SO}}\sum_{\boldsymbol{k}}\left(\sin k_y(c_{\boldsymbol{k}\uparrow}^\dagger c_{\boldsymbol{k}\downarrow} + c_{\boldsymbol{k}\downarrow}^\dagger c_{\boldsymbol{k}\uparrow}) + i\sin k_x(c_{\boldsymbol{k}\uparrow}^\dagger c_{\boldsymbol{k}\downarrow} - c_{\boldsymbol{k}\downarrow}^\dagger c_{\boldsymbol{k}\uparrow})\right) \\ & +\frac{1}{N}\sum_{\boldsymbol{k}}V^0(\boldsymbol{k},\boldsymbol{k}')c_{\boldsymbol{k}\uparrow}^\dagger c_{-\boldsymbol{k}\downarrow}^\dagger c_{-\boldsymbol{k}'\downarrow}c_{\boldsymbol{k}'\uparrow} \\ & +\frac{1}{N}\sum_{\mathbf{k}\mathbf{k}'}\sum_{\alpha\beta}\left(V_{\alpha\beta}^{\text{R}}(\boldsymbol{k}')c_{\mathbf{k}\alpha}^\dagger c_{-\mathbf{k}\beta}^\dagger c_{\mathbf{k}'\alpha}c_{-\mathbf{k}'\alpha} + V_{\alpha\beta}^{\text{R}}(\boldsymbol{k})c_{\mathbf{k}\beta}^\dagger c_{-\mathbf{k}\beta}^\dagger c_{\mathbf{k}'\beta}c_{-\mathbf{k}'\alpha}\right), \end{aligned} \tag{G.30}$$

where $\epsilon_{\mathbf{k}} \equiv -2t(\cos k_x + \cos k_y)$ and $V^0(\boldsymbol{k},\boldsymbol{k}') \equiv U - 2\frac{\Delta t}{t}(\epsilon_{\boldsymbol{k}} + \epsilon_{\boldsymbol{k}'})$ are the dispersion and interaction in the absence of spin-orbit coupling. The correlated hopping and Rashba terms are coupled via the interaction $V_{\alpha\beta}^{\text{R}}(\boldsymbol{k}) \equiv -2V_{\text{SO}}\frac{\Delta t}{t}(\sin k_x\sigma_{\alpha\beta}^y + \sin k_y\sigma_{\alpha\beta}^x)$.

Next, we transform the Hamiltonian to the Rashba helicity basis, with band index $s = \pm 1$ and dispersion $\epsilon_{\boldsymbol{k}s} = \epsilon_{\boldsymbol{k}} + 2sV_{\text{SO}}\sqrt{\sin^2 k_x + \sin^2 k_y}$. We retain only interaction

terms involving intra-band pairs, leaving the effective Hamiltonian

$$H = \sum_{\mathbf{k}s}(\epsilon_{\mathbf{k}s}-\mu)c^\dagger_{\mathbf{k}s}c_{\mathbf{k}s} + \frac{1}{4N}\sum_{\mathbf{k}\mathbf{k}'}\sum_{ss'}V_{ss'}(\mathbf{k},\mathbf{k}')c^\dagger_{\mathbf{k}s}c^\dagger_{-\mathbf{k}s}c_{-\mathbf{k}'s'}c_{\mathbf{k}'s'}, \quad \text{(G.31)}$$

where

$$\begin{aligned} V_{ss'}(\mathbf{k},\mathbf{k}') &= s'e^{i\theta(\boldsymbol{k}')}se^{-i\theta(\boldsymbol{k})}\Big(U + 8\Delta t(s_{\boldsymbol{k}}+s_{\boldsymbol{k}'}) \\ &\quad -4V_{\mathrm{SO}}\frac{\Delta t}{t}[s'\sqrt{\sin^2 k'_x+\sin^2 k'_y}+s\sqrt{\sin^2 k_x+\sin^2 k_y}]\Big). \quad \text{(G.32)}\end{aligned}$$

We have defined $s_{\boldsymbol{k}} \equiv \frac{1}{2}(\cos k_x + \cos k_y)$, as in Appendix G.1.

This time, we choose a pairing mean field of time-reversed electron pairs. As discussed in Chapter 7, this is represented in the helicity basis as $b_{\boldsymbol{k}s} \equiv se^{i\theta(\boldsymbol{k})}\langle c_{-\boldsymbol{k}s}c_{\boldsymbol{k}s}\rangle$. Writing $c_{-\boldsymbol{k}s}c_{\boldsymbol{k}s} = se^{-i\theta(\boldsymbol{k})}b_{\boldsymbol{k}s} + \delta c_{\boldsymbol{k}s}$ and neglecting terms of order $(\delta c_{\boldsymbol{k}s})^2$, we get the mean field Hamiltonian

$$\begin{aligned} H_{\mathrm{MF}} &= \sum_{\mathbf{k}s}(\epsilon_{\mathbf{k}s}-\mu)c^\dagger_{\mathbf{k}s}c_{\mathbf{k}s} - \frac{1}{2}\sum_{\mathbf{k}s}\Delta^*_{\mathbf{k}s}c_{-\mathbf{k}s}c_{\mathbf{k}s} \\ &\quad -\frac{1}{2}\sum_{\mathbf{k}s}\Delta_{\mathbf{k}s}c^\dagger_{\mathbf{k}s}c^\dagger_{-\mathbf{k}s} + \frac{1}{2}\sum_{\mathbf{k}s}\Delta_{\mathbf{k}s}se^{i\theta(\boldsymbol{k})}b^*_{\mathbf{k}s},\end{aligned} \quad \text{(G.33)}$$

where we have defined the gap parameter as

$$\Delta_{\mathbf{k}s} \equiv -\frac{1}{2N}\sum_{\mathbf{k}'s'}V_{ss'}(\mathbf{k},\mathbf{k}')s'e^{-i\theta(\boldsymbol{k}')}b_{\mathbf{k}'s'}. \quad \text{(G.34)}$$

Note that this gap function may be written as $\Delta_{\mathbf{k}s} = se^{-i\theta(\boldsymbol{k})}\bar{\Delta}_{\mathbf{k}s}$, where $\bar{\Delta}_{\mathbf{k}s}$ transforms under an irreducible representation of the lattice point group. The unusual phase factor $se^{-i\theta(\boldsymbol{k})}$ that is local in k-space is a feature of spin-orbit coupling and is discussed in Ref. [123].

The mean-field Hamiltonian may be diagonalized by means of a new Bogoliubov transformation

$$c_{\boldsymbol{k}s} = u^*_{\boldsymbol{k}s}\hat{\alpha}_{\boldsymbol{k}s} - se^{-i\theta(\boldsymbol{k})}v_{\boldsymbol{k}s}\hat{\alpha}^\dagger_{-\boldsymbol{k}s}, \quad \text{(G.35)}$$

where the coefficients $u_{\boldsymbol{k}s}$, $v_{\boldsymbol{k}s}$ are chosen to satisfy $u_{\boldsymbol{k}s} = u_{-\boldsymbol{k}s}$, $v_{\boldsymbol{k}s} = v_{-\boldsymbol{k}s}$, and $|u_{\boldsymbol{k}s}|^2 + |v_{\boldsymbol{k}s}|^2 = 1$. It is readily found that the values of these parameters that diagonalize the

Hamiltonian are given by the equations

$$|v_{\boldsymbol{k}s}|^2 = \frac{1}{2}(1-(\epsilon_{\boldsymbol{k}s}-\mu)/E_{\boldsymbol{k}s}) \tag{G.36}$$

$$|u_{\boldsymbol{k}s}|^2 = \frac{1}{2}(1+(\epsilon_{\boldsymbol{k}s}-\mu)/E_{\boldsymbol{k}s}) \tag{G.37}$$

$$u_{\boldsymbol{k}s}v^*_{\boldsymbol{k}s} = -\frac{\bar{\Delta}^*_{\boldsymbol{k}s}}{2E_{\boldsymbol{k}s}}, \tag{G.38}$$

where

$$E_{\boldsymbol{k}s} \equiv \sqrt{(\epsilon_{\boldsymbol{k}s}-\mu)^2+|\Delta_{\boldsymbol{k}s}|^2}. \tag{G.39}$$

The final mean-field Hamiltonian then reads

$$H_{\mathrm{MF}} = \sum_{\boldsymbol{k}s} E_{\boldsymbol{k}s}\hat{\alpha}^\dagger_{\boldsymbol{k}s}\hat{\alpha}_{\boldsymbol{k}s} + E_g, \tag{G.40}$$

where the ground state energy is given by

$$E_g = \frac{1}{2}\sum_{\boldsymbol{k}s}\left[(\epsilon_{\boldsymbol{k}s}-\mu) - E_{\boldsymbol{k}s} + \bar{\Delta}_{\boldsymbol{k}s}b^*_{\boldsymbol{k}s}\right]. \tag{G.41}$$

In terms of the new fermionic quasiparticle operators, we have

$$b_{\boldsymbol{k}s} = u^*_{\boldsymbol{k}s}v_{\boldsymbol{k}s}(2\langle\hat{\alpha}^\dagger_{\boldsymbol{k}s}\hat{\alpha}_{\boldsymbol{k}s}\rangle - 1), \tag{G.42}$$

which means the gap function must satisfy the finite temperature self-consistency condition

$$\Delta_{\boldsymbol{k}s} = -\frac{1}{2N}\sum_{\boldsymbol{k}'s'} V_{ss'}(\boldsymbol{k},\boldsymbol{k}')\Delta_{\boldsymbol{k}'s'}g_{\boldsymbol{k}s}, \tag{G.43}$$

where $g_{\boldsymbol{k}s} \equiv \frac{1}{2E_{\boldsymbol{k}s}}(1-2f(E_{\boldsymbol{k}s}))$ and $f(E)$ is the Fermi function.

G.3 Rashba superconducting density of states

Here we derive the superconducting density of states for the Rashba-Hubbard model with correlated hopping. Analogous derivations can be found in e.g. Ref. [121, 135].

The many-body theory of superconductivity requires knowledge of both the Green's function

$$\mathcal{G}_s(\boldsymbol{k},\tau) = -\langle Tc_{\boldsymbol{k}s}(\tau)c^\dagger_{\boldsymbol{k}s}(0)\rangle, \tag{G.44}$$

and the *anomalous* Green's function

$$\mathcal{F}_s(\boldsymbol{k},\tau) \equiv -\langle T c^\dagger_{-\boldsymbol{k}s}(\tau) c^\dagger_{\boldsymbol{k}s}(0)\rangle, \tag{G.45}$$

for each helicity band s (in the absence of interband pairing, the Green's function only has one band index). We work in imaginary time τ and T represents the imaginary-time-ordered product. Each Green's function satisfies an equation of motion:

$$\begin{aligned}
\partial_\tau \mathcal{G}_s(\boldsymbol{k},\tau) &= -\delta(\tau) - \langle T[H(\tau), c_{\boldsymbol{k}s}(\tau)] c^\dagger_{\boldsymbol{k}s}(0)\rangle & \text{(G.46)}\\
\partial_\tau \mathcal{F}_s(\boldsymbol{k},\tau) &= -\langle T[H(\tau), c^\dagger_{-\boldsymbol{k}s}(\tau)] c^\dagger_{\boldsymbol{k}s}(0)\rangle. & \text{(G.47)}
\end{aligned}$$

The Hamiltonian H is given by Eq. (G.33), and may be split into an unperturbed part H_0 and an interaction part V_{int} given by the $\Delta_{\boldsymbol{k}s}$-dependent terms. Making use of the commutators

$$\begin{aligned}
[H_0, c_{\boldsymbol{k}s}] &= -(\epsilon_{\boldsymbol{k}s} - \mu) c_{\boldsymbol{k}s} & \text{(G.48)}\\
\left[H_0, c^\dagger_{-\boldsymbol{k}s}\right] &= (\epsilon_{\boldsymbol{k}s} - \mu) c^\dagger_{-\boldsymbol{k}s} & \text{(G.49)}\\
[V_{\text{int}}, c_{\boldsymbol{k}s}] &= \Delta_{\boldsymbol{k}s} c^\dagger_{-\boldsymbol{k}s} & \text{(G.50)}\\
\left[V_{\text{int}}, c^\dagger_{-\boldsymbol{k}s}\right] &= \Delta^*_{\boldsymbol{k}s} c_{\boldsymbol{k}s}, & \text{(G.51)}
\end{aligned}$$

we obtain the coupled equations of motion

$$\begin{aligned}
\partial_\tau \mathcal{G}_s(\boldsymbol{k},\tau) &= -\delta(\tau) - (\epsilon_{\boldsymbol{k}s} - \mu)\mathcal{G}_s(\boldsymbol{k},\tau) + \Delta_{\boldsymbol{k}s}\mathcal{F}_s(\boldsymbol{k},\tau) & \text{(G.52)}\\
\partial_\tau \mathcal{F}_s(\boldsymbol{k},\tau) &= (\epsilon_{\boldsymbol{k}s} - \mu)\mathcal{F}_s(\boldsymbol{k},\tau) + \Delta^*_{\boldsymbol{k}s}\mathcal{G}_s(\boldsymbol{k},\tau). & \text{(G.53)}
\end{aligned}$$

Introducing the Matsubara frequencies $k_n = (2n+1)\pi/\beta$, $n \in \mathbb{Z}$, and Fourier transforming gives

$$\begin{aligned}
ik_n \mathcal{G}_s(\boldsymbol{k}, ik_n) &= 1 + (\epsilon_{\boldsymbol{k}s} - \mu)\mathcal{G}_s(\boldsymbol{k}, ik_n) - \Delta_{\boldsymbol{k}s}\mathcal{F}_s(\boldsymbol{k}, ik_n) & \text{(G.54)}\\
ik_n \mathcal{F}_s(\boldsymbol{k}, ik_n) &= -(\epsilon_{\boldsymbol{k}s} - \mu)\mathcal{F}_s(\boldsymbol{k}, ik_n) - \Delta^*_{\boldsymbol{k}s}\mathcal{G}_s(\boldsymbol{k}, ik_n), & \text{(G.55)}
\end{aligned}$$

as found in Ref. [98]. The solution to these equations for the Matsubara Green's function is

$$\mathcal{G}_s(\boldsymbol{k}, ik_n) = \frac{ik_n + \epsilon_{\boldsymbol{k}s} - \mu}{(ik_n)^2 - (\epsilon_{\boldsymbol{k}s} - \mu)^2 - |\Delta_{\boldsymbol{k}s}|^2}, \tag{G.56}$$

whose poles give the excitation energies $E_{\boldsymbol{k}s}$ (G.39).

The analytic continuation $ik_n \to \omega + i\eta$ gives the retarded Green's function, from which we extract the imaginary part to get the spectral function

$$\begin{aligned} \mathrm{Im}G_s^R(\boldsymbol{k},\omega) &= \lim_{\eta\to 0} \mathrm{Im}\left(\frac{u_{\boldsymbol{k}s}^2}{\omega + i\eta - E_{\boldsymbol{k}s}} + \frac{v_{\boldsymbol{k}s}^2}{\omega + i\eta + E_{\boldsymbol{k}s}}\right) && \text{(G.57)} \\ &= -\pi\left[u_{\boldsymbol{k}s}^2\delta(\omega - E_{\boldsymbol{k}s}) + v_{\boldsymbol{k}s}^2\delta(\omega + E_{\boldsymbol{k}s})\right], && \text{(G.58)} \end{aligned}$$

using the identity (2.22).

The superconducting density of states is then simply

$$\begin{aligned} N^{SC}(\omega) &= -\frac{1}{N}\sum_{\boldsymbol{k}s}\frac{\mathrm{Im}G_s^R(\boldsymbol{k},\omega)}{\pi} && \text{(G.59)} \\ &= \frac{1}{N}\sum_{\boldsymbol{k}s}\left[u_{\boldsymbol{k}s}^2\delta(\omega - E_{\boldsymbol{k}s}) + v_{\boldsymbol{k}s}^2\delta(\omega + E_{\boldsymbol{k}s})\right]. && \text{(G.60)} \end{aligned}$$

We may replace the sum over $\boldsymbol{k}$ with an integral over the single-particle normal state energies ϵ:

$$N^{SC}(\omega) = \frac{1}{2}\int d\epsilon g(\epsilon)\left[\left(1 + \frac{\epsilon - \mu}{E(\epsilon)}\right)\delta(\omega - E(\epsilon)) + \left(1 - \frac{\epsilon - \mu}{E(\epsilon)}\right)\delta(\omega + E(\epsilon))\right], \quad \text{(G.61)}$$

where $g(\epsilon)$ is the normal state density of states. We define $\epsilon_\pm$ as the solution to $\omega \pm E(\epsilon_\pm) = 0$, and note that the only non-zero contributions to the delta-functions occur when ω is outside the energy gap defined by Eq. (7.25) ($\omega > E_{\min}$ for the first term above, and $\omega < -E_{\min}$ for the second term). The resulting density of states is

$$\begin{aligned} N^{SC}(\omega) = \frac{1}{2}\sum_{\nu=\pm 1}\Bigg(&\frac{g(\epsilon_\nu)(\omega + \epsilon_\nu - \mu)}{|\epsilon_\nu - \mu - \Delta^s\Delta(\epsilon_\nu)/(4t)|}\theta(\omega - E_{\min}) \\ &+ \frac{g(\epsilon_\nu)(-\omega - \epsilon_\nu + \mu)}{|\epsilon_\nu - \mu - \Delta^s\Delta(\epsilon_\nu)/(4t)|}\theta(-\omega - E_{\min})\Bigg). \end{aligned} \quad \text{(G.62)}$$

This expression is used to compute tunneling currents as in Fig. 7.9.

Appendix H

Critical points of the free energy

The gap equations for the extended Hubbard model (8.6)-(8.10) can be reproduced from the solutions to the functional minimization problem:

$$\frac{\delta f}{\delta \Delta_{\boldsymbol{q}}^{\text{sing}}} = 0; \quad \frac{\delta f}{\delta \Delta_{\boldsymbol{q}}^{\lambda}} = 0 \tag{H.1}$$

while the chemical potential is fixed by the number equation

$$\frac{\partial f}{\partial \mu} = 0, \tag{H.2}$$

which upon using (H.1) becomes,

$$n = 1 - \frac{2}{N} \sum_{\boldsymbol{k}} \xi_{\boldsymbol{k}} g_{\boldsymbol{k}}. \tag{H.3}$$

The functional minimization of f can be thought of as a minimization with respect to the N terms of $\Delta_{\boldsymbol{k}}$ (one for each value of $\boldsymbol{k}$). However, we can alternatively think of this as a minimization over a lower-dimensional parameter space (Δ_0, Δ_s, Δ_d, Δ_x^{λ}, Δ_y^{λ}) along with the constraint (8.15), so that we need only solve

$$\frac{\partial f}{\partial \Delta_i} = \frac{\partial f}{\partial \Delta_i^{\lambda}} = \frac{\partial f}{\partial \mu} = 0 \tag{H.4}$$

for the all the components $\Delta_i \in \{\Delta_0, \Delta_s, \Delta_d\}$ and $\Delta_i^\lambda \in \{\Delta_x^\lambda, \Delta_y^\lambda\}$. The first derivative is given by

$$\frac{\partial f}{\partial \Delta_i} = \frac{2}{N}\sum_{\boldsymbol{k}} x_{\boldsymbol{k}}^i G_{\boldsymbol{k}}\left[\Delta_{\boldsymbol{k}}^{\text{sing}*} + \frac{1}{N}\sum_{\boldsymbol{k}'} V_{\boldsymbol{k}\boldsymbol{k}'}^{\text{sing}} \Delta_{\boldsymbol{k}'}^{\text{sing}*} g_{\boldsymbol{k}'}\right] \tag{H.5}$$

$$\frac{\partial f}{\partial \Delta_i^\lambda} = \frac{2}{N}\sum_{\boldsymbol{k}} x_{\boldsymbol{k}}^i G_{\boldsymbol{k}}\left[\Delta_{\boldsymbol{k}}^{\lambda *} + \frac{1}{N}\sum_{\boldsymbol{k}'} V_{\boldsymbol{k}\boldsymbol{k}'}^{\text{trip}} \Delta_{\boldsymbol{k}'}^{\lambda *} g_{\boldsymbol{k}'}\right], \tag{H.6}$$

where we have defined $G_{\boldsymbol{k}} \equiv g_{\boldsymbol{k}} + \frac{|\Delta_{\boldsymbol{k}}|^2}{E_{\boldsymbol{k}}}\frac{\partial g_{\boldsymbol{k}}}{\partial E_{\boldsymbol{k}}}$. Since $G_{\boldsymbol{k}}$ is positive definite, these equations simply restate what we already know; the critical points of f occur at the values of Δ_i that satisfy the gap equation. One conceptual advantage of this formulation is that we can now compute a simple Hessian in a low-dimensional parameter space. For simplicity, let us focus now on real singlet order parameters to better understand these critical points. In that case, the Hessian elements evaluated at the critical points are

$$\begin{aligned} H_{ij} &\equiv \left.\frac{\partial^2 f}{\partial \Delta_i \partial \Delta_j}\right|_{\text{c.p.}} \\ &= \frac{2}{N}\sum_{\boldsymbol{k}} x_{\boldsymbol{k}}^i G_{\boldsymbol{k}}\left(x_{\boldsymbol{k}}^j + \frac{1}{N}\sum_{\boldsymbol{k}'} V_{\boldsymbol{k}\boldsymbol{k}'} G_{\boldsymbol{k}'} x_{\boldsymbol{k}'}^j\right), \end{aligned} \tag{H.7}$$

where $G_{\boldsymbol{k}}$ is evaluated at the solutions to the gap equation.

It is important to note that the critical points have two symmetries apparent from the gap equation. First, there is inversion symmetry; if $(\Delta_0, \Delta_s, \Delta_d)$ is a critical point, then so is $(-\Delta_0, -\Delta_s, -\Delta_d)$. This is required by antisymmetry of the pair wavefunction. Second, there is mirror symmetry under reflection in the Δ_0-Δ_s plane, since any solution $(\Delta_0, \Delta_s, \Delta_d)$ has a corresponding solution $(\Delta_0, \Delta_s, -\Delta_d)$ upon replacing $k_x \leftrightarrow k_y$, $k_x' \leftrightarrow k_y'$. Moreover, the curvature (H.7) is a rank-2 tensor under these transformations. That is, under inversion,

$$H_{ij} \to \sum_{pq} \delta_{ip}\delta_{jq} H_{pq}, \tag{H.8}$$

and under reflection in the Δ_0-Δ_s plane,

$$H_{ij} \to \sum_{pq} (\delta_{ip} - 2\delta_{id}\delta_{pd})(\delta_{jq} - 2\delta_{jd}\delta_{qd}) H_{pq}. \tag{H.9}$$

This means that the gradient flow of f near the critical points respects these symmetries, and the *index* of any critical points related by these symmetries is the same. The index γ_i of a critical point i is defined as the number of orthogonal directions along which

i is a maxima of the corresponding function (in this case the free energy). The index plays a large role in the theory of *Morse functions* [125]. A Morse function is a smooth real function that has no degenerate critical points. For our purposes, the free energy is a Morse function, since the curvature can only vanish on a set of measure zero in the $\{T, U, V, n\}$ parameter space. As a consequence, the free energy satisfies the following Morse condition (valid for functions $f(\{\Delta_i\})$ that increase without bound as each $|\Delta_i|$ goes to infinity):

$$\sum_{i \in \{\text{critical points}\}} (-1)^{\gamma_i} = \chi(M), \tag{H.10}$$

where $\chi(M)$ is the Euler characteristic of the domain manifold of f [126]. We may choose M to be the three-dimensional space $\{\Delta_0, \Delta_s, \Delta_d\}$, or any of the pure subsets $\{\Delta_0, \Delta_s\}$ or $\{\Delta_d\}$, because any extrema of f on a pure subset is guaranteed to be a solution to the full gap equation. All of these cases correspond to flat manifolds with $\chi(M) = 1$. The combination of symmetries of f and the Morse condition restrict the possible minima of the free energy in this parameter space.

H.1 Corollaries of the Morse condition

The simplest question to ask is what can happen at T_c according to these restrictions. Above T_c we know the system is in the normal state, there is one critical point, and on any of the above manifolds, Eq. (H.10) reads

$$(-1)^0 = 1. \tag{H.11}$$

We immediately see that no mixed solution can emerge from this state. This is because mixed solutions are four-fold degenerate by inversion and mirror symmetry, so that the Morse condition reads

$$(-1)^{\gamma_N} + 4(-1)^{\gamma_m} = 1, \tag{H.12}$$

denoting the normal index by γ_N and the mixed index by γ_m. This equation has no integer solutions. Thus the condition expressed in Ref. [111] that mixed solutions cannot emerge at T_c is an immediate consequence of the symmetry of the gap equation.

We may also prove the uniqueness (modulo sign) of the pure d-wave solution. In fact, the following will hold for any single-parameter gap function, including the Hubbard model

with only on-site attraction. Existing proofs of the uniqueness the BCS gap solution are quite nontrivial [136]. Here we will see that it is a simple consequence of symmetry and the Morse condition.

Proof. For a single component gap $\Delta_{\boldsymbol{k}} = \Delta$, with a separable interaction $V_{\boldsymbol{k}\boldsymbol{k}'} = V x_{\boldsymbol{k}} x_{\boldsymbol{k}'}$, the Hessian reads

$$H = \frac{2}{N}\sum_{\boldsymbol{k}} x_{\boldsymbol{k}}^2 G_{\boldsymbol{k}}\left(1 + \frac{V}{N}\sum_{\boldsymbol{k}'} G_{\boldsymbol{k}'} x_{\boldsymbol{k}'}^2\right) \tag{H.13}$$

$$= \frac{2}{N}\sum_{\boldsymbol{k}} x_{\boldsymbol{k}}^2 G_{\boldsymbol{k}}\left(1 + \frac{V}{N}\sum_{\boldsymbol{k}'} x_{\boldsymbol{k}'}^2\left[g_{\boldsymbol{k}'} + \frac{|\Delta_{\boldsymbol{k}'}|^2}{E_{\boldsymbol{k}'}}\frac{\partial g_{\boldsymbol{k}'}}{\partial E_{\boldsymbol{k}'}}\right]\right). \tag{H.14}$$

The single-component gap equation reads

$$1 = -\frac{V}{N}\sum_{\boldsymbol{k}} x_{\boldsymbol{k}}^2 g_{\boldsymbol{k}}, \tag{H.15}$$

so that at a critical point

$$H = \frac{2V}{N^2}\sum_{\boldsymbol{k}\boldsymbol{k}'} x_{\boldsymbol{k}}^2 G_{\boldsymbol{k}} x_{\boldsymbol{k}'}^2 \frac{|\Delta_{\boldsymbol{k}'}|^2}{E_{\boldsymbol{k}'}}\frac{\partial g_{\boldsymbol{k}'}}{\partial E_{\boldsymbol{k}'}}.$$

$\frac{\partial g_{\boldsymbol{k}'}}{\partial E_{\boldsymbol{k}'}}$ is negative definite, while $G_{\boldsymbol{k}}$ is positive definite, so for any attractive interaction $V < 0$, the curvature is positive and all solutions must be minima of the free energy. Since, the solutions are symmetric under inversion $\Delta \to -\Delta$, they must come in pairs. For n such pairs, the Morse condition reads

$$(-1)^{\gamma_N} + 2n(-1)^0 = 1, \tag{H.16}$$

whose only solutions are $\{\gamma_N = 0, n = 0\}$ and $\{\gamma_N = 1, n = 1\}$.[1] Thus, the single-component BCS gap equation admits one solution modulo sign. □

Returning to the extended Hubbard model, this result applies to solutions that are pure d-wave (in this case, $x_{\boldsymbol{k}} \to d_{\boldsymbol{k}}$ and $V \to 4V$ in the arguments above), guaranteeing their uniqueness. In addition, this reasoning guarantees that as long as the d-wave solution exists, the normal state must be unstable. At a critical d-wave temperature T_c^d, two

[1] Since this is a one-dimensional problem, this last statement is just Rolle's theorem.

d-wave critical points emerge from the normal state critical point as the temperature is lowered. We now show that this kind of bifurcation of solutions is generic.

The solutions to the gap equation are continuous functions of T, so critical points cannot appear in pairs at arbitrary points in the parameter space but must grow from the normal state or an existing superconducting state as the temperature is lowered. The Morse condition then provides a conservation of indices. For example, a pure state with index γ_p that grows from the normal state at a temperature T_c^p is two-fold degenerate (barring pathological accidental degeneracies) and therefore must satisfy

$$(-1)^{\gamma_{N_1}} = (-1)^{\gamma_{N_2}} + 2(-1)^{\gamma_p}, \tag{H.17}$$

where γ_{N_1} is the index of the normal state at $T > T_c^p$, and γ_{N_2} is the index of the normal state at $T < T_c^p$. The solution is

$$\pm 1 = \mp 1 + 2(\pm 1). \tag{H.18}$$

So the normal state bifurcates into two pure states passing its index to the new solutions. The same thing occurs with mixed states which grow out of pure states according to

$$2(-1)^{\gamma_{p1}} = 2(-1)^{\gamma_{p2}} + 4(-1)^{\gamma_m}, \tag{H.19}$$

which is also solved by (H.18). A typical evolution of critical points as the temperature is lowered is shown in Fig. H.1.

Knowledge of these bifurcations provides an important numerical advantage for identifying the symmetry of the order parameter at a given temperature. This identification requires the global minimization of a multidimensional function that, as we have seen, is quite nonlinear. Without making use of these bifurcations, one would have to proceed by brute force search of a discretized parameter space in order to find all local minima [127]. Instead, we can leverage our knowledge by doing minimization within the lower-dimensional pure subspaces of the parameter space. The set of local minima found in this way might not contain the global minimum, but one of them will lie within the basin of attraction of the global minimum and can be used to initiate a local minimization procedure.

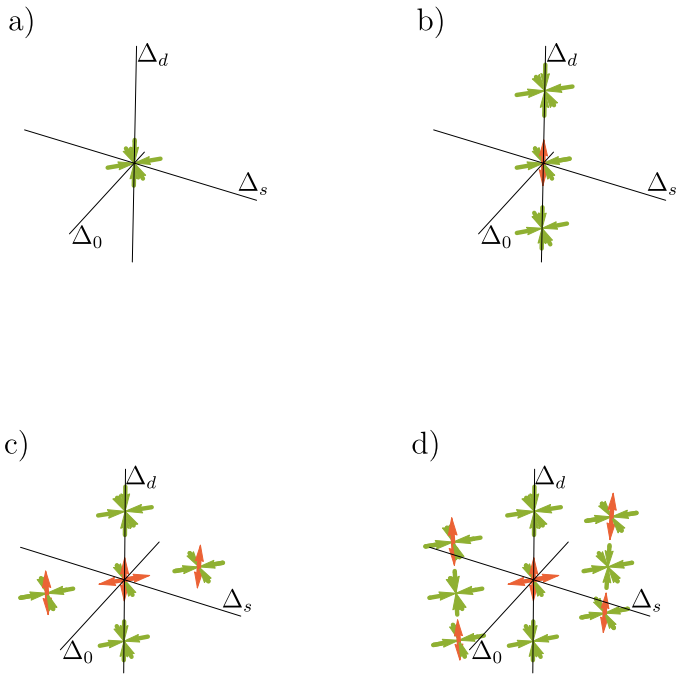

FIGURE H.1: Illustration of an evolution of solutions to the gap equation from high temperature (a), to low temperature (d). Inwards green arrows indicate minima of the free energy along those directions and outward red arrows indicate maxima along those directions. Note that in this example, the s-wave solution changes from a saddle point in (c) to a minimum in (d) by emitting a mixed critical point.